Tailoring the Etchability of Aluminium Foil by Laser Interference Metallurgy: Control of Pit Initiation Sites for High-Voltage Aluminium Capacitor Applications

DISSERTATION

zur Erlangung des Grades
des Doktors der Ingenieurwissenschaften
der Naturwissenschaftlich-Technischen Fakultät III
Chemie, Pharmazie, Bio- und Werkstoffwissenschaften
der Universität des Saarlandes

von

Mariela D'Alessandria

Saarbrücken

2010

Tag des Kolloquiums:	01.07.11
Dekan:	Prof. Dr. Wilhelm F. Maier
Berichterstatter:	Prof. Dr. Frank Mücklich
	Prof. Dr. Ralf Busch
Vorsitz:	Prof. Dr. Wilhelm F. Maier

Con todo mi amor a mis padres, hermanos y querido esposo

When God said "Let there be light"
he surely must have meant
perfectly coherent light.

Charles Townes

Acknowledgments

I would like to express my sincere gratitude to all the people who contributed with their expertise and encouraged me during the realisation of this Ph.D. thesis:

I am very thankful to Prof. Dr. Frank Mücklich (Functional Materials, Saarland University) for giving me the opportunity to work under his supervision in a very interesting research field and for his professional advice and scientific support.

I am grateful to Prof. Dr. Ralf Busch (Metallic Materials, Saarland University) for accepting the co-refereeing of this work and for his expert evaluation. His professional assistance and cooperation is greatly appreciated.

I acknowledge to Dr. Thomas Ebel and Dr. Evelina Oldani (Becromal S.p.A, Italy) partners of the project "Lasergestützte Mikro- Nanostrukturierung von 4N Aluminium" N°007197440158 for providing the fascinating issue developed in this work and for facilitating some of the studied materials. I want also to thank Dr. E. Oldani for the performance of the electrochemical etching test.

I am deeply grateful to Dr. Flavio Soldera for the proof reading and important suggestions about the scientific aspects of this work.

I would like to extend my thanks to Dr. Christian Holzapfel and Peter Leibenguth for their help on the TEM observations and Christoph Pauly for the EBSD characterisation of my samples. I also thank Dr. Andrés Lasagni for his help with laser assistance and useful discussion at the beginning of this thesis.

Many thanks also to Paula Souza for ongoing support and accurate reviewing of the manuscript.

I also thank Dr. Afrooz Barnoush and Mohammad Zamanzade (Prof. H. Vehoff) for their assistance in corrosion experiments.

I would also like to thank all my colleagues and the staff of the chair of Functional Materials for their constant support and friendly atmosphere over the course of all these years.

I express my gratitude to the German Academic Exchange Program (DAAD) for the funds granted to me.

Finally, special gratitude goes to my family, "mi amado francesito" Nicolas, and my friends for their constant support, unconditional love and kind words of encouragement in every moment.

Contents

Abstract

During the last decades, different surface patterning techniques have been developed to produce structures in the nano/submicron scale, Laser Interference Metallurgy (LIMET) being one of them. LIMET allows the production of direct periodic arrays over large areas by using the interference of several laser beams. This technique is an attractive tool to improve the etching process of anode aluminium during the manufacturing of high-voltage aluminium capacitors, where aluminium foils are etched so as to develop a high surface area thereby achieving the maximum possible capacitance.

The aim of this work was to develop a method for controlling the pit-site distribution during the etching process of aluminium foil. For this purpose, the mechanism that governs the surface patterning of metals and the physical/chemical changes induced by LIMET were investigated. It was demonstrated that the main forces producing the periodic structures on metallic surfaces are surface-tension-driven flow and recoil pressure. Moreover, the impact on aluminium etchability of ordered local oxidation and incorporation of small quantities of Pb and Cu was studied. It was found that periodic surface activation and/or passivation improve the pit distribution of the exposed aluminium. In all systems studied, the etching process followed the ordered array generated by laser interference. Finally, 3D quantitative characterisation of etched structures was performed using FIB tomography.

Kurzfassung

In den letzten Jahren wurden verschiedene Oberflächenbehandlungstechniken entwickelt, um Strukturen im Nano/Submikrometer-Bereich zu erzeugen, zu denen auch die Laser Interferenz Metallurgie (LIMET) zählt. LIMET ermöglicht die direkte Erzeugung von periodischen, großflächigen Strukturen durch die Interferenz einzelner Laserstrahlen. Diese Technik stellt ein vielversprechendes Werkzeug dar, um den Ätzprozess der Aluminiumanode für Hochspannungskondensatoren zu verbessern. Bei der Herstellung von Aluminium-Elektrolytkondensatoren werden Aluminiumfolien geätzt, um eine Vergrößerung der Oberfläche herbeizuführen und damit eine deutlich höhe Kapazität zu erzielen.

Das Ziel dieser Arbeit ist die Entwicklung eines Verfahrens zur Kontrolle der örtlichen Verteilung der beim Aluminiumätzprozess entstehenden Gruben. Es wurde demonstriert, dass die wichtigsten Effekte bei der Herstellung periodischer Strukturen sowohl der Oberflächenspannungsgradient als auch der Rückstoßdruck sind. Des Weiteren wurden die Auswirkungen von lokaler Oxidation und Einbau geringer Mengen von Pb und Cu auf die Ätzbarkeit von Aluminium untersucht. Es hat sich gezeigt, dass periodische Aktivierung und/oder Passivierung der Oberfläche die Grubenverteilung bei exponiertem Aluminium verbessert. In allen Fällen folgte der Ätzvorgang den durch Laserinterferenz vorgegebenen geordneten Mustern. Schließlich wurden die geätzten Strukturen mittels einer quantitativen 3D FIB-Tomographie charakterisiert.

Symbols and abbreviations

List of symbols

α	absorption coefficient
α_j	angle of the j-beam with respect to the perpendicular to the interference plane
β_T	volume expansion coefficient
ε	complex dielectric function, relative dielectric constant
ε_1	real part of the complex dielectric function
ε_2	imaginary part of the complex dielectric function
ϕ	incidence angle
ϕ_p	polarising angle or “Brewster” angle
γ	surface tension
γ_0	surface enthalpy
η	dynamic viscosity
κ	thermal conductivity
λ	wavelength
μ_0	permeability
ν_{vl}	velocity at the vapour – liquid interface
θ	incident angle of radiation for individual beams
ρ	density
σ	electrical conductivity
τ	surface shear stress
τ_e	collision time
τ_p	duration of laser pulse
ω_i	spatial directions of a cuboidal lattice in 3D image analysis
ω_p	electron plasma frequency
$1/\alpha$	optical absorption length
Λ_i	amplitude between the instabilities
ϵ_0	permittivity
A	absorptivity, constant of the recoil pressure, surface area
A_0	initial absorption of the surface
A_i	area of the orthogonal projection in *i*-direction
B	magnetic field
Bo	Bond number
B_0	magnetic field amplitude, constant of the recoil pressure

c	speed of light
C	capacitance of an aluminium electrolytic capacitor
Ca	capillary number
c_p	specific heat capacity
d	period
D	thermal diffusivity
$d\gamma/dx$	surface-tension gradient
d_c	electrode spacing (or thickness of the dielectric)
d_0	oxidation constant
E	electric field
e	charge of electron
E_0	electric field amplitude
erfc	error function
f_{LV}	vapour fraction
f_{SL}	solid fraction
FWHM	full width at half-maximum
g	acceleration due to Earth's gravity
Gr	Grahof number
h	roughness height
$\hbar$	reduced Planck constant
h_c	corrugation depth
I	irradiance
I_0	intensity amplitude
I_r	reflected intensity
k	extinction coefficient or damping constant
k^*	wave number
k_B	Boltzmann constant
$\vec{k}$	wave vector
l	depth of the molten pool
L	thermal penetration or thermal diffusion length
L_b	latent heat of vaporisation
L_i	length of the total projection corresponding to the direction of projection ω_i
l_i	mean chord length corresponding to the chord direction ω_i.
L_m	latent heat of fusion
Ma	Marangoni number
m_e	mass of oscillating electron
n	complex refractive index
n_1	real part of the complex refractive index
N_e	density of electron

Pe	Peclet number
Pr	Prandtl number
P_r	recoil pressure
P_s	saturated vapour pressure
q_a	added power per unit of volume
q_b	power per unit volume required to vaporise
q_m	power per unit volume required to melt
R	reflectivity
R_a	arithmetic roughness
r_b	beam radius
Re	Reynolds number
R_t	transition zone
$R_{\parallel}$	reflectivity for parallel polarised light
$R_{\perp}$	reflectivity for perpendicular polarised light
S	pointing vector, entropy, surface area
SA	surface area input
SA_R	superficial area ratio
SD	structure depth
T	temperature
t	time
t_0	pulse time
T_b	boiling temperature
T_d	activation energy of the oxidation
t_e	electron cooling time
t_l	lattice heating time
T_m	melting temperature
T_s	surface temperature
U	latent heat of evaporation per atom
V	velocity at the surface
V_{max}	maximal velocity at the surface
w	roughness width
x	oxide thickness

List of abbreviations

3D	three-dimensional
DC	direct current
EBSD	electron backscatter diffraction
EDS	energy dispersive X-ray spectroscopy
f.c.c.	face-centered cubic
FEG	field emission gun
FIB	focused ion beam
H_2SO_4	sulphuric acid
HCl	hydrochloric acid
HF	hydrofluoric acid, high laser fluence
HV	high voltage
IPF	inverse pole figure
IQ	image quality
IR	infrared
LF	low laser fluence
LIMET	laser interference metallurgy
LMIS	liquid metal ion source
LV	low voltage
MAVI	modular algorithms for volume images
MeanFeret	mean Feret diameter
Nd:YAG	Yttrium-Aluminium-Garnet crystal doped with 1 % Neodymium (3+) ions
OIM	orientation imaging microscopy
ppm	parts per million
SEM	scanning electron microscopy
UHR	ultra-high resolution
UV	ultraviolet
WLI	white light interferometer

CHAPTER 1

Introduction

In the field of materials science, the control of surface properties has been one of the most important issues in the last years. Nowadays, many scientific areas make special demands in the development of complex structures on the "nano" submicron scale for a wide range of applications (*e.g.*, miniaturised sensors, microelectronic devices, biochips, etc.). Several techniques have been developed to overcome this challenge, each with its own set of advantages and drawbacks. Laser Interference Metallurgy (LIMET) is a recently developed patterning technique which uses high-power pulsed laser to irradiate the sample surface and produce periodic structures. It is based on the spatial variation of the laser intensity created by the interference of several coherent beams, which induces local and periodic modifications on the surface of the material. It allows in a single-step and maskless, the direct production of periodic patterns with a well-defined long-range order in the submicrometer scale. This technique is a new approach to initiation of metallurgical processes such as melting, recrystallisation, recovery, etc., on surfaces. Hence its name: "Laser Interference Metallurgy".

Furthermore, the use of high-power pulsed lasers (as in LIMET) has become of great interest because they allow the modification of the surface morphology and/or structure without significant damages or alterations to the underlying material. This characteristic made them an attractive tool for the modification of anode aluminium foils for high voltage capacitor applications. An aluminium electrolytic capacitor consists of an anode foil on which an oxide is formed (dielectric), a suitable electrolyte and a cathode foil. In principle, a high capacitance device requires a large surface area of the anode foil. Formation of tunnel pits on aluminium by anodic etching in an electrolyte containing Cl^- anions has been extensively employed for the increase of the surface area. For the purpose of obtaining the maximal possible capacitance, the tunnel pits should be evenly distributed on the surface, and their size and interval must be precisely controlled.

This PhD thesis was motivated by the necessity to find a method for controlling the pit-site distribution during the etching process of aluminium foil. For this purpose, the mechanism that governs the surface patterning of metallic surfaces and the possible physical/chemical changes induced by LIMET were studied. Several metals with different physical and thermodynamic properties were used, paying special attention to aluminium. The

investigation of the parameters influencing the patterning of metallic surfaces and the factors that can modify the etching process of aluminium foils were the main focus in this study.

This work is structured as follows:

Chapter 2 introduces fundamental physical and chemical processes which take place during the interaction between laser and metal surfaces. The first part of that chapter presents background information about the fundamental optical properties of the metals, which are relevant to light absorption, and their dependence on some important laser parameters and material conditions. Thereafter, background information about the surface deformation of an irradiated metal is given addressing the influence of convection, recoil pressure, instabilities and structure formation (ripples). The second part is focused on the basic interaction mechanism between laser and material exposed to a chemically reactive or nonreactive surrounding medium. The objective is to present the recent progress in understanding the phenomena related to the laser-induced oxidation of metal surfaces.

Chapter 3 is composed of two parts. The first one provides a brief outlook of the more generic issues of pattern formation activated by light, electrons or beams, leaving out the non-conventional patterning methods based on contact printing. Here, the description of the patterning techniques, their advantages and limitations are reviewed. The second part of this chapter presents a short description of electrolytic aluminium capacitors focusing on the electrochemical etching process and the factors that can modify it. Finally, an overview of the most recent techniques for controlling the etching process is provided.

Chapter 4 describes the main experimental set-up performed for the formation of the periodic structures and the different characterisation techniques employed for the analysis of the patterned samples before and after etching processes.

Chapter 5 addresses the study of the structuring mechanism of metallic surfaces. The study includes the influence of some laser parameters and sample conditions (*e.g.*, laser fluence, laser configuration, sample roughness, etc.) on the formation of the micro-structures. The results are accompanied with thermal simulations to better understand the thermal effects which take place during laser patterning. Hence, a detailed analysis of the structuring mechanism is proposed and discussed. Finally, the process was characterised by dimensionless numbers to obtain additional information about the acting forces and flow regime during the structuring process.

Chapter 6 is focused on the chemical behaviour of aluminium foils modified by laser interference. Among the many morphological features and chemical modifications induced by

laser structuring, the formation of a periodic thin oxide layer is the most important one in relation to the chemical behaviour of patterned aluminium. The effect of the modulated oxide film on the direct control of pit distribution during the chemical etching is analysed and discussed.

Chapter 7 presents the effect of lead and copper addition on the site-controlled pitting during the chemical etching process. The incorporation of small quantities of metals in aluminium foil was performed by the combined action of physical vapour deposition (PVD) and laser structuring (LIMET). The effects of metal additions (*i.e.*, Pb and Cu), laser fluence and period of the micro-structures were investigated. The first sections include the results and analysis of Pb/Al, while the second one is addressed to the study of Cu/Al. Finally, the modification of the etchability promoted by Pb and Cu on the aluminium surface is discussed.

Chapter 8 is dedicated to the three-dimensional characterisation of the tunnel structures obtained by electrochemical etching of aluminium and Pb/Al samples. A new method was developed for the direct study of the tunnel morphology allowing the quantitative and statistical analysis of the structural features. The purpose of this study is to gain reliable information about the complex tunnel structures and the influence of lead on the tunnel formation.

Chapter 9 summarises the most important conclusions with regards to the objective of this work.

Appendices A to E contain technical and extra information about procedure, material properties, and also examples of the possible periodic structures that can be produced on different materials depending of the fluence and geometrical configuration of the laser.

CHAPTER 2

Laser – material interaction

Fundamental processes involved in laser beam interactions with materials are addressed here. The interaction mechanism is a complex phenomenon, which is a result of the combined action of physical and chemical processes. When a laser beam strikes a surface, it can be accompanied by some of the following chain of transient processes: (i) absorption of laser radiation, (ii) heat- and mass-transfer on the surface, (iii) redistribution of the excitation energy over the internal degree of freedom, (iv) photodecomposition of molecules and possible chemical reaction, and (v) removal of material from the surface. An initial stage in laser interaction is the absorption of the laser radiation, which depends on the laser parameters and the properties of the material.

2.1 Fundamental optical properties

The electromagnetic nature of laser light can be assumed, in good approximation, as a monochromatic, linearly polarised plane wave. Electromagnetic radiation can be represented as an electric and a magnetic vector field. The electric field of a wave propagating in a homogeneous and nonabsorbing medium can be represented as [1]:

$$E = E_0\, e^{i(\frac{2\pi z}{\lambda} - \omega t)}, \tag{2.1}$$

where z is the coordinate along the direction of propagation, ω is the angular frequency, and λ is the wavelength. The last two quantities are related through the phase velocity c/n_1, being c the speed of light, and n_1 the refractive index of the medium by:

$$\lambda = \frac{2\pi}{\omega} \cdot \frac{c}{n_1}. \tag{2.2}$$

The electric (E) and magnetic field (B) are always perpendicular to each other and the direction of propagation. Moreover, their amplitudes are related by $B_0=E_0 / c$.

The irradiance, I, is the energy flux per unit area (W/m^2). The pointing vector, S, can represent the energy flux of an electromagnetic wave. The pointing vector is defined as:

$$S = \frac{1}{\mu_0}|E \times B| = \frac{E_0^2}{2\mu_0 c} = I. \tag{2.3}$$

The essential content of this equation is that the intensity, *I*, is proportional to E^2. Substituting $c = \sqrt{\frac{1}{\mu_0 \epsilon_0}}$. in Equation (2.3) we find:

$$I = \frac{1}{2} c \, \epsilon_0 \, |E|^2. \tag{2.4}$$

where μ_0 and ϵ_0 are the permeability and permittivity of the material, respectively.

The concept of a beam implies that the irradiance is maximal near the optical axis and falls off laterally. The most common lateral distribution is a cylindrically symmetric Gaussian given by:

$$I(r) = I_0 e^{-\frac{r^2}{r_b{}^2}}, \tag{2.5}$$

where I_0 is the irradiance on axis ($r = 0$) and r_b is referred to as the beam radius.

In absorbing media the real refractive index n_1 must be replaced by a complex index [2]:

$$n = n_1 + ik, \tag{2.6}$$

being *k* the extinction coefficient (also named damping constant). The magnitude of the refractive index depends on the wavelength of the incident light (see Eq. 2.2).

Moreover, the electric field is composed of: *E = damped amplitude – undamped wave*. The meaning of *k* is clear when (2.6) is introduced into (2.2) and substituted in (2.1) obtaining the damped and undamped terms of *E*:[3]

$$E = E_0 e^{\left[\frac{2\pi kz}{\lambda}\right]} - e^{\left[\frac{2\pi ci}{\lambda}\left(t - \frac{zn}{c}\right)\right]}. \tag{2.7}$$

where E_0 is the electric field at the surface. Equation (2.7) shows that the electric field decreases exponentially with increasing depth, *z*, indicating that some of the light energy is absorbed, as schematically shown in Fig. 2.1.

The absorption coefficient for the irradiance (2.4) is:

$$\alpha = -\frac{1}{I} \cdot \frac{dI}{dz} = \frac{2\omega k}{c} = \frac{4\pi k}{\lambda}. \tag{2.8}$$

It is also called the (exponential) attenuation or absorbance. The inverse of α is referred to as the absorption length.

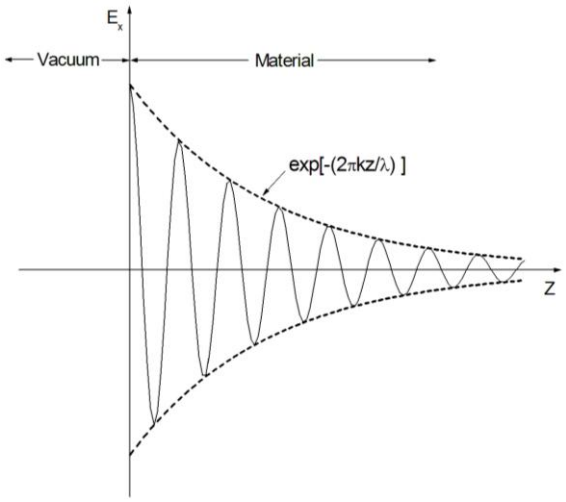

Figure 2.1. Damped light wave. The electric field decreases exponentially with increasing distance *z*, from the interface between vacuum and matter.

Although the electric field is hard to measure, *I* can be easily measured with light-sensitive devices. As the intensity is proportional to the square of the electric field (2.4), the damping term in Equation (2.7) may be written as [3]:

$$\mathrm{I} = \mathrm{I}_0 \exp\left(\frac{4\pi \mathrm{k} z}{\lambda}\right) = \mathrm{I}_0 \mathrm{e}^{-\alpha z}. \tag{2.9}$$

In Equation (2.7) and (2.9), E_0 and I_0 correspond to the amplitude of the electric field and intensity at the surface, respectively.

In inhomogeneous media the refractive index varies in space. Spatial variations of the refractive index deform the wave front, bend the beam path and cause secondary waves to split off the primary one. The ratio between reflected intensity I_r and incoming intensity I_0 of the laser light serves as a definition for the reflectivity (R). The reflection of a perpendicularly incident wave from vacuum or air onto the plane boundary of a solid with refractive index n is:

$$R = \left|\frac{n-1}{n+1}\right|^2. \tag{2.10}$$

For materials for which the extinction coefficient or damping constant $k \neq 0$ (metals, semiconductors, etc.) the Equation (2.10) needs to be modified as follows:

$$R = \frac{(n_1-1)^2 + k^2}{(n_1+1)^2 + k^2} = \left|\frac{\sqrt{\varepsilon_1^2+\varepsilon_2^2}+1-\sqrt{2(\sqrt{\varepsilon_1^2+\varepsilon_2^2}+\varepsilon_1)}}{\sqrt{\varepsilon_1^2+\varepsilon_2^2}+1-\sqrt{2(\sqrt{\varepsilon_1^2+\varepsilon_2^2}+\varepsilon_1)}}\right|, \tag{2.11}$$

$$\text{where} \qquad \varepsilon_1 = n_1^2 - k^2 \quad ; \quad \varepsilon_2 = 2n_1 k \tag{2.12}$$

Thus, ε_1 (polarisation) and ε_2 (absorption), are the real and imaginary parts of the *complex dielectric function*, ε, ($\varepsilon = \varepsilon_1 + i\varepsilon_2$), respectively. Rewritten n_1 and k as functions of ε we obtain:

$$n_1^2 = \frac{|\varepsilon| + \varepsilon_1}{2} \quad ; \quad k^2 = \frac{|\varepsilon| - \varepsilon_1}{2} \,, \tag{2.13}$$

The complex dielectric function can be regarded as a generalised response function of the material. The dielectric function completely describes the response of a material to weak electromagnetic radiation.

2.2 Absorption of light

The absorption mechanism of the light depends on the material. Insulators and semiconductors in absence of excitation have only bound electrons. The electron is usually represented as a harmonic oscillator (Lorentz model) driven by the oscillating force of the electric wave. The oscillating electrons produce a macroscopic polarisation of the material which superposes on the electric field of the incident wave. The dielectric function, ε, is simply the ratio of the total field (wave plus polarisation) to the field of the wave alone.

On the other hand, metals are viewed as a gas of free electrons which interacts with a background positive-ion lattice represented by photons (free electron model). Drude [4] developed a theory to predict the dielectric function for free electrons that is essentially a special case of the Lorentz model. The optical response of a metal is dominated by the conduction of electrons. The radiation is predominantly absorbed by free electrons in an "electron gas" (electrons in states close to the Fermi level). There is no resonance frequency for a free electron and the deposited optical energy is subsequently redistributed over the various energy states of the system by collision interactions with the lattice. Thus, the Drude theory for the dielectric function of a free-electron metal can be written as:

$$\varepsilon = 1 + \omega_p^2 \cdot \frac{-\tau_e^2 + i\tau_e/\omega}{1 + \omega^2\tau_e^2}, \qquad \text{being} \quad \omega_p = \sqrt{\frac{N_e e^2}{m_e \epsilon_0}} \,. \tag{2.14}$$

ω_p is the electron plasma frequency, τ_e is the collision time, e and m_e are the charge and mass of oscillating electrons and N_e is their number density. The plasma frequency is a measure of the number density of free electrons present. At frequency $\omega = \omega_p$ (which is vacuum

ultraviolet for most metals) both ε_1 and n_1 vanish. The plasma frequency is seen to separate two regimens of rather different optical properties: large R and α for $\omega < \omega_p$, and small R and α for $\omega > \omega_p$. The variation of the dielectric function and the associated quantities with the light frequency is shown in Fig. 2.2.

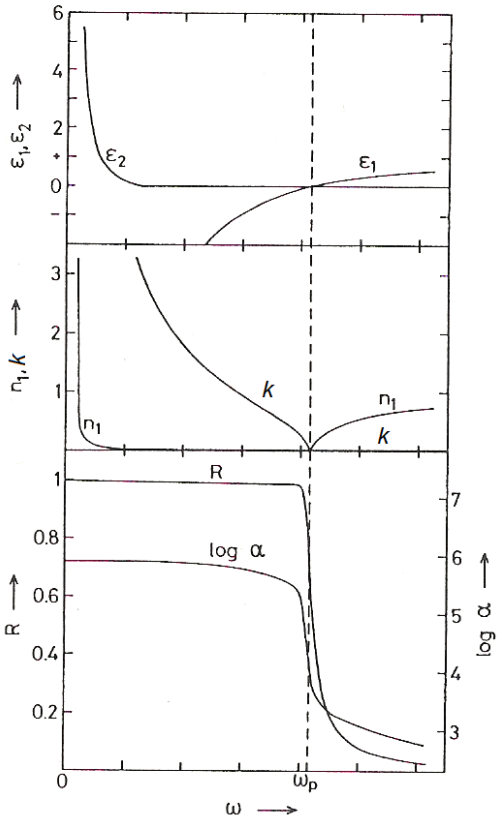

Figure 2.2. Frequency dependence of the dielectric function, the refractive index, the Fresnel reflectance and the absorption coefficient of a free-electron metal calculated for $\hbar\omega_p$ = 8.3 eV, ($\hbar$ is the reduced Planck constant), *Ne* = 5·1022 1/cm3, and τe = 3.29·10-14 s [1].

The optical properties of a free-electron metal for $\omega \leq \omega_p$ are related to its electrical conductivity, σ. With the aid of Drude's formula [4-6] useful approximations for the optical parameters can be obtained:

$$\sigma = \frac{N_e e^2}{m_e} \cdot \tau_e = \omega_p^2 \epsilon_0 \tau_e \,. \tag{2.15}$$

Rewritten $\tau_e = f(\sigma)$ from (2.15), substituting into (2.14) and using (2.13), the absorption coefficient, α, and the reflectivity, R, can be calculated from (2.8) and (2.11), respectively. Due to the dependence of the electrical conductivity with the temperature, $\sigma(T)$, it is possible to obtain good approximations of R and α as a function of this last parameter. The reflectance and the absorption coefficient determine the amount of beam power absorbed within the material.

The fundamental optical properties discussed until now, represent the response of material to laser energy that is weak enough so as not to perturb the states of electrons and atoms significantly. Powerful laser irradiation can alter the optical response of the materials which is no longer well-characterised by the static dielectric function but becomes a dynamic process. The amount of light absorbed in the material may turn out to be smaller or larger than expected from the fundamental optical properties. In real materials the free-electron behaviour is modified by secondary effects, in particular by interband transitions. In the case of gold, copper, and silver the interband transitions from d-band states make a bound-type contribution to the dielectric function, which shift ω_p to a lower frequency [1].

2.2.1 Influence of the wavelength on the light absorption in metals

The reflectivity is, like the complex index of refraction, wavelength dependent. For long wavelengths ($\lambda \geq 10$ μm), the Hagen-Rubens relation [7] postulates that:

$$n_1 \approx k \approx \sqrt{30\lambda\sigma} \gg 1, \qquad \lambda\sigma \text{ in } [\Omega^{-1}] \tag{2.16}$$

Substituting (2.16) into (2.11) leads to:

$$R \approx 1 - \frac{2}{\sqrt{30\lambda\sigma}} + \frac{1}{\sqrt{15\lambda\sigma}}, \qquad \lambda\sigma \text{ in } [\Omega^{-1}] \tag{2.17}$$

Equation (2.17) indicates that as the electrical conductivity becomes large, R approaches unity. The absorptivity ($1 - R$) for normal incidence is small for large wavelength, and tends to decrease as $1/\sqrt{\lambda}$. This dependence ($1/\sqrt{\lambda}$) is not predicted by the Drude theory (except for far infrared), nor is it observed with optically smooth surfaces. However, it often approximates the behaviour of polished (*i.e.*, not entirely smooth) surfaces.

The high reflectivity at wavelengths near to 10 μm means that much of the incident power is reflected and not absorbed by the surface. For highly conductive metals, like Al and Cu, the absorptivity is higher at shorter wavelengths and in this case it is better to employ an *Nd:YAG* laser (which typically emits light with a wavelength of 1064 nm), for which the reflectivity will be lower. For ferrous material, the conductivity is not so high and thus the reflectivity will be somewhat lower. Instead at shorter wavelength, the more energetic photons can be absorbed by a great number of bound electrons and so the reflectivity falls and the absorptivity of the surface is increased.

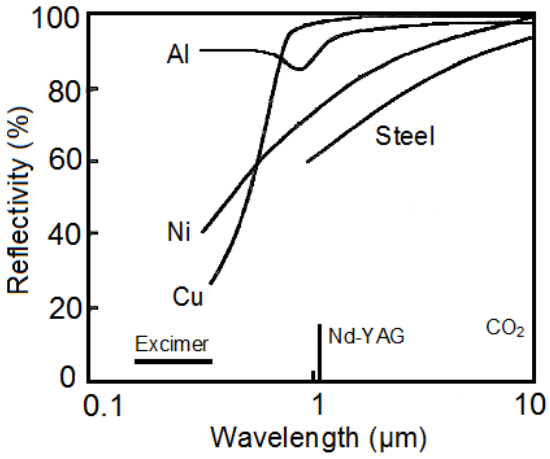

Figure 2.3. Spectral, normal reflectivity at room temperature for aluminium, copper, nickel, and steel [8].

This tendency can be observed in Fig. 2.3. It can be observed that aluminium has a dip in reflectivity centred at ~ 0.8 μm; this is due to bound electron transitions that are not considered by the Drude theory.

2.2.2 Directional dependence

Lasers tend to be strongly polarised, that is, there is a relationship between the planes formed for the electric field vectors of the individual waves making up a wavetrain. In the case of smooth surfaces the state of polarisation has a strong impact on the material reflectivity and vice-versa. The terms parallel and perpendicular mean that the electric field vector is parallel or perpendicular to the plane formed by the beam direction and the surface normal, and each component is reflected to a different extent.

The reflectivity of metals is governed by the complex index of refraction. Since generally metals have large electrical conductivity, both the real and imaginary part of the complex index of refraction, n_1 and k, become large, and Fresnel's relations for directional reflectivity simplify to:

$$R_{\parallel} = \frac{(n_1 \cos\phi - 1)^2 + (k\cos\phi)^2}{(n_1 \cos\phi + 1)^2 + (k\cos\phi)^2}\,; \qquad R_{\perp} = \frac{(n_1 - \cos\phi)^2 + k^2}{(n_1 + \cos\phi)^2 + k^2}, \tag{2.18}$$

$$R = \frac{1}{2}\left(R_{||} + R_{\perp}\right),$$

where $R_{\parallel}$ and $R_{\perp}$ are the reflectivities for parallel and perpendicular polarised light and R is the average value for unpolarised light. Equation (2.18) relates the variation of the reflectivity with both incidence angle, ϕ, and plane of polarisation. Figure 2.4 shows typical directional

behaviour of the reflectivity of metals in the infrared: the reflectivity tends to be higher at normal incidence, with very weak directional dependence up to incidence angles of 60° or more, followed by a sharp drop (due to the contribution of $R_{||}$) before becoming completely reflective at grazing angles [2, 9].

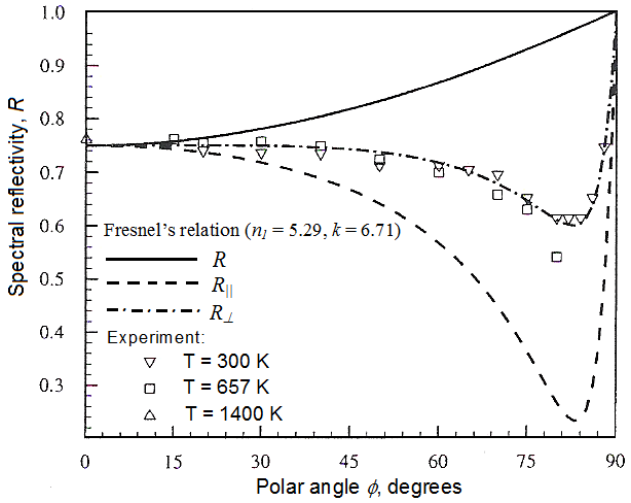

Figure 2.4. Spectral, directional reflectivity of platinum at 2 μm [2].

There is a particular angle – the "Brewster" or polarising angle, ϕ_p – at which the material is a perfect absorber for parallel-polarised light at an irradiance angle of:

$$\phi_p = \tan^{-1}(\text{refractive index}) \rightarrow n = \tan\left(\phi_p\right). \tag{2.19}$$

However, using oblique laser irradiation at that angle diminishes the incident energy per area as compared to normal incidence by a factor of $\cos\phi$. Absorbed energy is always higher at normal incidence.

2.2.3 Temperature effect

The initially high reflectivity of a metal surface may experiment a sharp and substantial decrease during an intensive laser pulse irradiation [8, 10-15]. Fig. 2.5 illustrates the temperature dependence of the reflectivity for some materials. Explanations of this behaviour have been based on an increase in electron-phonon collision frequency as the temperature of the metal surface rises to the melting point of the metal. The electrons are more likely to interact with the structure rather than oscillate and reradiate.

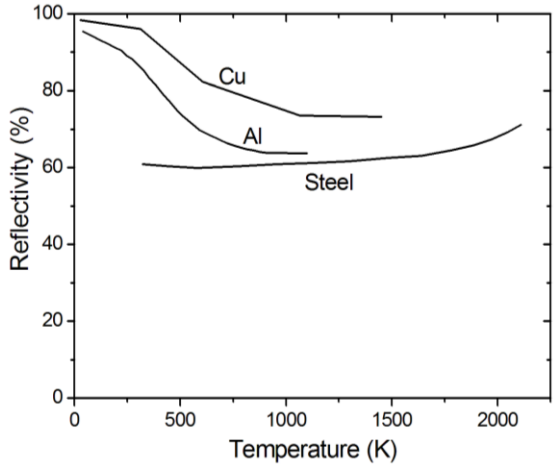

Figure 2.5. Reflectivity as a function of the temperature for 1064 nm radiation [8].

Few studies about *in situ* time-resolved reflectivity measurements on metals have been published. The general reflectivity curve as is observed in Fig. 2.6, has been reported for metal surface exposed to high-intensity radiation [12, 13]. This type of reflectance change was found using 1064 nm *Nd:YAG* laser with millisecond and nanosecond laser pulses. Three distinct regions within this reflectance curve can be distinguished:

1. AB – an initial steep decrease of the initial reflectance;
2. BC or BC' – a plateau region during which the reflectance remains approximately constant; and
3. C'D' – a complete reflectance recovery, or for higher intensity laser pulses CD, a further decrease of the reflectance followed by a partial recovery.

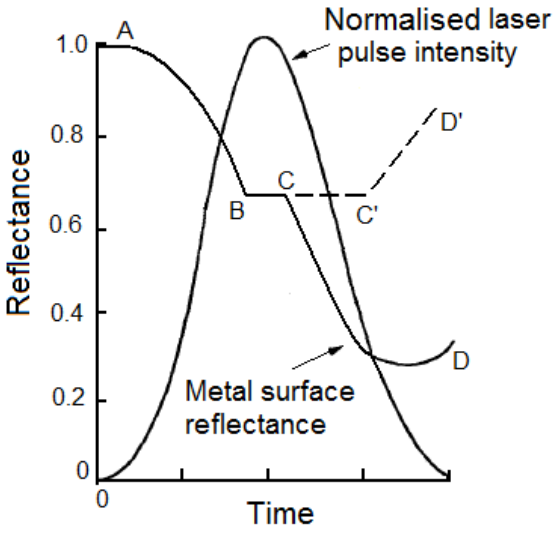

Figure 2.6. General reflectivity behaviour for a metal surface subjected to high-intensity radiation.

This curve can be explained as follows: the initial sharp decrease in the reflectance curve, AB, is associated to the heating of the metal surface to the melting point and with the drop in the electrical conductivity which accompanies heating. However, there are some different interpretations for the plateau region BC or BC'. According to Bonch-Bruevich *et al.* [12] the

metal was melted during the BC region. This zone indicates that the temperature of the molten layer remained constant while the absorbed radiant energy propagated a melting wave into the solid. The further reflectance drop during region CD was attributed to a decrease in the amount of energy conducted to the liquefaction wavefront and, therefore, indicates a second region of increasing surface temperature. Zavecz *et al.* [13] reported similar reflectance curves but conclude that the melting occurs during the second decrease in reflectance, CD of Fig. 2.6. Ready *et al.* [14] used a probe laser to subtract plasma absorption and concluded that no recovering of reflectance occurred during or after the laser pulse. These different interpretations come mainly from the type of reflectance experimentally measured as well as from the method of the surface preparation. Bonch-Bruevich [12] trials measured total reflectivity while those of Zavecz [13] were specular reflectance measurements. The specular reflectance is a sensitive indicator of surface deformation. The specular reflection is referred to as the mirror-like reflection of the light from a surface, in which the laser light is reflected in a single outgoing direction.

In addition to the suggestion that the initial steep decrease in reflectance is associated with the heating of the metal surface to melting, three classes of alternative explanations have also been proposed: (1) surface deformation which directs the reflected beam away from the detector, (2) plasma formation which absorbs or scatters the reflected light, or (3) non-linear process causing enhanced absorption within the metal.

2.2.4 Influence of surface conditions

The material surface is often assumed as isotropic and optically smooth. But very few real material surfaces come close to this idealisation. As the reflectivity is essentially a surface phenomenon the material surface condition may have a large effect on it. Under intense laser irradiation, causing breaking of molecular bonds, melting, decomposition of the material and/or ablation, even an initially ideal material will have its surface composition and quality altered.

In the next subsections a brief discussion is given of how the effect of surface roughness and surface layers affect the reflectivity (or absorption) of opaque surfaces.

2.2.4.1 Roughness

A surface is “optically smooth” if the average length scale of surface roughness is much less than the average of the electromagnetic wave. A surface that appears rough in visible

light (λ= 0.5 μm) may well be optically smooth in the far infrared (λ= 50 μm). In general as the surface roughness increases, the surface becomes less reflective and the behaviour of the reflection turns out more diffuse and less specular [2]. This behaviour can be explained through geometric optics, since a laser beam may undergo multiple reflections in the undulation (local peaks and valleys) resulting in an increase of the absorption, after which it leaves the surface spread in all directions as a diffuse reflection. Also, "stimulated absorption" can take place due to the beam interference with sideways reflected beams [2, 8].

Several models [16] predict that the reflectivity can present sharp peaks in the specular reflection direction, and less reflection in the other directions, with the strength of the peak depending on the surface roughness. This has also been confirmed experimentally, but only in the case where the incidence angle was not too large. For large incidence angles rough surfaces tend to display off-specular peaks, apparently due to shadowing of parts of the surface by adjacent peaks.

More recently, Ang *et al.* [17] used a simple model to evaluate the fraction of the laser light absorbed on a metal surface with large scale surface roughness. The investigation considers the case where the roughness scale, in both height (h) and width (w), is much larger than the wavelength. In this work a KrF Excimer laser pulse was used to ablate a pure solid aluminium target using perpendicular polarisation. The model assumes a rough surface with rectangular distribution function. Figure 2.7 shows the fraction of absorption of aluminium as a function of the surface roughness using different laser wavelengths at room temperature. The degree of surface roughness (h_0 / w_0), is defined as the value (h, w) at the peak of the rectangular distribution function. This figure shows that a rough surface may increase the laser absorption by an order of magnitude over a flat surface [17].

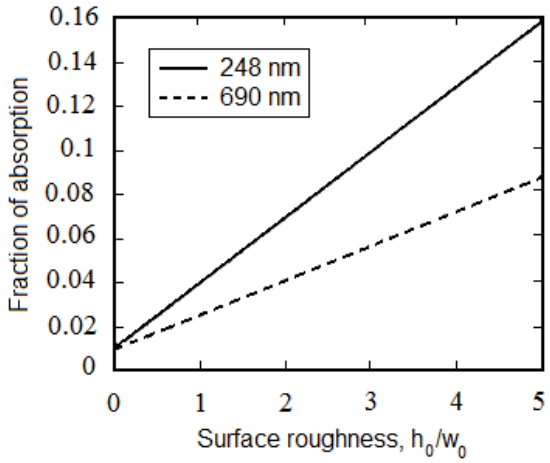

Figure 2.7. Calculated cumulative absorption fraction of laser radiation by two different wavelengths on a solid aluminium target, where h_0 / w_0 is the degree of surface roughness [17].

2.2.4.2 Surface layer and oxide films

Normally, the surface structure of a material differs from the rest of its bulk, due to either surface damage or the presence of a thin layer of foreign material. Surface damage is usually caused by the machining process, particularly for metals and semiconductors, which modifies or distorts the crystal lattice near the surface. Foreign coats may be formed by chemical reaction (mostly oxidation), absorption (*e.g.*, coats of water or grease) or electrostatics (*e.g.*, dust particles). All these factors may considerably influence the radiation properties of the material.

As shown in Fig. 2.8, the spectral, normal emissivity (or absorptivity) of aluminium changes according to its surface finishes. While ultra-high vacuum aluminium follows the Drude theory for $\lambda > 1$ μm, polished aluminium surface has much higher reflectivity over the entire spectrum. It is important to highlight that the overall absorptivity level remains very low and the reflectivity remains rather specular. The reflectivity is still much larger for aluminium with commercial finish, probably due to a combination of roughness (see Section 2.2.4.1), contamination, and slight oxidation. In the case of aluminium coated with a thin alumina layer the absorptivity increases appreciably. Thus, metal surfaces exposed to prolonged high-temperature oxidising environments, generally have radiative properties similar to those of their oxide layer, *i.e.*, anodised aluminium (see also Section 2.5).Otherwise, for very thin oxide its properties are not considerably affected [2, 9].

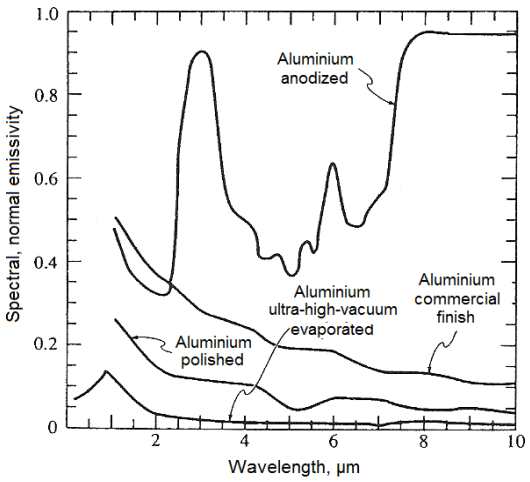

Figure 2.8. Spectral normal emissivity for aluminium with different surface finishes [9].

2.3 Laser processing of materials

The interaction mechanism between laser light and matter depends on the laser parameters and the physical and chemical properties of the material. In this way, laser

processing can be classified in two groups: “conventional” and “chemical” laser processing. Conventional laser processing is mainly performed in an inert atmosphere and can take place without any changes to the overall chemical composition of the material being processed. In general, the energy absorbed is dissipated into heat within a time which is short compared to any other time involved in the process.

On the other hand, laser chemical processing is characterised by an overall change in the chemical composition of the material or the activation of a chemical reaction. Its objective is the patterning, coating or physicochemical activation of a solid surface by activation of real chemical reactions (such as oxidation, nitridation, etc.). Laser-induced activation or enhancement of a reaction can take place heterogeneously or homogeneously, or via combination of both. Both heterogeneous and homogeneous reactions may be activated thermally (photothermally, pyrolytically), or photochemically (photolytically). For purely photochemical processes the temperature rise within the ambient medium and on the substrate surface can be ignored [18]. In many cases, a unique classification into chemical and non-chemical laser processing is difficult or impossible, but often one of them dominates during the process.

2.3.1 Photothermal, photochemical and photophysical process

A strict definition of thermal (photothermal) and non-thermal (photochemical) laser processes requires detailed knowledge of laser interaction with matter and of relaxation times involves. Normally a laser-induced process is considered as thermally activated if the thermalisation of the (laser) excitation energy is fast compared to the reaction. In this case the laser can be considered simply as a heat source, and the state of the system is described by the temperature and the total enthalpy. In photochemical laser processing, the first reaction step is faster than the thermalisation of the excitation energy. The specimens are dissociated as a consequence of selective electronic or vibrational excitation within the volume of the laser beam. If both thermal and non-thermal mechanisms directly contribute to the overall processing rate, the process is denoted as “photophysical”. Thermal and photochemical processes can be considered as limiting cases of photophysical processes.

High laser intensities allow high excitation densities to be generated thermally or non-thermally. The time for the thermalisation of the excitation energy depends on the type of material and laser parameters. The next section introduces the more relevant time scales

involved during laser pulse interaction, addressing the influence of laser pulse duration and energy relaxation of the material.

2.3.2 Characteristic time scale

The primary interactions between light and matter are always non-thermal effects [18]. The first phenomenon is the absorbed laser energy by free electrons (see Section 2.2). The absorbed energy then propagates through the electron subsystem to be transferred to the lattice. The laser pulse width determines the way that the laser energy is deposited into these states. The initial electronic excitation is followed by a complex hierarchy of secondary processes, which eventually end in the final structural modification of the material. The timescale of the energy relaxation process in the laser – solid interaction is classified as shown in Fig. 2.9.

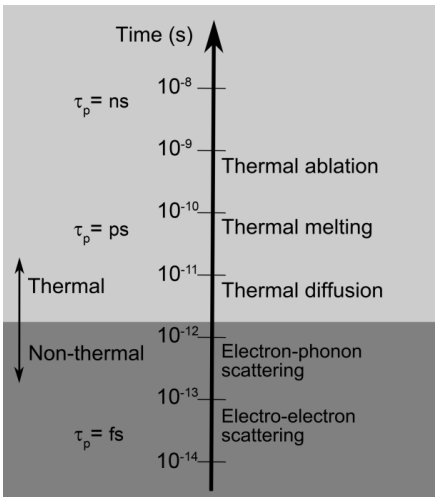

Figure 2.9. Timescales of the energy relaxation processes in laser – solid interaction [19, 20].

Three important characteristic time scales in laser processing are: the electron cooling time (t_e), which is in the order of 1 ps; the lattice heating time (t_l); and (τ_p) the duration of laser pulse. t_e and t_l are proportional to their heat capacity divided by the same constant, and the heat capacity of electrons is much less than that of lattice, therefore $t_l >> t_e$. These parameters, t_e, t_l, and τ_p, define different regimes of the laser – metal interaction which we will call continuous laser, nanosecond (10^{-9} s), picosecond (10^{-12} s), and femtosecond (10^{-15} s) regimes as detailed below.

For τ_p in the order of millisecond or infinite (continuous wave laser), τ_p> 1ms>> t_l>> t_e, the timescale is much larger than the electron lattice energy coupling time, and the primary material removal mechanism is melting with molten metal being often ejected. Classical heat and mass transfer laws are fully appropriate when applied to modelling those processes [21].

In the case where τ_p is in the nanosecond scale, $\tau_p > 1\text{ns} >> t_l >> t_e$, the electron absorbed laser energy has enough time to be transferred to the lattice. Electron and lattice can reach thermal equilibrium, and the main source of energy loss is the heat conduction into the solid target. The material is first melted, and when the laser fluence is strong enough, evaporation occurs from the liquid state. Thus, the heat-affected zone is smaller than that for continuous laser processing.

With picosecond laser pulses the following condition is fulfilled: $t_e << \tau_p << t_l$. In this regimen the electron cooling is due to the energy exchange with the lattice. The laser ablation is accompanied by the electron heat conduction and formation of a melted zone inside the material. The presence of the liquid phase inside of the material can reduce the precision of laser processing in this regime. Laser processing with picosecond laser pulses can be characterised as rapid thermal process (thermal ablation in nature [20]).

When the laser pulse is shorter than the electron cooling time, $\tau_p << t_e << t_l$, τ_p in femtosecond scale, electrons are heated instantly and they transfer the energy to their positive lattice ions in a time frame of picoseconds for most materials. Energy relaxation time of metals is on the order of 10^{-13} s. At high laser intensity, those ions get enough energy to break off the bond of the material structure instantly without having time to transfer their energy to the neighbouring lattice ions, thus directly solid – vapour (or solid – plasma) transition occurs [22]. The heat conduction into the material can be neglected and the thermal damage is greatly reduced or minimised [23].

Experimental investigations of laser ablation of metals and semiconductors [19, 20, 24-27] have been conducted using femtosecond (fs), picosecond (ps), and nanosecond (ns) pulse lasers. In these works ablation efficiency as well as microstructure evolution depend on the laser regime used. In general, the highest ablation efficiency was obtained for femtosecond lasers. This can be explained due to the very rapid creation of vapour and/or plasma phases, negligible heat conduction and the absence of liquid phase. The absence of liquid phase allows a better control of the ablation process.

In the work of Chichkov *et al.* [24] the production of holes drilled in metals and semiconductors were compared with laser pulses at different regimes. Using femtosecond laser there is no trace of molten material (Fig. 2.10 a). However, employing pico- and nanosecond pulses the trace of molten material can be recognised (Fig. 2.10 b, c). The material is removed both in vapour and liquid phase, since the evaporation process creates a recoil pressure that expels the liquid (see Section 2.4.3). The presence of liquid phase leads to

an unstable drilling process. At picosecond and nanosecond laser pulses the formation of a "corona" (ablated material around the crater) has been observed. Its formation has been related with the recoil vapour pressure created during the ablation process (Fig. 2.10 c) [24]. The "corona" formation around the crater boundary depends on the material, the laser energy and the pulse number [25]. Some works suggest that the crater "corona" formation is a result of not only liquid phase expulsion, but of plasma particle recondensation [28] as well.

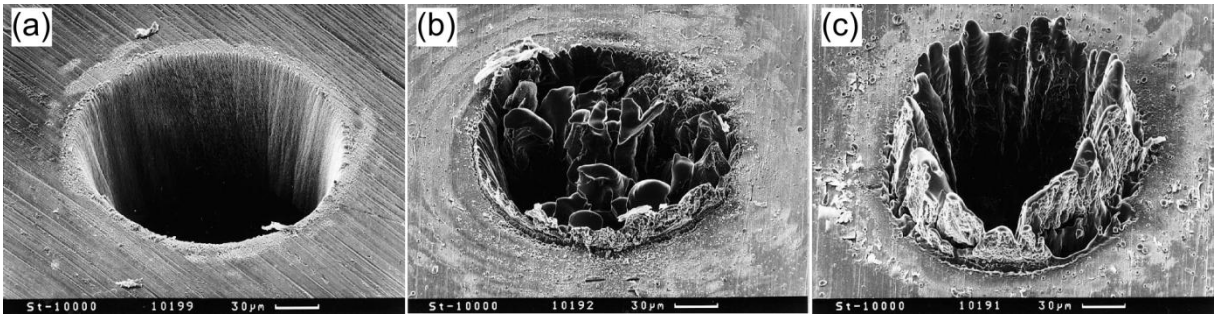

Figure 2.10. SEM images of holes drilled in a 100 µm thick steel foil performed at different laser pulse duration and laser fluence (F): (a) 200 fs, F= 0.5 J/cm^2, (b) 80 ps, F= 3.7 J/cm^2, and (c) 3.3 ns, F= 4.2 J/cm^2.

2.4 Surface deformation on metals

Powerful laser beams not only tend to modify the optical properties (see Section 2.2) but they can also produce permanent surface deformation ("shape" change) of an irradiated material. Shape effects are almost always related to melting or evaporation processes.

2.4.1 Surface melting

Surface melting is involved in many types of conventional and chemical laser processing. The process of laser absorption and its conversion to thermal energy leads to heating of the material. Thermal transfer in condensed matter is carried out via heat conduction mechanisms, among them, electron heat conduction is more important in metals and degenerate semiconductors, whereas phonon heat conduction is mostly responsible for heating of non-degenerate semiconductors. The thickness of the surface layer where interaction takes place is comparable initially to the optical absorption length of the material in question, $1/\alpha$ (see Eq. 2.8); and increases with the time according to the thermal penetration (also called thermal diffusion length) L, [18, 29-32]:

$$L = 2\sqrt{Dt}\,, \tag{2.20}$$

where D is the thermal diffusivity of the solid, which is given by:

$$D = \frac{\kappa}{\rho c_p}. \tag{2.21}$$

being κ the thermal conductivity, ρ the density, and c_p the specific heat capacity of the material [33]. The above equation can be used to estimate heat penetration depth for a certain pulse duration. If the thermal diffusion length, L, is smaller than the absorption length, $1/\alpha$, the heat source must be treated as a volume source whose distribution within the material corresponds to Lambert's law of radiation absorption. On the other hand, if the depth of the layer heated through heat conduction is much larger than the absorption depth, $L >> 1/\alpha$, the heat source can be treated as a surface source. Such a situation is typical for metals.

The irradiance can be physically transformed into permanent deformation in the material. The mechanism of deformation depends on the absorbed fluence as well as the material properties. Depending on the laser intensity, the target surface can be melted, and the liquid can successively undergo the normal heating process, the superheating process and/or the explosive phase change. Also, the vapour may get ionised forming plasma before the laser pulse is over. It is important to point out that even for lower laser intensity a heterogeneous evaporation occurs at the liquid surface. Thus, during the laser melting process the material is exposed to transient surface temperature and transient surface pressure. The surface temperature determines the grade of superheating in the liquid. On the other hand, the surface pressure determines the evaporation rate.

There are many forces acting on the melt pool which can produce material flow in the irradiated zones. Several competing mechanism can be responsible for the laser removal of material such as vaporisation, recoil pressure, surface tension and its gradient (convection) [34]. In the next sections, a brief introduction of the more relevant transport mechanisms during laser surface melting will be presented.

2.4.2 Convection

The surface tension γ of a liquid is a direct measure of the intermolecular forces acting at the surface and may be written as:

$$\gamma = \gamma_0 - ST \,, \tag{2.22}$$

where γ_0 is the surface enthalpy, S is the surface entropy, and T is the temperature. Expressed in terms of free surface energy, it can be defined as the work necessary to increases the surface by unit area. Since the surface entropy S is positive ($S > 0$), the temperature coefficient $\partial\gamma/\partial T$ of the surface tension of most liquids is negative ($\partial\gamma/\partial T < 0$). Thus, the surface tension of liquids usually decreases with increasing temperature.

The two principal parameters affecting the surface tension are the chemical composition of the phases and the temperature. The surface tension of any solvent can be markedly reduced by the presence of relatively low levels of certain ("surface active") solutes which are preferentially adsorbed at the surface. Exceptionally, some liquids exhibit positive values of $\partial\gamma/\partial T$ in a determined range of temperature from the melting point. Some of these systems are: slag melts containing high levels of SiO_2 [35] and molten iron containing group VI elements [36]. In the first case, as the temperature rises, complex molecular structures dissociate, producing an increasing number of unsatisfied molecular bonds at the surface, with the consequent increase of the free surface energy. In the latter case, as the temperature increases, the surfactant (O, S, Se, and Te) progressively desorbs from the surface layer leading to an increase of the surface tension. It should be noted that it is the soluble (*e.g.*, O and S) and not the total (O and S) element content which are responsible for the dramatic effect on surface tension [37, 38].

Thermodynamically it is unlikely that pure metals exhibit positive values for ($\partial\gamma/\partial T$) and occasional positives values found in the literature correspond to contaminated material. Surface tension cannot increase indefinitely with temperature, since it always tends to zero as the critical temperature is approached. Thus, for all systems which present $\partial\gamma/\partial T > 0$, there must be a maximum in the $\gamma(T)$ curve [38].

When a surface tension gradient exists along the free surface of a liquid, a convective flow (Marangoni flow) is induced in the surface layers. Marangoni flow is the motion of liquid due to surface-tension gradients along the molten surface. At irradiance above the melt threshold, uniform melting occurs, and lateral variations of the melt temperature become the relevant force for imprint deformation in the material [39, 40]. As the surface tension of the liquid decreases with increasing temperature, the molten material tends to pull away from hotter regions towards cooler regions. The Marangoni convection effect in laser melting is illustrated in Fig. 2.11. The surface tension gradients impart a shear force to the liquid surface,

causing surface flow in the direction of higher surface tension (Fig. 2.11 a, b), and therefore the sign of $\partial\gamma/\partial T$ will control the direction of the convective fluxes.

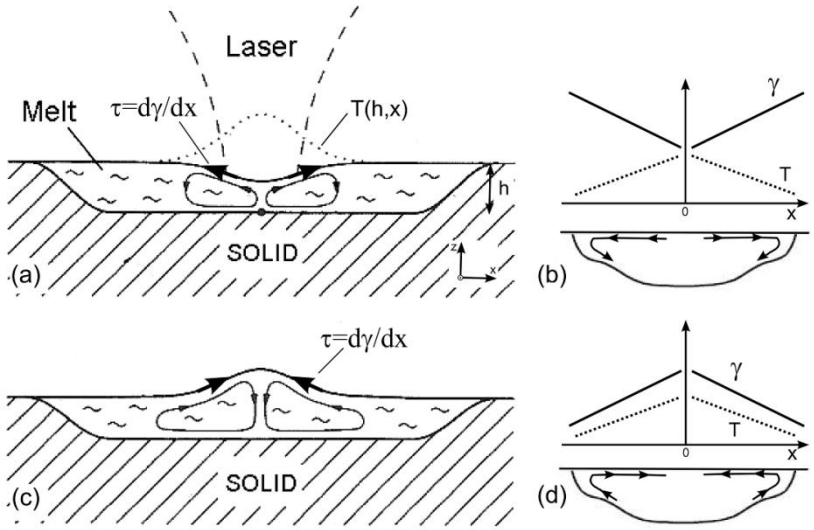

Figure 2.11. Illustration of the Marangoni convection due to localised melting. "*h*" is the melt depth away from the laser-irradiated zone. (a, b) $\partial\gamma/\partial T < 0$ and (c, d) $\partial\gamma/\partial T > 0$: (a, c) Marangoni eddies in a melt pool, (b, d) surface tension as a function of the temperature.

In some cases a surface deformation as shown in Fig. 2.11 c, d is observed. This type of deformation can be obtained only if the direction of the flow changes sign due to the concentration dependence (chemicapillarity force) of γ. Consider the alloying of *A* and *B*. The concentration (*N*) of *A* in *B* depends on the temperature, $N_A = N_A(T)$. For certain types of species $\partial\gamma/\partial T$ may be written as:

$$\frac{d\gamma}{dT} = \frac{\partial\gamma}{\partial T} + \frac{\partial\gamma}{\partial N_A}\frac{\partial N_A}{\partial T} > 0\,. \qquad (2.23)$$

A Marangoni effect has been reported in nanosphere-enhanced direct laser-nanopatterning of silicon surfaces. A monolayer of silica nanosphere with hexagonal array was first created on silicon substrate. The sample was then irradiated with KrF Excimer laser. Each transparent sphere may act as a lens to focus the laser beam onto the substrate for surface modification. Due to the optical field enhancement between the laser beam and the substrate, the silicon surface was locally melted. The molten material was redistributed due to surface tension forces, resulting in the formation of nanodent array, which follows the same order than the silica nanospheres. The morphology of the nanodents changes from bowl-type to dome (or "sombrero")-type with the increment of laser intensity as a result of a Marangoni effect. This nanodent shape change arises due to the competition between a thermocapillarity force (temperature gradient) and chemicapillarity force (chemical potential of a compositional gradient) acting on the molten material [41].

Marangoni convection can have a dramatic effect on the penetration depth of the melt pool [42]. In the work of Tsotridis *et al.* [43] a computational study of the role of sulphur in

the hydrodynamic flow during laser welding and its effect in the molten pool shape of stainless steel type AISI 316 was performed. The results obtained showed that the computed shape of molten pool for steel having a high bulk impurity content of sulphur and a positive temperature coefficient of the surface tension, lead to a deep and narrow (good penetrability) liquid pool. The direction of Marangoni surface flow is from the periphery to the centre, where the surface tension in this case is higher. For steel with low sulphur levels and negative thermocapillarity gradient, the direction of the Marangoni flow is radial from the centre to the periphery, from low to high surface tension. The hydrodynamic flow pattern tends to laterally extend the molten zone leading to a broad and shallow pool. The results are in accordance with the experiment reported by [36, 42]. The shape of the surface around the centre of the laser beam is determined by the thermal expansion of the material and the surface tension of the liquid.

Numerous works have studied the effect of Marangoni flow on the formation of surface shapes during laser irradiation [44-47]. This effect was also observed during thermal modifications in amorphous films. Laser-induced hole formation in a thin film can be initiated by different thermal process: melting with consequent material flow, internal boiling with consequent interface adhesion failure and/or surface evaporation [48, 49]. A mechanism that was often observed is the formation of a dome caused by thermal expansion of trapped gas. The most common gases are argon, added unintentionally during sputter deposition, and water adsorbed (during or after preparation) at an interface or even in the film itself. Figure 2.12 illustrates the action of radial material flow causing the build-up of a rim at the perimeter, bulging caused by vapour pressure generated during laser irradiation due to trapped gasses, which produces local film detachment and finally hole opening in the centre. The dome height was ~ 1 μm. When the laser intensity is even higher, complete opening of the hole occurs. This example shows that both melting and dome formation take place as previous steps to the hole opening [1, 50-52].

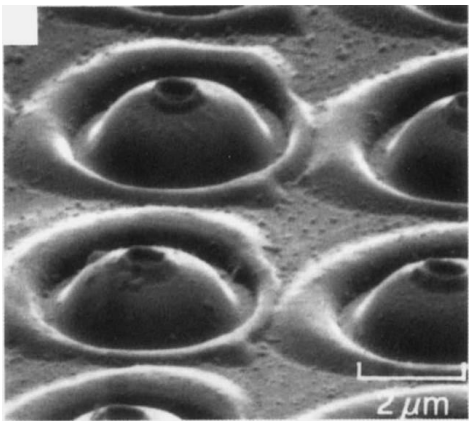

Figure 2.12. Scanning electron micrographs of laser-recorded imprints in a 52 nm thick amorphous In37Sb50Ge13 film produced with 40 mW and 20 μs Ar+ laser irradiation [1, 50].

2.4.3 Recoil pressure

The evaporated material can induce a recoil moment over the irradiated zones, which leads to a surface depression and/or "flushing" of the liquid metals out of the melt pool. The recoil pressure (P_r) can be calculated using [53, 54]:

$$P_r = A\frac{B_0}{\sqrt{T_s}}\exp\left(-\frac{U}{k_B T_s}\right), \tag{2.24}$$

where A is a factor dependent on the external pressure, B_0 is an evaporation constant, T_s is the surface temperature, U is the latent heat of evaporation per atom and k_B is the Boltzmann constant. According to the calculations performed by [54], the coefficient A depends on the ambient pressure and its value varies from 0.55 for evaporation in vacuum to unity for the case of evaporation under a high ambient pressure. Also, this study has shown that, for practical values of ambient pressure, the coefficient A is close to its minimal value. If the surface temperature reaches the boiling point, the recoil pressure would have to be higher than or equal to 0.55 p_s, where p_s is the saturated vapour pressure, which by definition is 1 atm at the boiling temperature. Thus, at the boiling temperature the recoil pressure would be at least 0.55 atm, which, for typical laser processing exceeds the highest possible value of the surface-tension pressure.

2.4.4 Instabilities and structure formation

Structures that can be developed under the action of laser light are classified into coherent or non-coherent structures. Coherent structures are directly related to the coherence, the wavelength and the polarisation of the laser light. Normally, they are generated by the interference between the incident laser beam and scattered/excited surface waves [55]. Non-

coherent structures are not directly related to any spatial periodicity of the energy input caused by interference phenomena. In this case, the feedback results in either spontaneous symmetry breaking or in non-trivial spatiotemporal ordering of the entire system.

Frequently observed coherent structures in laser surface-processing are the ripples (also referred to as laser-induced periodic surface structures or laser-driven corrugation). These are spatially periodic structures. Ripple formation is quite a general phenomenon which is observed on solid or liquid surfaces within certain ranges of laser parameters. However, the physical mechanism of the origin of the ripple is still unclear. The most accepted interpretation is attributed to the interference between the incident and the scattered radiation field, which leads to an inhomogeneous energy input that can cause surface instabilities [56-59]. Other authors attributed its formation to capillary waves or face acoustic waves [60, 61], or instabilities in the vapour–liquid–solid contact line of evaporation [62]. It has been observed that the period of the ripples depends on the wavelength and angle of incidence of the laser beam. Its orientation is determined by the light polarisation and, in some cases, by the incident angle. In metals and semiconductors the ripples are mostly oriented perpendicularly to the electric vector of the laser light. Recently the influence of initial surface roughness on the ripple characteristics has been reported [63].

2.4.5 Hydrodynamic instabilities

Hydrodynamic stabilities can be classified in Kelvin–Helmholtz and Rayleigh–Taylor type instabilities [64]. Kelvin–Helmholtz instabilities are created at interfaces of heterogeneous (or even homogeneous) liquids when different layers of the liquid are in relative motion, characterised by a velocity. In laser processing the velocity can be related to the expansion of the laser plume, the recoil pressure, surface tensions and/or the gas jet in liquid-phase expulsion. Rayleigh–Taylor instabilities arise at the interface between liquids of different densities that are superimposed over each other and which are in an external field (centrifugal force, gravity, etc.). These types of instabilities occur when the lighter fluid is pushing the heavier fluid. In laser processing, such instabilities can cause:

- Fast mixing of gases at the contact between the plasma plume and the ambient medium in reactive laser ablation.
- The formation of droplets in laser surface-melting and vaporisation.

Different mechanisms related to droplet formation are schematically shown in Fig. 2.13. The recoil pressure and the expansion of the vapour plume generate a (relative) lateral velocity v_{vl}, at the vapour – liquid interface generating Kelvin–Helmholtz instabilities (Fig. 2.13 a). If the laser fluence is high enough, droplets with characteristic radii of 10 – 100 nm may be formed, even with single pulse irradiation.

The surface corrugation is another factor which can promote droplet formation (Fig. 2.13 b). The motion of the liquid out of the (hotter) valleys increases the amplitude of corrugation and causes centrifugal forces near the hills. This last effect can result in Rayleigh–Taylor instabilities leading to the formation of droplets. Such effects can be observed during multiple-pulse irradiation. If the amplitude of the corrugation becomes very large (Fig. 2.13 c) the velocity of the vapour along the walls, may cause shear force (Kelvin–Helmholtz) instabilities leading to the droplet formation. Thus, if the amplitude between the instabilities (Λ_i) is comparable to its corrugation depth (h_c), this mechanism may cause necking and the formation of solid particulates with radii of 0.1 to several μm [18].

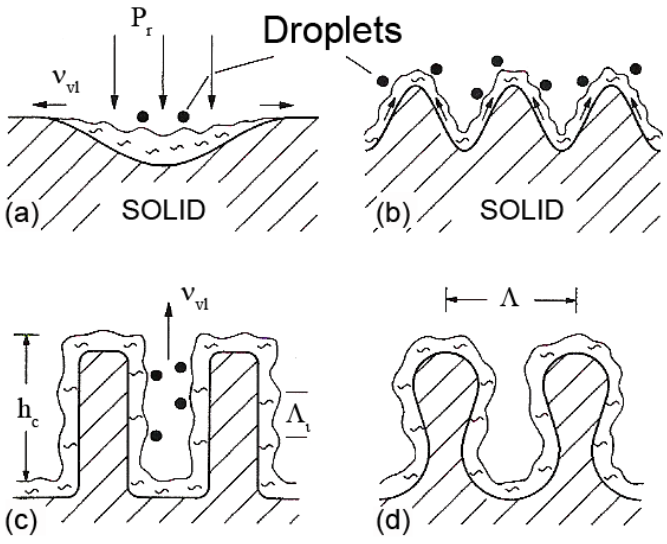

Figure 2.13. Droplet formation due to hydrodynamic instabilities generated during laser-induced melting and ablation. (a) Lateral velocity induces surface capillary waves via Kelvin–Helmholtz instabilities. (b) Centrifugal force near the hills may cause Rayleigh–Taylor instabilities. (c) Shear forces (Kelvin–Helmholtz) instabilities, and (d) necking and formation of solid particulates.

2.5 Laser-induced oxidation of metals

The reaction mechanisms of metal with oxygen can be considered as a multi-sequence process which involves transport in the gas phase, oxygen decomposition in the gas or at the solid–gas interface, adsorption, dissociation, transport of the species to the reaction site through the oxide layer, chemical reaction, nucleation of the oxide(s), etc. Some of these events are schematically represented in Fig. 2.14. Two different theories are important for describing the oxide layer growth: Wagner's theory for thick films [65] and Cabrera and Mott

theory for thin films [66]. The Wagner theory is based on diffusion of the slowest particles (usually metal and/or oxygen ions) across the grown oxide film, assuming that local chemical equilibrium exists everywhere in the film and there are no electric (ionic or electronic) currents flowing across it. This theory leads to the parabolic rate equation for oxide growth. On the other hand, the Cabrera–Mott theory is based on the assumption that electrons can freely pass from the metal to ionise adsorbed oxygen atoms or molecules at the oxide–gas interface. Since this model applies to very thin films, the role of the electric field is crucial. This theory yields to different film growth laws depending on the defect creation mechanism.

Laser-induced oxidation is a very complicated process involving different laser parameters which may influence the oxidation kinetics and dynamics [67, 68]. It has been shown that laser-induced oxidation has very noticeable differences compared to the classical isothermal oxidation of metals. Laser irradiation not only acts as a special heat source. Its electromagnetic nature may give rise to specific effects that are not found under furnace annealing conditions. Generally, the effect of laser irradiation can be classified into three categories: thermal, electronic and feedback effects [18, 69, 70].

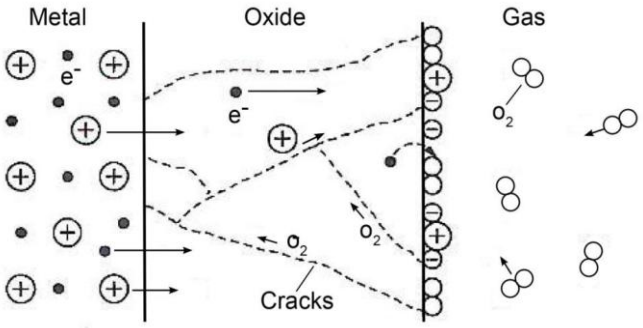

Figure 2.14. Possible mechanisms involved in the reaction of metals with oxygen: transport of the species in the gas phase, oxygen decomposition, adsorption and/or desorption, diffusion of the species in the oxide and at grain boundaries, chemical reaction, nucleation of the oxide(s), formation of cracks, etc.

The thermal effect results from heating and from the existence of strong temperature gradients. These temperature gradients are also responsible for altered surface tensions, and induced stress, and/or strain, (see also Section 2.4.2). The laser-induced temperature rise enhances the diffusion flux and the reaction rate of species within the irradiated zone. This enhancement is based on different mechanism: the temperature dependence of atomic diffusion, the thermal generation of defects such as vacancies, and the thermal excitation of electrons. The effects of temperature gradients are expected to play an important role in the mechanisms in which atomic diffusion takes place, but they are not expected to influence oxygen decomposition, adsorption, desorption and/or nucleation. The electronic effect results from optical absorption via the excitation of electrons from occupied to unoccupied states. Various types of excited electronic states may thereby be created, which are very sensitive to the photon energy of the laser beam. The increase in electrons expelled from the metal may

result in a rise in electric field intensity in the oxide layer and, consequently, in an increase of the oxidation rate.

In the case of feedback effects, the starting and final materials are characterised by different physical properties. If the final reaction product absorbs the laser irradiation more efficiently than the starting substrate, "positive feedback" occurs and self-acceleration of the reaction rate results. On the contrary, "negative feedback" is produced when the starting substrate absorbs more efficiently than the reaction product, and the oxidation process stabilises (for example, the oxidation of Zn [71]). A third situation is observed when interference effects cause the amount of absorbed energy to fluctuate with the oxidation process: the reaction self-accelerates for a period of time, then slowly decreases as the reaction continues, then accelerates again, and so on. This gives rise to oscillating reaction rates. This phenomenon has been observed during laser assisted oxidation of Cu [72, 73]. The oxidation of thin Cu films on sapphire substrate via cw–Ar^+ laser radiation is one of the more investigated systems. The laser–grown oxide consisted mainly of Cu_2O. Figure 2.15 depicts the time-resolved reflectivity measure *in situ* for different laser powers.

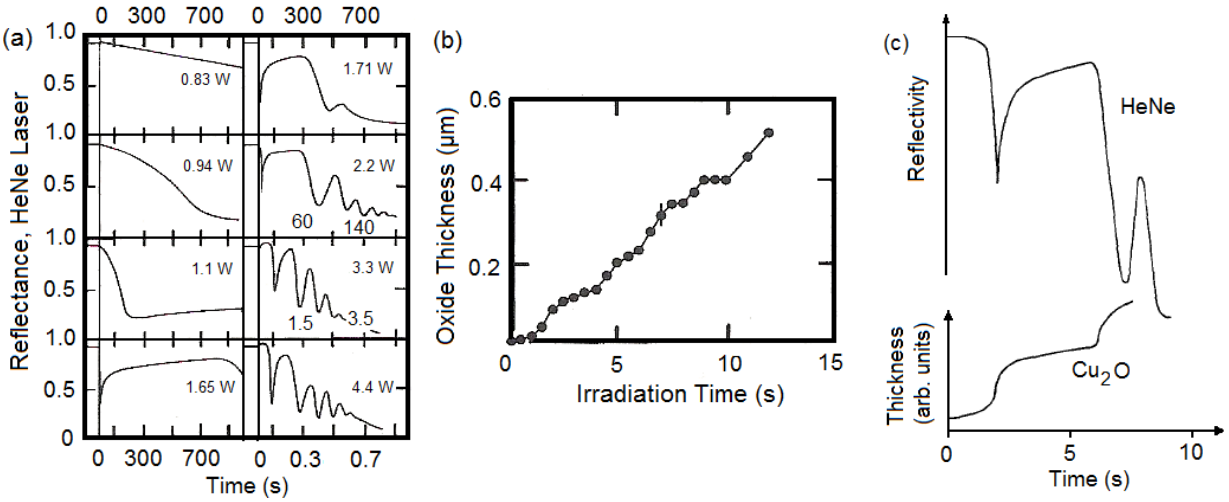

Figure 2.15. Laser-induced oxidation of 0.05 μm thick Cu films on sapphire. (a) Time-resolved reflectance measurements by HeNe-laser probe beam. Vertical lines indicate the beginning of the irradiation. Note changes in time scale with 2.2 W, 3.3 W and 4.4 W curves. (b) Oxide-layer thickness as a function of the irradiation time. The incident laser power was 2.8 W. (c) Schematic representation of Cu oxidation showing an oxidation feedback effect.

The reflected light intensity shows damped oscillations due to interference (Fig. 2.15a). The decrease in time between oscillations observed with increasing laser power is due to the increase in film growth rate. The variation of the oxide thickness with time, under cw–Ar^+ laser irradiation, has been measured via interference effects [73] and depth profiling [72] for

Cu_2O as shown Fig. 2.15b,c. These behaviours are interpreted on the basis of a thermal model, in which temperature fluctuations are taken into account.

The reaction stops either when the entire film is oxidised or in a region of negative feedback. In particular, the maximum dimension of the oxidised zone of thin films on transparent substrates is expected to be given by conditions of negative feedback, when the oxide is itself transparent; such is the case of Zn [71] on glass substrates.

One of the most important effects involved in laser-induced oxidation in metals is the change of the absorptivity with the increase of the growing oxide layer and/or film thickness [18, 72, 74] (see Fig. 2.16). The absorptivity itself is a function of optical and thermal parameters (see Section 2.2) and in most general cases can be expressed as a function of the optical parameters and oxide thickness *x*, as:

$$A(x) = \frac{n^2 A_0 + 2k[\alpha x - \sin(\alpha x)]}{n^2 + (1 - n^2)\sin^2(\alpha x/2)} \,, \tag{2.25}$$

being A_0 the initial absorption of the surface [18, 75]. The oscillations in the absorptivity (Eq. 2.25) are due to interference of the laser light within the thin layer.

The above equation is usually applied to multilayer structures for weakly absorbing films. The period Δx and number Z of oscillations in the absorptivity can be determined by:

$$\Delta x = \frac{2\pi}{\alpha} \;; \text{ and } \; Z = \frac{x}{\Delta x} \approx \frac{n}{2\pi k} \,. \tag{2.26}$$

The latter approximation, Z, estimates the number of pronounced oscillations which occurs up to a thickness, x, of approximately $1/\alpha$ (absorption length, see Eq. 2.8). For an oxide of Cu_2O and 10.6 µm CO_2-laser radiation, the estimated number of oscillations is Z=14 (see Fig. 2.16) [18].

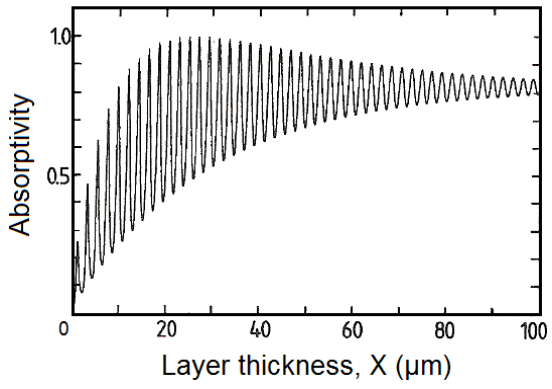

Figure 2.16. Absorptivity calculated as a function of layer thickness. The parameter A_0 = 0.02, n = 2.45, and k = 0.027 correspond to a Cu_2O layer on Cu substrate and CO_2-laser radiation [18] .

However, the number of oscillations observed experimentally also depends on the surface roughness and wavelength. *A(x)* can be an indicator of interference changes into the

system. For $dA/dx < 0$ the system is characterised by negative feedback leading to self-stability of the process, while for $dA/dx > 0$, due to the positive feedback between the thermal and optical parameters, some instabilities can surge in the system (*e.g.*, self-sustained oscillation, chaotic flows, etc.). Such kinds of instabilities have been observed for the case of W and V oxidation [76, 77]. Vanadium oxidation induced by continuous IR laser has been one of the few systems studied in which liquid phase was involved. The most saturable vanadium oxide is V_2O_5, which has a very low melting point (~ 670°C). In the work of Nánai *et al.* [77] the growth of vanadium oxide in air under the action of IR laser irradiation was investigated. The parabolic rate law was assumed. This law can be written for kinetics measurements as:

$$\frac{dx}{dt} = \frac{d_0}{x} e^{-(T_d/T)}, \tag{2.27}$$

where T temperature, d_0 and T_d are the oxidation constant and the activation energy, respectively. It was found that the activation energy of the oxidation (T_d) varies only slightly with the temperature, while the oxidation constant (d_0) changes dramatically (by more than nine orders of magnitude) compared with the isothermal process of oxidation (Fig. 2.17).

In pulsed-laser oxidation, thermodynamically unstable phases may remain, while other phases cannot nucleate within such short times. In practice, the formation of different oxides is evidence of the presence of different kinetic laws. Additionally, in the case of reactive metallic substrates irradiated with a pulsed laser at ambient conditions (without neutral gas covering), limited oxidation is always observed or assumed [78].

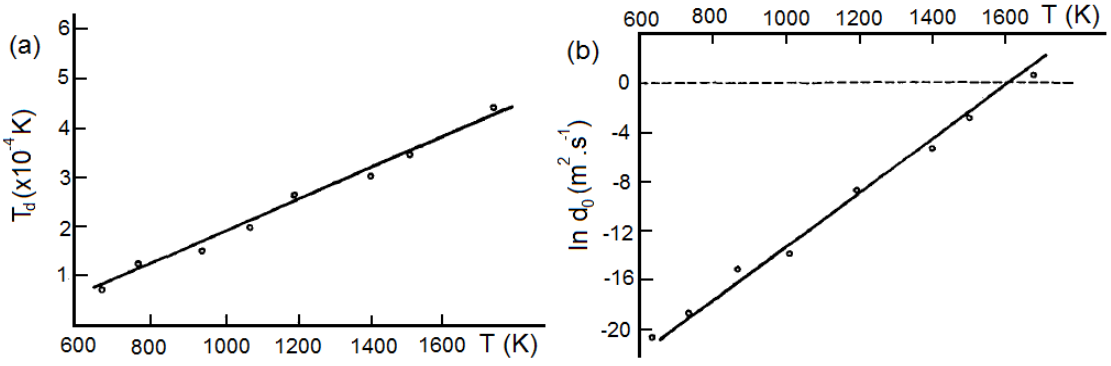

Figure 2.17. (a) Energy T_d of activation as a function of the temperature. (b) Temperature variation of the oxidation constant for vanadium target oxidation [77].

Recently, titanium oxidation during laser heating in air and controlled atmosphere has been investigated because of its important technological applications such as photocatalysts, gas sensors, biocompatibility and optical coatings [79-81]. A theoretical model [82] has been

developed to describe oxide film growth of titanium films due to its surface heating by a moving beam of a pulsed *Nd:YAG* laser. The numerical approach takes into account the three-dimensional solutions of the heat diffusion equation coupled with the parabolic growth law. The theoretical and experimental results obtained for the TiO_2 thickness as a function of laser intensity are shown in Fig. 2.18. As can be observed, the oxide layer increases monotonically with increasing laser energy. Nowadays theoretical models are still too incomplete to offer a good understanding of the physical–chemical mechanism involved in laser assisted oxidation of metals. The physical processes that take place at the metal film surface, in the formation and growth of oxide film by the pulsed laser irradiation are still poorly understood. Even for a classical Al/Al_2O_3 comprehensive and fundamental knowledge of the relationship between mechanism(s) that govern the oxide-film growth is lacking. One of the most important problems is that the thermal field produced by pulse laser irradiation during oxidation of metals is variable and transient, whereas the oxidation kinetics laws (Wagner theory or Cabrera–Mott theory) are based on a defined temperature (or temperature range). Thus, the oxidation models developed until now do not take into account phase changes or surface modifications in the material.

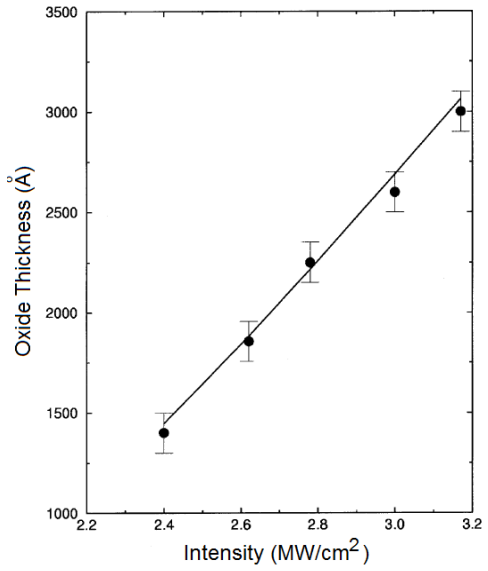

Figure 2.18. Dependence of the oxide thickness on laser intensity for 200 pulses. The full line corresponds to the theoretical value and the dots to the experimental data.

Since Al melts at 660°C, the growth of Al_2O_3 on solid substrates at high temperature can only be studied using alloys of Al with refractory metals [83-86]. Few studies concerning aluminium oxidation at temperatures above the melting point have been published. In the work of Bergsmark *et al.* [87] the thermal oxidation of molten aluminium at different oxygen partial pressure at 800-950°C was investigated. It was found that the reaction kinetics are complex and cannot be described by simple rate equations. Plots of the oxidation rate (weight gain vs. time) curves have an approximately *S*-shaped form. Also, it has been reported that the

growth rate of an oxide layer at the liquid surface is much lower than in the case of a solid surface [88]. Almost no data exists on the oxidation of aluminium induced by laser radiation.

It is very important to point out that the oxide layers built up during laser irradiation are very stable and can enhance the chemical stability of the irradiated zones. This phenomenon can be effectively used for coating in laser biomaterials processing, as a masking layer in several processes, such as lithography [70].

CHAPTER 3

State of the art: patterning techniques and electrolytic capacitors

The literature presented in this chapter will familiarise the reader with the depth, breadth and scope of the research topic and establish the body of knowledge that this research will contribute to. It starts with a short review of the different patterning techniques most used for surface structuring, paying special attention to the Laser Interference Metallurgy method.

In the second part of the chapter a brief description of electrolytic aluminium capacitors and their manufacturing procedure are reported, focussing on the electrochemical etching process as well as the factors that can influence it. Finally, the definition of the problematic in the field of capacitor production is exposed, which will serve as the baseline to justify the approach proposed here.

3.1 Surface patterning

Nowadays, patterning is of great interest in many areas of materials science due to its diverse applications, ranging from the production of integrated circuits, miniaturised sensors, biochips, micro-optical components, and diffractive optical elements, among others. The process of patterning is usually referred to as lithography [89]. The general term, lithography, refers to a process in which a surface is structured by first coating it with an irradiation-sensitive polymer layer ("resist"), then forming a desired pattern in the resist coating by exposing it with light, and finally transferring the pattern into the surface. Figure 3.1 shows the different pattern transfer techniques (from the resist to the substrate) after lithography.

The critical feature size of the test pattern is probably one of the most important issues to consider when selecting a specific lithography technique. The design and engineering of micro-nanostructures are specific to a given application. We provide, in this part of the chapter, a brief outlook of the more generic issues of patterning formation activated by light, electron or ion beams leaving out the non-conventional pattern methods based on contact printing.

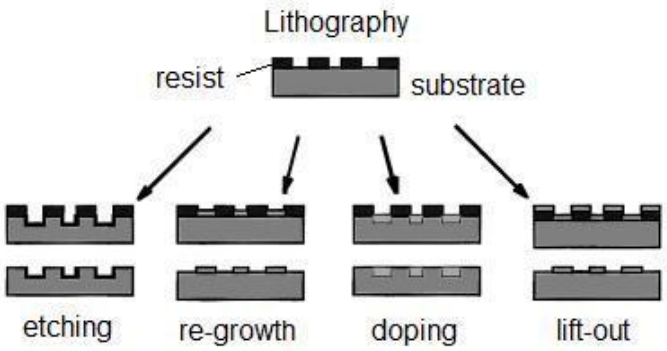

Figure 3.1. Schematic representation of lithography and pattern transfer techniques [90].

3.1.1 Electron beam lithography

A typical electron beam (e-beam) system consists of a column of electron optics for forming and controlling the electron beam, a sample stage and control electronics. Its set-up is similar to a Scanning Electron Microscope. During the e-beam lithography process, the electrons are continuously slowing down providing a cascade of secondary electrons which are responsible for the resist reaction, such as polymerisation, polymer cross-linking, etc. The resolution of e-beam lithography is essentially defined by the e-beam spot size and the forward-scattering range of the electrons [91]. In the resist, electrons undergo small angle forward-scattering and some back-scattering coming from the substrate. The forward-scattering tends to broaden the initial beam diameter, whereas the back-scattering can spread over a large volume (proximity effects) [90]. E-beam lithography is a high-resolution technique but, it is not suitable for mass production because of the limited writing speed. It is used for primary patterning of the resist, which is performed directly from a computer-designed pattern. Depending on the design, e-beam energy varies in the range of 1-200 KeV with a spot size of some nanometers. A variety of materials have been used for e-beam lithography, including polymers [92] and inorganic materials [93] among others. Poly (methyl methacrylate) (PMMA) is the classical resist for this technique.

3.1.2 Focused ion beam lithography

Focused ion beam lithography is conceptually analogous to e-beam lithography. The ion source is typically made of a sharp W tip coated with a liquid metal, Ga for example. As the ions penetrate the material, they lose their energy at a rate several orders of magnitude higher than that of electrons because of their mass. Therefore, the penetration of ions, and thus the back-scattering-caused proximity effects, are much reduced compared to that of electrons. Very thin resist layers are generally required for heavy ions. Other advantages include the

possibility of highly localised implantation doping, mixing, micromachining, controlled damage as well as ion-induced deposition. The drawback of the focused ion beams is their limited writing speed because the ion current density is 1 or 2 orders of magnitude smaller than that of electron beams [89, 90].

3.1.3 Optical lithography

Optical projection lithography is normally used for mass production. In this technique, the printing process is carried out by the projection of the pattern image on the substrate surface using a light source and a photo-mask. The typical exposing energies are visible light, ultraviolet (UV) and also deep UV light sources. The light source is used to expose a photoresist through the mask containing alternating opaque and clear features, made of chromium absorber on a glass substrate. The feature sizes are usually on the order of the wavelength of the light employed, with the finality to avoid diffraction effects. The light exposure creates a chemical change in the resist film which, depending on the tone resist material, makes the exposed resist region more or less soluble in a developing solvent. The response of the resist (tone resist) to exposure can be either positive or negative, depending on whether the expose or unexposed portion will be removed from the substrate after development. The exposed resist film is developed to produce the desired protective relief pattern. The resolution of optical projection lithography depends on the wavelength, numerical aperture of the optical system, and an empirical factor depending on the details of the experimental conditions. Also, the focus depth is another important parameter to define the process latitude (tolerance) in optical lithography [90, 94]. The process latitude is the degree by which a resist can be over or under exposed, and still recover an acceptable level of quality from an exposure.

3.1.4 Holography patterning

Holography lithography produces periodic structures in a thin-film resist. Typically, the optical standing waves used in this technique are obtained by splitting a laser beam in two or more beams and then intersecting them via mirrors. Essentially, it involves the formation of a stationary spatial variation of the intensity which can be readily recorded in a thin film of photoresist. The technique of holography interference lithography allows creating 1D, 2D and 3D periodic patterns using coherent laser beams. In the case of two coherent laser beam

interference, an array of parallel lines will be created in the photoresist film, in which the spacing (d) between the lines is:

$$d = \frac{\lambda}{2n} sin(\theta/2)\,, \tag{3.1}$$

where λ is the wavelength of the laser light, n is the refractive index of the resist, and θ is the angle of intersection between the beams [89, 95]. This technique is widely used in the photonics industry to manufacture holographic diffraction grating and antireflection coatings. More complex structures can be formed by intersecting more than two laser beams or by using multiple sequence exposure [96]. The symmetry and grating distance of the structures are determined by the configuration of the laser beams, and can be predicted in advance by calculations. One of the advantages of this technique is that it is a relatively simple and fast process, and the exposure and development steps can be completed in short times (minutes) making it well-suited for high-throughput production. As a drawback of this technique, the materials that can be directly patterned are based on polymers that are usually characterised by low refractive indices [89].

3.1.5 Direct laser interference

The different techniques presented until now consist of many steps in between (such as pre-design patterns in the form of a mask or master, transfer or replication of the patterns, etc.) to form ordered array structures. Each one of these steps may impose the possibility of information loss and/or pattern distortion. Direct laser interference is unique inasmuch that it allows in one single step and maskless the direct production of periodic patterns, spanning the range of submicron to several microns. This technique is analogous to holography lithography, but here a light sensitive medium (photoresist) is not needed and, consequently, nor is any development step. One of the most important requirements to employ this method is that the material to be structured must absorb the laser energy at the selected wavelength. The micro-structuring formation is based on photophysical effects (see Section 2.3.1) [18]. Additionally, this technique has been successfully applied in diverse kinds of materials such as polymers [97], semiconductors [46, 98], and thin metal films [99, 100].

3.1.5.1 Interference – theoretical background

The electric field associated with a monochromatic plane wave was already described mathematically in Chapter 2 (see Eq. 2.1). The total electric field of the interference pattern created by a set of beams can be obtained by the superposition of each individual "*j*" beam:

$$E = \sum_{j=1}^{n} E_j = \sum_{j=1}^{n} E_{j0} e^{i(\vec{k}.\vec{r}-\omega t)} . \tag{3.2}$$

The wave vector $\vec{k}$ can be expressed in terms of the beam angles with respect to the interference plane (*x*, *y*, *z*) (see Fig. 3.2) as:

$$\overrightarrow{k^*} = -k^*(\hat{x} \sin\alpha_j \cos\beta_j + \hat{y} \sin\alpha_j \sin\beta_j + \hat{z} \cos\alpha_j). \tag{3.3}$$

where k^* is the wave number defined as:

$$k^* = \frac{2\pi}{\lambda}. \tag{3.4}$$

Considering that the sample is located at $z = 0$ (in *x*, *y* plane) and $\omega = 0$, we can rewrite Eq. (3.2) in terms of α_j, β_j, *x* and *y* obtaining:

$$E = \sum_{j=1}^{n} E_{j0} e^{-ik^* \sin\alpha_j (x\cos\beta_j - y\sin\beta_j)} . \tag{3.5}$$

As it was mentioned in Section 2 of Chapter 2, the spatial intensity distribution for each individual source is given by Eq. (2.4).

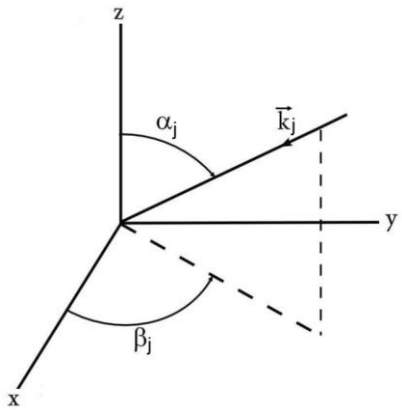

Figure 3.2. Representation of one wavenumber $\vec{k}$ of the angular spectrum of the electric field [101].

Substituting *E* in (2.4) by the amplitude of the resultant sinusoidal wave E_0 the intensity distribution of the overlapped beams is given by:

$$I = \frac{1}{2} c \in_0 |E_0|^2. \tag{3.6}$$

The particular beam conditions to create 1D and 2D structures are summarised in Table 3.1 [102, 103]. Two-beam interference produces a line-type interference pattern. Assuming the conditions shown in Table 3.1 for linear pattern, the intensity distribution can be expressed as:

$$I = 2c \in_0 E_0^2 \cos^2(kx \sin\alpha). \tag{3.7}$$

where 2α is the angle between the laser beams.

In particular, the maximal intensity I_0, which occurs when the cosine has the value ± 1, is:

$$I = 2c \in_0 E_0^2 . \tag{3.8}$$

According to Equation (3.8), the maximum intensity is four times greater than the intensity from each individual beam (Eq. (2.4)).

Table 3.1 Particular beam parameters to achieve 1D and 2D structures.

Conditions	Linear pattern (1D)	Dot pattern (2D)
Beam numbers (n)	2	3
E_{0j}	$E_{01} = E_{02} = E_0$	$E_{01} = E_{02} = E_{03} = E_0$
α_j and β_j	$\alpha_1 = \alpha_2 = \alpha$; $\beta_1 = 0$, $\beta_2 = \pi$	$\alpha_1 = \alpha_2 = \alpha_3 = \alpha$; $\beta_1 = 0$, $\beta_2 = \frac{2}{3}\pi$, $\beta_3 = -\frac{2}{3}\pi$
Period (d)	$d = \frac{\lambda}{2\sin\alpha}$.	$d = \frac{\lambda}{\sqrt{3}\sin\alpha}$.

Three-beam interference leads to different 2D arrays depending on the magnitude of the electric field of each beam and the geometrical configuration. A symmetrical configuration (see Table 3.1) produces hexagonal dot-like pattern, whose intensity distribution $I(x,y)$, is given by [102, 103]:

$$I = \frac{9}{2}c \in_0 E_0^2 \left[\left(-\cos(kx\sin\alpha) - \cos\left(k\sin\alpha\left(-\frac{x}{2} - y\frac{\sqrt{3}}{2} \right) \right) - \cos\left(k\sin\alpha\left(-\frac{x}{2} + y\frac{\sqrt{3}}{2} \right) \right) \right)^2 + \left(-\sin(kx\sin\alpha) + \sin\left(k\sin\alpha\left(-\frac{x}{2} - y\frac{\sqrt{3}}{2} \right) \right) - \sin\left(k\sin\alpha\left(-\frac{x}{2} + y\frac{\sqrt{3}}{2} \right) \right) \right)^2 \right]. \tag{3.9}$$

3.2 Aluminium electrolytic capacitors

An aluminium electrolytic capacitor consists of two electrically conductive material layers that are separated by a dielectric layer (see Fig. 3.3). The anode is formed by a high-purity aluminium foil with an enlarged surface area. The oxide layer (Al_2O_3) that is built up on this, by anodic oxidation, is used as the dielectric. In contrast with other capacitors, the cathode of an aluminium electrolytic capacitor is a conductive liquid, the operating electrolyte. The liquid has the advantage of filling the fine etching pits, therefore optimally fitting into the anode structure. A second aluminium foil, the so called cathode foil, serves as a large contact area to pass current to the operating electrolyte. The two aluminium foils are separated by paper spacer. The paper serves as a container for the electrolyte and also as a spacer to prevent electric short-circuits as well as ensuring the required dielectric strength between the anode and cathode foils [104, 105].

The effective surface area of the anode foil is greatly enlarged by electrochemical etching in order to achieve the maximum possible capacitance values (capacitance per foil volume). The capacitance of an aluminium electrolytic capacitor may be calculated by

$$C = \epsilon_0 \cdot \varepsilon \cdot \frac{A}{d_c} , \tag{3.10}$$

where ϵ_0 is absolute permittivity, ε is the relative dielectric constant, A the electrode surface area, and d_c the electrode spacing (thickness of the dielectric) [104]. To attain a higher capacitance device, the dielectric constant and the surface area of the anode foil must increase while the dielectric thickness must decrease. The dielectric layer is created by anodic oxidation (forming) to obtain an aluminium oxide layer whose thickness (d_c) can be freely controlled according to the forming voltage used.

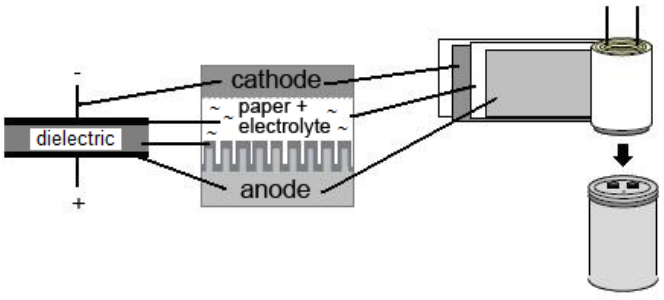

Figure 3.3. Basic construction of high-voltage aluminium electrolytic capacitor [105].

The process to enlarge the anode foil surface (etching structure) for low-voltage (LV) and high-voltage (HV) applications differs enormously. The next discussion is focused on the production of HV anode foils. From the standpoint of HV capacitors, the surface area of

etched aluminium basically determines its capacitance. The main process flowchart is represented in Fig. 3.4a.

DC etchings are usually adopted for HV capacitors. The etch process is typically carried out in hot chloride solutions under constant applied current or voltage, and results in the formation of a high density (as high as $10^8/cm^2$) of micrometer-wide corrosion tunnels. The anodic dissolution of high-purity aluminium foil occurs preferentially in the ⟨100⟩ direction, so the basis structural unit is half a cubic pit. In the DC etch, the pits grow initially, but, after a brief time (~100 ms), the pit walls passivate and only the pit bottom continues to dissolve. Passivation of new wall continues at the same pace as dissolution of the bottom surface, producing crystallographic etch tunnels of the order of 1 μm wide and 50 μm long. Normally, the etch treatment is run at temperatures superior to 65°C. In this process, dissolution occurs parallel to passivation. The steady state dissolution potential is the repassivation, because this is the only potential at which passivation and dissolution can occur. Pit nucleation and growth are essential steps in the etch treatment [106]. An example of an etching structure generated in an HCl / H_2SO_4 mixing solution is shown in Fig. 3.4b.

The enlargement of the tunnels is mainly performed electrochemically and should conserve the etching structure produced in the first etching process to obtain the high capacitance values. By etching, the effective surface area of the foil can be enlarged 30-40 times as compared to the apparent area for high-voltage capacitors [107].

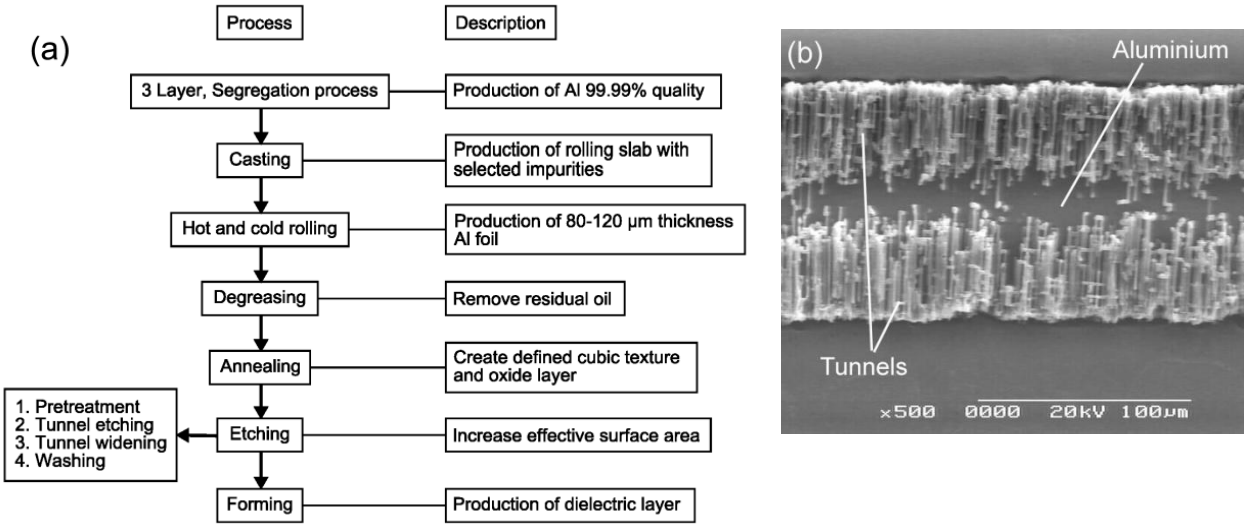

Figure 3.4. Aluminium HV capacitors: (a) material flow, (b) typical cross section of etched Al foil showing the tunnel structure [105].

3.3 Factors which affect the chemical behaviour of aluminium

For the purpose of obtaining the maximum possible capacitance, the tunnel pits should be evenly distributed on the surface, and their size and interval must be precisely controlled [108-110]. Multiple factors such as grain size, cubic texture (proportion of cubic grain having ⟨100⟩ orientation), uniformity of the oxide layer, impurity concentration and/or pre-treatments can influence the tunnel etching. In general, the grain size of aluminium foil for high-voltage capacitors is very large, ~ 50-200 μm. The high cubic texture fraction (*cubicity*) is one of the most important factors during the etching process, because the tunnels are formed preferentially along the ⟨100⟩ direction in hydrochloric acid. Otherwise, the effects of impurities, present in the aluminium foil at ppm levels, are applied to increase the number of tunnel pits so as to enhance etchability [111-115]. The distribution of the etch pits can also be modified by the uniformity of the oxide layer. It was reported that the initial pits are probably caused by etching at areas where the oxide layer is significantly distorted and therefore less protective (cracks and thin sections) [116, 117]. Furthermore, etching conditions such as temperature, chemical composition of the bath, surface pre-treatments (*e.g.*, chemical etching in sodium solution or phosphoric acid solution) could also influence the electrochemical etching behaviour.

However, the ideal enlargement of the surface area by electrochemical etching is difficult to find due to a disorderly pit distribution and the growth of merged pits by lateral dissolution. Therefore, improvements in pit distribution and the homogeneity of the pit sizes, avoiding an excessive dissolution of the aluminium surface, are essential for maximising the surface area of etched aluminium. In order to overcome this challenge, numerous studies have been published which try to control the pit-site distribution by different methods. Some of them will be described below.

3.3.1 Chemical composition

The distribution of the pit initiation sites on aluminium has been improved generally by changing the chemical composition of the surface. As was mentioned above, aluminium anode is composed of a high-purity aluminium foil which contains a selected number of impurities, such as Fe, Cu, Sn, Mn, Zn, Pb, In, etc. The total amount of impurities is of ~ 100 ppm. Heat treatment of the foil is an essential step prior to tunnel etching, because it leads to the segregation of some impurities to the near-surface regions. The diffusion

coefficients of some microelements in aluminium matrix as a function of the temperature are shown in Fig. 3.5. A number of studies have reported the effect of the nature and distribution of the impurities on the outcome of electrochemical etching. Many researchers have indicated that the distribution of surface impurities could be even more important than the impurity content [118-122]. Recent studies suggest that a small addition of lead (Pb) strongly affects the formation of uniform and fine tunnel pits in aluminium foil [120, 123-126].

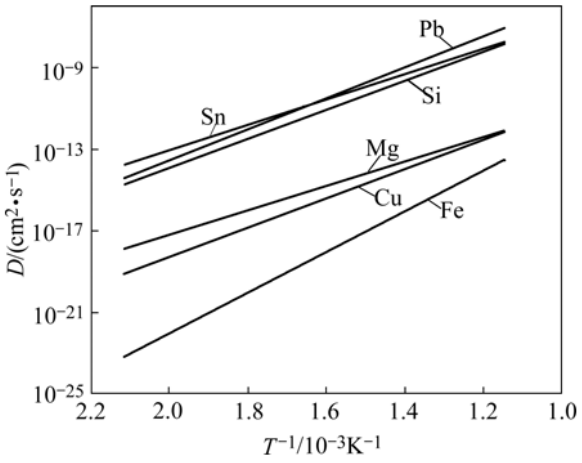

Figure 3.5. Diffusion coefficient of microelements in aluminium matrix [127].

The Pb addition promotes the development of regular distribution of fine tunnels, compared with the relatively coarse tunnels produced in the foil without lead. This positive effect has been related to the enrichment of lead at the annealed aluminium surface. However, the precise location of lead is uncertain, owing to limitations in the sensitivity and spatial resolution of available analytical techniques. Some studies have concluded or suggested that lead segregates at the aluminium metal surface or just beneath oxide film [119, 124, 126], whereas other authors concluded that lead segregates predominantly at the oxide film and not at the aluminium surface or oxide/aluminium interface [115]. The mechanism by which Pb actives the aluminium surface is still unknown, but usually the electrochemical activation of the surface is manifested by a significant shift in the corrosion potential and significant increase in the anodic current output [120].

Some studies about the diffusion of lead implanted into aluminium have been realised [128, 129]. Changes were reported in the lead profiles after annealing of the samples to temperatures around 380°C (*i.e.*, somewhat higher than the bulk melting point of lead). These profile changes were associated with “Brownian-like motion” of the molten lead inclusions modified by an intensive flow of thermal vacancies to the surface.

From Fig. 3.5 it can be observed that the coefficient of both lead and tin are higher than any other alloying elements, therefore very high concentrations of tin atoms in the Al surface

have also been studied. Song *et al.* [121] investigated the effect of Sn on the pitting morphology of anode aluminium foil. It was found that the micro-alloyed Sn enriches the external aluminium surface. The superficial enrichment with Sn provides a large number of sites for the initiation of pitting corrosion, while the pitting sites appear relatively inhomogeneous for Al foil without the presence of this element.

The effect of indium impurities on the etched morphology of aluminium has also been investigated [122]. Saidan *et al.* [130] studied the activation mechanism of aluminium alloyed with indium. It was concluded that aluminium activation is obtained only when indium comes into a true metallic contact with aluminium within an active pit in the presence of chloride ions.

Furthermore, the addition of copper at the ppm level has been found to greatly improve the capacitance [124, 131, 132]. In contrast to lead behaviour, the superficial enrichment of Cu during heat treatment is negligible. Copper appears to play a less direct role in initiation of the tunnel etching, but its addition can modify the cellular boundaries of the aluminium foil, and hence, possibly also the distribution of lead. Moreover, the copper may influence the tunnel growth, including tunnel widening. Tanno *et al.* [133] investigated the effect of Cu on the microstructure of aluminium and how it affects the pit initiation sites. The aluminium microstructure, which consists of a fine network of cells, was revealed by chemical polishing process of Al foil. It was found that the cellular structure changed with impurity content and that the initiation of the etch pits occurred on the wall and propagated to the interior of the cellular structure.

Chen *et al.* [118] claimed that silver content in Al foils promoted Al-Fe-Mn and Al-Fe-Mn-Si precipitation as well as enhanced surface etching, resulting in a large amount of small pitting sites. The capacity increased with increasing silver content up to 0.2 %, where the precipitations becomes oversized and drop off from the matrix. As a result, large holes are produced and the etching surface area decreases, leading to a fall of the capacity.

Although the impurity effects may improve the pit-site distribution and the etchability of Al anode foil, the excessive introduction of them can also have a prejudicial effect on the electrochemical etching. For example, an excessive incorporation of Fe and/or Cu element could also decrease the cubic texture fraction of the foil.

3.3.2 Direct control of pit-sites

Although the dispersibility of the pit initiation sites has been generally improved by changing the chemical composition of the aluminium substrate [120-126], another approach to the direct control of the pit initiation sites, independently of the surface activation state of the substrate, has recently been proposed [134-137]. For high-voltage electrolytic applications, a certain interval between adjacent pits will be optimal to reach the maximum surface area available. For this purpose, methods based on pattern transfer of regular arrays seem to be a useful tool to overcome this challenge.

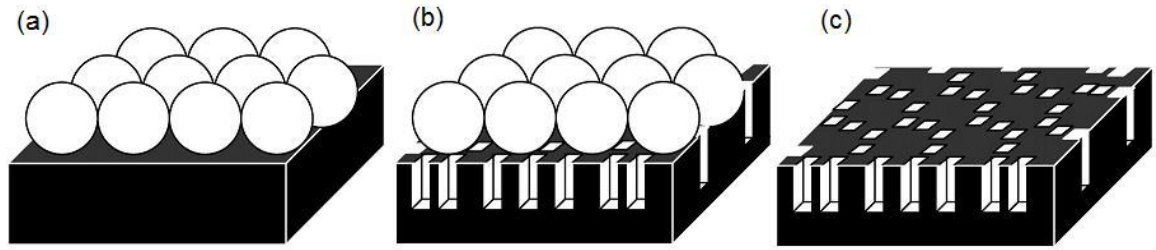

Figure 3.6. Schematic for etching process using colloidal crystal as mask: (a) self-assembled polystyrene spheres on aluminium substrate; (b) electrochemical etching of aluminium coated with colloidal crystal; (c) removal of spheres [134].

Asoh *et al.* [134] proposed a novel control method for pit initiation sites on aluminium using a direct physical mask for etching. A two-dimensional array of colloidal spheres, used as a mask, was prepared by self-assembly on an aluminium substrate (Fig. 3.6a). The transfer of the hexagonally ordered patterns of the spheres to the substrate could be achieved by the selective electrochemical etching of an exposed aluminium surface (Fig. 3.6b). The etch pits were generated only in the triangular void space between three adjoining spheres on the aluminium surface (Fig. 3.6c).The authors claim that using this process, improvement in the pit distribution and in the homogeneity of the pit size can be achieved. By changing the diameter of the spheres the excessive dissolution of aluminium is easily avoided, in comparison with the conventional process.

Masuda *et al.* [135] presented a method to control the etched tunnel pits using pretexturing of aluminium foil prior to the electrochemical etching in HCl solution. Pretexturing of an Al foil was carried out based on an imprinting process using a metal mould. The mould has an ideally ordered array of convexes in triangular lattice with interval of about 10 μm (Fig. 3.7a). Shallow concaves formed by imprinting led to the formation of tunnel pits, and generated an ordered array of etched tunnel pits propagating along the (100) plane (Fig. 3.7b).

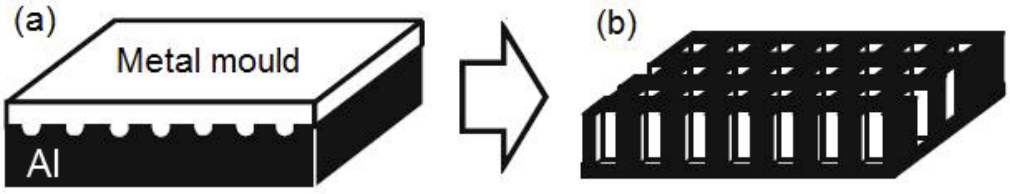

Figure 3.7. Schematic of etching sites control of Al foil using an imprinting process (a) pretexturing of Al foil and, (b) ordered array of tunnels after etching process [135].

Similar pitting control results were also found by the deformation of aluminium using a nanoindenter [136]. During the etching process, pitting was initiated at the edges of a triangular impression, and square pits were found as a result of anisotropic dissolution of the material (see Fig. 3.8). Using this technique, 4 x 4 arrays of square pits were obtained.

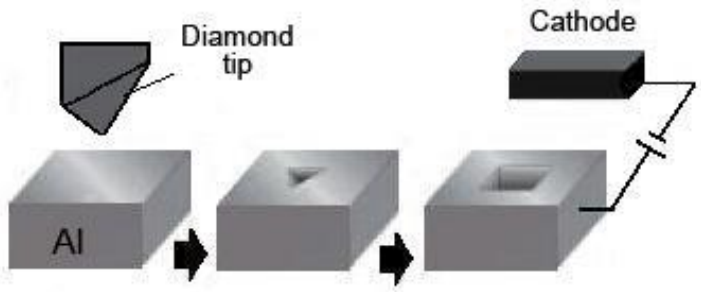

Figure 3.8. Schematic of pitting sites controlled by the deformation of aluminium foil using a nanoindenter [136].

In most reports of controlling pit sites by mechanical imprinting, nothing is mentioned about its reproducibility or possible texture changes of the substrate, which can lead to its lateral dissolution. Moreover, the changes of the chemical compositions and the impurities distribution in the substrate could modify its mechanical properties and also generated leakage of the current due to an undesired oxide film increase during the segregation process (annealing). The etching pit sites are also related with Al foil defects including mechanical flaws present in the Al foil surface, dislocations, and also cracks present in the oxide, which are associated with its crystallisation. These factors are not easy to control. Therefore, it is necessary to find a method to improve the fabrication of pit sites so as to achieve the optimal pit distribution minimising undesirable changes on the aluminium foil properties.

CHAPTER 4

Experimental

This chapter describes the experiments carried out for the study of different metallic systems: thin films and bulk metal, their preparation and characterisation. The structuring of the samples was achieved using different laser parameters. Chemical and electrochemical etching of pristine and laser irradiated specimens were performed to investigate their chemical behaviour as well as the influence of some metallic elements on the etchability of the samples. Polarisation measurements were also carried out to study the electrochemical behaviour of the specimens.

4.1 Samples

4.1.1 Bulk metals

Commercial aluminium foil for high-voltage capacitor applications was investigated. The samples consisted of high purity (> 99.99%) and degreased rolled aluminium substrates. The foils under study presented two different conditions: (1) annealed and (2) non-annealed samples. The thickness of the foils was approximately 120 µm. In some cases, annealed aluminium samples foils were metallographically prepared by electropolishing.

Furthermore, high-purity copper (99.99 %), titanium (99.99 %) and aluminium (99.98 %) were metallographically prepared and polished to a mirror surface using standard procedures. The thickness of the specimens was around 2 mm.

4.1.2 Thin film coating systems

Aluminium foil was coated with different metallic thin films. The films were produced by physical vapour deposition in an Ar-ion gun facility (Roth & Rau, UniLab) under an Ar atmosphere of $4x10^{-4}$ mbar. The thickness of the films was monitored in-situ by a microbalance (Tectra, MTM-10). The configuration of the different systems used in this work is summarised in Table 4.1.

Table 4.1. Metallic elements and selected layer thickness to coat annealed aluminium foil.

Element	Lead	Copper
Thickness (nm)	2, 5, 7, 10 and 30	2, 5, 7, and 10
Nomenclature	Pb/Al	Cu/Al

4.2 Laser interference structuring

A high-power pulsed *Nd:YAG* laser (Quanta-Ray PRO 290, Spectra Physics) was used for laser interference experiments. The fundamental wavelength of the *Nd:YAG* laser is 1064 nm, in the infrared electromagnetic spectrum. However, these kinds of lasers are typically operated in the so called Q-switching where the high-intensity pulses may be efficiently frequency doubled (second harmonic) to generate laser light at 532 nm, or higher harmonics at 355 nm and 266 nm (third and fourth harmonics, respectively).

The laser patterning was carried out under ambient conditions using wavelength of 266 nm, 355 nm and a repetition frequency of 10 Hz. The pulse duration of the 355 nm radiations was 10 ns. A mechanical shutter (Uniblitz Electronic VS25S2ZMO) was employed to select the number of pulses.

The LIMET experiments were performed by splitting the output beam into two or more coherent beams to interfere with each other on the sample surface. A schematic of the experimental setup is shown in Fig. 4.1. By regulating the laser beam size one can control the energy density impinging on the sample surface. The intensity of each individual beam can be controlled by using suitable lenses and mirrors. Their energy was measured by using a power meter, Power Max ® model PM30V1.

For chemical investigations, a square mask was used to obtain a laser beam area of approximately 2.3 x 2.3 mm^2. The total structured areas were produced by using a sample holder (Kleindiek) controlled by computer micro-positioning stages. These were triggered with the laser. Two structured area sizes of 20×20 mm^2 and 40×40 mm^2 were created. The structuring of thin aluminium foils was accomplished perpendicularly to the line rolling direction.

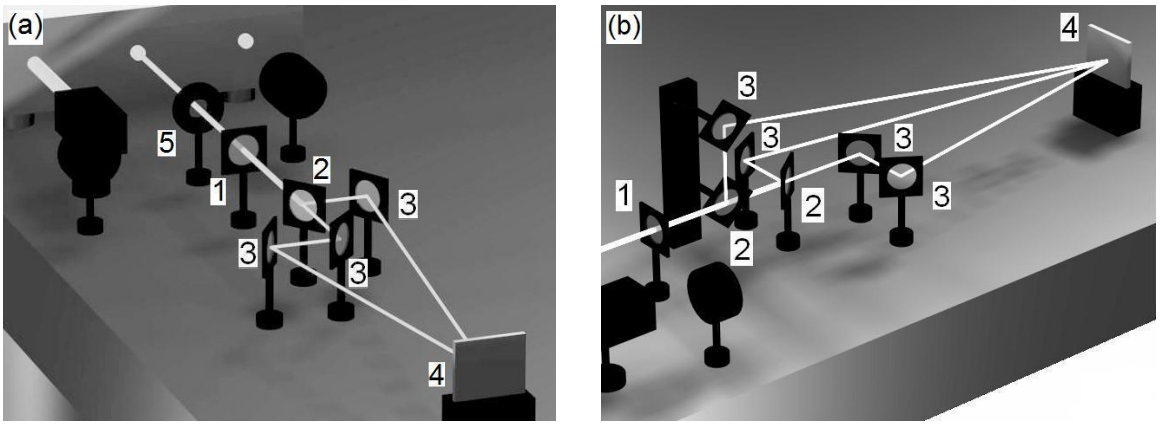

Figure 4.1. Schematic set-up of laser interference system using (a) two, and (b) three split laser beams. The optical components correspond to: (1) lens; (2) splitter; (3) mirrors; (4) sample; (5) beam mask [103].

4.3 Chemical and electrochemical etching

In order to investigate the laser's effect on the chemical reactivity of the irradiated samples, structured Al foils, Pb/Al and Cu/Al systems were etched using two different etchants:

- aqueous hydrochloric acid solution, HCl, 1N at 85°C (named etchant 1).
- aqueous hydrochloric and hydrofluoric acid solution, known as *Flick's etchant*, at room temperature. Table 4.2 describes the etchant composition.

The chemical etching was chosen as a valid method to evaluate and understand the influence of laser irradiation and some metallic elements on the chemical behaviour of the treated samples. The etching conditions above described have been established in the literature as effective for the etching of Al samples. The dimension of the specimens under study was 20 × 20 mm^2. The etching time was varied from 2 to 30 seconds.

Table 4.2. Chemical etchant description.

Etchant name	Composition	Temperature (°C)
Etchant 1	hydrochloric acid (HCl), 1N	85
Flick's	15 ml hydrochloric acid (HCl) 32 % 10 ml hydrofluoric acid (HF) 40 % 90 ml distilled water	25

The chemical etching is appropriate to examine the initial pit sites formed at the first stages of the etching process, but not to find the tunnel etching structure characteristic of etched Al foils. Therefore, electrochemical etching was performed in this study as an effective way to produce the tunnel etching morphology. The etching process was realised by Becromal S.p.A (Milano, Italy). This company manufactures etched aluminium foils used in the production of electrolytic capacitors. The etching process was carried out using direct current (DC) in aqueous hydrochloric acid solution, (in which acids as sulphuric, nitric and phosphoric acid are added), at temperatures above 65°C. The accuracy of etching conditions cannot be reported because they correspond to an industrial process. However, in all cases, the same etch condition was used in order to obtain reliable analyses of the etched samples.

4.4 Sample characterisation

As-received and irradiated samples were investigated by different techniques such as scanning electron microscopy (SEM), focused ion beam (FIB), X-ray diffraction, white light interferometry (WLI), and electron backscatter diffraction (EBSD) among others.

4.4.1 White light interferometry (WLI)

The surface features of the pristine and structured samples were characterised by using a Zygo New view 200 3D Image Surface Analyser equipped with a Mirau interferometric objective. This technique provides quantitative information about topography without contacting the surface.

WLI utilises a light source with very low temporal coherence. By means of a beam splitter, this light is separated into a reference beam (reflected to a reference mirror) and an object beam that strikes the surface to be measured. The light reflected from both, the reference mirror and the measured object, is overlayed. This interference pattern is captured by a camera. Whilst performing the topography measurement, the objective is gradually moved in small steps in *z*-direction. At each position the camera takes a single image. Then, all images are compiled into an image stack, which is used to render the 3D topography. A MetroPro software was used to convert the intensities into images. The advantages of this system are the high-accuracy resolution in the nanometer range in combination with an extended measuring range up to several hundred micrometers. The vertical resolution is on

the order of 0.3 nm, whereas the lateral resolution varies between 0.73 µm and 11.8 µm depending on the objective used [138, 139].

Roughness, periodicity, superficial area ratio, and structuring depth were examined by means of this method. The periodicity or randomness of the surface profile was analysed using the autocorrelation function. For periodic surfaces, this function presents a characteristic sinusoidal shape that is related to the period of the dominant spatial frequencies of the profile. Otherwise, the superficial area ratio was represented by the ratio between the superficial area input and the planar area occupied by the input data excluding the effects of high variations, and finally the structured depth was defined as the vertical distance between the interference maxima and minima.

4.4.2 FIB/SEM dual beam technique

The dual beam incorporates both a focused ion beam (FIB) column used for site-specific milling, and a scanning electron microscope (SEM) column to image the samples. This combination made it especially useful for the reliable and accurate characterisation of the samples under study. The FIB instrument consists of an ion optic column with Ga^+ liquid metal ion source (LMIS) and an electron optic column (SEM) with a field emission gun (FEG). The typical dual-beam column configuration is a vertical electron column with an ion column tilted at 52° from the vertical (see Fig. 4.2). To enable ion milling and electron imaging of the same region, the dual-beams have an incident point where the two beams intersect with the region of interest on the sample (known as “eucentric” point). [140].

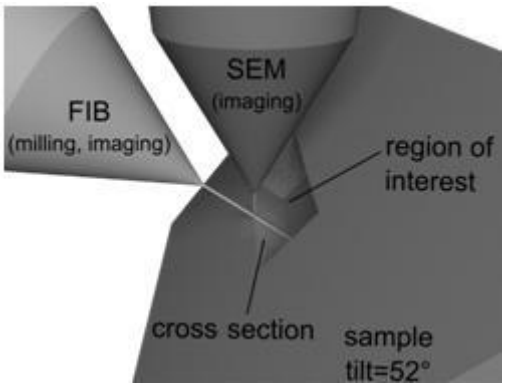

Figure 4.2. Schematic illustration of the geometrical relationships of the imaging plane with electron and ion beams.

All samples were examined with a FEI Strata DB 235 FIB/SEM dual beam workstation equipped with energy dispersive X-ray spectrometry (EDS) and electron backscattered diffraction (EBSD) cameras.

4.4.2.1 Scanning electron microscope (SEM)

The morphology of the samples was examined with a high-resolution scanning electron microscope (SEM) using an acceleration voltage of 5 kV. SEM images were acquired in the secondary electron modus at different tilts and magnifications. In some cases, in-lens SE detection was also employed to obtain ultra-high resolution (UHR) and precise imaging.

4.4.2.2 Energy dispersive X-ray spectrometry (EDS)

Chemical characterisation of the samples was performed using energy dispersive X-ray spectrometry (EDAX instrument). The software EDAX Genesis^{MR} was used for acquisition analysis, image acquisition, X-ray mapping, etc. Elemental mapping and line scans were used to identify the elemental distribution of heat-treated and structured samples. An acceleration voltage of 12 kV was used for imaging the samples.

4.4.2.3 EBSD characterisation

The crystallographic orientation of the samples was determined by using electron backscattered diffraction analysis. This technique helps us to examine the possible preferred orientation (texture), grain boundaries and morphological analyses. EBSD data were acquired using 5 and 20 kV acceleration voltages.

4.4.2.4 TEM foil preparation and TEM investigation

TEM foils were also prepared using the dual-beam workstation. The preparation procedure consisted firstly in the in-situ deposition of a Pt layer of about 1-2 µm thickness on the area to be characterised (Fig. 4.3a). The Pt deposition was carried out in two consecutive steps: (1) deposition of a thin Pt layer by electrons beam at an acceleration voltage of 3 kV, and (2) further Pt deposition using an ion beam at 30 kV acceleration voltage. The first Pt layer deposition was realised to avoid any surface deformation induced by the ion beam. The entire Pt band was used mainly to protect the surface against ion beam damaging during the following milling steps.

Afterwards, a TEM wizard program was executed to produce a thin foil. In this step, two trenches were milled at both sides of the area of interest. The specimen was thinned down to 1 µm by gradually decreasing the ion beam currents. After reaching this thickness, the sample is back-tilted to 7° and the foil is partially cut with a U-shape pattern, still connected to the substrate via two thin branches at the top (Fig. 4.3b). The lift-out of the foil was performed in site with a micromanipulator “Kleindiek MM3A” which was inserted into the

chamber. The manipulator tip was slowly set in contact with the top of the foil, where both were welded by Pt deposition using electron beam. At this moment, the specimen was cut free from the substrate (Fig. 4.3c). The specimen, only fixed to the tip of the manipulator, was lifted out and placed on a pre-cut Cu TEM grid where it was fixed by Pt deposition (Fig. 4.3d). Finally, the foil is thinned with ions down to a thickness of approximately 70-100 nm.

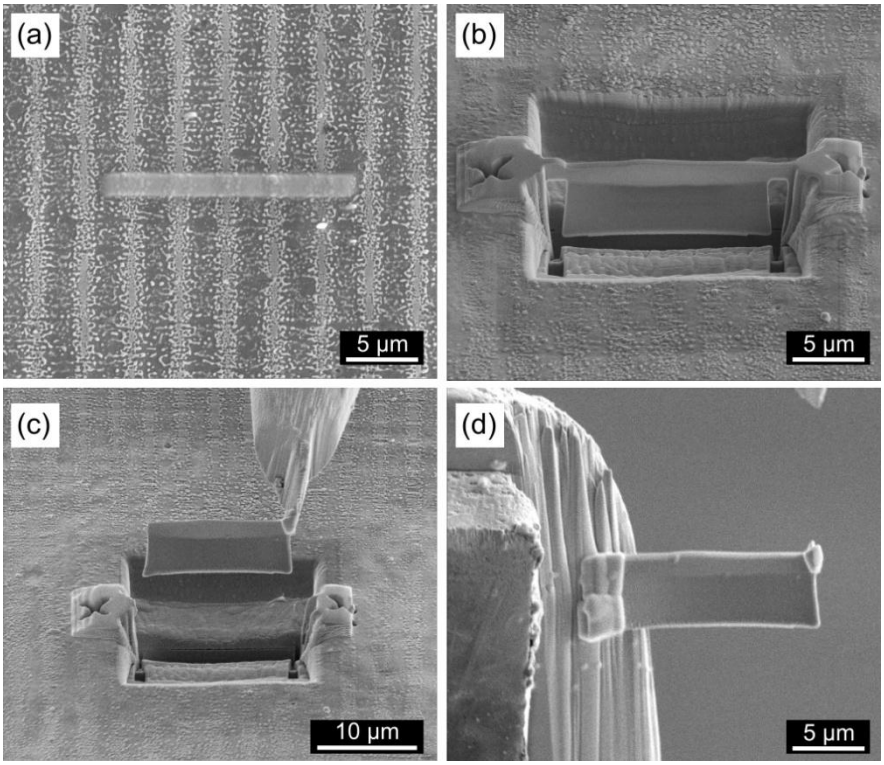

Figure 4.3. SEM images describing the four major steps of TEM foil preparation by FIB. (a) Deposition of a protective Pt layer at the desired position, (b) milling process imaged in SEM mode after TEM wizard, (c) in-situ lift-out of the foil using a micromanipulator, and (d) foil fixed to the Cu grid with Pt deposition. (b-d) Tilt angle: 52°.

Further TEM investigations were carried out with a JEOL 200 CX instrument at an operating voltage of 200 kV. Imaging of the microstructure, selected area diffraction and EDS analysis (Oxford Isis system) were carried out.

TEM foil analysis has been of great importance in the characterisation of the laser structured samples. This technique allowed the local, selective and independent examination of the maximal and minimal interference zones keeping the original surface condition of the samples.

4.4.2.5 FIB Nanotomography – general principles

A three-dimensional characterisation of the tunnel morphology obtained by electrochemical etching of the samples was performed. The specimens under study were as-received Al and structured Pb/Al samples. The investigation was carried out using focused ion-beam (FIB) tomography, which uses serial sections to reconstruct three-dimensional features with the help of a suitable software [140-143].

Prior to the FIB cutting, a protective layer of Pt (~ 1 µm thickness) is deposited over the surface to be cut. This overlayer prevents milling or gallium (Ga) implantation on the surface, so the original sample surface is preserved. The Pt layer also helps to reduce the so-called curtaining effects, protect the sample, reduce charging effects, and provides a sharp cross section edge which will be later used as a vertical reference for slice alignment [140, 144]. Afterwards, a cube of suitable size has to be prepared (Fig. 4.4). The cube is formed by milling trenches at both sides and in front of the volume under study. It permits the adequate accessibility to the *x-y* planes for image acquisition with the electron beam and to avoid shadow effects from the side walls. The sectioning and imaging parameters depend strongly of the required resolution.

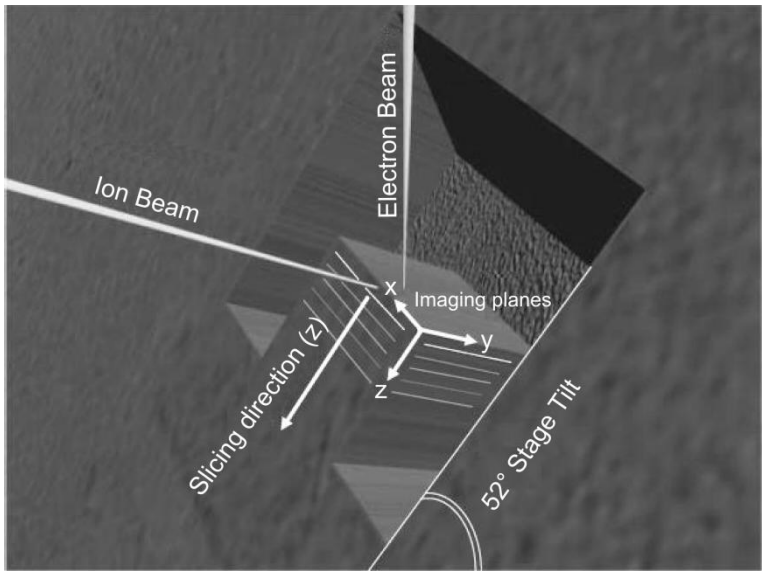

Figure 4.4. Schematic illustration of a sample cube and geometrical relationships of the image plane with electron and ion beams [142].

After cube preparation, the serial sectioning procedure can be started. In principle, the method consists of performing serial FIB cross sections through the volume chosen to be investigated. In this step, a thin layer of material from the cube face is precisely eroded with the ion beam and the newly exposed surface is subsequently imaged by SEM (Fig. 4.4). The FIB prepared imaging planes are defined as *x-y* planes and their secondary images are taken from an angle of 52° [142]. The serial cross sectioning is performed automatically using a

scripting routine. The series of layers are eroded with a constant thickness in *z*-direction. The resolution in the *z*-direction corresponds the spacing between sections (theoretically down to 10 nm), whereas the resolution in *x*- and *y*-directions correspond to the resolution of the SEM image (down to 3 nm for SEM imaging). The FIB was operated at 30 kV acceleration voltage while for secondary electron imaging, an acceleration voltage of 5 kV was employed.

Finally, the image stack collected during the serial sectioning procedure was analysed using the 3D reconstruction software package Amira ®. Since the sample is tilted with respect to the electron beam, the cross section planes are firstly aligned in order to account for the aforementioned projection displacement and for any image drift. Afterwards, the segmentation of the re-aligned image stacks was carried out with the purpose to separate the tunnel structures from the Al matrix. A surface generation of the segmented regions is performed by the software via triangulation. For further quantitative analysis MAVI software was employed.

4.5 Corrosion test

The polarisation technique was used to investigate the electrochemical behaviour of the specimens. The electrochemical tests were carried out using an electrochemical workstation IM6eX equipped with the Zahner Thales software for data analysis. The samples under study consisted of unmodified annealed Al foil and structured Pb/Al samples. Before starting the experiments, all the samples were polarised at -1V vs. OCP (open circuit potential) to the OCP with scan rate of 200 µV/s. The electrochemical measurements were performed in a 1N HCl solution exposed to ambient air at 25 ± 1°C. In all cases, the polarisation curves were recorded at least three times in order to ensure reproducibility of the plotted results.

CHAPTER 5

Structuring of metallic surfaces

In this chapter, the structuring of metallic samples is presented investigating the effect of laser fluence, period, and roughness on the formation of microstructures (Section 5.1). The results are accompanied with thermal simulation in order to calculate the temperature distribution at the surface and understand how some laser parameters and surface conditions can modify it. In Section 5.2, a detailed analysis of the mechanisms involved in the formation of the micro-structures is performed. Finally, the process was characterised by dimensionless numbers to obtain additional information about the acting forces and flow regime during micro-patterning of the metallic surfaces.

5.1 Direct micro-pattering of metals

5.1.1 Topographical design and surface morphologies

Aluminium, copper and titanium samples were irradiated using diverse laser-interference configurations and fluences (energy per unit area). The influence of the laser fluence on the building of the structures was analysed by means of topographic measurements and FIB/SEM imaging technique. The interest of studying other metals, apart from aluminium, comes from the requirement to compare the different phenomena that can be involved in the formation of the micro-structures during laser structuring of the metallic surfaces.

As-received aluminium foils were irradiated using laser fluences ranging from 700 to 2700 $mJ.cm^{-2}$. Different morphologies are observed on the surface depending on the fluence used (Fig. 5.1). For a relativly low fluence of 700 $mJ{\cdot}cm^{-2}$, only a small quantity of molten metal can be observed at the interference maxima (Fig. 5.1a). At higher values (approx. 800 $mJ{\cdot}cm^{-2}$), the volume of molten material increases and the liquid metal is pushed outward from the interference maxima positions to the interference minima (Fig. 5.1b). When the laser fluence further increases, the molten metal pushed outward from one maxima meets the molten metal pushed outward from the neighbouring maxima, forming a band of

resolidified material at the interference minima positions and leading to the formation of well-defined line micro-patterns (Fig. 5.1c, d).

Cross sections of these structures performed perpendicularly to the lines are displayed in Fig. 5.1e. At a fluence of 1500 mJ.cm^{-2}, the bands present voids in their center, resulting in micro-tunnel-like structures (Fig. 5.1e (*c*)), whereas at a higher fluence of 1900 mJ.cm^{-2}, closed and compact structures are obtained (Fig. 5.1e(*d*)).

The surface morphology of structures produced at even higher laser irradiation is shown in Fig. 5.2. At laser fluences above 2100 mJ.cm^{-2}, the quality of the line pattern decreases and numerous droplets of ejected molten metal are observed (Fig. 5.2a). In this range of fluence the structure loses its homogeneity and starts to collapse, as is shown in Fig. 5.2b. These effects occur when the total energy density (fluence) exceeds a certain value that we estimated to be around ~ 2300 mJ.cm^{-2} for aluminium samples.

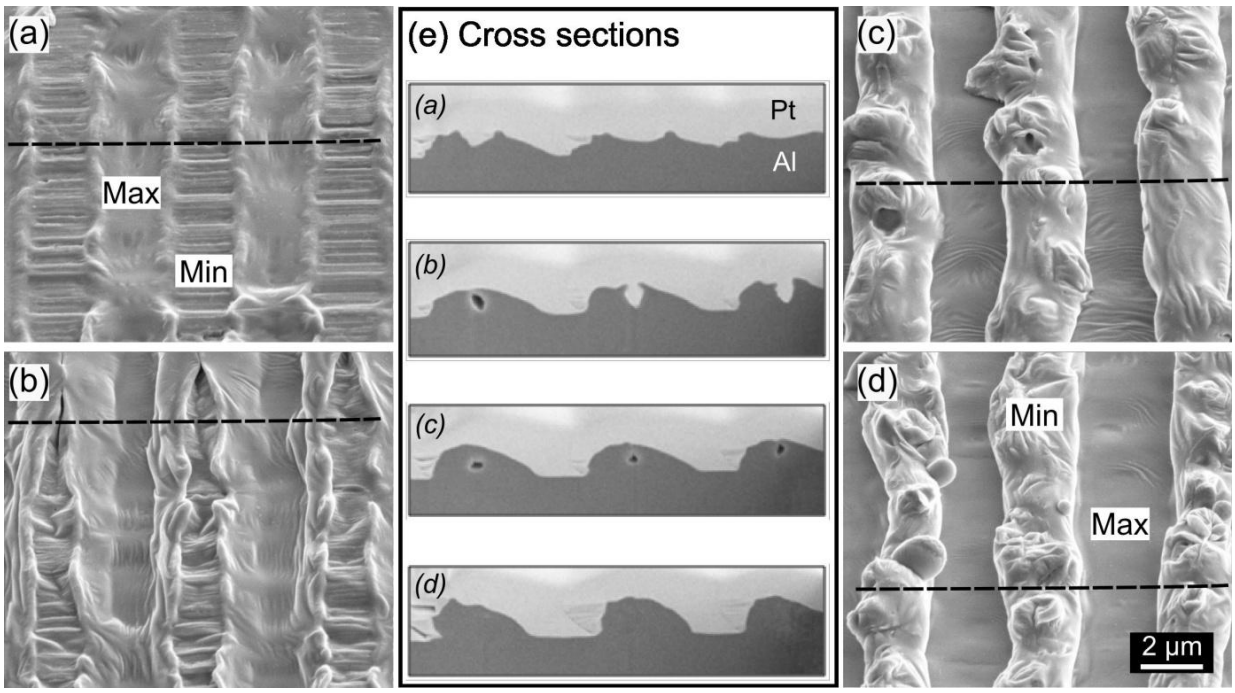

Figure 5.1. SEM images of samples irradiated at different fluences using two beams (line pattern) with a period of 4.5 µm: (a) 688 mJ/cm^2, (b) 1015 mJ/cm^2, (c) 1500 mJ/cm^2, and (d) 1916 mJ/cm^2. (e) Cross sections of the respective surfaces (*a-d*). The dashed lines correspond to the positions where the cross sections were realised. All the images have the same magnification. Tilt angle: 52°.

Furthermore, grid and dot patterns were also produced. The grid pattern was built by producing two consecutive linear patterns and by rotating the sample 90° after the first line patterning (Fig. 5.3a). The dot patterns were realised using the interference of three (Fig. 5.3b) and four (Fig. 5.3c) beams. Independently of the pattern shape (line, grid or dot) the material is always removed from the interference maxima towards the interference minima (Fig. 5.1

and Fig. 5.3). More periodic structures created at different fluences and laser configurations are given in Appendix A.1.

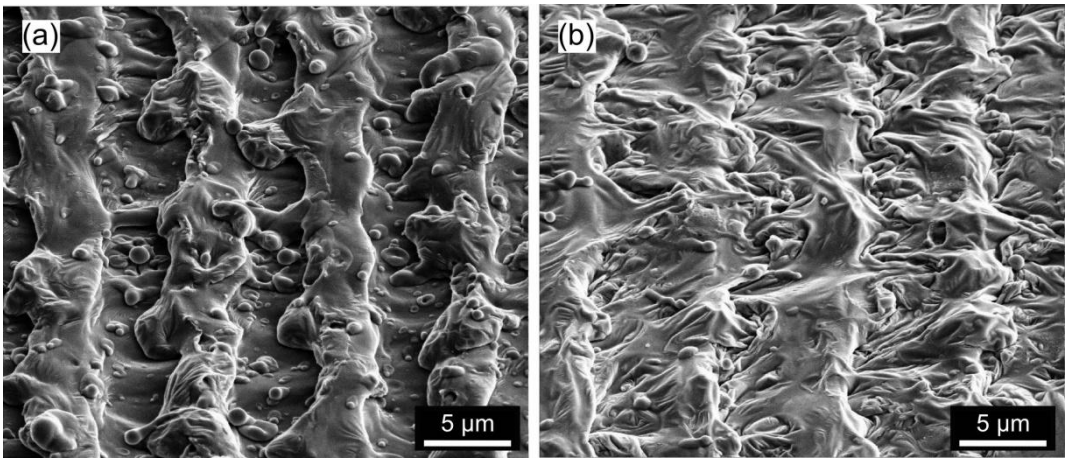

Figure 5.2. Morphology of aluminium structured at high fluences with a period of 7 µm: (a) 2040 mJ/cm^2 and (b) 2700 mJ/cm^2 showing the ejection of droplets and the collapse of the structure. Tilt angle: 52°.

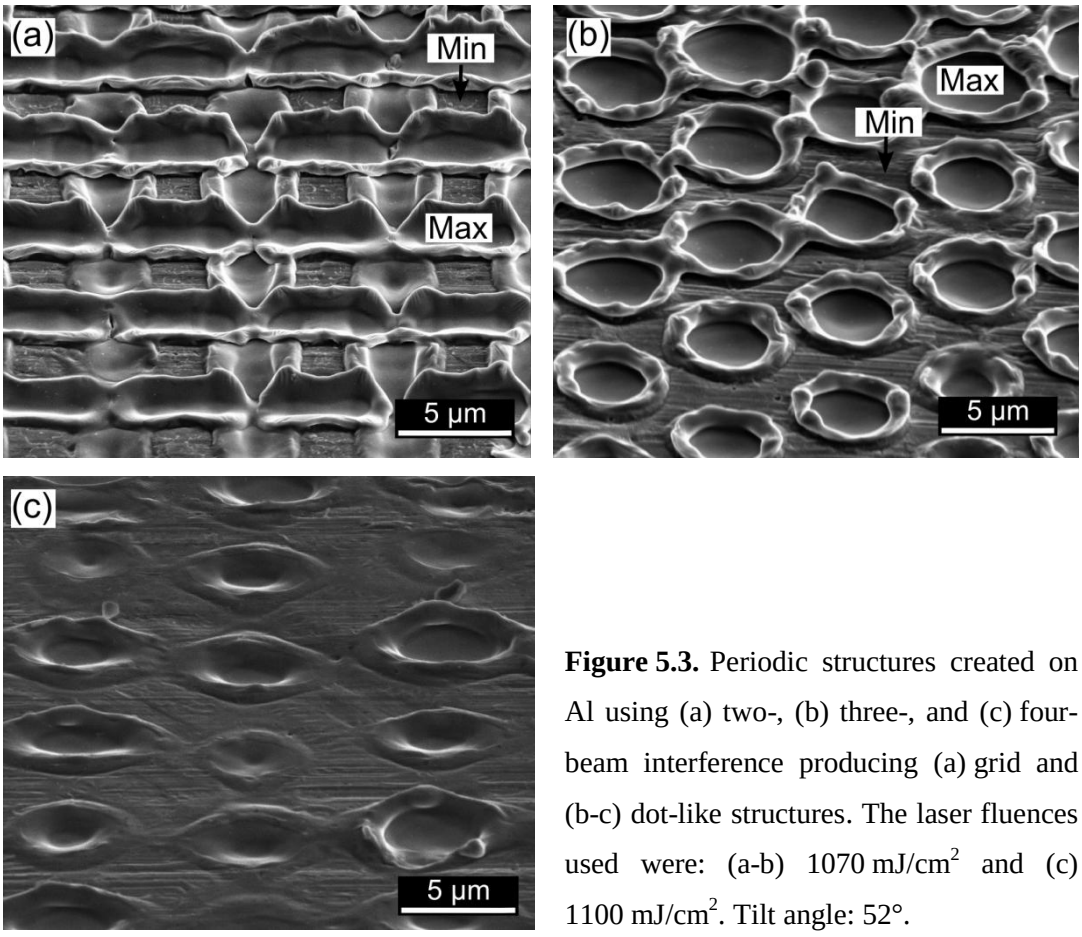

Figure 5.3. Periodic structures created on Al using (a) two-, (b) three-, and (c) four-beam interference producing (a) grid and (b-c) dot-like structures. The laser fluences used were: (a-b) 1070 mJ/cm^2 and (c) 1100 mJ/cm^2. Tilt angle: 52°.

Similar results were observed for copper and titanium samples. In all the cases, material is removed from the interference maxima towards the interference minima positions and the obtained periodic structures have the negative shape of the intensity distribution of the interference patterns. However, the fluence value where the patterns become less homogeneous and/or droplet ejections are present varies from one material to another.

For copper, the threshold fluence is estimated to be ~ 1700 mJ.cm^{-2} when the sample is structured using two laser beams interference and a period of 3.4 µm. Above this fluence value, numerous droplets were noticed (see Fig. 5.4).

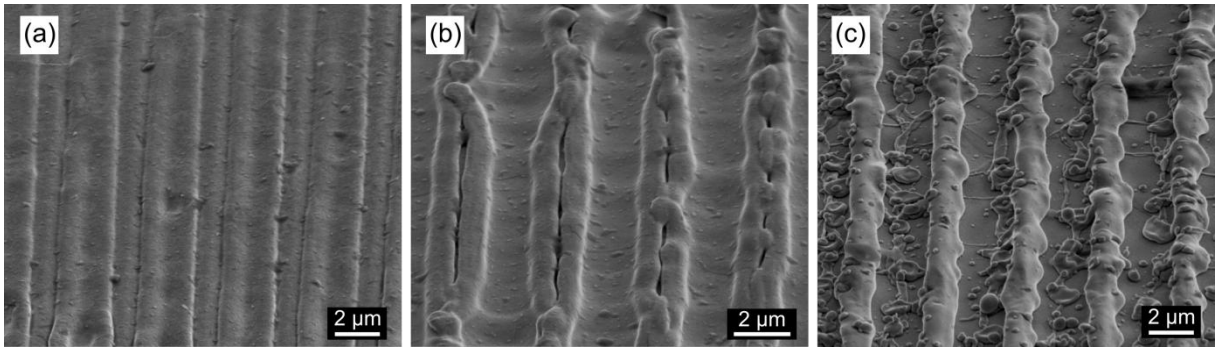

Figure 5.4. Morphology of copper structured at different laser fluence: (a) 560 mJ/cm^2, (b) 1430 mJ/cm^2 and (c) 1780 mJ/cm^2. Tilt angle: 52°.

On the other hand, titanium samples structured under similar conditions, presented a quite irregular surface morphology. The microstructures are less uniform and more irregular than those found in copper and aluminium samples. The SEM images present in Fig 5.5 depict the surface morphology of structured Ti at different fluences. In Fig 5.5a, it is possible to see that even at low fluence values some pores are found at the interference maxima positions.

5.1.2 Structure depth

The structure depth (SD) is defined as the vertical distance between the interference maxima and minima. Fig. 5.6 shows the dependence of the structure depth on the laser fluence for aluminium, copper and titanium samples structured using two-beam interference to produce linear patterns. The angle between the laser beams was changed in order to produce different periodic structures. The selected incident angles were 9.25°, 5.98°, 4.52° and 2.9°, which, according to Table 3.1, result in periods of 2.2, 3.4, 4.5 and 7.0 µm, respectively. Independently from the metal used, the curves show a sigmoidal behaviour, which becomes more pronounced as the period increases (discontinuous lines).

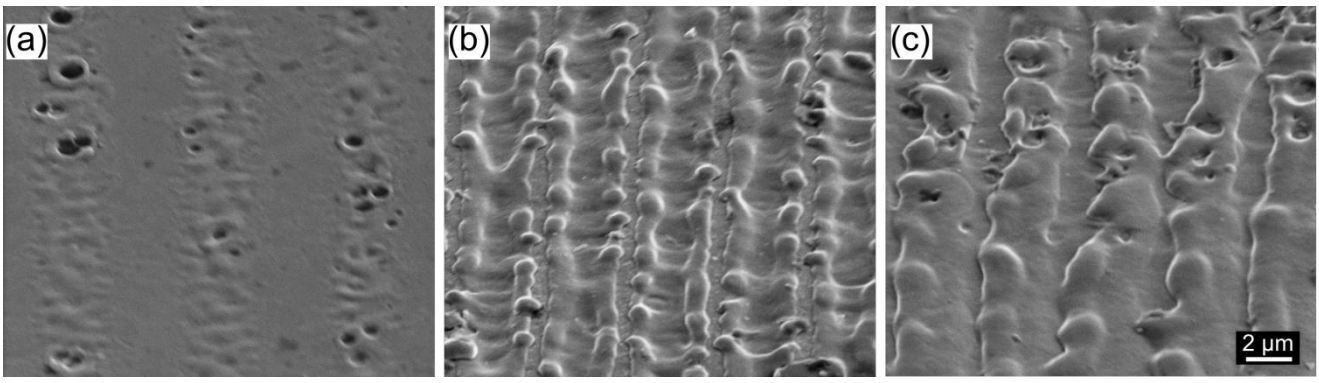

Figure 5.5. Morphology of titanium structured at different laser fluence: (a) 564 mJ/cm^2, (b) 885 mJ/cm^2 and (c) 1660 mJ/cm^2. All the micrographs have the same scale Tilt angle: 52°.

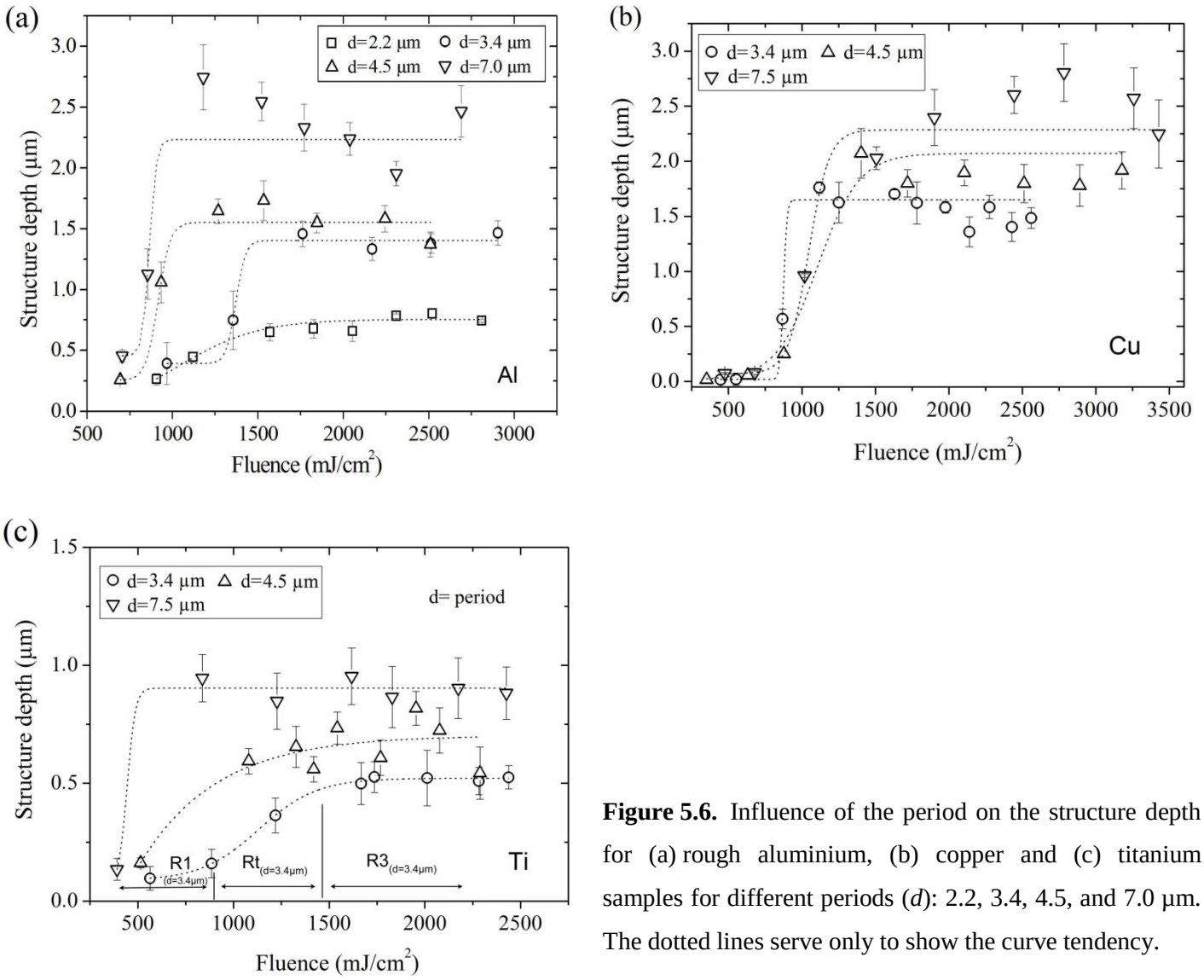

Figure 5.6. Influence of the period on the structure depth for (a) rough aluminium, (b) copper and (c) titanium samples for different periods (*d*): 2.2, 3.4, 4.5, and 7.0 µm. The dotted lines serve only to show the curve tendency.

For a selected period, each individual curve presents three well-defined regimes which can be distinguished depending on the fluence used. The first regime (R1), corresponding to low fluences, is characterised by small volumes of molten material as well as low structure depths. The second regime is a "transition" zone (Rt) where the structure depth abruptly increases. The threshold fluence, that is the energy density necessary to go over the first regime to the transition zone, is shifted to lower fluences when the period becomes greater. In the third regime (R3), corresponding to high laser fluences, the maximal structure depths are reached and remain practically constant with the fluence. The different regimes (R1, Rt and R3) were illustrated in Fig 5.6c for titanium structuring by using a period of 3.4 µm. The results show that higher structure depths are reached for larger periods.

Although the behaviour of the structure depth with the laser fluence is similar for the different samples, its maximum reachable value depends on the material to be structured. Fig. 5.6 indicates that in the case of aluminium and copper (Fig. 5.6a, b) higher structure depths can be obtained compared with titanium samples (Fig. 5.6c).

Furthermore, the thickness of the samples did not modify the behaviour or the values of the structure depth. Due to the fact that thick (~2 mm) and thin (~120 µm) aluminium samples with comparable surface conditions reached similar structure depths, only the results corresponding to aluminium foil (thin specimens) are presented (Fig. 5.6a).

5.1.2.1 Superficial area ratio

The increase of the structure depth with the fluence can lead to higher surface area. In order to quantify this increase, the superficial area ratio of aluminium samples structured at different periods, corresponding to the results reported in (Fig. 5.6a), was measured by WLI. The measurements were performed with a suitable objective, providing a lateral resolution of 0.73 µm. The vertical resolution of the equipment is about 0.1 nm. The superficial area ratio, SA_R, can be defined as [145]:

$$SA_R = \left(\frac{SA}{A}\right) - 1\,, \tag{5.1}$$

where SA represents the surface area input including the effects of height variation such as roughness and waves, and A is the planar area occupied by the input data excluding these effects. The results are shown in Fig. 5.7a. The maximal SA_R values were reached at fluence range from 1200 mJ.cm^{-2} to 2200 mJ.cm^{-2} approximately. Later on, a further increase of the fluence leads to a decrease of the superficial area ratio. It must be emphasised that the samples

structured at small period (d= 2.2 µm), did not present a noticeable increase of SA_R, reason for which its corresponding data was not included in Fig. 5.7a.

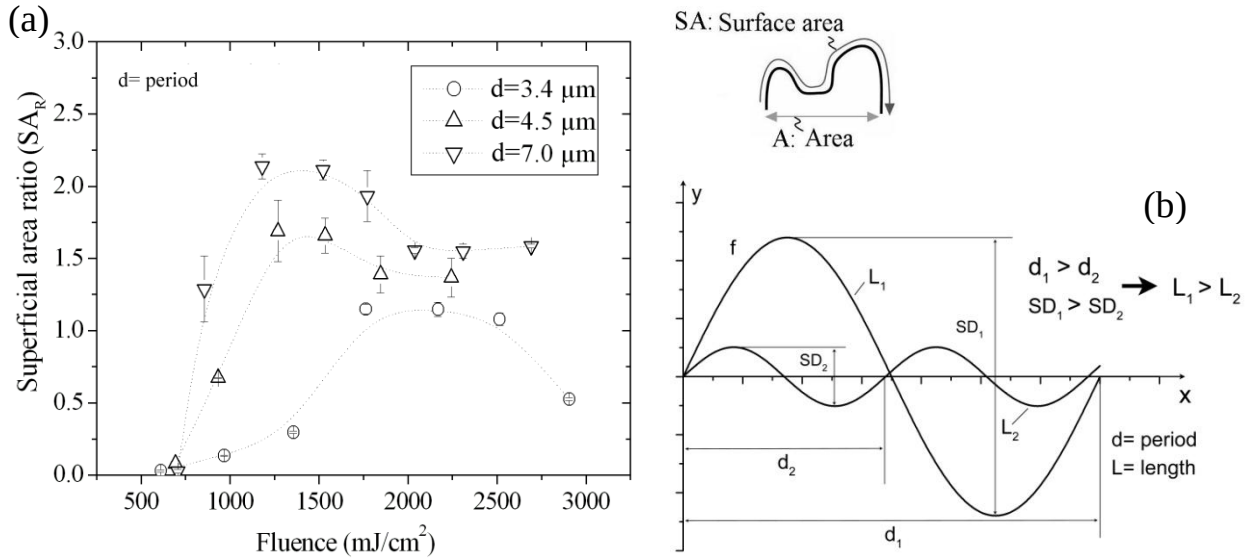

Figure 5.7. (a) Experimental superficial area ratio vs. laser fluence. The dotted lines serve only to show the SA_R curve tendency. (b) Schematic diagram of an ideal periodic function, *f*, represented at different periods and structure depths. It shows a general case where the curve with large period (d_1) and higher structure depth (SD_1) possesses the longer length, L_1.

The tendency of the SA_R curves is similar to those found during the structure depth measurements. Normally, smaller periods must lead to higher surface areas. However, contrary to expectations, the surface area increases as the period increases. This behaviour can be explained by the fact that not only the period of the structures is important to increase the superficial area, but also the structure depth attained for a selected laser fluence. As large periods produce deeper structure depths (see Fig. 5.6), the total superficial area is higher for large periods than for smaller ones, at least under the studied conditions. Fig. 5.7b illustrates this effect using two sine waves schematically representing surfaces structured using two different periods. In spite of the period differences, the curve with small period (d_2) has also low structure depth (SD_2) leading to shorter surface length (L_2) or smaller surface areas. This means that, the increase of the surface area depends on the period as well as the structure depth of the periodic structures.

5.1.3 Roughness effect

In order to investigate the effect of the roughness on the formation of periodic structures, rough and metallographically polished aluminium were irradiated. The arithmetic

roughness values R_a of the surfaces were measured using a white light interferometer and were found to be 146 ± 41 nm for the rough sample and 8 ± 1 nm for the polished sample. Fig. 5.8a shows the structure depth as a function of the laser fluence for a period of 3.4 µm. Both specimens present the same sigmoidal behaviour and similar maximal structure depths (~1.5 µm) are reached.

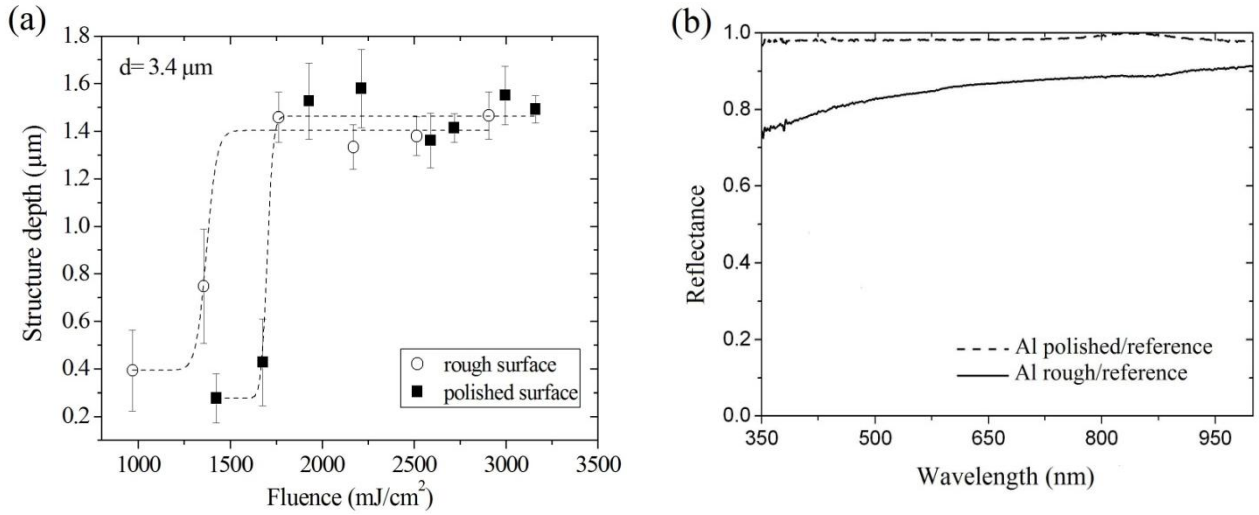

Figure 5.8. Aluminium samples. (a) Effect of the roughness on the structure depth. The period (*d*) selected was 3.4 µm. (b) Total reflectance as a function of the wavelength for rough and polished surfaces.

At high fluences, the surface is largely molten and the original roughness of the sample no longer affects the structure depth. However, the transition from low to high structure depths occurs at lower laser intensities for the rough sample compared to the polished sample. This behaviour can be explained by the influence of the surface roughness on the reflectivity of the samples during laser treatment. Therefore, the reflectivities of both surface conditions were measured experimentally. The result is shown in Fig. 5.8b. At a wavelength of 355 nm, the reflectivity was measured to be approximately 70% for the rough aluminium and 92% for the polished sample.

5.1.4 Thermal simulation

5.1.4.1 Model description

Aluminium and copper were selected in this part of the study. The thermal simulation developed in [102] was employed in order to determine the temperature distribution of the irradiated samples. The thermal simulation is based on the heat diffusion equation:

$$\rho c_p \frac{\partial T}{\partial t} = q_a - q_m - q_b + \nabla(\kappa \nabla T)\,, \tag{5.2}$$

where $T = T(x, z, t)$ is the temperature at the position (x, z) at the time t; q_a the power per unit of volume added; q_m and q_b the power per unit of volume required to melt and vaporise the material, respectively; c_p the specific heat; κ the thermal conductivity; and ρ the density. The material properties c_p, κ and ρ are assumed temperature dependent in the simulation (see Appendix B).

For the analysis of the problem, the following conditions are adopted [103]:

- no radiation is lost from the surface,
- when the material melts, there is no convection due to gravitational or electromagnetic effects,
- the intensity of the laser is considered to have a Gaussian shape in the time scale (see Eq. 3.7),
- the heat conduction problem includes, solid-liquid, and liquid-vapour transitions, considering the energy required for melting and vaporising the metal.

The terms q_m and q_b are the power per unit of volume involved in the solid-liquid and liquid-vapour phase transitions, respectively. They can be defined as [146]:

$$q_m = L_m \rho \frac{\partial \left[0.5 erfc\left(\frac{T - T_m}{\Delta T_{0m}}\right)\right]}{\partial t}\,, \tag{5.3}$$

$$q_b = L_b \rho \frac{\partial \left[0.5 erfc\left(\frac{T - T_b}{\Delta T_{0b}}\right)\right]}{\partial t}\,, \tag{5.4}$$

where L_m and L_b are the latent heat of melting and vaporisation, *erfc* is the complementary error function, T_m and T_b are the melting and the boiling temperatures, and ΔT_m and ΔT_b are the temperature interval to smooth the solid-liquid and liquid-vapour transitions, respectively. The temperature intervals were selected to be 50 K ($\Delta T_m = \Delta T_b = 50$ K). Since there are no spatial derivates in Eqs. (5.3) and (5.4), it is possible to introduce a small coefficient to act as a noise filter.

The solid fraction is represented by the variable f_{SL}, whose value varies from 1 to 0. For f_{SL} = 1 the material is in the solid state and for f_{SL} = 0 the entire metal is molten [146, 147]. The fraction f_{SL} changes as a function of the temperature and was defined as follows:

$$f_{SL} - 1 \cdot 10^{-12}\nabla \cdot (\nabla f_{SL}) = 0.5 erfc\left(\frac{T - T_m}{\Delta T_{0m}}\right), \tag{5.5}$$

being $1 \cdot 10^{-12}\nabla \cdot (\nabla f_{SL})$, the coefficient of the noise filter. The liquid-vapour transition f_{LV} was similarly considered.

The laser energy is introduced into the material following the intensity distribution of the interference pattern given by Eqs. (5.6) and (5.7):

$$q_a = \alpha \frac{I_{(x)}}{\sigma\sqrt{2\pi}} \exp\left(-\frac{(t - t_0)^2}{2\sigma^2}\right)(1 - R)\exp(-z\sigma), \tag{5.6}$$

$$\sigma = \frac{\tau_p}{2\sqrt{2\ln 2}}, \tag{5.7}$$

where α is the absorption coefficient, t_0 the pulse time, τ_p the pulse duration (full width at half-maximum, FWHM), and R the reflectivity of the surface. The simulations were performed for different period and reflectivity values.

5.1.4.2 Influence of the reflectivity

As it was discussed in Chapter 2, the initially high reflectivity of a metal surface may experiment a sharp decrease during the laser pulse irradiation. Therefore, the heating process could be accelerated significantly. In this study, aluminium and copper were simulated at a laser wavelength of 355 nm. For copper samples, the reflectivity value for a wavelength of 355 nm is below 65%. In this case, large variations of the reflectivity do not significantly affect the heating rate. Consequently, the copper reflectivity was considered to be constant during the thermal simulation (see Appendix B).

On the other hand, the reflectivity of aluminium is reported to undergo a substantial decrease to a value of 65% at the melting point during laser treatment [8, 13, 148]. Explanations have been proposed based on an increase of the electron–phonon collision frequency as the temperature of the metal rises to the melting point (see Section 2.2.3). For the thermal simulation analysis of aluminium substrates, the reflectivity change with the temperature in the solid state ($T < T_m$) is considered according to the next empirical equation [149]:

$$R = 1.048 - 3.989 \cdot 10^{-4} T\,, \tag{5.8}$$

where T_m is the melting temperature of aluminium. At $T > T_m$, two different reflectivity values, 80% and 65%, are studied.

Four conditions are considered for the thermal simulations: the cases where the reflectivity of aluminium specimen remains constant at 70% and 92%, and the cases were the reflectivity changes from 92 to 80% and from 92 to 65% when the temperature increases up to the melting point. The calculated temperatures at the minima and maxima positions as functions of the laser fluence for a period of 3.4 µm are shown in Fig. 5.9. The lower the final value of the reflectivity is, the higher the temperature at the maxima position and the temperature difference between maxima and minima are. According to the simulation results, if the reflectivity of the polished aluminium is considered to remain constant at 92% during laser structuring, the metal starts to melt at the interference maxima at about 2000 mJ.cm^{-2} (Fig. 5.9). Experimentally, the increase of the structure depth was found to take place at a lower fluence of 1700 mJ.cm^{-2} (Fig. 5.6a). Since the increase of the structure depth is related to the melting of the surface, a decrease of the reflectivity with the temperature should take place.

Figure 5.10 shows the simulated molten and vaporised depths as a function of the laser fluences for the different reflectivity conditions. Samples with high reflectivity present smaller molten depths. Since the structure depth is the result of the displacement of molten material from the maxima to the minima position, one can consider that both structure and molten depths should be on the same order. At a fluence of 1700 mJ.cm^{-2}, the molten depth is only 0.6 µm for a shift of reflectivity from 92 to 80% and reaches 1.1 µm for a shift from 92 to 65%. Therefore, this last reflectivity condition is considered to be more consistent with the structure depth of 1.5 µm obtained experimentally (Fig. 5.6a). In this range of reflectivity, the material starts to evaporate at fluence near 1500 mJ.cm^{-2} (Fig. 5.10).

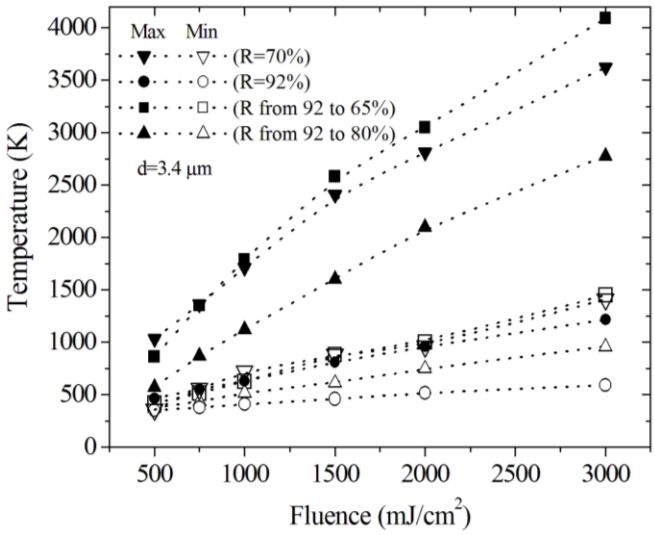

Figure 5.9. Simulated temperature at the interference minima and maxima for aluminium depending on the reflectivity behaviour.

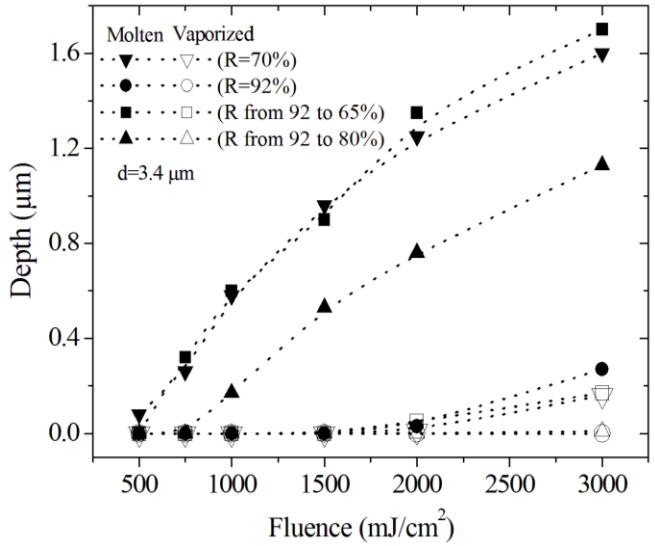

Figure 5.10. Simulated molten and vaporised material depths as a function of the laser fluence for aluminium with different reflectivities values.

5.2 Discussion

From the above results it is easy to see that the structuring of the different metal surfaces presented analogous topographical characteristics. However, there are some important sample conditions, such as the surface roughness, which can modify the laser requirements necessary to create the micro-structures, as is revealed in the Fig. 5.8a. This is strongly related to reflectivity decrease. Due to the multiple reflections and multiple absorptions occurring in the local peaks and valleys of the rough aluminium sample, the reflectivity decreases (Fig. 5.8b), and the reflection becomes less specular and more diffuse [2, 8, 17]. Consequently, lower fluences are required for heating the surface up to the melting point and for structuring the surface (Fig. 5.8a). Since as-received aluminium foil (rough

surface) presented lower reflectivity (70 %), this reflectivity value will be take into consideration in this section.

On the other hand, it is expected that the laser fluence plays an important role in the formation of the micro-structure. By increasing the laser fluence, more energy is absorbed by the material and the temperature at the interference maxima increases (Fig. 5.9). As a result, a larger volume of metal is molten (Fig. 5.10) explaining the larger structure depths observed experimentally (Fig. 5.6). A strong correlation is also observed between the period of the structure and the maximal structure depth that can be achieved. Figure 5.11 represents the calculated temperature at the maxima and minima positions as a function of the period for copper and aluminium samples at constant laser fluence of 1000 mJ.cm^{-2}.

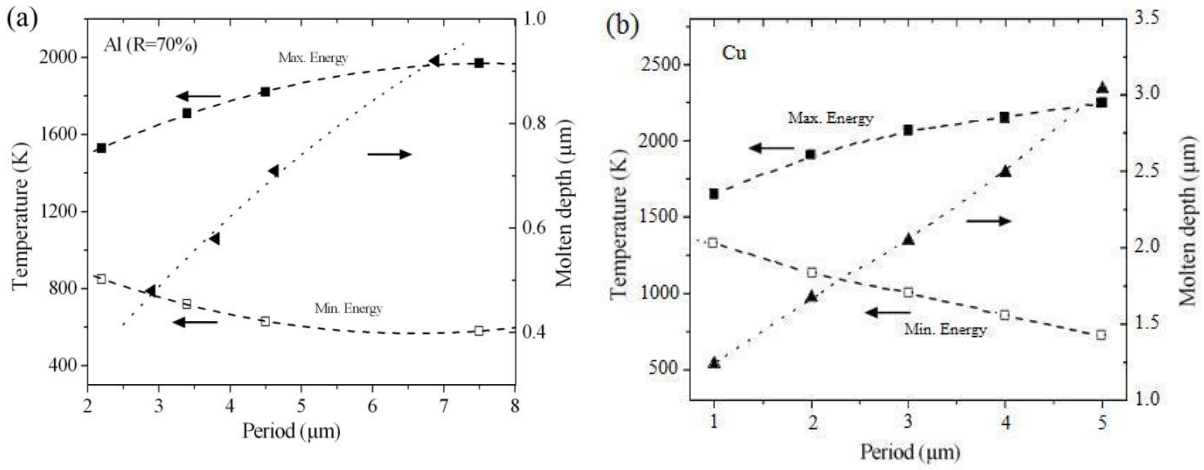

Figure 5.11. Simulated temperature at interference maxima and minima positions as a function of the grating period *d* for (a) aluminium, (b) copper. The simulation was carried out at a constant fluence of 1000 mJ/cm^2.

The results show that the temperature at the energy maxima increases and the temperature at the minima decreases as the period becomes larger. For a period of ~ 2.2 µm the temperature difference ΔT is approximately 680 K and 700 K for aluminium and copper respectively, and about 1400 K and 1780 K for a period of ~ 7.5 µm. The rate of temperature rise depends on the energy balance between absorption and dissipation in the sample [70, 150-152]. The size of the heat-affected zone is determined initially by the depth of the laser penetration, $1/\alpha$; and increases with the time according to the thermal penetration depth, (also called thermal diffusion length), L, see Eq. (2.20). A schematic representation of the zone affected during laser micro-structuring of the samples is presented in Fig. 5.12.

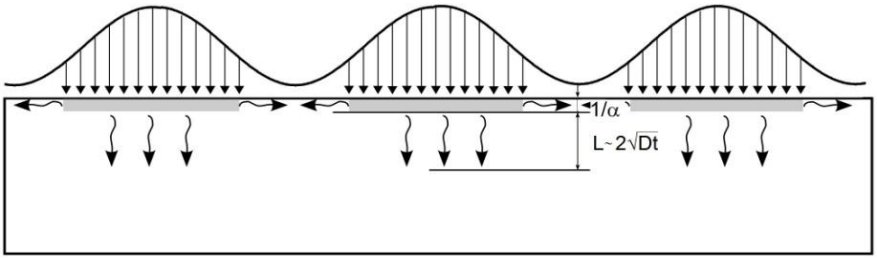

Figure 5.12. Schematic of the zone affected during the micro-structuring of bulk metals. The laser structuring pattern is represented on the metal surface.

Thermal penetration depth, L, absorption coefficient, α, and the average of the structure depth reached for aluminium, copper and titanium at a $t = \tau_p = 10$ ns, are summarised in Table 5.1. All the metals investigated present maximal structure depths similar to their correspondent thermal penetration depths, L. This means that the thermal penetration confines the structure depth that can be reached during laser structuring of metals.

The simulated lateral temperature profile of the interference pattern of aluminium structured with a laser fluence of 1000 mJ.cm^{-2} and two different periods is shown in Fig. 5.13. The temperature difference (ΔT) was about 1400 K for aluminium structured with a period of 7.5 µm, and 900 K for a period of 3.4 µm. Consequently, as the period decreases and comes close to the thermal diffusion length, the temperature difference (ΔT) between maxima and minima decreases, leading to a more homogenous heating of the surface. At large periods, however, the heat is highly localised at the interference maxima positions, giving rise to larger molten depths and deeper structures.

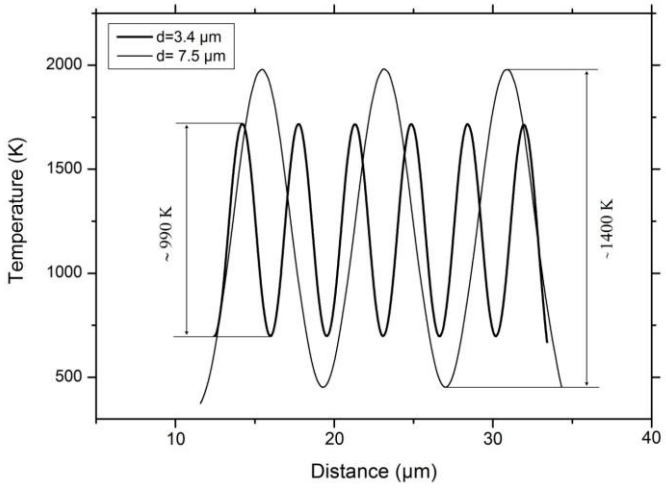

Figure 5.13. Simulated lateral temperature profiles of the interference pattern of aluminium for two different periods (d) and a laser fluence of 1000 mJ/cm^2. The temperature difference between the interference maxima and minima positions were about 900 K and 1400 K for a period of 3.4 µm and 7.5 µm, respectively.

From Fig. 5.6, one can observe that the titanium micro-structures attained lower structure depths than those of copper or aluminium specimens. This effect is strongly related with their thermal conductivities. From Eqs. (2.20) and (2.21) one can see that the thermal diffusivity and consequently the thermal diffusion length, depends directly on the thermal conductivity of the material. It is known that the conductivity of Ti is at least ten times lower than those of Al and Cu (see Appendix B). Therefore, smaller penetration depths as well as higher temperatures are achieved at the irradiated zones. Many reports have shown that the temperature increases very significantly when the thermal conductivity is low [42]. In this kind of material, the high temperature values confined at the maximal interference positions can lead to strong evaporation even at low laser fluences, which can explain the several pores found during the structuring of titanium samples (Fig. 5.5a). In this case, the evaporated material at the interference maxima positions may absorb a part of the output laser energy. The intensity attenuation in the vapour plume of titanium has been investigated in several works [153, 154], which propose the incorporation of a laser transmission coefficient as a function of the incident laser intensity for different environmental pressures.

On the other hand, as aluminium and copper samples have analogous penetration depths, the maximal structure depths reached by these samples were also similar.

Table 5.1. Thermal penetration depth and structured depth for aluminium, copper and titanium.

Sample	Thermal diffusion length *(L)* (μm)	Maximal structure depth (μm)*
Aluminium	1.98	2.38
Copper	2.16	2.40
Titanium	0.61	0.84

*Values taken from Fig. 5.6 at larger period: 7.5μm for Al and 7.0 μm for Cu and Ti samples.

The fact that deeper structures depths are achieved for larger periods is also supported by the superficial area ratio results. It is evident that the micro-patterning of the surface improves the entire superficial area, which increases as the period increases. However, it was found that this improvement has a threshold which is related to homogeneity loss of the micro-structures.

Because of the forceful influence of the advection, convection, and conduction effects during the laser irradiation, surface deformation is not negligible. Several competing mechanisms can be responsible for the laser removal of material such as vaporisation, recoil pressure due to evaporated atoms, and surface-tension gradients, among others [34]. In order

to know the main driving force for the flow of molten material during laser interference structuring, an analysis is carried out based on the temperature distribution estimated by the thermal simulation. Special attention is given to the competitive influence between Marangoni and evaporation.

Surface-tension-driven convection (also called Marangoni flow) has an important effect on the molten depth and fluid motion of irradiated zones (see Section 2.4). Marangoni flow is the motion of liquid due to surface-tension gradients along the molten surface. At irradiance above the melt threshold, uniform melting occurs, and lateral variations of the temperature of molten material become the relevant force for imprint deformation in the material [39, 40, 155-157]. As the surface tension of Al, Cu and Ti liquid decreases with increasing temperature (Appendix B), the molten metal tends to pull away from hotter regions towards cooler regions (see Fig. 5.1 and Fig. 5.3–5.5). Aluminium and copper will be the materials of consideration hereafter in this section.

The surface tension is the cohesive force whose net effect is to minimise the surface area of the molten material. As it varies with the temperature, any temperature gradient established across of the surface of the molten metal will be accompanied by a gradient in surface tension. The surface shear stress τ which arises due to the temperature gradient $\partial T/\partial x$ can be formulated as [39, 158, 159]:

$$\tau = \frac{d\gamma}{dx} = \frac{\partial \gamma}{\partial T}\frac{\partial T}{\partial x} \ , \tag{5.9}$$

where $d\gamma/dT$ is the variation of the surface tension with the temperature. The surface-tension gradients $d\gamma/dx$ are induced both by the temperature gradient along the pool surface ($dT/dx < 0$) and the temperature dependence of the surface tension ($d\gamma/dT < 0$, which is the case for most materials). Here, $\left| d\gamma/dT \right|$ was taken to be equal to 3.5×10^{-4} N m^{-1} K^{-1} and 2.8×10^{-4} N m^{-1} K^{-1} for aluminium and copper, respectively [160, 161]. The maximum velocity is located at and tangent to the surface pool.

A relative measure of the convective driving force is given by the dimensionless Marangoni number Ma. The Marangoni number denotes the ratio between heat flux induced by Marangoni flow and the conduction heat flux, which can be stated as follows:

$$\mathrm{Ma} = \left|\frac{\partial \gamma}{\partial T}\right| \frac{l \Delta T}{\eta D_l} \ , \tag{5.10}$$

where ΔT is the temperature difference in the system, l is the depth of the molten pool, η is the dynamic viscosity, and D_l is the thermal diffusivity of the liquid metal [162, 163]. In this study ΔT was selected according to two different approaches: (1) in the case were the temperature at the interference minimum did not reach the melting point T_m, ΔT was selected as the temperature difference between the maxima and T_m; and (2) when the minimum irradiance zones reached T_m, ΔT was represented by the temperature difference between the interference maxima and minima.

An increase of Ma represents an enhancement of the Marangoni effect. With low Marangoni numbers, the fluid flow at the surface is laminar, but above a critical value for Ma the flow characteristic changes and becomes oscillatory or turbulent. Convection is primarily responsible for mixing in the melt pool and therefore controls of the composition during surface alloying [164].

For higher melt surface temperatures generated either by higher absorbed laser intensities or by exothermic reaction with a chemically active assisting gas, such as oxygen, the vaporisation recoil pressure could become the primary factor removing melt from the interaction zone. But, it can also be the dominating mechanism for lower laser power and consequently, for lower metal surface temperatures. This is the case of short laser pulses, for which, due to inertia, the melt cannot be ejected from the interaction zone before its solidification [53]. The evaporated material can induce a recoil moment over the irradiated zones, which leads to surface depression of molten areas. In order to study this effect, the recoil pressure for aluminium and copper are calculated.

The recoil pressure is proportional to the saturated vapour pressure, P_s, which in turn depends on the melt's surface temperature [53, 54, 165]. Rewriting Eq. (2.24), the recoil pressure P_r can be expressed as:

$$P_r = 0.55\mathrm{P_s}(T_s) = A\frac{B_0}{\sqrt{T_s}}\exp\left(-\frac{U}{k_B T_s}\right), \tag{5.11}$$

where A is a factor dependent on the external pressure, B_0 is an evaporation constant, T_s is the surface temperature, U is the latent heat of evaporation per atom and k_B is the Boltzmann constant (see also Section 2.4.3). The recoil pressure of aluminium was calculated using $B_0 = 2.05\cdot10^{12}$ Kg.m^{-1}.s^{-2} , which is known from the literature [53], and taking $A = 0.55$. In the case of copper, B_0 is not known, and the recoil pressure was determined using its saturated vapour pressure. The vapour pressure value P_s is reported in Appendix B.

The evolution of the recoil pressure, shear stress, and Marangoni number as function of the laser fluence are represented in Fig. 5.14 for aluminium and in Fig. 5.15 for copper. As the laser fluence is increased, Ma increases indicating a stronger Marangoni convection. As a matter of fact, the temperature difference ΔT (which is the driving force for Marangoni convection) and molten depth both increase with increasing laser fluence, which explains why Ma becomes higher when the fluence increases. At the very beginning of melting, heat conduction is the only dominating mechanism in the heat transport.

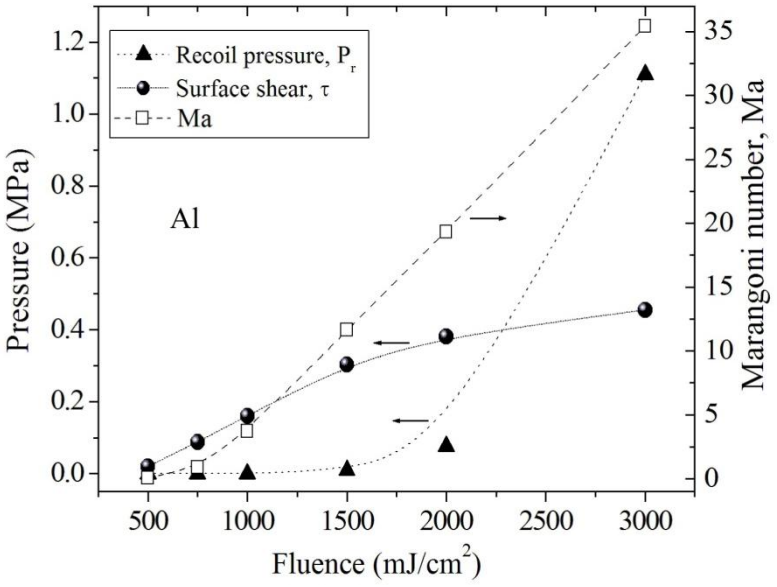

Figure 5.14. Marangoni number Ma, surface stress shear τ, and recoil pressure *Pr* as function of the laser fluence. The transport of molten metal material is dominated by Marangoni convection flow below 2300 mJ/cm^2 and by recoil pressure due to evaporation above this threshold.

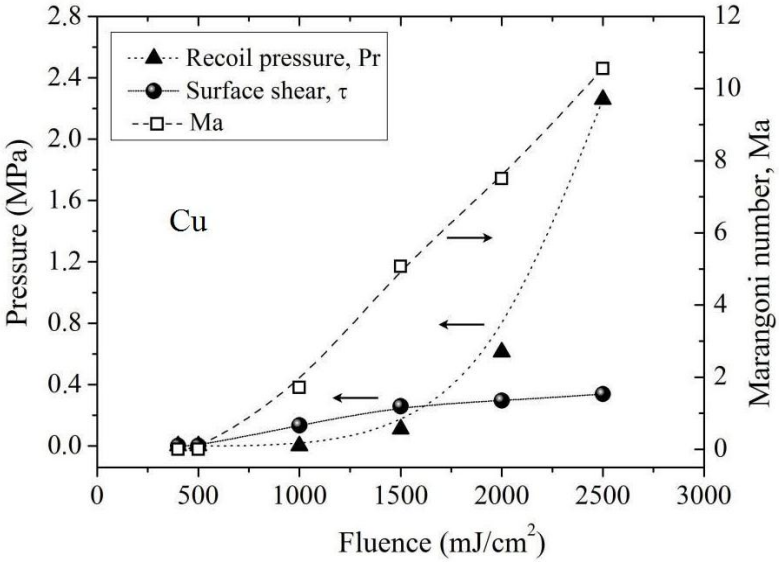

Figure 5.15. Marangoni number Ma, surface stress shear τ, and recoil pressure *Pr* as functions of the laser fluence. The transport of molten metal material is dominated by Marangoni convection flow below 1700 mJ/cm^2 and by recoil pressure due to evaporation above this threshold.

For higher laser intensities other mechanisms like surface-tension-driven flow become significant [163]. Due to the high thermal conductivity of aluminium and copper, Ma values are not so elevated, which indicates that conduction plays a significant role in heat transport during the structuring of both materials. Moreover, as the thermal conductivity of copper is

almost twice that of aluminium, its respective Ma values are smaller in comparison to Ma of aluminium. With low Marangoni numbers, the fluid flow at the surface is laminar but above a critical value of Ma, the characteristic flow changes and becomes time-dependent in nature (*e.g.*, oscillatory or turbulent) [35]. In any case, the higher Ma, the stronger the Marangoni convection and the higher the maximum outward surface velocity *V*.

Although for both aluminium and copper samples the shear stress increases as the laser fluence increases, the fluence ranges where they prevail vary depending on the material. For aluminium, the shear stress exceeds the recoil pressure for fluences up to 2300 mJ.cm^{-2}. In this range of fluences, Marangoni convection dominates the laser structuring process and the effect of evaporation recoil seems to be negligible (Fig. 5.14). This can be observed in Fig. 5.1b, where the flow of molten aluminium towards the minima positions can be clearly recognised. The same behaviour is shown in Fig. 5.3 for the dot- and grid-like patterns on aluminium substrates. In the case of copper, the formation of the micro-structures is dominated mainly by surface-tension-driven flow at fluence values below 1700 mJ.cm^{-2}.

Above the corresponding threshold laser fluences (~2300 mJ.cm^{-2} for aluminium and 1700 mJ.cm^{-2} for copper), the recoil pressure may be considered as the dominant structuring force. Indeed, the presence of droplets was observed in this range of fluence (Fig. 5.2 and Fig. 5.4c). The droplet formation is related to centrifugal forces near the hill caused by the motion of liquid out of the (hotter) valleys [18, 166]. The representation of this phenomenon is depicted in Fig. 5.16a. When the recoil pressure becomes important, it generates a relative velocity at the vapour–liquid interface which can also stimulate the formation of droplets (see Fig. 5.16b).

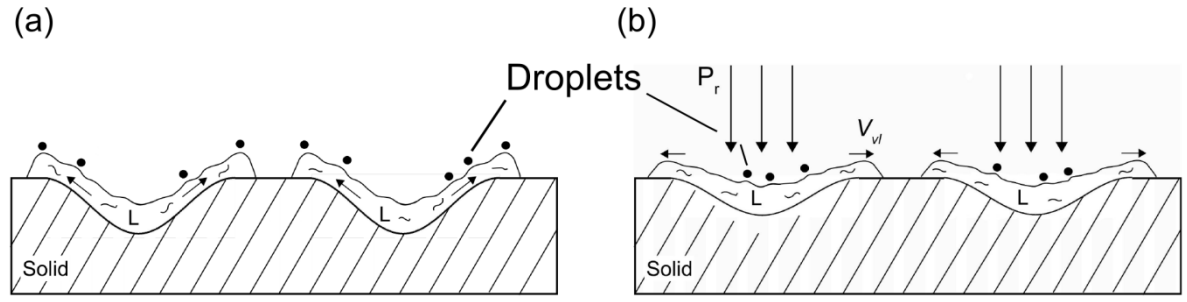

Figure 5.16. Droplet formation generated during laser structuring due to (a) the motion of molten material from interference maxima (valleys) to the interference minima positions which causes centrifugal force near the hills; and (b) lateral velocity at the valour-liquid interface, V_{vl}, induced by recoil pressure, P_r.

According to hydrodynamic law, if the Marangoni numbers of two fluids are close to each order, similar Marangoni convection is expected [167]. Usually, dimensionless numbers are used in fluid dynamics to describe comparable physical problems and to present specific information such as flow behaviour and acting forces. Table 5.2 summarises the dimensionless numbers, including their physical background, used to compare aluminium and copper flow during laser structuring.

Table 5.2. Dimensionless numbers and the physical meaning of their ratios.

$\mathrm{Ma} = \left\lvert\frac{\partial\gamma}{\partial T}\right\rvert \frac{l\Delta T}{\eta D_l}$	intensity of Marangoni force
$\mathrm{Pr} = \frac{\eta c_p}{\kappa}$	kinematic viscosity/conductibility of temperature
$\mathrm{Pe} = \frac{\lvert V_{max}\rvert \rho c_p l}{\kappa} = \frac{\lvert V_{max}\rvert l}{2D_l}$	convective/conductive heat transport
$\mathrm{Ca} = \left\lvert\frac{\partial\gamma}{\partial T}\right\rvert \frac{\Delta T}{\gamma}$	Marangoni/surface tension force
$\mathrm{Gr} = \frac{g\beta_T \Delta T \rho^2 \left(\frac{l}{8}\right)^3}{\eta^2}$	buoyancy/viscosity force
$\mathrm{Re} = \frac{\rho V_{max} l}{\eta}$	inertial/viscosity force

The characteristic length, *l*, was defined in all the cases as the depth of the molten pool [168], V_{max} is the maximum surface velocity, η is the dynamic viscosity, γ is the surface tension, g is the gravity and β_T the volume expansion coefficient.

As it was previously mentioned, material flow is a response to forces acting within/upon the molten pool. The dimensionless numbers help us to know the flow characteristic and also which forces act during the process. A very important characteristic number is the Prandtl number, Pr. The lower the thermal conductivity, the higher Pr (see Table 5.2). The calculated Prandtl numbers of molten aluminium and copper are about 0.012 and 0.006, respectively. Although both materials have low Prandtl numbers, the corresponding value for Cu is one order of magnitude lower than for Al. This suggests that, in both cases thermal conduction primarily governs energy transport in the molten pools, but this effect is likely to be stronger in copper. Hence, although the outwards surface flow induced by Marangoni convection is strong, the heat transport down into the pool by conduction cannot be neglected. Only to illustrate the influence of the Prandtl numbers, the Pr corresponding to liquid titanium was also calculated. The calculated Pr values for titanium is approximately 0.11. As the thermal conductivity of titanium is significantly lower than those of aluminium and copper, higher

Prandtl number is obtained. This indicates a strong convectional flow during the laser treatment but a weaker heat transport into the material. In this case, a molten pool with low aspect ratio (the ratio of the height to width) is expected. These conclusions are in good agreement with the low structure depths found during the patterning of titanium (see Fig. 5.5 and Fig 5.6c).

Another very important characteristic number is the Peclet number, Pe, which offers information about the heat transfer mechanism. The Pe number is the measure of relative heat transport by convection and conduction from the center to the edge of the molten pool. High values match a dominating convective transport. The purpose of using Pe here is to discuss the effect of Marangoni convection on the shape of the molten pool in the absence of surface-active agents. Table 5.2 depicts that Pe depends on the maximum surface velocity generated at the surface, V_{max}. The maximum flow velocity in the molten pool has to be calculated empirically as [169]:

$$V_{max} \approx \left(\frac{\partial \gamma}{\partial T} \frac{\partial T}{\partial x} \frac{l^{0.5}}{0.664 \rho^{0.5} \eta^{0.5}} \right)^{2/3}. \tag{5.12}$$

This expression allows the estimation of the flow motion and the expected surface deformation. The maximum Pe for aluminium and copper calculated at different laser fluences is shown in Fig. 5.17a. Pe increases as the laser fluence increases. This indicates that the convective transport becomes stronger than the conductive in the molten pool with a rise of laser density. When the value of Pe is much greater than 1, the rate of transport of heat convection from the center to the periphery of the pool is much higher than that by conduction. For aluminium the convective transport is almost 3 times higher than conductive at high fluences (~3 J.cm^{-2}). It indicates that heat transport is stronger in the direction parallel to the surface. For copper the Peclet number is always lower than 1, evidencing that both convection and conduction transfer play significant roles along the entire laser fluence employed. Hence, the Pe values for copper are smaller than those one for aluminium.

Besides, there is a relationship between Pe and Ma for various materials under different processing conditions [161]:

$$\mathrm{Pe} = 0.08 \mathrm{Ma}^{0.95}. \tag{5.13}$$

The calculated Pe numbers using Eq. (5.13) for aluminium and copper are also represented in Fig. 5.17a. One can observe that this correlation matches well with the behaviour of Pe calculated using the equation given in Table 5.2. In conclusion, large Ma

values (strong driving force for convection) leads to high values of Pe. As the laser fluence rises, the spatial gradient of the temperature in the molten pool surface increases, leading to higher Ma values. Thus, higher surface velocity also results in higher Pe numbers. Peclet and Marangoni numbers depend on the thermal diffusivity of the material. For materials with high thermal diffusivity, such as aluminium and copper, low values of Ma and Pe are obtained (Figs. 5.14 – 5.15 and Fig. 5.17).

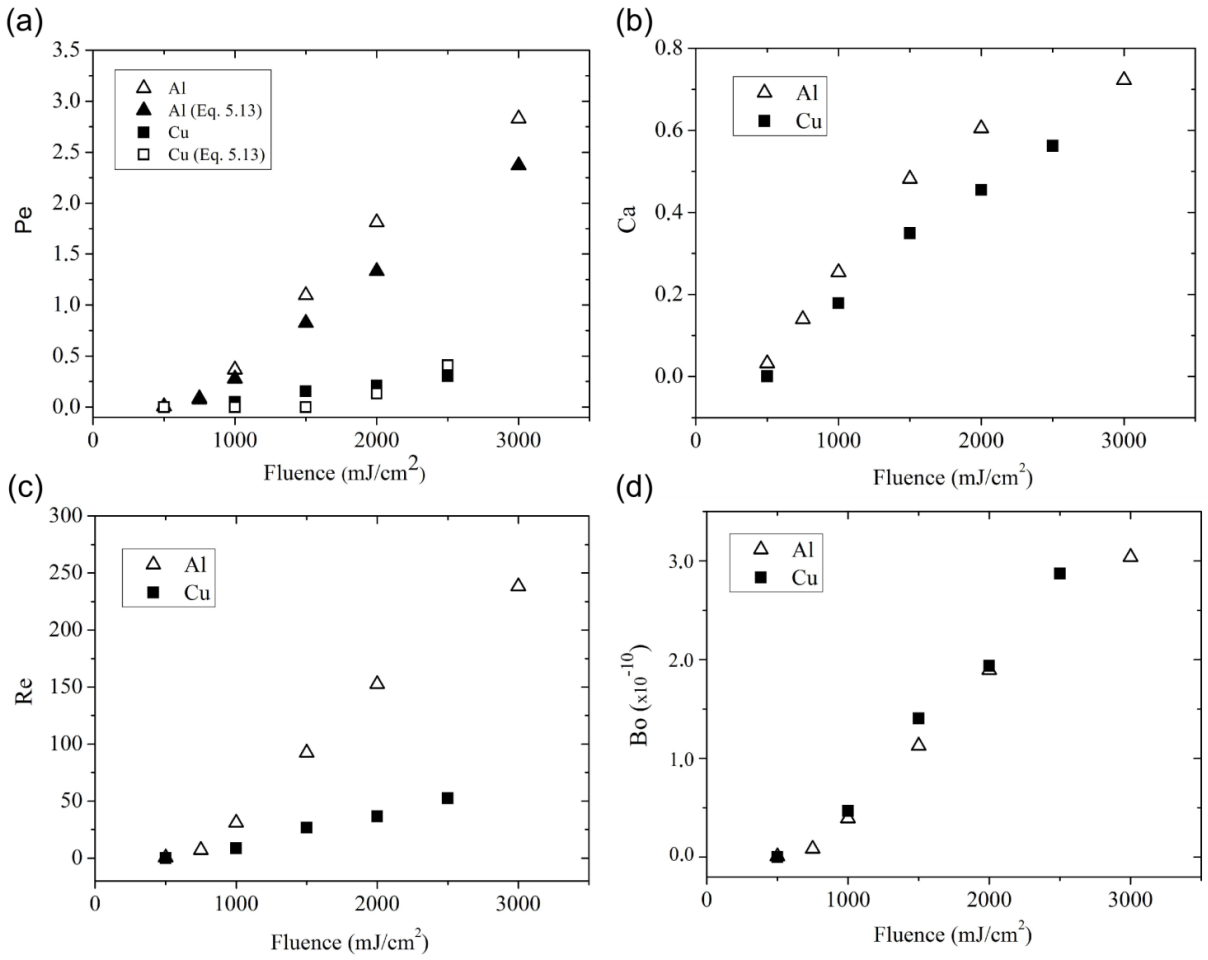

Figure 5.17. Dimensionless numbers, for aluminium and copper, of the entire molten pool during laser structuring at different laser fluences: (a) Peclet, (b) capillary, (c) Reynolds and (d) Bond numbers.

Furthermore, Peclet and Prandtl numbers can be used to predict the molten pool shape. The pool can change from concave to flat and even to convex as the Peclet number increases. With Pe<< 1, heat transport is dominated by conduction and the pool shape is concave. On the other hand, with Pe>> 1, heat transport is dominated by convection and the shape of the pool bottom can change form concave to flat or, in special cases, convex. The smaller the thermal

diffusivity, the more significant the effect of convection on the pool shape is [162]. This effect was seen in steel in absence of surface-active agents and significant electromagnetic forces. Steel has relatively low thermal diffusivity ($\sim 3.9\times10^{-6}$ $m^2.s^{-1}$) and high Pr (~ 0.2). The resulting Peclet number (~ 40) was sufficiently high at high laser fluences to affect the steel pool shape due to convective heat transfer [161, 170]. A high convective flow toward the edge of the molten pool created a strong return flow, which made the pool periphery deeper than the center (convex shape) [161].

For materials such as aluminium and copper (low Pr numbers), the thermal conductivities are so high that conduction always plays a significant role in heat transport. Even at very high Peclet numbers, an aluminium (or copper) molten pool is still concave rather that flat or convex [161]. Although outwards flow (convection) contributes to the heat transport to the pool edge, this heat is distributed by the high conductivity base metal instead of causing convex shapes. As a result of this, aluminium and copper presented narrow and deep structures, whereas flat or low structure depths were obtained for titanium (high Pr number).

In relation to surface deformation, the capillary number Ca is the main determining parameter. It describes the ratio of the Marangoni forces to the surface tension forces. The calculated Ca numbers are plotted in Fig. 5.17b. Both aluminium and copper presented similar Ca values, being slightly higher for aluminium. This suggests that the deformation is similar for both materials. For low values close to zero, the resulting melt pool shape can be assumed to be flat. This phenomenon can be seen during the structuring of both metals at low laser fluences. The increase of Ca with the increase of the fluence indicates that the deformation cannot be neglected. The acting forces become very strong and countervail the surface tension. If Ca increases to values up to 1, melt ejection is possible. In our study, the Ca values for both materials remain below 1. This means that melt ejection promoted by Marangoni forces is unlikely. This last conclusion enhances the hypothesis that melt ejection (or drop formation) during the structuring of Al and Cu comes from the combined action of hydrodynamic instabilities and recoil pressure.

In a molten pool there are diverse driving forces responsible for the fluid flow. The temperature gradient into the molten pool also generates density differences in the fluid producing natural convection (also called free convection). If a parcel of fluid is heated, it becomes less dense and rises. It enters into a region of greater average density and is therefore

subject to an upward buoyant force. The surrounding, cooler fluid then moves to replace it. This cooler fluid is then heated and the process continues, forming a convection current. This kind of convection creates a vertical heat transport from the bottom of the pool to the top [171, 172]. The buoyancy force is opposed by viscous drag and by heat diffusion. The drag force is always directed opposite to the motion of the fluid, and its magnitude is determined by the kinematic viscosity. Figure 5.18 illustrates the flow direction induced by surface tension and buoyancy driving force in the molten pool.

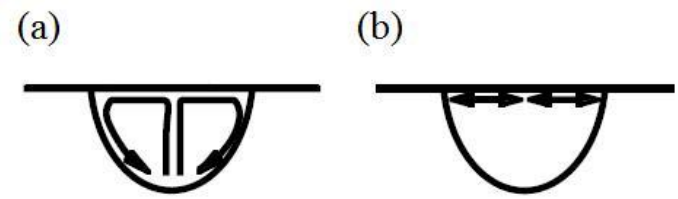

Figure 5.18. Flow directions induced by (a) buoyancy and (b) surface tension driving forces [172].

The influence of the buoyancy forces was also investigated. The describing parameter is the Grahof number, Gr. It is defined as the ratio of buoyancy to viscous force acting on the metal pool. The Gr numbers were calculated to be in the range of $10^{-13} < Gr < 10^{-8}$ for aluminium and copper structured at different laser fluences, which are significantly lower than their respective Ma values. In a physical sense, the calculations verify the dominating influence of Marangoni convection.

Additionally, it is possible to get information about the flow regime (laminar or turbulent) by determining the Reynolds number, Re. Laminar flow occurs at low Reynolds numbers, where viscous forces are dominant. In this case, the system is characterised by smooth, constant fluid motion. On the other hand, turbulent flow occurs at high Reynolds numbers and is dominated by inertial forces, which tend to produce random eddies, etc. The calculated Re values for aluminium and copper are shown in Fig. 5.17c. It can be observed that the Re numbers rise with the laser fluence. In the literature, there are almost not data available for critical Reynolds numbers in molten pools in order to derive laminar to turbulent flow. Atthey *et al.* [173] indicated that in molten metal pools, laminar to turbulent transition occurs at a Reynolds number of approximately 600. In addition, it has been reported that surface instabilities observed in the molten pool at high fluences might eventually lead to turbulent flow [174]. Chakraborty *et al.* proved that the turbulence may significantly affect the momentum transport of the pool whereas the thermal transport is marginally affected [175]. The Re values calculated for aluminium and copper were smaller than 600 in all cases. It suggests that the flow regime during laser structuring is mainly laminar.

Moreover, some dimensionless number relations have been used to provide additional information on the forces acting in the molten pool. The relative magnitude of Grahof and Reynolds numbers determine which form of convection is relevant. If $Gr/Re^2 >> 1$ forced convection may be neglected, whereas if $Gr/Re^2 << 1$ natural convection will be neglected. In the case where the ratio is approximately one, both forced and natural convection need to be taken into account. In this study, the calculated ratio Gr/Re^2 for both materials was much lower than one, which indicates that forced (Marangoni) convection plays an important role during the structuring of aluminium and copper. In the same way, the ratio Gr/Re defines the Bond number, Bo. For $Bo << 1$, the role of Marangoni flow would be more significant than that of natural convection. Fig. 5.17d illustrates the calculated Bo number for Al and Cu at different laser fluence. Both materials present similar Bo numbers, whose magnitudes are much lower than 1. This result supports also the dominating influence of Marangoni convection during the laser patterning of metal samples.

CHAPTER 6

Tailoring the chemical behaviour of aluminium for selective etching

This chapter is addressed to the chemical behaviour of aluminium modified by laser interference. In Section 6.1 the characterisation of pristine aluminium foils with different heat treatments is presented. After that (Section 6.2), an investigation of the local oxidation induced by laser treatment is performed. The goal of this study is to gain information about the nature and thickness of the oxide layer built up by laser treatment. The above results are accompanied with thermal simulation in order to relate the oxide layer thickness with the calculated surface temperature. For studying the stability of the irradiated zones, the structured samples were exposed to suitable etchants (Section 6.3). The influence of laser configuration, laser fluence as well as etching time on the chemical etching process was also investigated. Finally, the effect of the modulated oxide film thickness on the direct control of pit distribution during the chemical etching was analysed and discussed. Based on this process, the final morphology of the electrochemically etched surfaces was analysed by Fourier transformation.

6.1 Characterisation of as-received aluminium foils

In this part of the work, the samples consisted of annealed and non-annealed aluminium foils for high-voltage (HV) capacitor applications. As-received samples were investigated by white light Interferometry WLI and SEM observations. In both aluminium conditions, similar results were obtained. Figure 6.1 shows the representative 3D topography, lateral profile and SEM morphology of the specimens. The results show that the overall surface is composed of numerous grooves coming from the previous rolling process. Its respective lateral profile revealed that the grooves present an irregular distribution (Fig. 6.1b). The average roughness R_a was 0.103 ± 0.023 µm and 0.134 ± 0.031 µm for non-annealed and annealed Al, respectively

Another important parameter to be evaluated is the crystallographic orientation of the samples. Texture analyses were carried out in order to compare the preferential orientation of aluminium induced by the annealed process. The texture test was performed by X-ray diffraction (Philips X'Pert) using Cu-Kα radiation and Ni filter. The results presented in

Fig. 6.2 show that non-annealed aluminium consists basically of a mixture of two textures, a strong cubic texture and a weak R texture (Fig. 6.2a, b). The {124} <211> texture is commonly called R texture [176]. However, a unique cubic texture was obtained after the recrystallisation process (Fig. 6.2d, e). The orientation positions of cube and R textures in the {200} pole figure are illustrated in Fig. 6.2c.

As it was previously mentioned (see Section 3.3), the cubic texture denotes the case where the crystals are oriented in such a way that (100) is substantially parallel to the plane of the foils, while their crystallographic direction [010] is parallel to the direction in which the foil is rolled. A texture of this kind is represented by {100} <100>.

A similar definition can be given for R texture in which its planes and directions corresponds to {124} <211>. The cube and R texture are the main recrystallisation textures in aluminium foils, and normally, no other strong texture is produced. Moreover, it has been established that the ratio of cube to R texture is influenced by the chemical composition of the foil and the annealed parameters used [177].

Additional information concerning the crystallographic orientation and grain size of annealed samples was obtained by electron backscatter diffraction, EBSD. The measurements were done using an EBSD system equipped with a TSL OIM (orientation imaging microscope) analysis unit. To produce a crystallographic orientation map the electron beam is scanned over a selected surface area and the resulting Kikuchi patterns are indexed and analysed automatically. An image quality, IQ, is recorded for each such Kikuchi pattern. The IQ is calculated as the average values of the heights of the most prominent detected peaks in the Hough transformation. A high IQ value usually indicates a good quality EBSD pattern [143, 178]. The outcomes of EBSD analysis are represented in the form of maps; the more important thereof are the so-called inverse pole figure, IPF, maps. However, IQ can be affected by various factors including surface topography, material type, grain orientation, etc [179]. Hence, annealed aluminium samples were electro-polished before EBSD data acquisition. The results of the EBSD measurements are summarised in Fig. 6.3. Figure 6.3a shows the SEM image of the electropolished aluminium surface. In this condition, the grain can be observed by simple SEM observation.

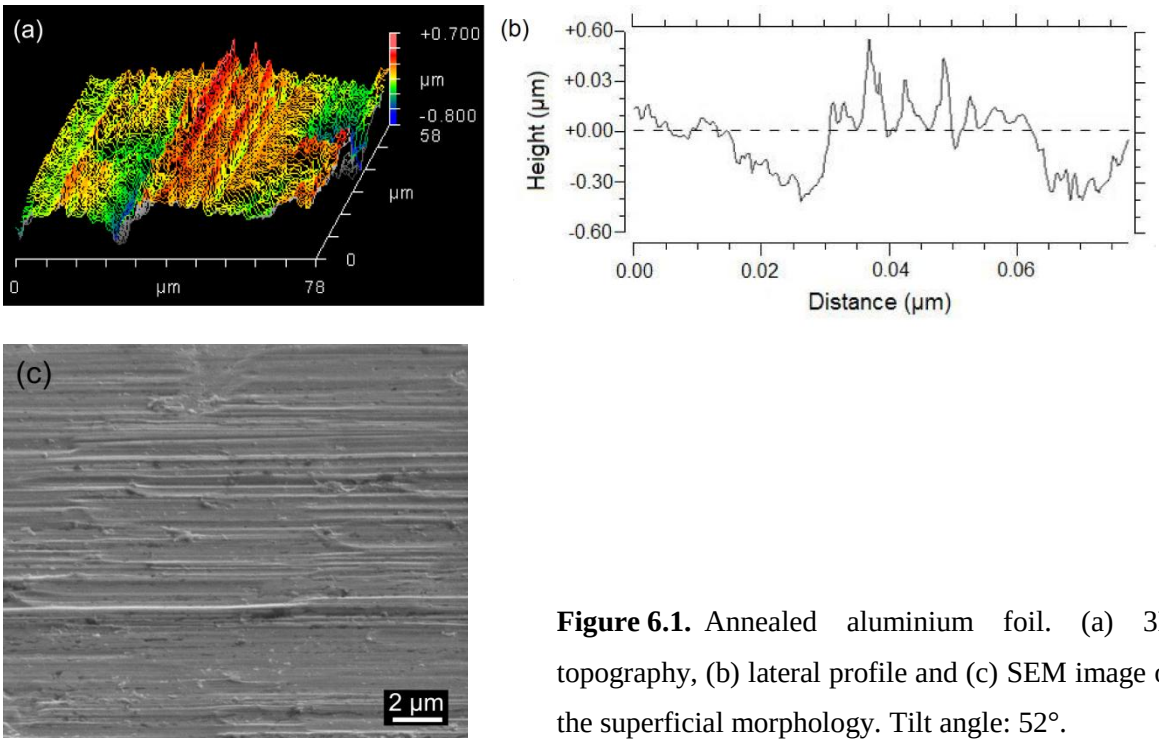

Figure 6.1. Annealed aluminium foil. (a) 3D topography, (b) lateral profile and (c) SEM image of the superficial morphology. Tilt angle: 52°.

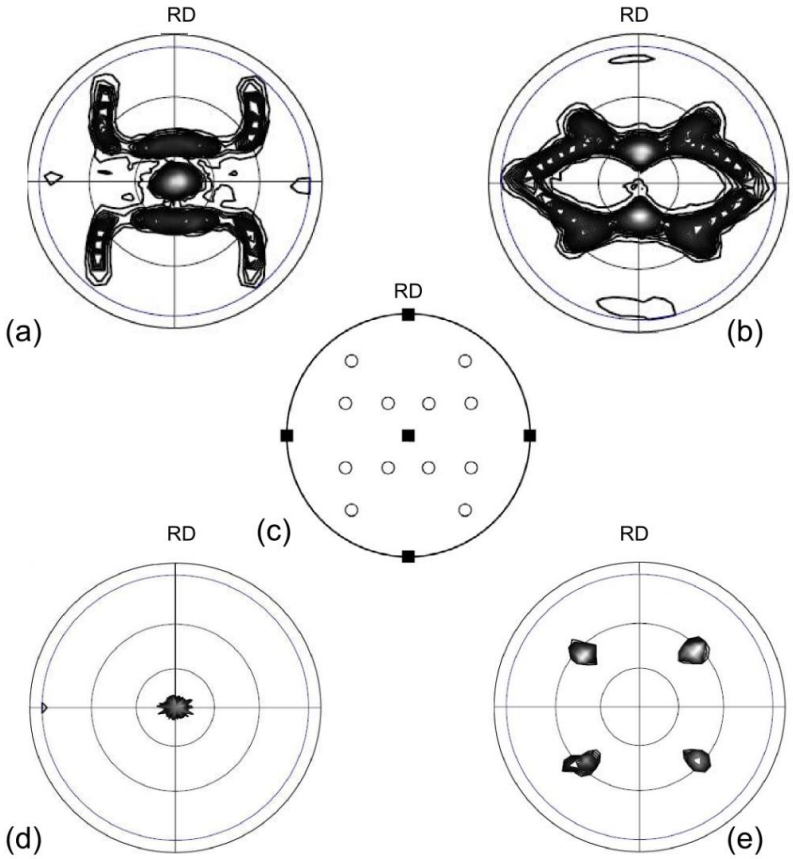

Figure 6.2. (a, d) {200} and (b, e) {111} pole figures indicating the texture types in aluminium: (a, b) non-annealed foil and (d, e) annealed foil. (c) Positions of the {200} pole density peaks (■: cube, o: R) [180].

The image quality map gives information about the Kikuchi pattern quality for each measured datapoint. As the corresponding image quality of aluminium is high, a reliable measurement of grain orientation is possible. On the other hand, the IPF map provides a colour-coded map of the orientation of the grains. In order to facilitate grain boundary observation, IQ and IPF [001] maps were overlapped in Fig. 6.3b. It is an evidence that the samples exhibit a very strong preferred {100} <100> orientation. The texture analysis is also plotted in the form of {100} and {111} pole figures in Fig. 6.3c. These results are in good agreement with those found with X-ray diffraction analyses, where a unique and stronger cubic texture is observed. From the measured EBSD data, the grain size of the aluminium can be also determined. This analysis shows that the size of most grains are about 230 µm, while some grains have a size of around 103-148 µm.

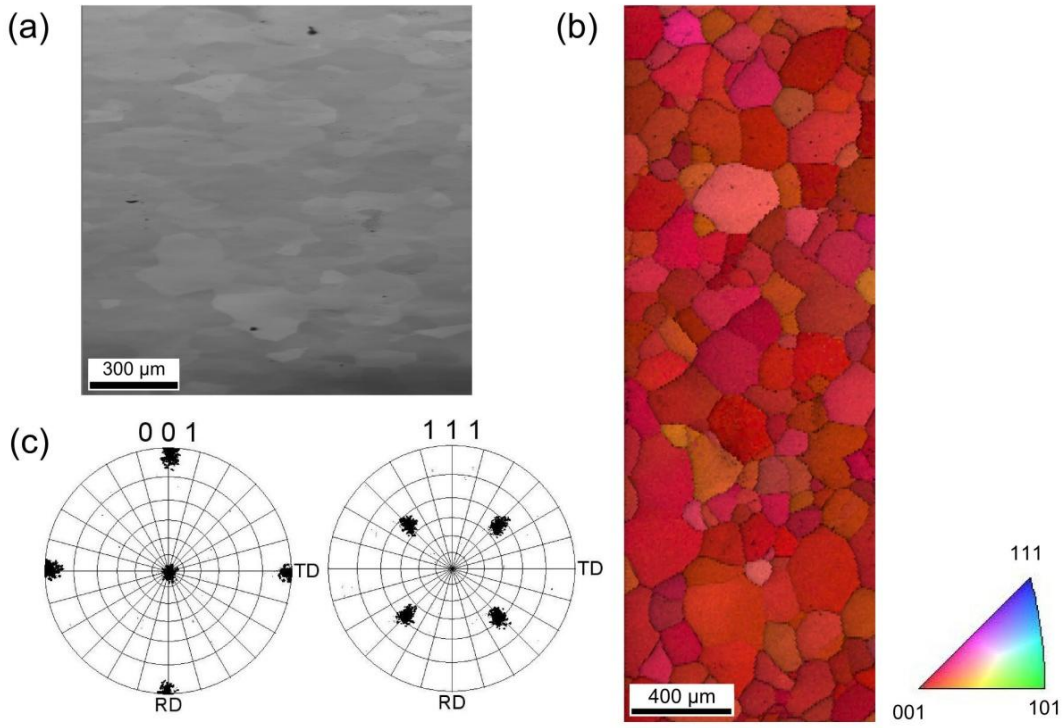

Figure 6.3. EBSD of electropolished annealed aluminium: (a) SEM images of the surface, (b) image quality plus [011] inverse pole figure where the preferred orientation and grain size can be seen; (c) {001} and {111} pole figures evidencing the strong cubic texture.

6.2 Laser-induced oxidation of aluminium

In addition to the precise formation of advanced periodic structures, laser interference metallurgy can also induce local thermal reactions on aluminium surfaces. In order to

investigate this phenomenon, annealed aluminium samples were structured using two laser beams in a symmetrical configuration at different laser fluences. The period of the structures was selected to be 4.5 µm.

TEM examinations were carried out in non-irradiated (Fig. 6.4) and laser-structured (Fig. 6.5) Al samples. The TEM observations of the original annealed aluminium surface (pristine sample) show a regular and continuous thin oxide layer over the entire aluminium surface (Fig. 6.4a). The native oxide layer thickness is approximately 5.2 ± 0.48 nm. The amorphous Pt layer results from the in-situ deposition of Pt prior to the preparation of the TEM foil (Fig. 6.4b).The respective electron diffraction of aluminium substrates (Fig. 6.4c) reveals a typical spot pattern of Al (f.c.c.) single crystal.

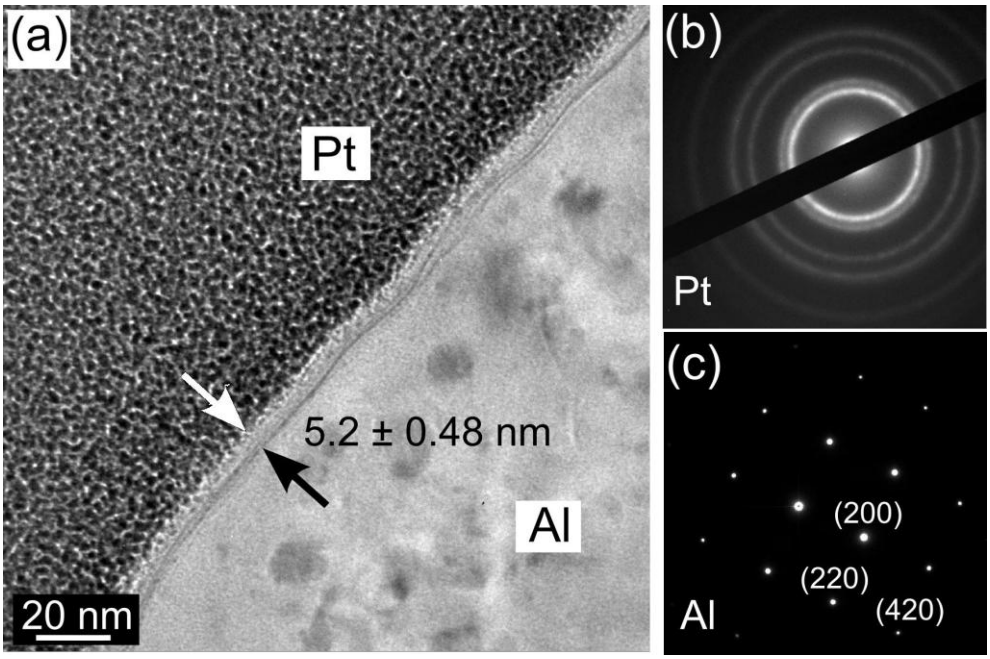

Figure 6.4. TEM observation of the native oxide layer of aluminium. (a) Bright field image of the surface. (b) Select area electron diffraction (SAD) pattern of the Pt layer protection. (c) SAD pattern of aluminium substrate.

TEM examinations were also carried out in Al samples after laser irradiation. Figure 6.5a shows the SEM image of a TEM lamella from a sample structured at 2020 $mJ.cm^{-2}$. At this high fluence, the interference maxima and minima zones can be recognised due to the pronounced structures formed on the surface. The SEM image inserted in the corner of Fig. 6.5a shows the in-situ lift-out of the lamella using a micro-manipulator during the TEM preparation. One can see on the picture that the TEM lamella was realised perpendicular to the linear pattern. TEM observations show that laser interference irradiation causes local and periodic oxidation on the surface. The thickness of the oxide layer measured at the minima positions (Fig. 6.5b) is 11 ± 0.94 nm, while at the maxima positions (Fig 6.5c)

it is 19 ± 0.88 nm. This indicates that, at this high laser fluence value (2020 mJ.cm^{-2}), the oxide thickness at the maxima positions is almost twice as thick as than at the minima positions. The indexed diffraction pattern shown in Fig. 6.5d allows identifying the oxide layer as α-Al_2O_3.

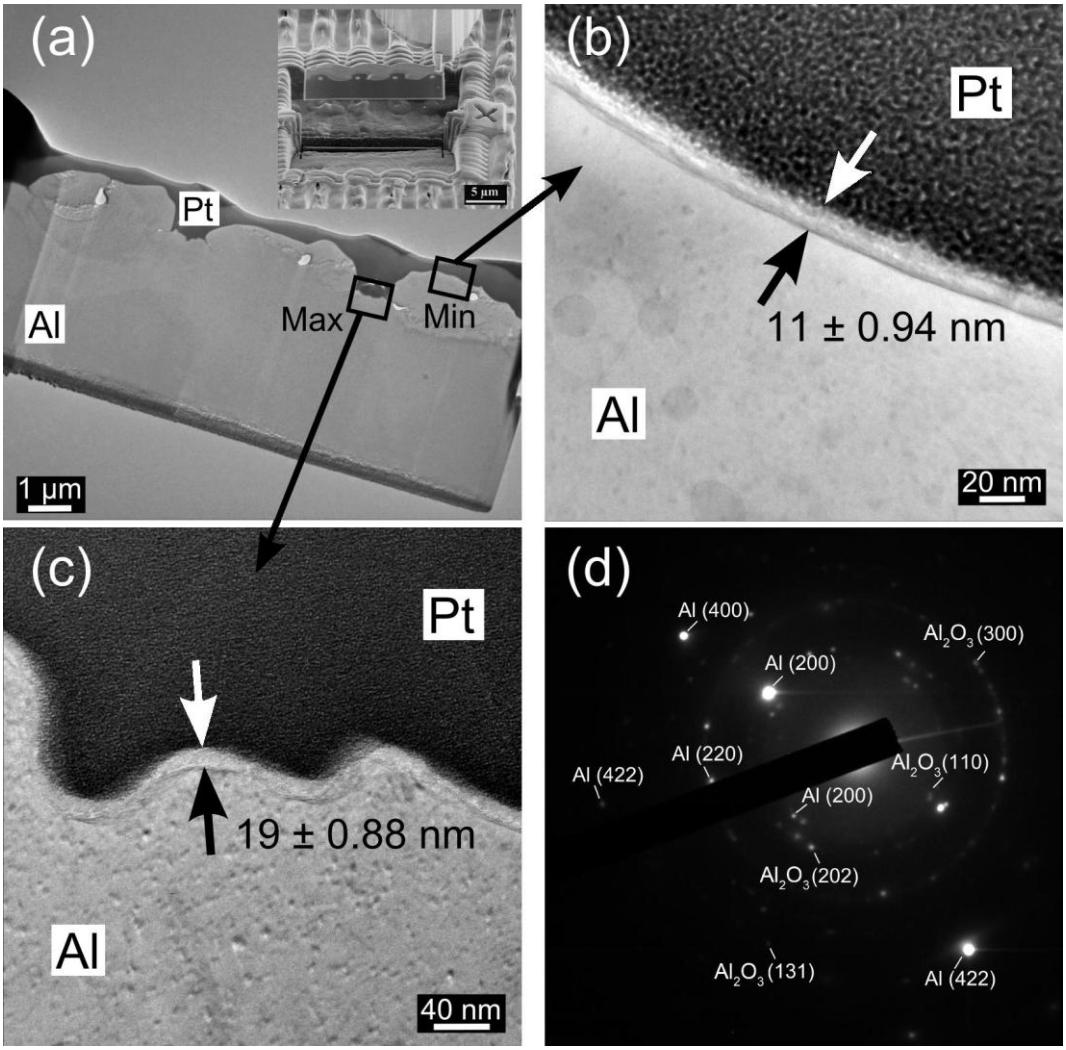

Figure 6.5. TEM investigation of the oxide layer formed during laser structuring of aluminium foil. The laser fluence used was 2020 mJ/cm^2. (a) Bright field of the TEM lamella showing the maximal and minimal interference positions; the *insert* reveals the zone where the TEM foil was realised. (b), (c) High magnification of the oxide layer thickness at the minimal and maximal interference zones, respectively. (d) Electron diffraction pattern of the oxide film.

Similar investigations were performed for aluminium samples structured using low and moderate laser fluences and the respective oxide layer thicknesses were measured. The results are plotted in Fig. 6.6. In each case, a periodic oxidation of the surface takes place. As the laser fluence increases, the oxide layer thickness grows at both the maxima and minima.

Furthermore, the difference in oxide layer thickness between the maxima and minima also increases. Note that the oxide thickness at a laser fluence equal to zero corresponds to the thickness of the native oxide layer.

A similar increase of the oxide layer thickness with the laser fluence was reported in the literature for aluminium-magnesium alloy [78]. In this study, a Q-switched *Nd:YAG* with a pulse duration of 10 nm and a wavelength of 1064 nm was used to irradiate the aluminium-magnesium substrate in air. The aim of this work was to characterise the transient oxidation that can occur below the laser energy domain leading to any phase change (melting, ablation) of the samples. Using X-ray photoelectron spectroscopy (XPS) measurements, the sputtering time at the intersection point between the curves of metallic aluminium and oxygen was determined as a function of the laser fluence for irradiated aluminium-magnesium alloy. In order to correlate the above sputtering times with the thickness of aluminium oxide, pure aluminium samples were anodised at different voltages producing uniform aluminium oxide film with a well-known thickness. XPS measurements were also carried out on anodic oxide of different thickness on pure aluminium. Assuming that there was no significant difference in the sputtering rate between the anodic oxide and the oxide formed by laser treatment, the thickness of the oxide formed during laser irradiation was calculated. It was found that a thermal oxidation induced by the laser irradiation took place and the thickness of the formed oxide increased with the increase of the laser fluence.

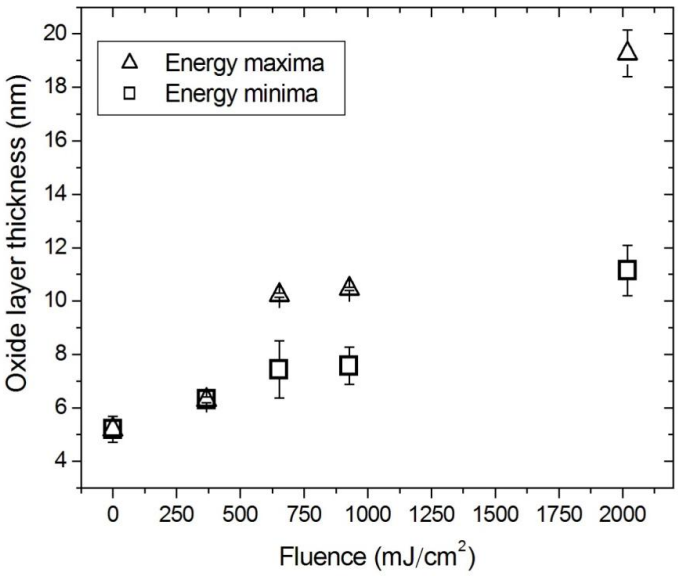

Figure 6.6. Experimental oxide layer thickness at the interference maxima and minima formed during laser irradiation using a laser fluence range from 0 (non-irradiated surface) to 2020 mJ.cm^{-2}.

6.3 Selective etching

It was shown that pulsed laser interference metallurgy causes local and periodic oxidation on the aluminium surface and that the oxide layer thickness is determined by the laser fluence. The thin oxide layer built up during laser irradiation may enhance the chemical stability of the irradiated areas. SEM images of non-etched and etched aluminium surfaces under different conditions are shown in Fig. 6.7. The etchant used was an aqueous HCl and HF solution (Flick's etchant, see Section 4.3) at room temperature.

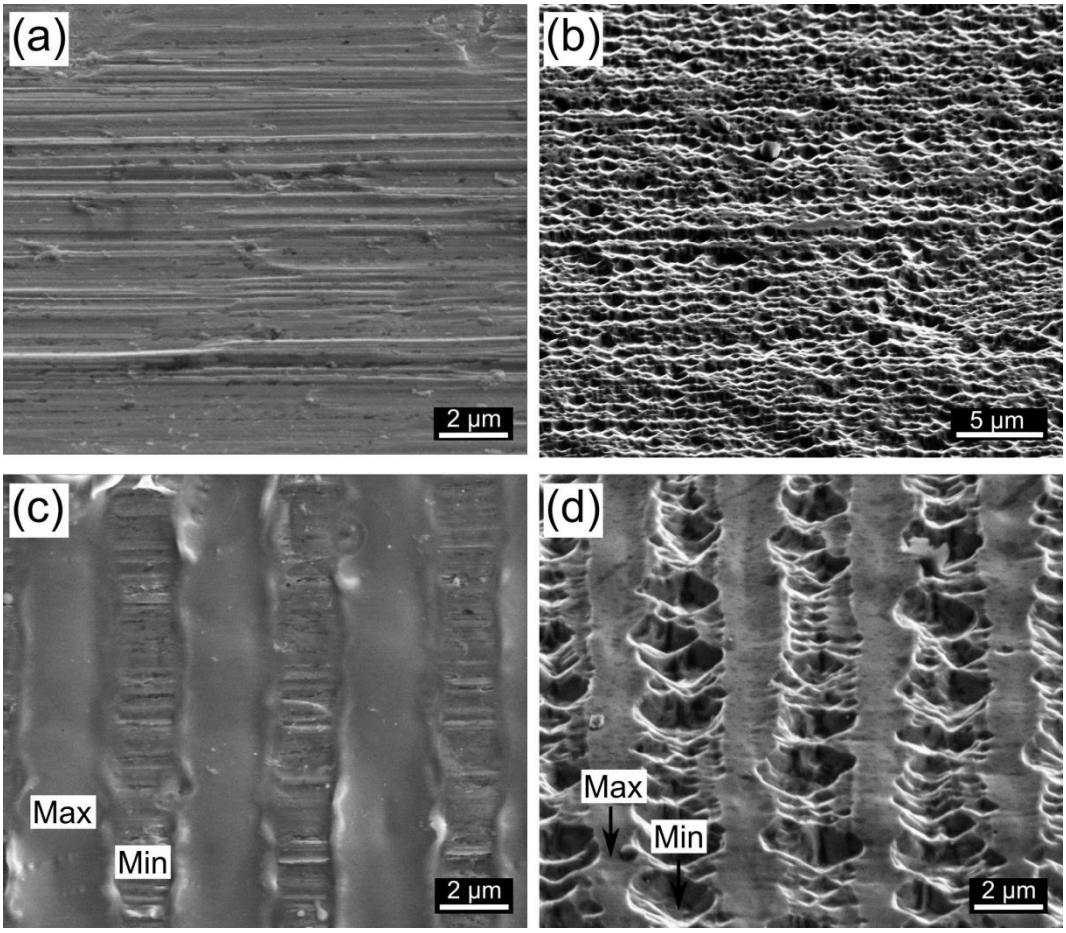

Figure 6.7. SEM images of non-structured and structured aluminium surfaces before and after etching. Etching was carried out in a mixture of HCL and HF at room temperature for 30 s. Morphology of non-irradiated (pristine) aluminium before (a) and after (b) the etching process. (c), (d) Morphology of aluminium structured at a laser fluence of 700 mJ/cm^2: (c) non-etched, (d) after chemical etching.

Figure 6.7a shows a SEM image of the pristine aluminium. A steep topography is observed on the surface due to the previous rolling process. In these surface conditions, the etching process generates a large number of pits at the surface, following more or less the rolling lines as shown in Fig. 6.7b. In some places the coalescence of several tunnel initiation

pits occurs, forming big etched zones (overetching), whereas other zones are completely unetched. This phenomenon is not convenient to achieve a large surface area. Figure 6.7c reveals the morphology of Al structured at 700 mJ.cm^{-2} using two laser beams. For this fluence value, the topography of the material at the interference maxima positions is smooth. The corresponding etched surface shown in Fig. 6.7d reveals that etching occurs preferentially at the interference minima.

The etching morphology of Al structured at a fluence of 1100 mJ.cm^{-2} indicates that the preferential and periodic etching is also achieved at higher fluence values Fig. 6.8a. However, as the laser fluence is greater, both the topography of the surface and the oxide layer thickness increase, resulting in larger unetched zones compared to the structure formed at 700 mJ.cm^{-2}. Preferential etching is not possible in the entire range of fluence values studied. At high laser fluences, the whole surface becomes passive as shown in Fig. 6.8b for a laser fluence of approximately 2000 mJ.cm^{-2}.

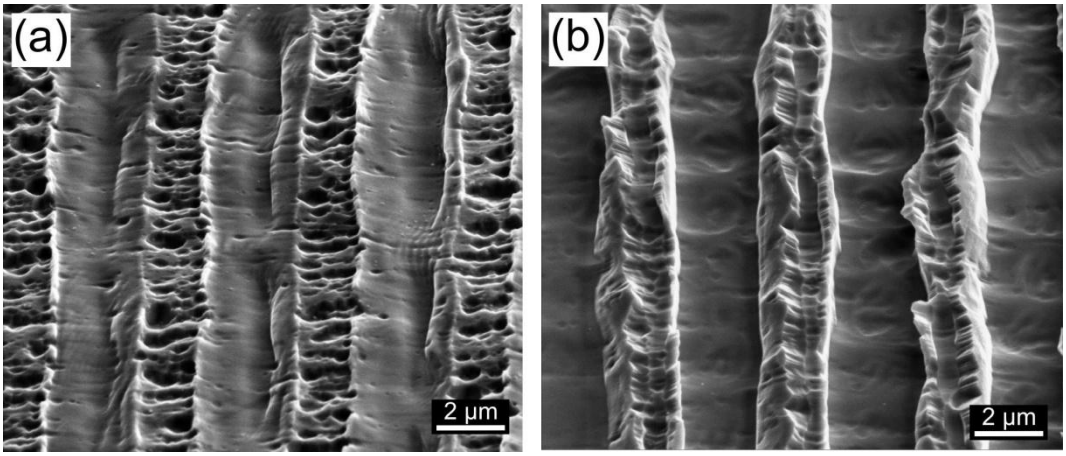

Figure 6.8. Aluminium structured at different laser fluences and chemically etched. The laser fluences used were: (a) 1100 mJ/cm^2 and (b) 2020 mJ/cm^2. Etching was carried out in a mixture of HCL and HF at room temperature for 30 s.

Analogous results were found for aluminium surfaces structured with other interference configurations. Figure 6.9 shows the selective etching of an Al surface structured using a grid-like pattern. In this case, the etchant used was an HCl solution at a temperature of 85°C. Like in the case of samples structured with line-like patterns, the initial pit-sites occur only at the minima positions. Both etchants, the HCl solution at high temperature and the aqueous HCl + HF solution at room temperature, produce a high pit density on the surface of the aluminium foils. However, with Flick's etchant, the pits are larger and show a more regular square shape than with only the HCl solution.

Moreover, as the etching time increases, an interesting etching behaviour is observed. Figure 6.10 shows the dependence of selective etching on the etch time. The aluminium surfaces were structured with three laser beams to form dot-like patterns. At 30 sec etch time, the selective etching is localised only at the minimal interference positions (Fig. 6.10a), whereas after 1 min, the maximal interference zones also start to be etched (Fig. 6.10b). It is important to highlight that these etch times are longer than the etch time used normally for electrochemical etching. The chemical etching used in this work aims to study the start pit-site distribution of aluminium samples trying to avoid the influence of other intrinsic parameters of the electrochemical process such as current density, voltage, etc.

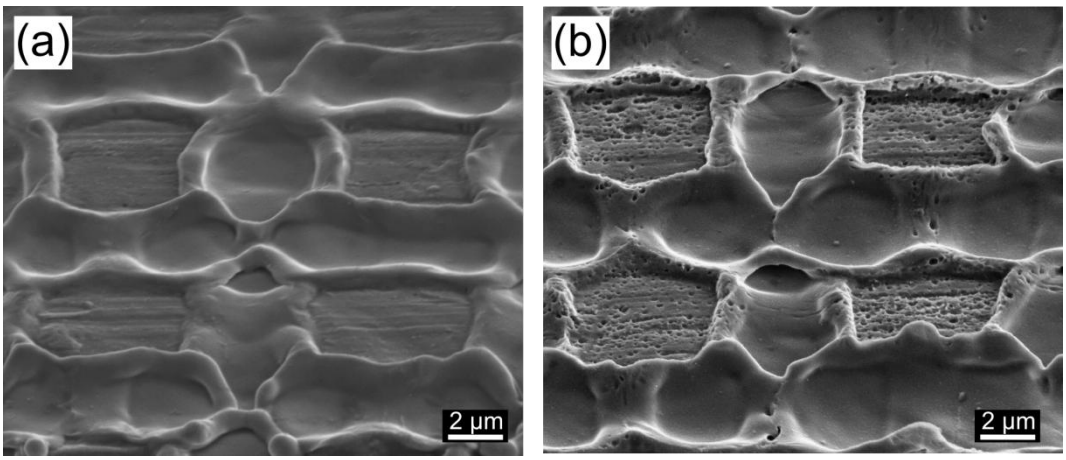

Figure 6.9. Periodic grid patterning of aluminium foil irradiated with 1070 mJ/cm^2 laser fluence: (a) morphology of the structured Al samples; (b) sample etched using HCl solution at 85°C for 30 s.

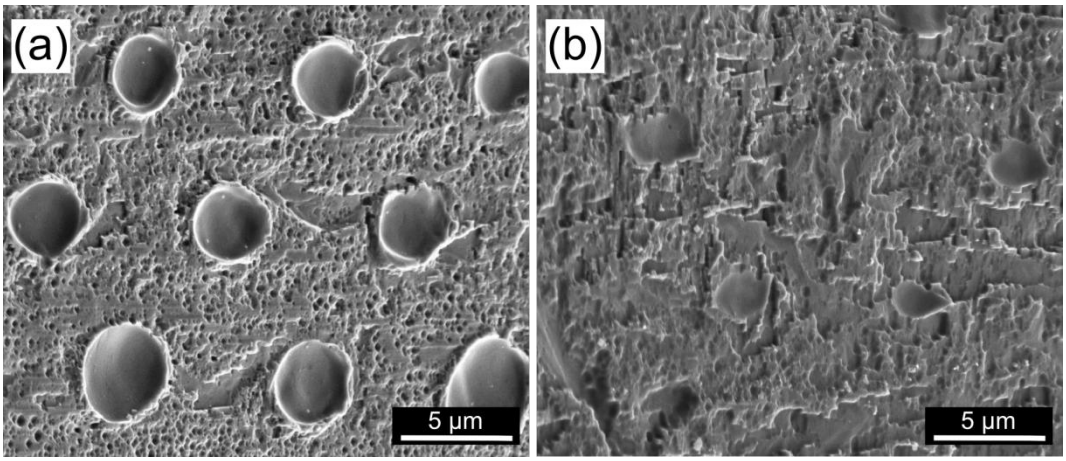

Figure 6.10. SEM image of the aluminium samples structured with dot patterns at 900 mJ/cm^2 and etched with HCl solution at 85°C for (a) 30 s and (b) 1 min.

6.4 Discussion

Because of the high affinity of Al with oxygen the exposure of aluminium surface to laser irradiation results in the formation of an Al_2O_3 film. The TEM results afore-mentioned indicate that by varying the laser fluence during the structuring process of Al, it is possible to modulate the oxide thickness in an appropriate controlled manner.

In the case of classical oxidation of aluminium, the oxide formed at high temperatures (> 1000°C) is α-Al_2O_3, while at low temperatures the oxide film usually comprises some of the metastable forms of Al_2O_3, particularly γ-Al_2O_3, or amorphous Al_2O_3 below 400°C [181]. The nature of the oxide changes from amorphous oxide film to crystalline oxide depending on oxidation temperature, time, thickness, etc. [182]. Due to the transient and high temperature values reached during laser structuring, the built-up oxide layer is also found to be α-Al_2O_3. Consequently, the oxide structure obtained by laser-induced oxidation seems to be the same as in the case of classical oxidation. It is also important to emphasise that the oxide layers formed at the maxima as well as the minima positions exhibit high density and homogeneity. The Al_2O_3 was characterised to be coherent and pore-free thin film. Even though the thicknesses obtained with a single laser pulse are not very thick, the oxide layers are very stable. In the literature it has been demonstrated [183] that several laser pulses are necessary to obtain a sufficiently thick oxide layer.

In pulsed-laser oxidation, thermodynamically unstable phases may remain, while other phases cannot nucleate within such short times. Furthermore, the formation of different oxides is evidence of the presence of different kinetic laws. For convectional oxidation it has been established that the Al_2O_3 film is amorphous at temperatures below 400°C and that the film grew by the outward migration of Al interstitial ions (cf. O migration at high temperatures) [181]. On the other hand, growth of Al_2O_3 film on molten Al (in the range of 600°C – 850°C) leads to different kinetic laws. Logarithmic-type kinetics were found at temperatures below 700°C and mainly parabolic at higher temperature. Nevertheless, the oxide growing on molten aluminium was deduced to be η-Al_2O_3, rather than α-Al_2O_3 [184]. However, several reports indentified the oxide film as α-Al_2O_3 by XRD analysis of the cooled samples. It is possible that other oxides are formed on the surface of liquid Al (such as γ-Al_2O_3), which transform into α-Al_2O_3 depending on the atmosphere [87, 185]. Stucki *et al.* [88] claimed that the growth rate of an oxide layer at the liquid surface is much lower than in the case of a solid surface. Other researchers reported that the oxidation behaviour of liquid aluminium is quite complex and cannot be described by simple rate equations (linear, parabolic, etc.) due to

cracking of the oxide scale, which leads to complex reactions [185]. In this study a quantitative kinetic analysis of the process is hardly possible due to the unknown chemical and physical processes taking place during the laser oxidation.

However, it is known that, in the case of reactive metallic substrates irradiated with a pulsed laser in ambient conditions (without neutral gas covering), limited oxidation is always observed or assumed [78]. In order to correlate the above measured oxide layer thicknesses with the superficial temperature distribution during laser structuring, thermal simulations were carried out following the model presented in Sec. 5.1.2. It was assumed that the oxide formation does not significantly influence sample heating (no feedback effects) [186]. Figure 6.11 depicts the experimental oxide layer thickness as a function of the calculated surface temperature at maximal and minimal energy positions in the range of the examined laser fluences. It was found that when the sample temperature is higher the oxide layer is thicker. Oxide layer thickness increases linearly with the maximal temperature reached during the laser pulse.

Furthermore, the laser-induced temperature rise can also enhance the diffusion flux and the reaction rate of the species within the irradiated areas. The thermal excitation of electrons increases the rate of electron transfer from the material to oxygen and thereby the electric field [66], which could induce faster oxidation kinetics of aluminium.

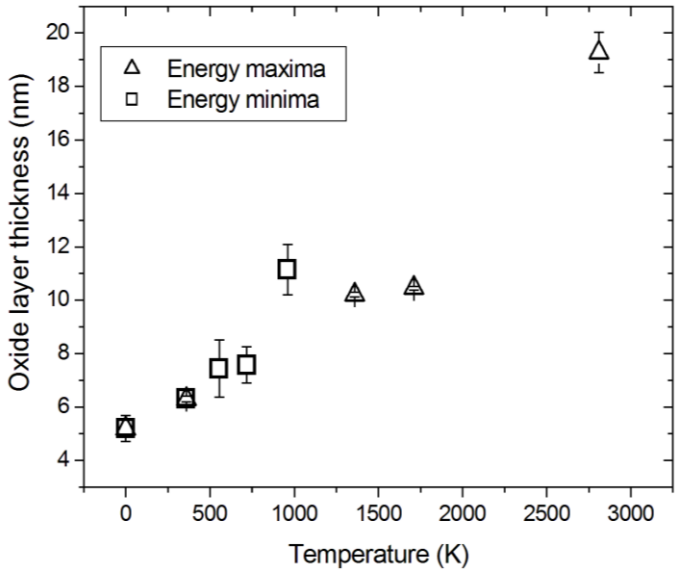

Figure 6.11. Oxide layer behaviour as a function of the calculated surface temperature during laser structuring of aluminium.

The oxide layer which is built up after laser structuring could become a powerful tool to improve the control of the first stages of the etching process. The oxidation-patterning promotes local protective oxide zones on the metal surface. When structured aluminium is placed in a suitable etchant, the interference minima zones are etched, while the interference

maxima positions remain unchanged, at least at the beginning of the etching process. Preferential etching occurs due to the difference in oxide layer thickness between the maxima and minima positions. The corresponding etched surface shown in Fig. 6.7d illustrates the local and preferential etching at the minima positions where the oxide layer thickness at the minima and maxima zones are of 7.43 ± 1.07 nm and 10.22 ± 0.08 nm, respectively. Extensive research work has reported that pitting of passive metals usually starts where the passivating oxide film is thinner or otherwise defective [187]. The preferred etching occurs because the oxide layer at the maxima is sufficiently thick to protect the metal from the etchant at the beginning of the corrosion process. The oxide layer is very stable, and enhances the chemical stability of the irradiated zones. The protection afforded by Al_2O_3 is obviously the result of the high coherence and low concentration of defects. As a consequence, the pit distribution follows the patterns imprinted by laser structuring. Nevertheless, preferential etching does not occur at higher laser fluences. In these surface conditions (see Fig. 6.8b), it is not possible to produce tunnel pit nucleation on the sample surface due to the thick oxide layer at both the maxima and minima positions. According to the above results, when the oxide layer thickness reaches or exceeds 10 nm, the surface becomes completely passive.

Another important effect to take into account is the possible crystallographic orientation changes of aluminium during laser structuring. As it was previously explained, the texture of aluminium foil is one of the more important parameters to achieve a high surface area by etching (see Section 3.3). Depending on the laser density used, the metal surface can be locally melted and liquid motion can take place during the structuring process. All these phenomena could modify the original texture of the samples. In order to obtain information of the crystallographic orientation before and after laser structuring, EBSD measurements were carried out firstly at the edge of the irradiated zone. Due to the laser having a Gaussian distribution, at this position it is possible to observe the surface deformation transition.

Figure 6.12a shows the SEM image on the border of the irradiated area of aluminium structured with 2100 $mJ.cm^{-2}$. The corresponding overlap of IQ and IPF maps is represented in Fig. 6.12b. In this case only a section of the structured aluminium surface (Fig. 6.12a) was analysed.

The IQ + IPF map depicts the orientation of one grain in which the structure evolution takes place. It is quite evident that the liquid aluminium re-solidifies following the same orientation as the original grain. The cubic texture is so strong that the liquid aluminium tends to re-solidify in the same grain orientation. An additional EBSD measurement performed at

the middle of the irradiated zone is presented in Fig. 6.12c. This figure shows the crystallographic orientation of three grains after laser structuring. In all cases, aluminium re-solidifies following the same orientation than its respective original grains. This result confirms that even using high fluences the cubic texture of aluminium remains unchanged (Fig. 6.12).

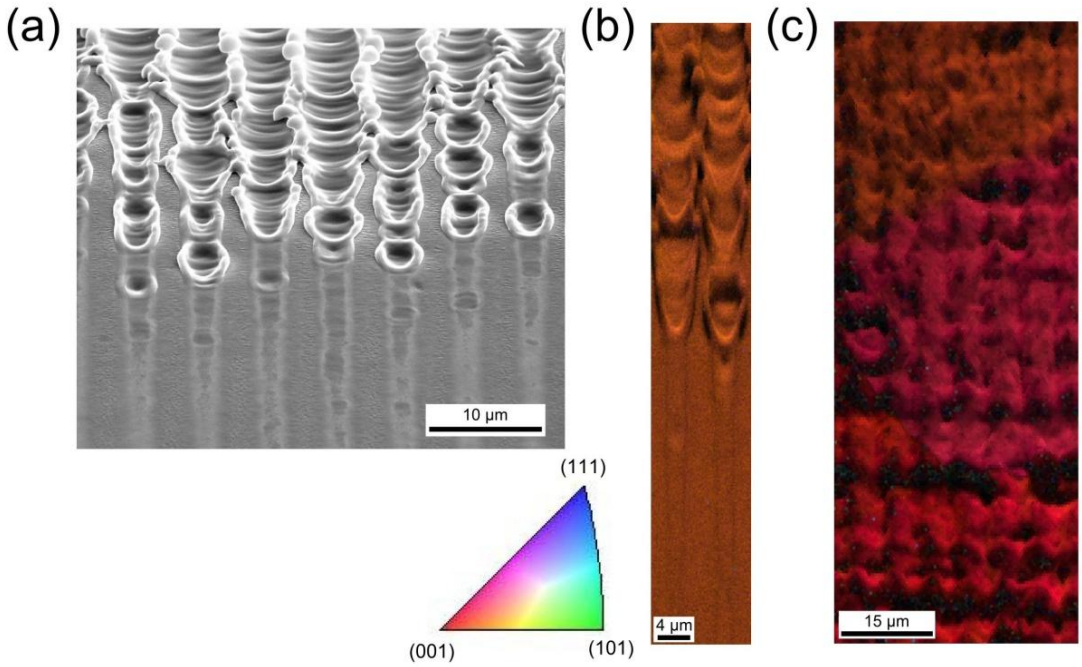

Figure 6.12. EBSD of annealed aluminium structured at 2100 mJ/cm^2: (a) SEM images of the surface at the edge of the irradiated zone. Tilt: 25°. (b), (c) Image quality plus [011] inverse pole figure of: (c) a section of the surface showed in (a) corresponding to a single grain; and (c) a large Al surface completely structured showing the orientation of three grains after laser structuring.

Moreover, in all the examined TEM foils, the molten and resolidified region cannot be distinguished from the unmodified one because the growth of the new grains does not differ from the original grains. This also corroborates the effect that the aluminium texture does not change after laser patterning.

The selective etching was achieved independently of the etchants used. Nevertheless, the characteristic of the pits differs from one acid solution to another. Both etchants created square pits at the aluminium surface but in the case of Flick's etchant, bigger pit sizes are observed. For hydrochloric solution the pits seem to be finer and more uniform. Flick's etchant is an aqueous acid composed of HCl plus HF (see Section 4.3). Due to its great aggressiveness Flick's etchant may lead to an excessive dissolution of aluminium surface which is harmful to an ideal enlargement of the surface area. Another parameter which can influence the mean pit size is the Al^{3+} concentration. An increase in Al^{3+} concentration in the

solution decreases the number of pit nucleation sites and in turn increases the current density per pit, resulting in an increase in pit size [188].

Electrochemical etching of the samples was also carried out in order to investigate the effect of laser interference metallurgy on the real industrial process. Fourier transformation analysis of the SEM images of electrochemically etched surfaces was realised in order to correlate the laser structuring periodicity with the final etched morphology. Fig. 6.13 shows the SEM image, the power spectrum (insert) and the radial function of two etched surfaces.

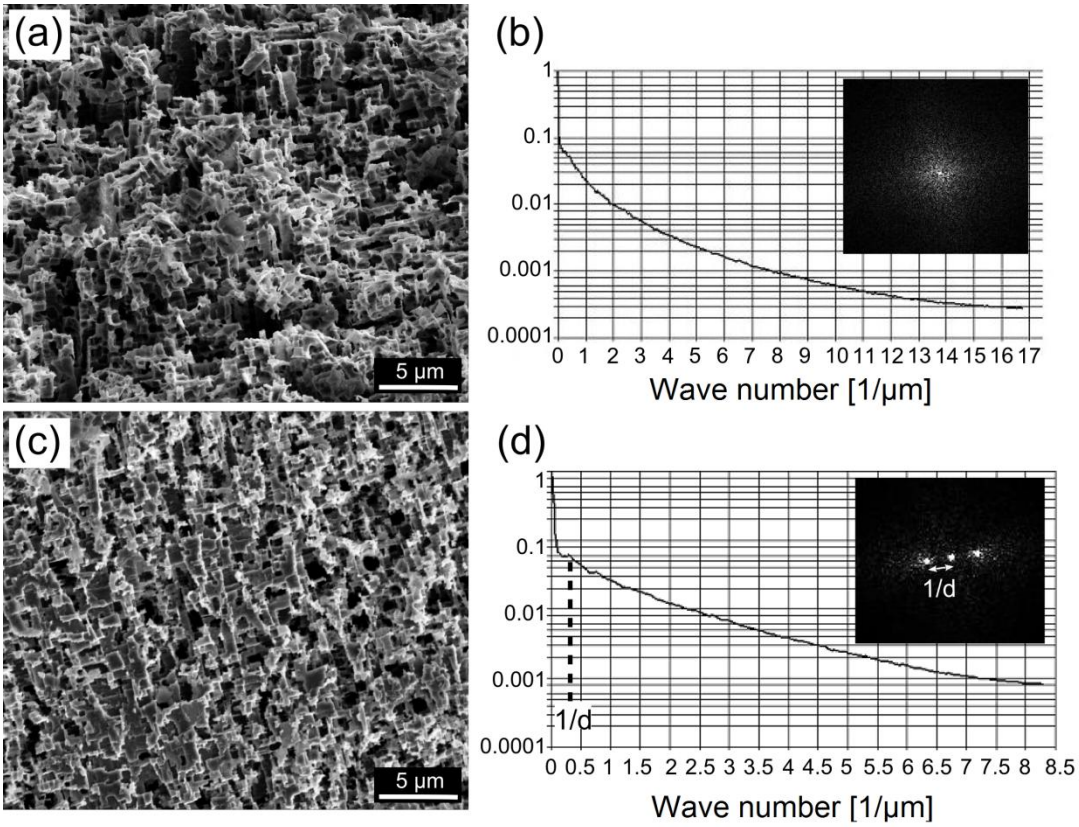

Figure 6.13. Scanning electron micrographs and spectral analysis of electrochemically etched Al surface. (a), (b) Non-structured aluminium: (a) surface morphology and (b) its respective radial power spectrum. (c), (d) Al structured at 700 mJ/cm^2: (c) surface morphology and (d) its corresponding radial power spectrum. The inserts show the discrete Fourier transformation in each case. The radial function is shown using a logarithmic scale. In both structured and non-structured aluminium, electrochemical etching was performed using HCl solution at high temperature.

The power spectrum or discrete Fourier transformation is a representation of the magnitude of various frequency components of a 2D image that has been transformed through the Fourier transformation command from the spatial domain into the frequency domain. The origin is customarily located in the centre of the power spectrum. Higher frequency components of the images are located at greater distances from the origin [189]. Different directions from the

origin represent different orientations of features in the image. Figure 6.13a shows a representative SEM image of the morphology of a non-structured Al foil after electrochemical etching. One can observe an overetching of the surface in some zones. The insert in Fig. 6.13b shows the random power spectrum of the pristine sample indicating that no frequency patterns are present.

This result is confirmed by the radial power spectrum plot, where an invariable falling curve is obtained (Fig. 6.13b). The aluminium surface structured by LIMET at 700 $mJ.cm^{-2}$ and electrochemically etched under the same conditions reveals homogeneous etching despite no periodicity being apparent using simple SEM observation (Fig. 6.13c). Fourier transformation analysis of the SEM image, however, reveals that a periodicity exists in the etched structure of the sample. The insert in Fig. 6.13d shows the discrete Fourier transformation of the SEM image. It shows a defined and periodic point pattern along the horizontal direction. This pattern is related with the spacing of the pit zones which follows the line pattern imprinted by the laser. In the reciprocal space, line patterns are represented by points, which have a distance between them equal to the inverse of the pattern period ($1/d$). The corresponding radial power spectrum shows an inflection in the curve at about 0.23 1/µm (Fig. 6.13d). This first local maximum gives an estimation of the mean period spacing of the surface. The value of 0.23 1/µm corresponds very well to the inverse of the period used to structure the sample (d= 4.45 µm). This result indicates that the final etched microstructure is not completely random but that the etching process rather tends to follow the patterns generated by LIMET. In summary, not only the first stage of pit nucleation can be controlled using LIMET but also the final morphology of electrochemically etched samples.

CHAPTER 7

Effect of Pb and Cu on the pitting behaviour of aluminium foil

As it was mentioned above, the distribution of the pit initiation sites on aluminium has generally been improved by changing the chemical composition of the surface. The chemical surface modification is usually induced by segregation of some impurities at the surface of the specimen promoted by heat treatments (see also Sec. 3.3.1). In this work, the incorporation of small quantities of metals has been performed by means of the combined action of physical vapour deposition (PVD) and laser interference metallurgy (LIMET). The first section (Section 7.1) includes the structuring and etching of Pb/Al systems. Results about the laser structuring and chemical etching of Cu/Al systems are presented in the second part (Section 7.2) of this chapter. The influence of the layer thickness, laser fluence and period of the micro-structures was investigated. Finally, the modification of the etchability promoted by Pb and Cu on the aluminium surface is analysed and discussed.

7.1 Lead/aluminium systems

7.1.1 Characterisation of lead film deposited on Al substrate

Annealed aluminium samples were coated with thin lead layers by physical vapour deposition. Diverse deposition times were employed to produce different layer thicknesses: 2, 5, 7, 10, and 30 nm approximately. The surfaces of as-deposited Pb/Al systems were characterised by SEM and some results are shown in Fig. 7.1. As the layer thickness increases, the coating becomes denser. In order to facilitate the reading, the thickness of the lead layer will be hereafter written between parentheses beside the element symbol. In Pb(7)/Al (Fig. 7.1a, b), it was possible to observe one of the stages of coating growth. In this condition, the coating is composed of lead islands because the deposition time was not high enough to produce a dense layer. However, in Pb(10)/Al system, a completely different surface is revealed, as shown in Fig. 7.1c, d. The surface presents a more compact structure

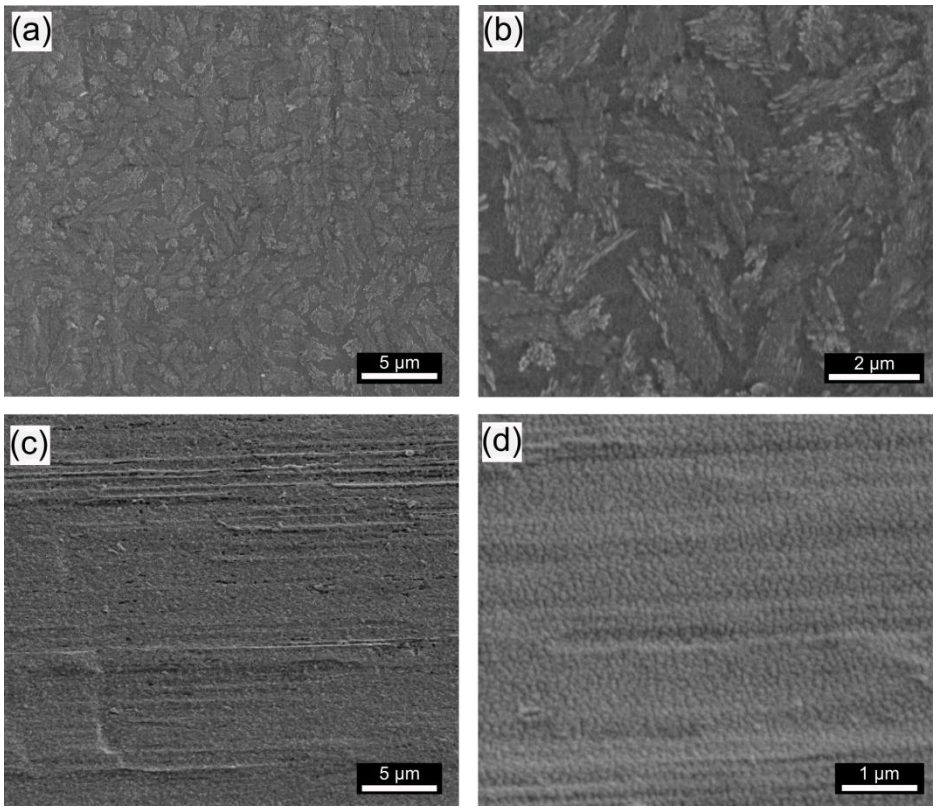

Figure 7.1. Morphology of lead layers deposited by PVD on annealed aluminium substrates. The lead layer thicknesses are: (a, b) 7 nm and (c, d) 10 nm. Tilt angle: (a, b) 0°and (c, d) 52°.

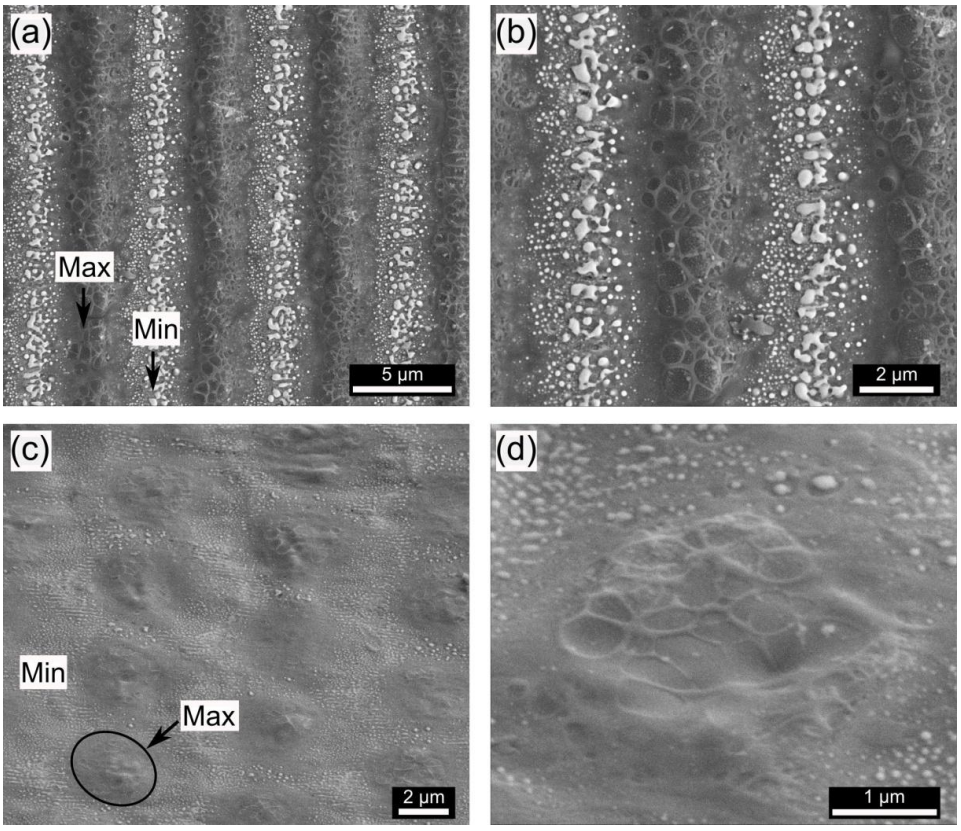

Figure 7.2. Periodic structure obtained on Pb(10)/Al using low laser fluence. (a, b) Line-like structure and (c, d) dot-like structure generated by using 1000 mJ/cm^2, and 683 mJ/cm^2, respectively.

where the typical “cauliflower” morphology of the PVD coatings is recognised. In magnified Fig. 7.1b, d, it is possible to see the details of the deposited layers. In the case of Al coated with a lead layer thickness of approximately 2 nm and 5 nm, the thin Pb layer present almost exactly the same topography as the substrate, which makes it difficult to be distinguished by simple SEM observations. On the other hand, Pb(30)/Al presented denser and more compact structures, similar to that found in Pb(10)/Al.

7.1.2 Structuring and etching of the surfaces

Pb/Al samples were irradiated with interfering laser beams using different fluences. Afterwards, the structured samples were chemically etched, varying the etching times. The 1N HCl solution at 85°C will be the etching conditions of consideration hereafter in this section.

The Pb(10)/Al surface morphologies formed with two- and three-beam interference at low laser fluences are illustrated in Fig. 7.2. The interference maxima (Max) and minima (Min) positions are indicated in the SEM images. Substantial changes in the lead profiles are observed at the interference maxima positions. At these fluence values aluminium and lead are molten and resolidified. The morphology of the etched samples examined in Fig. 7.2 did not lead to a control of the etching process (selective etching). Moreover, the chemical etching seems to be inhibited (see Appendix. D.1).

The line patterning of Pb(10)/Al obtained by using two-laser-beam interference and the subsequent surface etching are provided in Fig. 7.3. The SEM images presented in (Figs. 7.3a, c) indicate that at these fluences the micro-structures are not completely closed. The interference maxima and minima can be easily recognised as well as the displacement of molten material due to Marangoni convection (see also Chap. 5). Clearly, the structuring of Pb(10)/Al evidenced the melting of the lead layer at the interference minima (Figs. 7.3a, c).The SEM images of Fig. 7.3a, c reveal the open and scattered lead layer morphology after laser structuring. It is seen as white features at the interference minima. However, this behaviour was not found in all cases. Depending on the laser fluence and period of the structures, the lead layer at the interference minima may be melted or not. These both parameters influence the temperature distribution at the maximal and minimal interference zones.

The chemical etching results of the Pb(10)/Al examined in Fig. 7.3a, c are shown in Fig. 7.3b, d. The SEM images of the etched surface (Figs. 7.3b, d) revealed a preferential and selective etching at the maximal interference zones. Moreover, a large number of pits are generated homogeneously and regularly following the long-range order of the pattern

structures. It is important to point out that even at high laser fluences, the whole surface is etched (Fig. 7.4). The surface morphology of Pb(10)/Al structured at high laser fluences using two-laser-beam interference is shown in Fig. 7.4a. In this case, the line pattern is composed of closed and compact structures. The material bind coming from the two contiguous interference maxima can be recognised. It is seen as a fine line over the minimal interference positions. In Fig. 7.4b, the etched surface of Fig. 7.4a is presented demonstrating that the whole structured surface is etched.

Comparative studies were performed creating dot- and grid-like patterns on Pb(10)/Al in order to confirm the zones where the preferential etching takes place (Fig. 7.5). After structuring, the samples were etched under the same etching conditions as those used for Pb(10)/Al structured with line patterns. In Fig. 7.5a, one can observe the resolidified lead layer at the interference minima, while in Fig. 7.5c the lead layer remains unmodified at the minimal interference positions. This effect is related to the period and the laser fluence employed. Figures 7.5b, d show the surface morphology after etching of the samples presented in Fig.7.5a, c. The SEM images confirm that the preferential etching is performed at the maximal interference zones. In all cases, the pit arrays were arranged following the patterns generated by laser interference. Similar results were obtained by Pb(2)/Al, and Pb(5)/Al. However, the excessive load of Pb on Al may inhibit the controlled growth of the pits [123]. Indeed, in the case of Pb(30)/Al, longer etching times were required to achieve similar surface morphologies as Pb(10)/Al etched under the same conditions. It has to be emphasised that as the etching time increases the etched zones become more strongly etched, while the interference minima zones remain unetched. This behaviour is observed for low and moderated fluences were the structures are not yet closed. In the case of high fluence, where compact and closed structures are formed, the whole structured surface is etched and the resulting structure is intensified with the etching time. One should be aware that the tunnel growth cannot be achieved by simple chemical etching. It is only possible by means of electrochemical etching, where the tunnels can growth perpendicular to the surface ([100] direction).

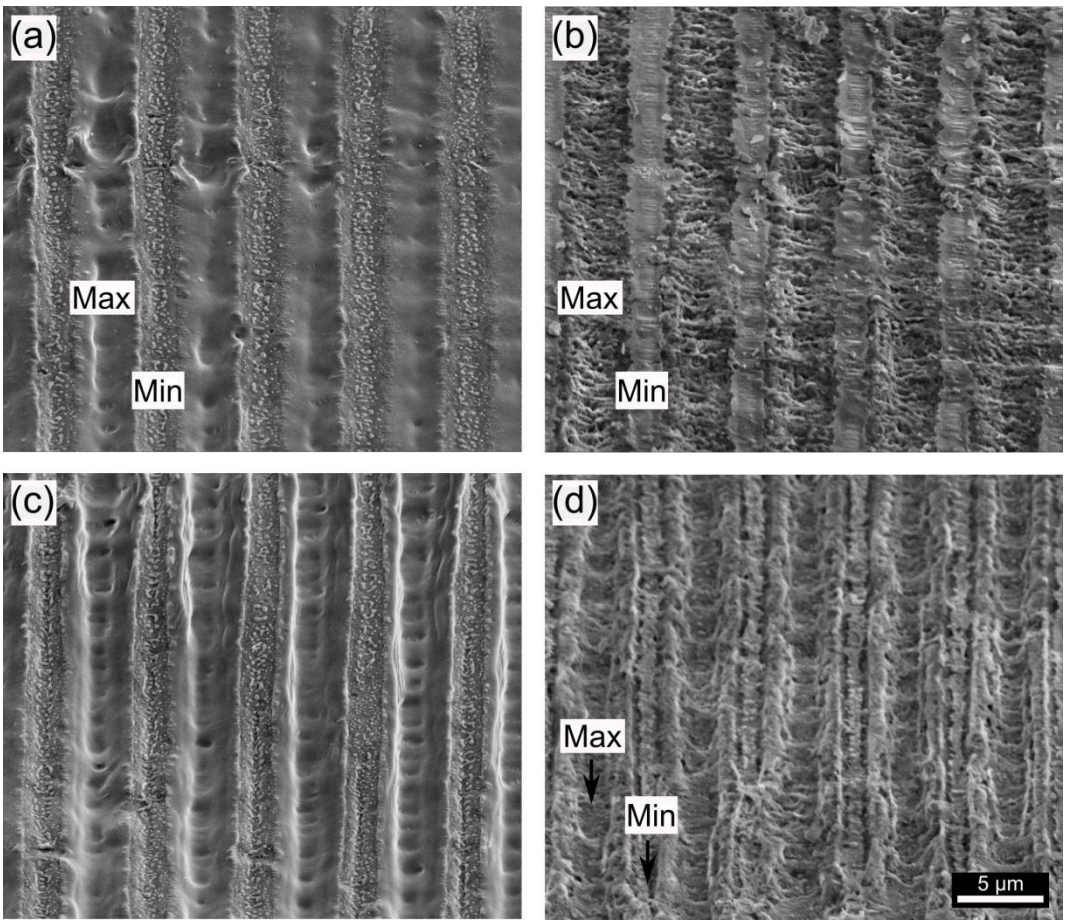

Figure 7.3. SEM images of Pb(10)/Al: (a, c) after laser structuring, and (b, d) their respective etched morphologies.The laser fluences used were (a, b) 1420 mJ/cm^2, and (c, d) 1650 mJ/cm^2. Period: 5.6 µm. Etching time: 15 s. All the images have the same magnification. Tilt angle: 52°.

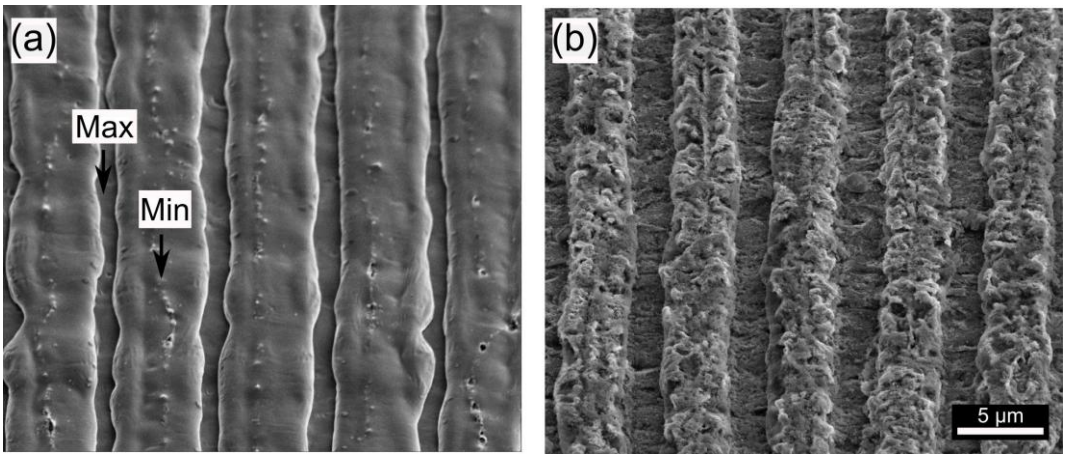

Figure 7.4. Periodic line-like patterning of Pb(10)/Al irradiated with 1910 mJ/cm^2 laser fluence: (a) morphology of the structured Al samples. Period: 5.6 µm; (b) sample etched using HCl solution at 85°C for 15 s. Tilt angle: 52°.

Figure 7.6 shows TEM micrographs of structured Pb(10)/Al using a laser fluence of 1600 mJ.cm^{-2}. The TEM lamella was prepared perpendicular to the line-like patterns (Fig. 7.6a). The presence of some lead nanoparticles (dark features) lying in the oxide–metal interface is revealed in Fig. 7.6b-d. The lead nanoparticles, down to ~ 10 nm diameter, are essentially concentrated toward the oxide side of the oxide metal interface. Close inspections of the TEM lamella (Fig. 7.6b, c) show that the lead nanoparticles form a continuous or semi-continuous Pb-containing film at the interface between the metal and the oxide along the whole structured aluminium surface. Likewise, the oxidation of aluminium substrate during laser structuring was reduced in comparison with the structuring of Al foil without the presence of lead.

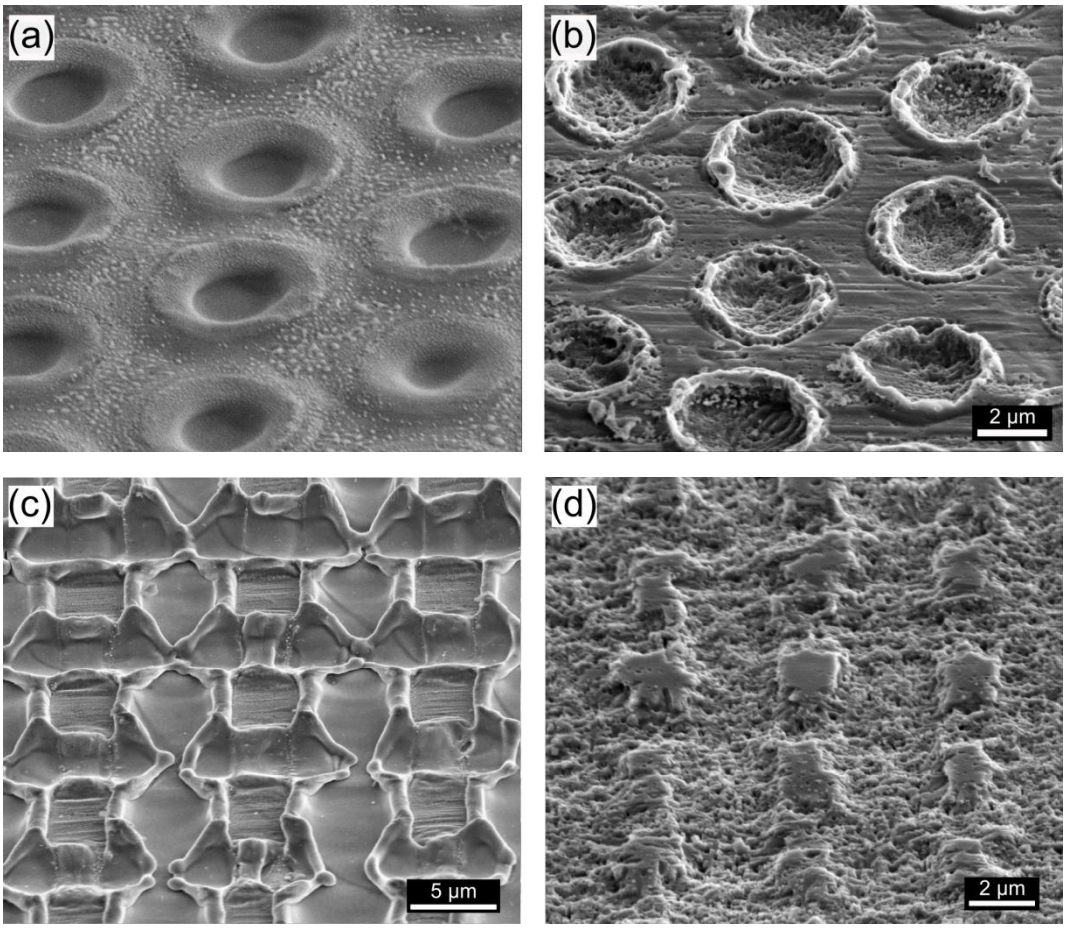

Figure 7.5. Periodic structures created on Pb/Al using: (a, b) three laser beams and a laser fluence of 1325 mJ/cm^2. Period: 5 µm, and (c, d) two laser beams and a laser fluence of 953 mJ/cm^2. Period: 10 µm. (b,d) SEM images of the etched surface. The images show a preferential etching at the maximal interference positions. Etching time: 15 s.

Coarse Pb particles can also be distinguished at the meeting position of the molten material coming from the two contiguous interference maxima (Fig. 7.6d). In this case, the Pb sizes were consistent with the original dimensions of as-deposited coating.

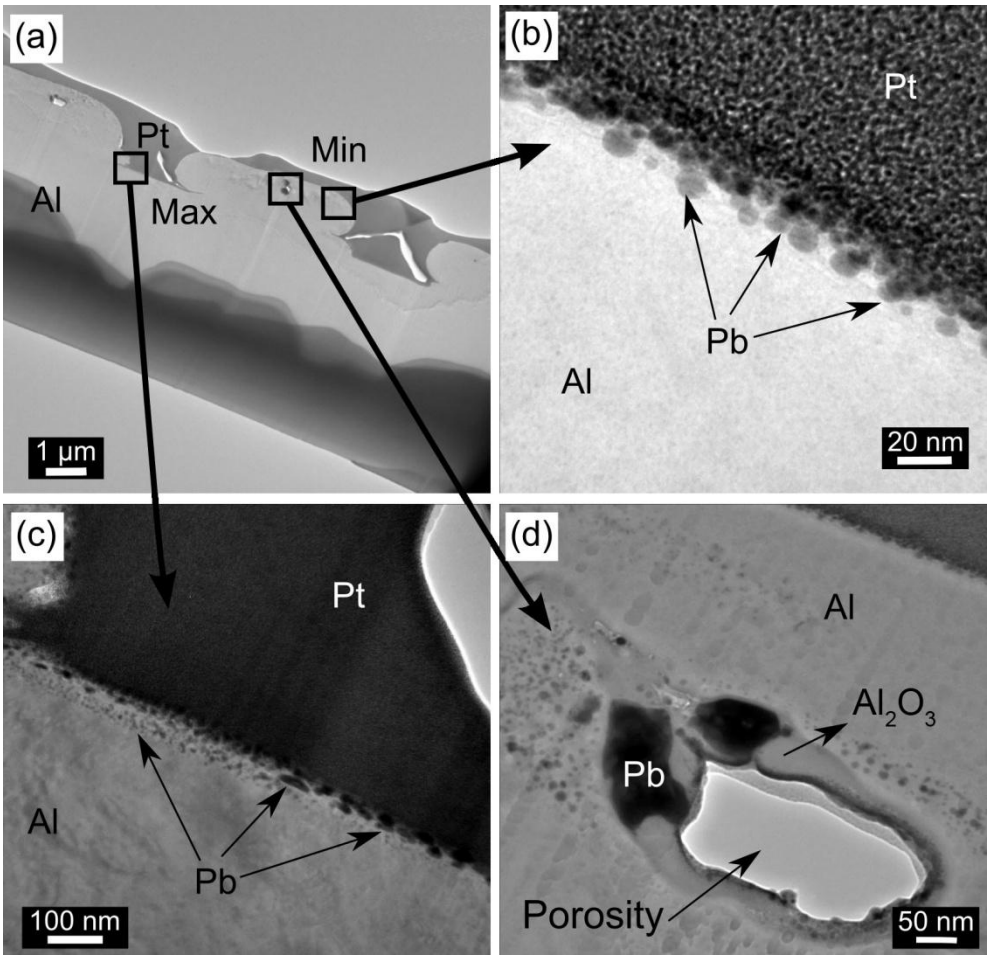

Figure 7.6. TEM images of Pb(10)/Al structured at 1600 mJ/cm^2. (a) TEM lamella overview, High magnification of the minimal (b) and the maximal (c) interference positions. (d) Enlargement of the minimal interference zone enclosed in (a). The images show the incorporation of lead nanoparticles preferentially at the metal–oxide interface.

7.1.3 Discussion

The above results show that the behaviour of the etching process totally changes with the presence of lead. As a matter of fact, incorporation of lead into Al substrate has led to a selective and localised etching behaviour at the maximal interference areas, *i.e.*, where Pb/Al samples were irradiated, while the non-irradiated zones remained un-etched. This behaviour is completely opposite to that found during the structuring of aluminium without the presence of lead (see Chapter 6). In this last case, the local etching was produced at the non-irradiated

zones, *i.e.*, minimal interference positions. Furthermore, lead addition strongly accelerated the etching of aluminium surfaces. The etching times used for structured Pb/Al were shorter in comparison to only irradiated aluminium to achieve similar etching morphologies.

Because the potential of lead is higher (cathodic) than that of aluminium (anodic), local cell formation between both these materials could explain the observed selective etching. In order to verify this hypothesis, Pb(7)/Al was structured using the adequate fluence values to produce only the ablation of the upper Pb(7) layer. The sample was irradiated using two laser beams obtaining a line-like structure whose period was 4.5 µm. The SEM image of the ablated surface is depicted in Fig. 7.7a. The removal of lead layer at the interference maxima position can be easily recognised. The EDS maps (line-scan map and area map) confirm the periodic ablation of the upper Pb layer (Fig. 7.7 b, c). Thus, the sample is composed of a periodic distribution of elemental Al and Pb. A SEM image of the etched surface examined in Fig. 7.7a is provided in Fig. 7.7d. One can see that the initial etch pits do not have a preferential zone and they follow more or less the rolling line direction of the Al substrate. We can conclude that the selective etching could not be associated to the presence of Pb on the surface of the sample producing a local galvanic cell between both materials. However, as aluminium has a high reactivity with oxygen, the laser radiation could activate the local oxidation (very thin oxide layers) at the interference maxima positions (where the ablation took place) chemically stabilising these zones. This effect cannot be determined by simple EDS analyses due to its low limitation in the sensitivity and spatial resolution. With the finality to clarify this important point, ordered Pb arrays were also formed using a grid mask during PVD deposition. A SEM image of the coated Al samples is shown in Fig. 7.8a. It is possible to see a small amount of Pb(10) periodically deposited on Al surface. After that, the chemical etching was performed using an etching time of 40 s. In this case, the preferential and selective etching was not achieved (Fig. 7.8b). This result was consistent with the fact that not only the presence of Pb on Al surface can explain the selective etching behaviour of Pb/Al samples.

On the other hand, Pb/Al samples structured with lower fluence values (*i.e.*, where aluminium substrate starts to melt) seem not to significantly improve the etching process. Because the mutual solubility of lead on aluminium is negligibly small even in liquid phase (Pb and Al are practically immiscible [190], see Appendix D.2) and have very different densities, heavy segregation can be expected during the solidification.

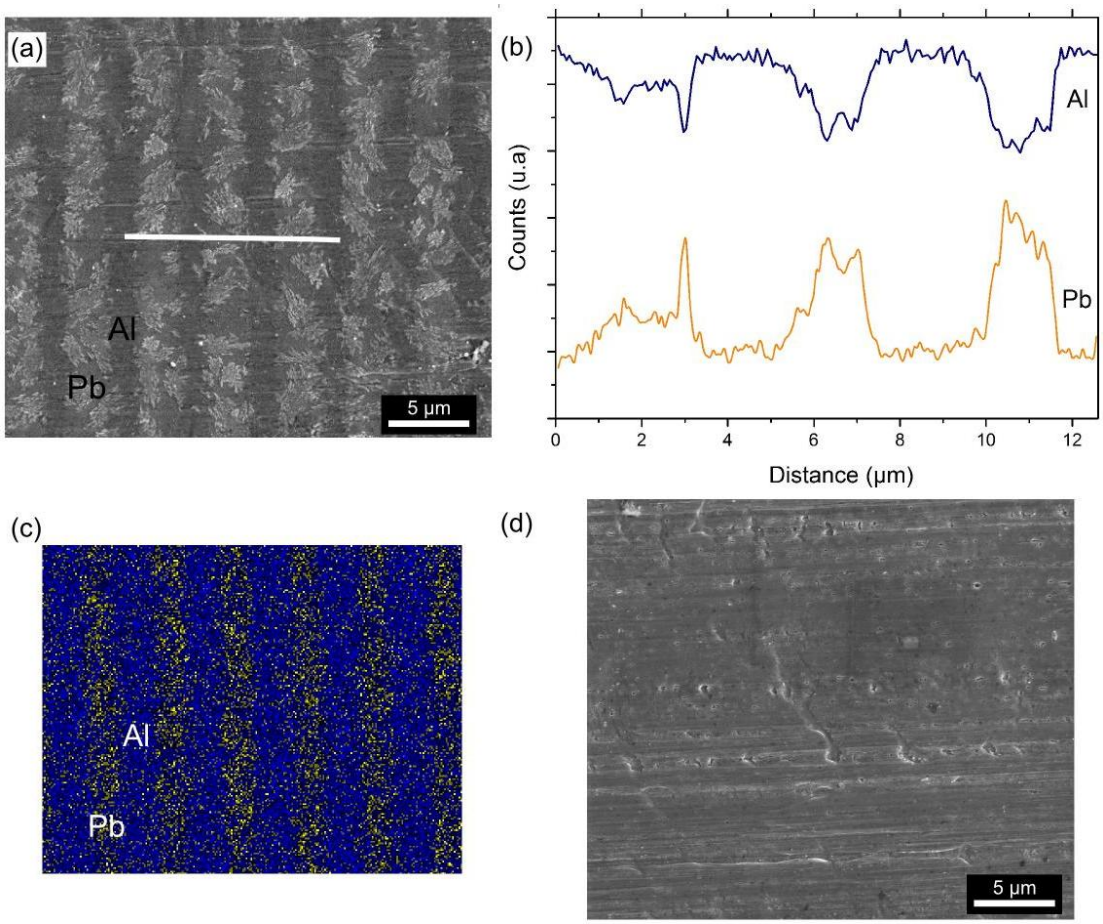

Figure 7.7. Pb(7)/Al sample structured at 622 mJ/cm^2. (a) SEM image, (b) EDS line-scan of the sample showing three interference maxima, (c) EDS mapping overlap of the elements Al and Pb, and (d) SEM morphology of the structured sample showed in (a), etched with 1N HCl etchant at 85°C during 30 s.

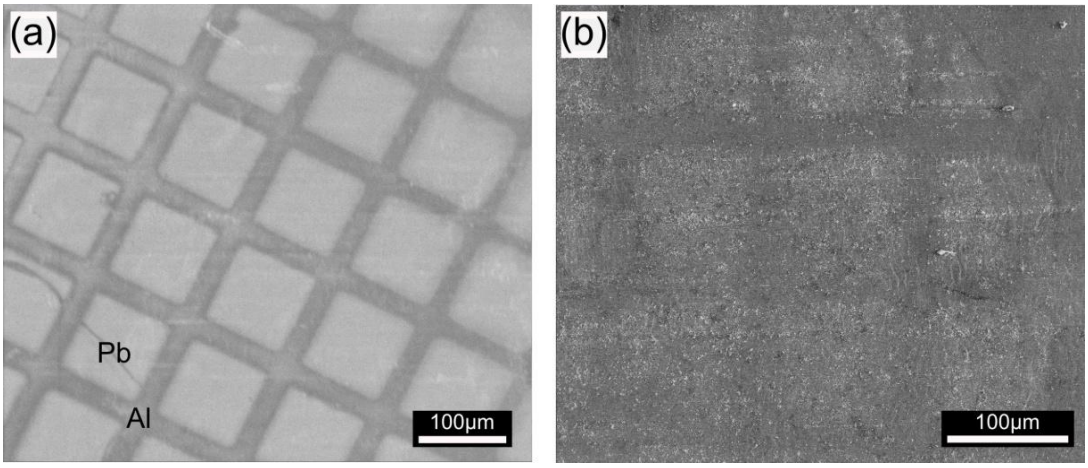

Figure 7.8. SEM images of Al foil coated with Pb(10 nm) layer using a mask with hole array pattern. (a) As-deposited morphology, and (b) chemically etched with 1 N HCl at 85 °C for 40 s.

This segregation may explain the cell-like structures found at the maxima positions in Fig. 7.2. Cellular array morphology [191] has also been observed in Pb-Sn alloy single-crystal samples directionally solidified along [100] direction. In the case of Pb-Sn alloy the cellular array comes from the density inversion occurring in the melt which induces convection and finally produces macro-segregation along the growth direction. During Pb/Al solidification, the aluminium solid grains would nucleate first and grow with lead-rich liquid afterwards [192]. In this condition, it is possible that the Pb particles are not in direct contact with aluminium metal.

The above-mentioned segregation can be overcome if the molten Pb/Al is rapidly solidified. Using higher laser fluences, rapid solidification can be achieved which lead to nano-sized inclusions of Pb in aluminium (Fig. 7.6). This phenomenon has also been found in earlier works [193, 194]. Some authors claim that the shape, size and orientation of the Pb inclusions in the grain boundaries depend on the orientation of the aluminium grain boundary plane. Moreover, the average size of lead inclusions formed in the grain boundaries is about twice as large as the average size of the inclusions formed in the interior of the grains [194]. The size of the inclusions presented after the structuring of Pb/Al (Fig. 7.6) are in good agreement with earlier observations for inclusion formed inside the grain in lead-implanted aluminium [194]. In this PhD thesis, the lead incorporation into aluminium foil was mainly assisted by laser interference. Because the main mechanism to create micro-structures is the surface-tension gradient induced by lateral variations of the temperature (Marangoni convection, see Chap. 5), it promotes the incorporation of lead particles in aluminium foil.

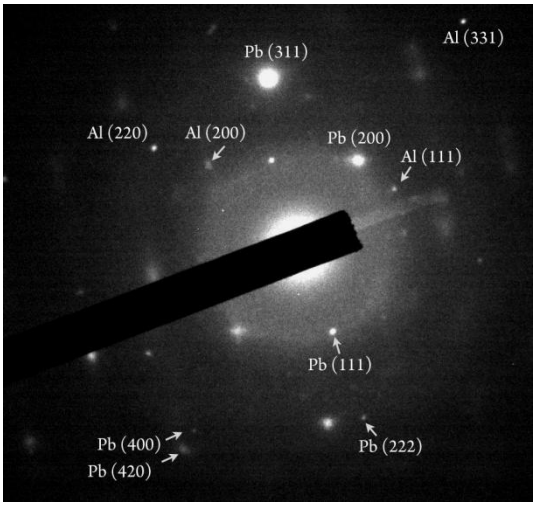

Figure 7.9. Selected area difraction patterns of irradiated Pb(10)/Al of Fig. 7.6 showing metallic Al and Pb elements.

The selected area diffraction pattern, corresponding to the TEM foil of Fig. 7.6, is shown in Fig. 7.9. It reveals that the Pb particles are not oxidised during laser treatment.

Therefore, after structuring of Pb(10)/Al, the substrate surface is composed of nano-film of metallic Pb nanoparticles which remain in contact with the metallic aluminium surface.

Knowing the etching behaviour of the Pb/Al samples structured at different laser fluences (Figs. 7.3-7.5 and App. D.1), one can conclude that the selective etching takes place only when the Pb particles are in contact with aluminium metal (Fig. 7.6). The nonwetting Pb nanoparticles did not contribute to the selective etching of the specimens (Figs. 7.2, 7.7-7.8 and App. D.1). Moreover, the direct contact of Pb particles with Al metal along the whole sample surface is attained when the laser fluence used is enough to produce closed structures. This result confirms the SEM observations presented in Fig. 7.4: at high laser fluences (*i.e.*, where closed structures are formed), the whole irradiated surface is etched.

Investigations of the electrochemical behaviour were also performed. The anodic polarisation method involves changing the potential of the total surface. It cannot provide information about the local potential differences between the maximal and minimal interference positions, reason why the study of Pb/Al samples structured at low laser fluences will not lead to reliable results. Therefore, as-received annealed Al foil and irradiated Pb(10)/Al using high laser fluence were the specimen conditions investigated. The Pb(10)/Al samples were structured by using two laser beams, 5 µm period and a laser fluence of 1850 $mJ.cm^{-2}$ approximately. Anodic polarisation curves for Al and Pb(10)/Al samples in 1 N HCl solution, shown in Fig. 7.10, indicate that Pb(10)/Al is activated, as characterised by a significant negative shift of the pitting potential (–0.99 V_{SCE}) relative to the pitting potential at –0.830 V_{SCE} of pure aluminium. These values are consistent with others reported in the literature. Depending on the annealing temperature, the pitting potential value of as-received aluminium can vary, which is related to the enrichment of the trace element Pb during the heat treatment [195].

Normally, the enrichment of Pb at the aluminium surface promoted by heat treatment also causes a significant electrochemical activation of the surface when is exposed to chloride solution [195, 196]. According to the above results, one can assume that the activation of aluminium surface by Pb requires: (i) enrichment of the surface by metallic lead, in the form of a thin nano-film distribution along the whole irradiated surface, (ii) the wetting (or metallic contact) between the enriched Pb particles and aluminium metal and (iii) passivity breakdown of the Al oxide film caused by the surface enrichment with Pb nanoparticles. These requirements combined with the synergetic destabilising role of chloride ions (Cl^-) in the solution lead to the surface activation of aluminium surface.

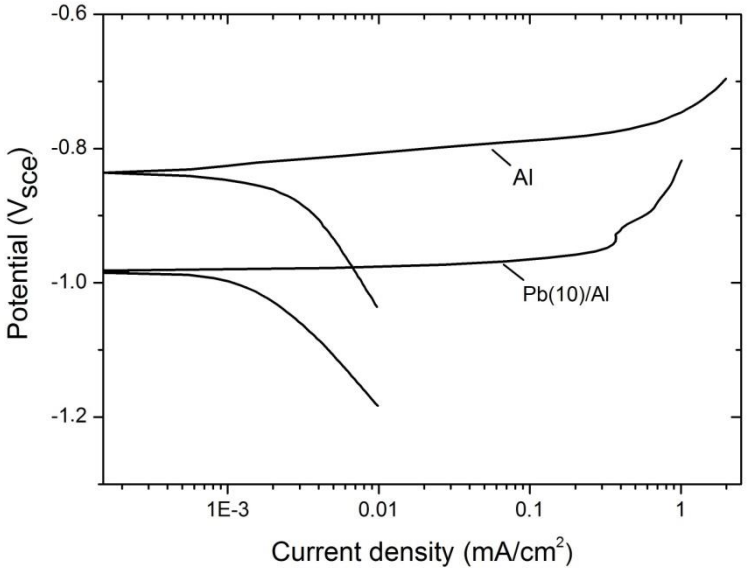

Figure 7.10. Polarisation data of as-received Al foil and structured Pb(10)/Al samples in 1N HCl solution at 25°C.

The role of chloride must be similar to its significance in localised corrosion. It takes part in the further destruction of the oxide film, whose passivating properties were reduced by the presence of underlying Pb nanoparticles, giving rise to enhanced dissolution of aluminium [196].

The surface activation of aluminium by the combined action of Pb and laser irradiation is consistent with the aluminium activation found in the literature by using heat treatment to segregate lead impurities. One should be aware that for structured Pb(10)/Al, the precise location and distribution of Pb nanoparticles is revealed *i.e.*, most lead nanoparticles are placed at the oxide–metal interface, as demonstrated in Fig. 7.6. Therefore, these results could be used to predict the location of segregated Pb nanoparticles, disclosing the controversy existing in the literature [109, 112, 115, 124].

Several reports have found that the lead content has important influence on the morphology of the etched tunnels. By increasing the amount of Pb some of the etched tunnels tend to combine together and have different orientations, which can reduce the etched surface as well as the capacitance [123].

7.2 Copper/aluminium systems

In order to understand the role of copper in the site-controlled formation of tunnel pits, annealed Al foil was coated with thin copper films by physical vapour deposition. The coating conditions were similar than those used during the coating of aluminium with lead. The sputter time was changed to produce copper films with different thickness: 2, 5, 7, and 10 nm.

After Cu deposition, Cu/Al samples were structured using different laser configuration and laser fluences. The morphology evolution of Cu(10)/Al depending on the laser fluence is illustrated in Fig. 7.11. In this case, the samples were structured using two laser beams and a period of 10 µm. At low laser fluence, the ablation or local removal of the upper Cu film is performed (see Fig. 7.11a). However, as the fluence further increases, the flow of molten material from the interference maxima towards the interference minima is easily recognised (Marangoni convection), as demonstrated in Fig. 7.11b-c. It is also possible to observe that using large period (d= 10 µm), the minimal interference positions are not completely molten. As is shown in Fig. 7.11c, the non-irradiated zones are wrapped up with the molten material coming from the two neighbouring maximal interference zones, and finally using higher laser fluences compact structures can be formed (Fig. 7.11d). This structuring mechanism assures the ordered copper ablation at the Al surface and/or its incorporation into aluminium foil depending on the laser energy density employed.

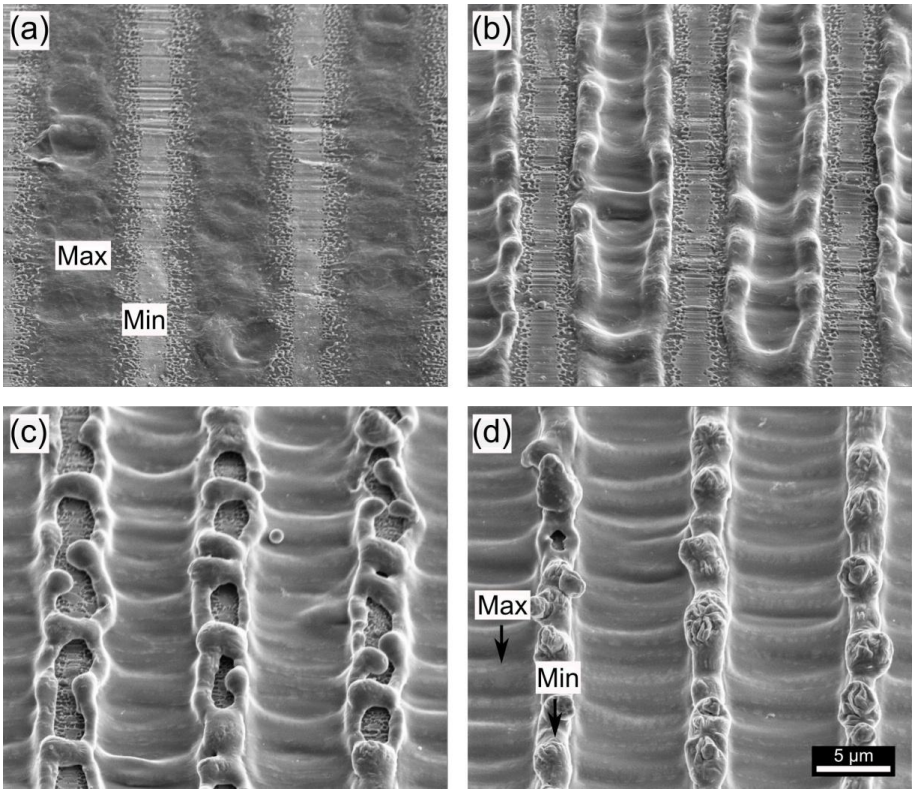

Figure 7.11. Morphology of Cu(10)/Al showing the line-like structures formation as a function of laser fluence: (a) 650 mJ/cm^2, (b) 780 mJ/cm^2, (c) 920 mJ/cm^2, and (d) 1100 mJ/cm^2. Period: 10 µm. All the images have the same magnification. Tilt angle: 52°.

The morphology of the line- and dot-like patterns created at low laser fluences on Cu(10)/Al (before etching process) are presented in Fig. 7.12. In this figure, the copper placed at the

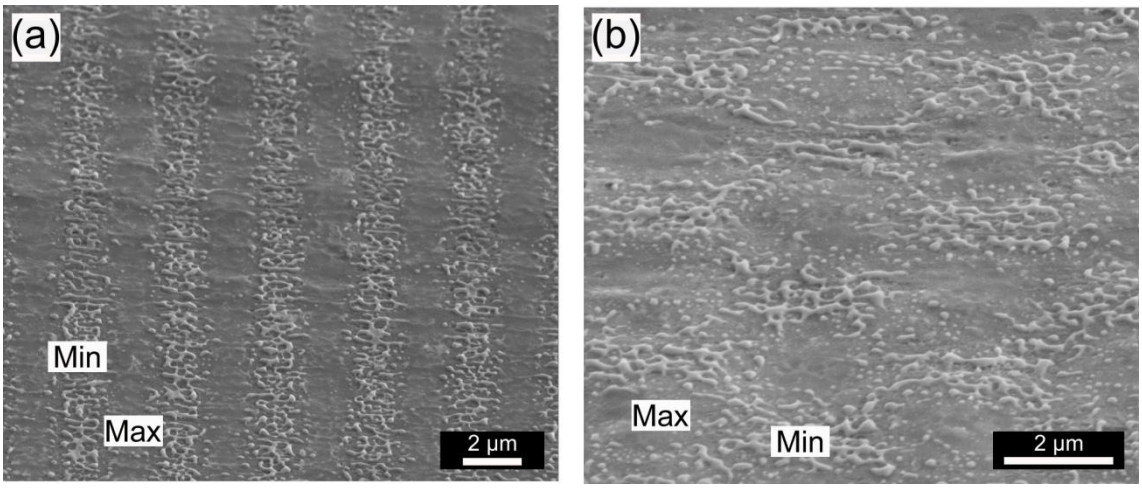

Figure 7.12. SEM morphology of Cu(10)/Al samples structured with: (a) two laser beams at a fluence of 400 mJ/cm^2. Period: 3.3 µm, (b) three laser beams producing a dot-like pattern. Laser fluence used: 644 mJ/cm^2.

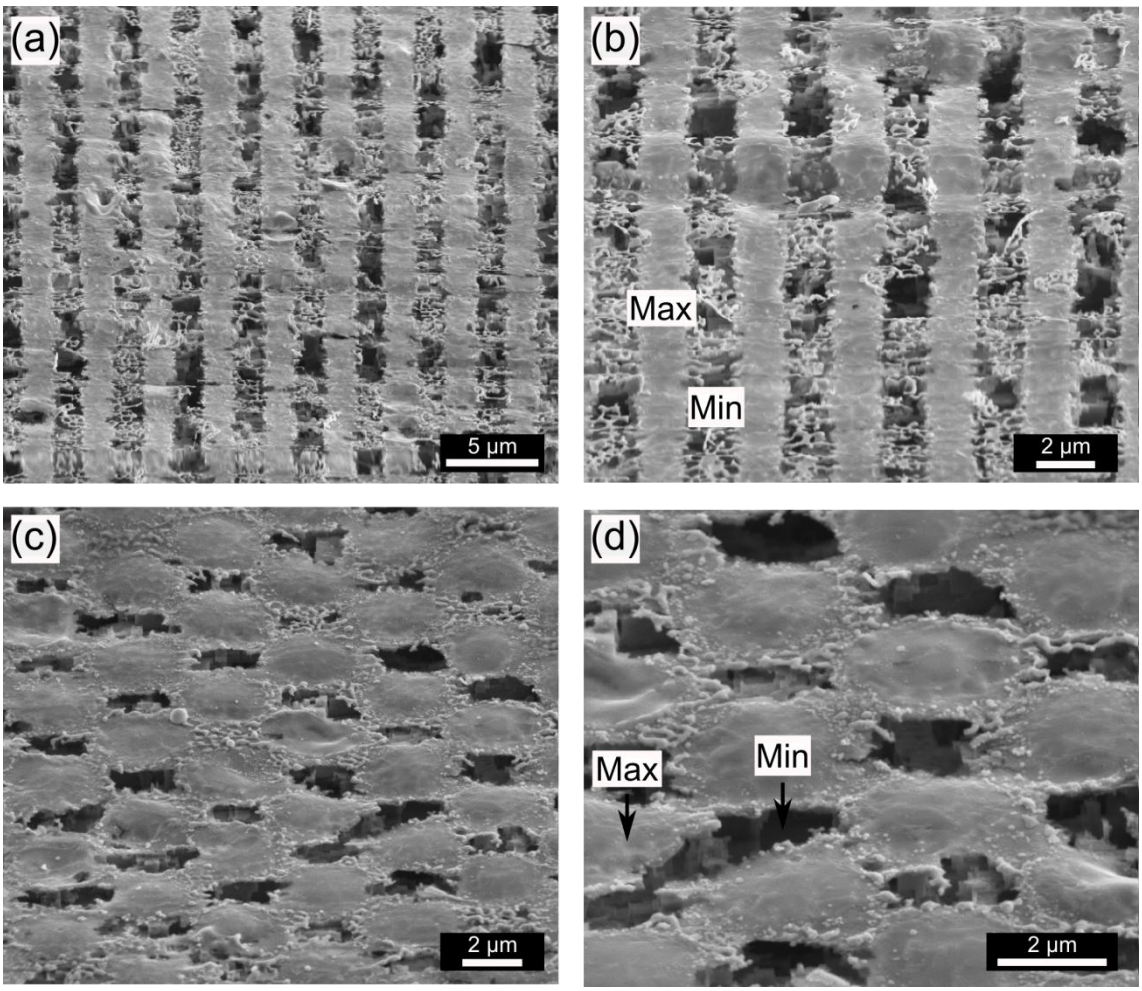

Figure 7.13. SEM images of etched Cu(10)/Al after laser structuring using: (a, b) two interfering laser beams, laser fluence of 400 mJ/cm^2. Period: 3.3 µm. (b) High magnification of image (a); (c, d) Three-laser-beam interference and 644 mJ/cm^2 laser fluence.(d) High magnification of image (c). Etching time: 2 s. Tilt angle: 52°.

minimal interference positions shows an open morphology demonstrating that in these conditions the Cu layer was molten and resolidified. After laser structuring, the patterned Cu/Al samples were chemically etched in 1N HCl solution at 85°C. The morphology of the etched samples examined in Fig. 7.12 is presented in Fig. 7.13. The SEM images indicate a preferential and localised etching behaviour which follows the ordered array imprinted by laser interference.

The preferential etching occurs at the minimal interference areas *i.e.*, the non-irradiated zones where the Cu remains, while the irradiated area or maximal interference positions remain unetched, at least at the beginning of the etching process. It has to be emphasised that the etching times were considerably shorter than those used during the etching of structured Al foil and Pb/Al samples and even as-received annealed aluminium foil, for obtaining similar results. By using etching times as short as 10 s, etched morphologies similar to those found during electrochemical etching are obtained (Fig. 7.14).

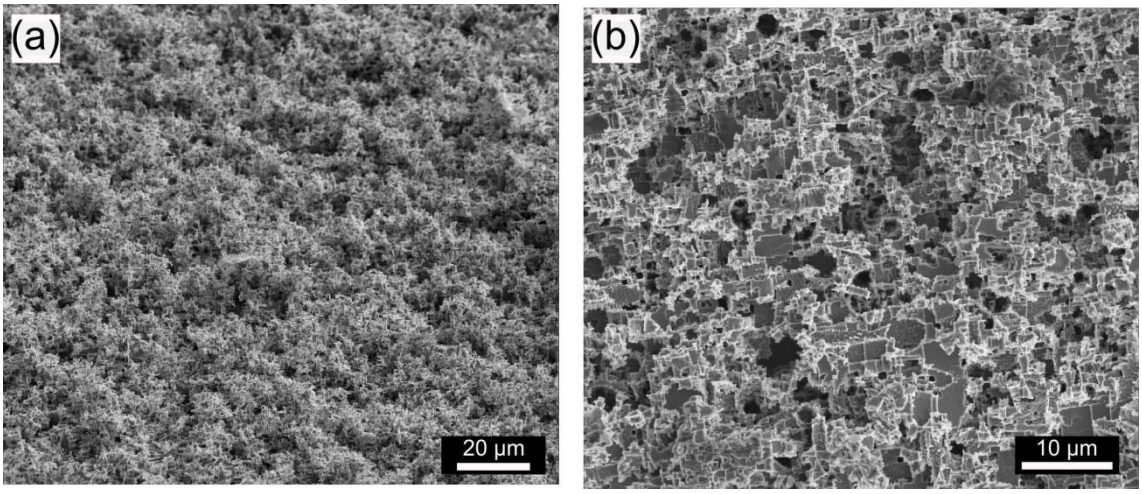

Figure 7.14. Etched surface morphology of Cu(10)/Al structured with: (a) line-like pattern, laser fluence: 780 mJ/cm^2 and period:10 µm. Tilt angle: 52°; (b) dot-like pattern using a laser fluence of 710 mJ/cm^2. Tilt angle: 0°.

Nevertheless, it was not possible to achieve selective etching when compact and closed structures were formed (Fig. 7.11d). The structuring of Cu/Al samples using high laser fluence did not produce a control of the etching process. In fact, the samples were not etched at all (see App. D.3). Since the results of Cu/Al with 2, 5, and 7 nm copper thickness were very similar, only those related to Cu(10)/Al were reported here.

Figure 7.15 shows TEM micrographs of Cu(10)/Al structured with two laser beams and a period of 3.3 µm. The morphology of the sample under study is very similar to the SEM image of Fig.7.12a. At the maximal interference positions the thin copper layer is ablated

while at the energy minima resolidified Cu is presented. In Fig. 7.15b, some copper inclusions inside of aluminium are observed beside a very thin aluminium oxide layer. This result demonstrates that not only the ablation of copper occurs at the maxima positions but also the local melting of aluminium, using the laser condition previously reported. On the other hand, at the minimal interference position, Fig. 7.15c, copper nanoparticles remain at the surface of the aluminium foil, above the pristine aluminium oxide layer.

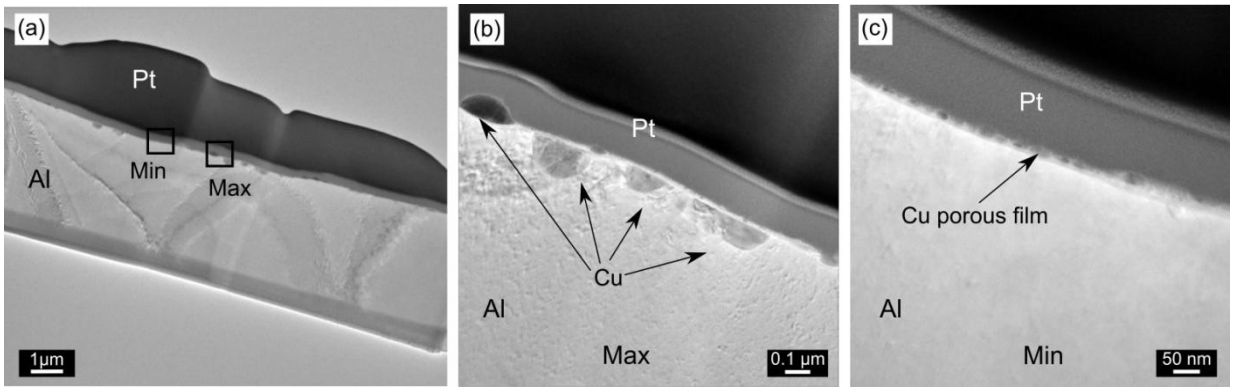

Figure 7.15. TEM images of Cu(10)/Al structured with two laser beams using a laser fluences of 470 mJ/cm^2. (a) TEM lamella overview, (b, c) high magnification of the interference maxima and minima positions, respectively. Pattern period: 3.3 µm.

7.2.1 Discussion

Although the enrichment of the aluminium surface with Pb nanoparticles produced anodic activation of the surface, this mechanism cannot explain the selective etching observed after copper addition. As a matter of fact, copper incorporation into aluminium promoted by laser irradiation (using high laser fluences) did not lead to an enhancement of the etching process (App. D.3). However, the presence of a small amount of copper on aluminium markedly improved the control and even the growth of tunnel pits during the chemical etching (Fig. 7.13 and Fig. 7.14).

Depending on the laser fluence and period used, the Cu located at the minimal interference positions showed different morphologies (see Figs. 7.11 and 7.12). The EDS analysis of structured Cu(10)/Al depicts in Fig. 7.16a, gives evidence of the Al and Cu distribution after laser irradiation by using low laser fluences. The open and discontinuous morphology of copper at the non-irradiated areas can be easily recognised, in accordance with results shown in Fig. 7.12. It has to be emphasised that as-deposited Cu films, which were effective for the production of site-controlled tunnel pits, presented a discontinuous (or

interrupted) morphology due to their nominal layer thicknesses: 2, 5, 7 and 10 nm. Nevertheless, the melting and later re-solidification of the upper copper film induced by laser enlarge these discontinuities.

The distribution of copper after laser structuring was investigated by TEM, as shown in Fig. 7.15. The presence of some Cu inclusions and the formation of a very thin oxide layer at the maximal interference positions were demonstrated, while at the minimal interference zones the porous and resolidified Cu layer was observed. It denotes that at this low fluence value not only the local ablation of Cu film is obtained but also the slight melting of aluminium, which lead to the incorporation of some Cu inclusions and the formation of a thin oxide film at the maximal interference positions.

The morphology of structured and etched Cu(10)/Al samples presented in Fig. 7.13 shows that the preferential and selective etching starts at the minimal interference zones *i.e.*, where the discontinuous Cu layer remains, while the irradiated areas stay unetched. However, as the etching time increases both zones are etched forming tunnel pits with high aspect ratios, even by chemical etching (see Fig. 7.14). It has to be highlighted that with this kind of aluminium foil it is not possible to create (by simple chemical etching) the tunnel morphology produced by the electrochemical process. However, the Cu addition generated tunnel pits with sufficiently high aspect ratios and also allowed the uniform development of pits following the patterns formed by laser interference.

On the basis of the results above one can conclude that the mechanism by which copper induced the uniform development of tunnel pits on aluminium is due to localised galvanic corrosion. It is well-known that an electrochemical potential almost always exists between two dissimilar metals when they are immersed in a conductive solution. Since the potentials of aluminium and copper are very different, local micro-cells can be formed during the etching of structured Cu/Al. As the potential of copper is much higher than that of aluminium, Cu acts as a cathode and aluminium as an anode. Corrosion potentials of copper metals generally range from −0.2 V to −0.4 V when are measured against a saturated calomel electrode (SCE); while the potential of pure copper is about −0.3 V [197]. The contact between aluminium and copper leads to the corrosion of the more anodic metal, in this case aluminium. As one can see from Fig. 7.13, the galvanic cells are not formed between the interference maxima and minima positions but rather between the discontinuous copper and exposed aluminium at the minimal interference zones. The above etching behaviour is also demonstrated by the etching of Cu(10)/Al with dot-like patterns (Fig. 7.13c, d), where the

local etching initiates at the minimal interference zones. In magnified Fig. 7.13b, it is possible to see that the interference minima positions consist of unetched copper films, which cover the etched aluminium areas. These results are confirmed by EDS observations of structured and etched Cu(10)/Al samples (Fig. 7.16b): the selective etching starts by the dissolution of non-irradiated aluminium due to the formation of galvanic micro-cells between Al and Cu at the minimal interference zones. The porous copper film remains unchanged over the etched aluminium surfaces.

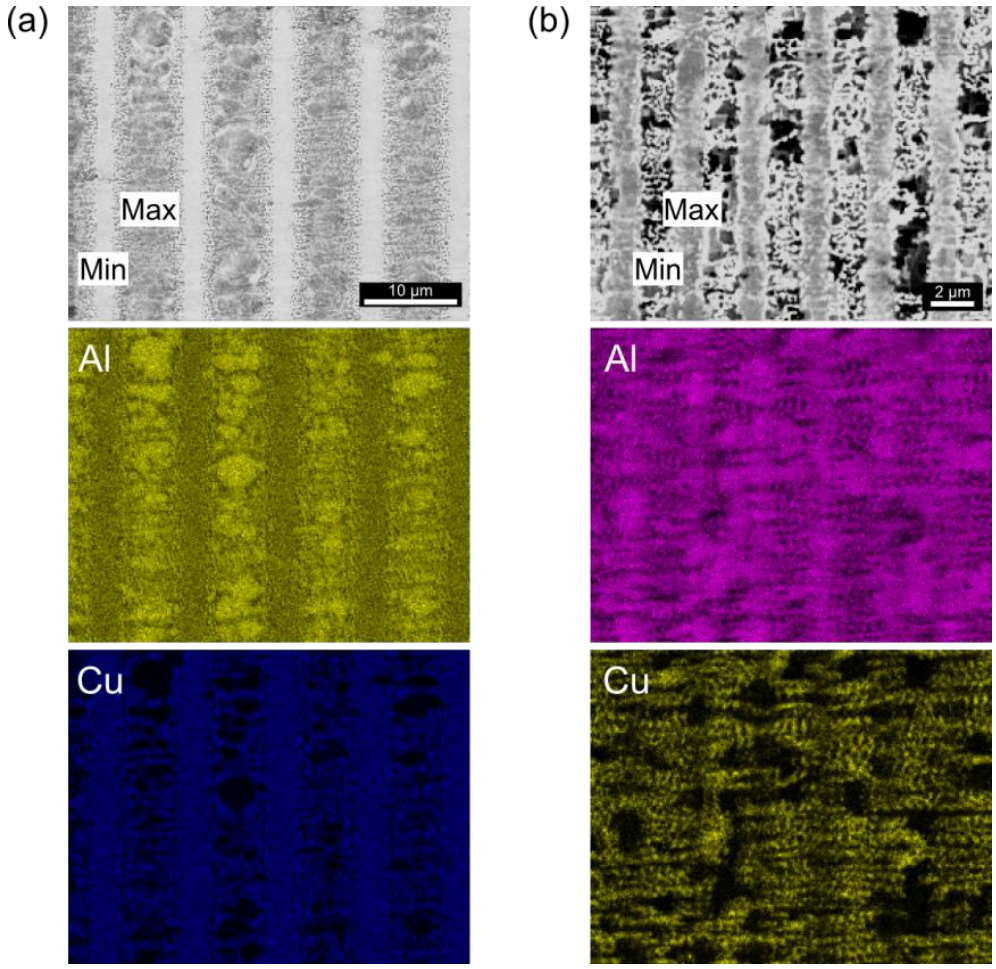

Figure 7.16. SEM images and EDS maps of the elements Al and Cu of Cu(10)/Al samples: (a) structured by using two laser beams, 10 µm period and 650 mJ/cm^2 laser fluence; (b) Structured and etched morphology. Structuring conditions: line-like pattern, period:3.3 µm and 400 mJ/cm^2. Chemical etching was conducted in 1N HCl solution at 85°C for 2 s.

On the other hand, at the beginning of the chemical etching the maximal interference zones are stabilised by a thin aluminium oxide formed during the ablation of the upper Cu layer, which enhances the chemical stability of these areas. As it was previously reported (see Chap. 5) the oxide layers built up by laser irradiation are very stable, coherent and generally are characterised by having low concentration of defects. Those results are consistent with

others in the literature which claim that the passivation of aluminium can provide protection against pitting corrosion induced by copper and chloride [198]. Furthermore, the presence of some Cu inclusions at the irradiated zones can modifiy the corrosion potential of aluminium shifting to the nobler direction with respect to the corrosion potential of pure aluminium [198, 199]. As a consequence, the pit-sites start at the interference minima where the etching of exposed and non-irradiated aluminium takes place. It has to be emphasised that the preferential etching starts at the minimal interference positions and then spreads over the maximal interference zones as the etching time increases (Fig. 7.14).

The selective etching of Cu/Al samples was achieved when copper was in contact with non-irradiated aluminium surface *i.e.*, at the minimal interference positions. The introduction of Cu element in aluminium foil did not enhance the etching process (App. D.3). The etching behaviour observed denotes that Cu is not an anodic activator of aluminium but rather induces the development of the tunnel pits on aluminium foil due to localised galvanic corrosion. Moreover, during the ablation of the upper Cu layer the zones of maximal interference were more chemically stable due to the formation of a thin oxide layer and introduction of some Cu inclusions. According to these results, it is also possible to predict that only the load of a small amount of Cu on the Al foil in an ordered way (*e.g.*, using a patterned mask during PVD deposition) could lead to the site-controlled formation of the tunnel pits. In this last case, the galvanic cells will be formed between the Cu-deposited areas and uncoated aluminium zones.

However, the role of copper during the conventional process of high-voltage capacitors, *i.e.*, heat treatment of aluminium foils, is completely different. In this case, copper element is presented at very low concentrations (ppm) in aluminium foil. Recently, studies report that copper appears to play a less direct role in the initiation of tunnel etching and that its distribution does not change after heat treatment *i.e.*, the enrichment of the surface with copper promoted by heat treatment is negligible. Nevertheless, it has been seen that the trace of copper can modify the cellular boundaries of aluminium foil, which may be preferred paths for diffusion of lead impurities, and hence, possibly also the lead distribution. Furthermore, some research reports that copper may influence the growth of tunnels, including tunnel widening [124, 200].

CHAPTER 8

3D characterisation of etching structures

This part of the work will focus on the three-dimensional characterisation of the tunnel morphology. FIB tomography was accomplished in the etching structures obtained by electrochemical etching performed by Becromal S.p.A. The specimens under study consisted of as-received annealed Al foil and laser structured Pb(10)/Al samples. The purpose of this study is to gain reliable quantitative information about the complex tunnel structures and at the same time to analyse the influence of lead element on the tunnel formation.

8.1 FIB nanotomography applied to the tunnel structures

Besides the difficulties to obtain the suitable tunnel etching distribution, another complication is finding a suitable technique to characterise it. Several reports adopted the replica technique as a solution. In this technique, the replicated oxide structures of tunnels are formed by anodisation of the sample and the subsequent selective dissolution of Al in an adequate saturated acid [109, 123, 134, 201, 202].

Although surface replication can be accomplished effortlessly and made possible the research of the etching morphology in the depth direction, this method is indirect, *i.e.*, requires a deep understanding of the chemical etching leading to the surface topography eventually imaged. Additionally, the technique presents multiple steps in between which lead to unavoidable loss of information, in particular if the feature sizes approach to the nano/micro scale. Other drawbacks of this anodising technique is that the initial morphology of the etch pits or the tunnels may not be retained because the density of aluminium is different from that of aluminium oxide, and also sharp corners tend to become blunted. Moreover, it does not bring the possibility of statistic analyses of the etched tunnels.

In this work, a new method has been developed for the direct characterisation of tunnel morphology obtained by electrochemical etching of aluminium. The investigation was performed using focused ion beam (FIB) tomography [140-142]. In general, FIB tomography reveals internal structural information within an object reconstructing it mathematically from a series of projects (see also Sec. 4.4.2.5).

8.1.1 Sample and cube preparation

The first challenge associated with tunnel characterisation is finding a correct sample preparation method to ensure the preservation of the original tunnel morphology and to obtain a series of images with the suitable contrast for the 3D reconstruction.

In a first attempt, the zone to be characterised was selected by simple cutting process of electrochemical etched Al foil. The corresponding cross section is shown in Fig. 8.1. It can be seen that the distribution and depth of the tunnels are not homogenous around the whole etched surface (Fig. 8.1a). Moreover, during the cutting process a deformation of the tunnel structures was produced (Fig. 8.1b). The black arrow presented in Fig. 8.1b indicates the direction of this deformation. In general, the tunnels grow perpendicular to the Al surface following the [100] direction, however, it is easy recognise the tilt of the tunnels with respect to the aluminium core, which evidenced the distortion of the tunnel structures induced during the cut of the sample. Further, the contrast between the tunnel pits and the aluminium matrix is not enough for the segmentation and later reconstruction of the tunnel morphology (see App. E.1).

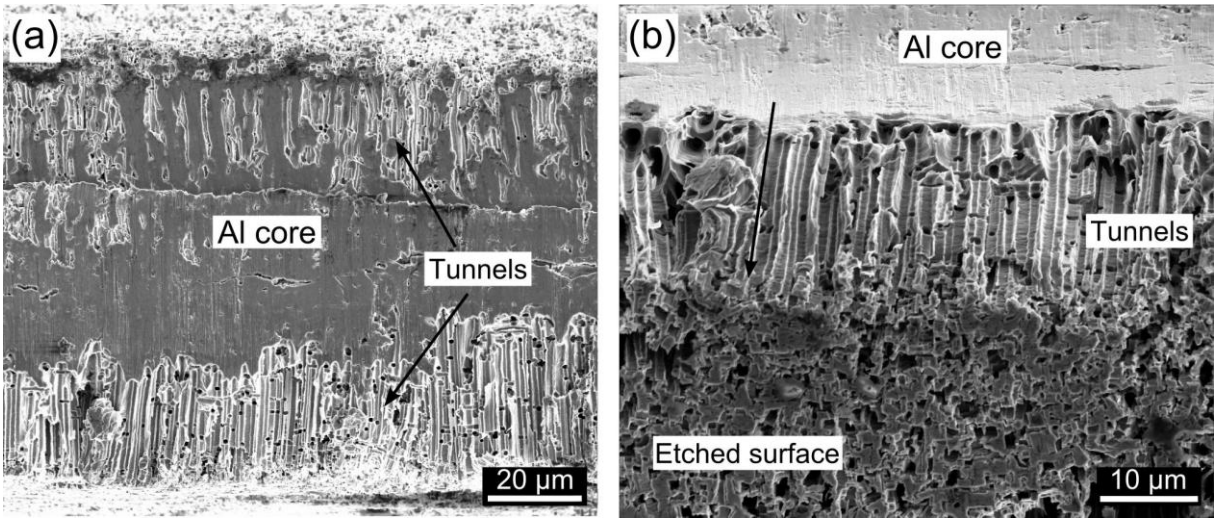

Figure 8.1. SEM image of the cross section realised by simple cutting of etched Al foil showing: (a) the entire tunnel morphology and aluminium core. Tilt angle: 0°; and (b) High magnification of (a) representing etched surface, Al core, and deformed tunnel structures. The black arrow indicates the deformation direction of the tunnels during the cutting process.

Therefore, a new method was developed in order to preserve the original tunnel morphology: firstly, the etched samples were infiltrated with an epoxy resin in order to fill the tunnels (porous) structures. Afterwards, the infiltrated specimens were sectioned using a diamond cutter disclosing the tunnel cross section, and finally the samples were embedded for

their posterior metallographic preparation. The conventional metallographic preparation was realised to achieve a flat surface parallel to the tunnel direction. The result is shown in Fig. 8.2a. By using this preparation process we assure a deformation-free volume *i.e.*, no possible distortions generated during the cutting step, as well as getting a satisfactory contrast between the infiltrated tunnels and Al matrix, which is of great importance during image sequence processing. The FIB-prepared imaging planes are defined as *x-y* planes. Secondary electron images of the *x-y* planes are taken from an angle of 52°. Before the serial sectioning can be started, the cube form was produced in the volume to be analysed was performed with the purpose to avoid redeposition and shadowing which can lead to a decrease of accessible sample surface for imaging (Fig. 8.2b) [142]. In order to render the *x-y* planes accessible for image acquisition, a trench was eroded in front of the cube (Fig. 8.2b and Fig. 8.3). The initial morphology of the tunnel pits was also revealed by carefully milling in front of the cube. In Fig. 8.3, the initial tunnel-pit morphology (*i.e.*, the original etched surface) is depicted for annealed Al foil and laser-patterned Pb(10)/Al samples. A SEM image is provided in Fig. 8.3 demonstrating the tunnel morphology of pristine Al foil and irradiated Pb(10)/Al.

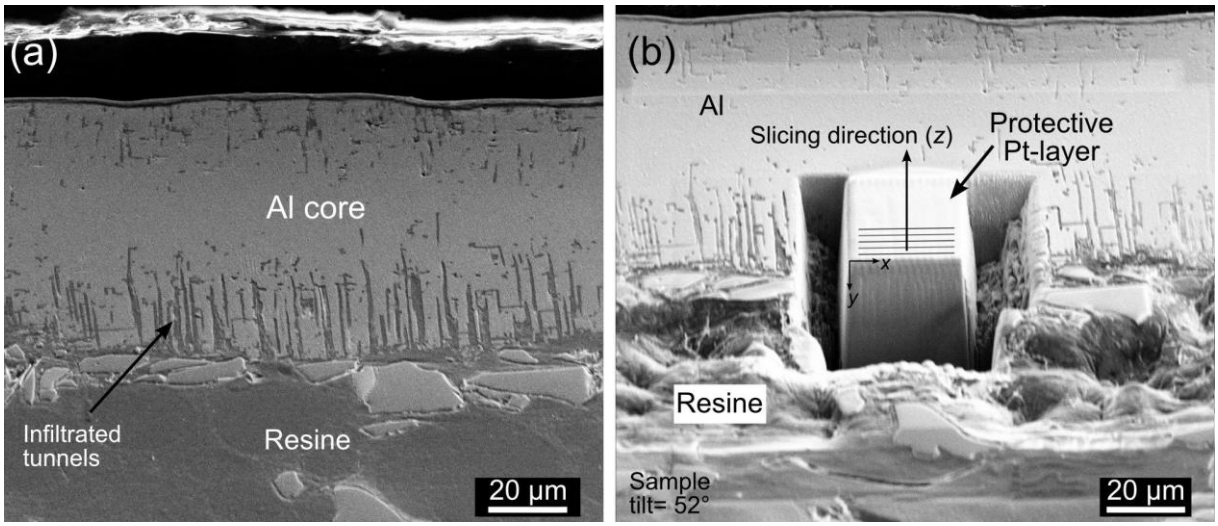

Figure 8.2. SEM image of infiltrated and metallographically-prepared etched Al foil: (a) cross section overview, and (b) cube preparation. Tilt angle: 52°.

Pb(10)/Al sample was structured by using three laser beams and a combinatory arrangement of laser fluences ranging from 845 to 2100 mJ.cm^{-2} approximately (see App. E.2 and Table E.1). The Pb(10)/Al etching structures were characterised at two different fluence values: 845 and 1890 mJ.cm^{-2}. Low and high laser fluences were selected with the finality to understand the effect of lead on the tunnel-pits formation, for the ultimate purpose of engineering their distribution. The addition of lead together with laser structuring (Fig. 8.3b) has led to improvement of the excessive dissolution of aluminium by coalition of pit sites in

comparison with non-irradiated Al foil in absence of lead (Fig. 8.3a). In the case of electrochemically etched Pb(10)/Al structured at high laser fluences, one can clearly see an increase in the refinement of the initial etching sites and an enhancement of their distribution (Fig. 8.3b).

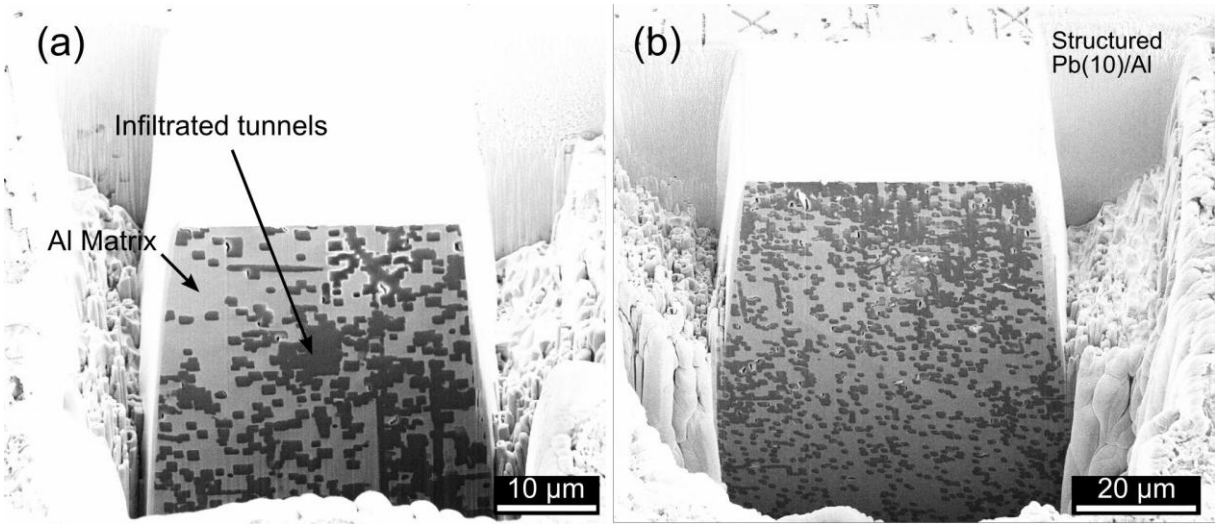

Figure 8.3. SEM image showing the initial tunnel-pit morphology of: (a) as-received annealed Al foil and (b) laser structured Pb(10)/Al employing a laser fluence of 1890 mJ/cm^2. Tilt angle: 52°.

Furthermore, the tunnel growth direction seems to be orientated mostly perpendicular to the surface (*z* direction) for Pb(10)/Al (Fig. 8.3b), while for annealed Al foil the etched holes tend to combine together and a three-dimensional tunnel growth (in *x*, *y*, and *z* direction) is observed (Fig. 8.3a). Although a regular distribution of the fine tunnel pits is recognised for Pb(10)/Al structured at high laser fluence, this was not the case for Pb(10)/Al irradiated with low laser fluence (see App. E.3). Moreover, a decrease of the tunnel pits was obtained. These results are in accordance with the above results shown in Fig. 7.7, where no significant improvement of the etching process was observed for Pb(10)/Al structured with a laser fluence enough to produce only the ablation of the upper Pb layer.

After cube preparation, the serial sectioning procedure was started. During this section, a series of layers were eroded with a constant thickness in *z*-direction and SEM pictures of each cross section were collected automatically (see also Sec. 4.4.2.5).

8.1.2 Data processing and 3D reconstruction of the tunnel morphology

The data processing of the image stack acquired during serial sectioning was performed using the software package Amira ®. The image processing and 3D reconstruction included:

(a) Determination of the voxel dimensions, which are determined by the magnification of the SEM image;

(b) Correction of the image length in the *y*-direction to compensate projection effects due to the tilt of the sample (52°) during SEM imaging. The voxel size in the *z*-direction is equal to the *z*-separation between slices and is often the limiting factor for the resolution of the reconstruction (voxel="3D pixel"). The voxel sizes for 3D characterisation, number of slices and some FIB parameters are summarised in Table 8.1;

(c) The images were aligned using the Pt–sample interface as reference. For reconstruction, the slices have to be aligned in order to account for the aforementioned projection displacement.

Table 8.1. Some FIB parameters and voxel sizes of the samples studied.

Sample	Magnification	Voxel size (nm)			Number of slices
		x	*y*	*z*	
Al (1)	2500	59	75	132	350
Pb/Al (1)	2000	74	94	133	300
Pb/Al (2)	1500	99	135	132	280

Figure 8.4 depicts some SEM images of the serial sectioning procedure. In this figure, 4 slices out of 350 are shown for electrochemically etched aluminium. The slices correspond to a depth from the surface of: 0.0, 14.0, 31.5 and 48.0 µm approximately. It is possible to see the variation of the tunnel-pit form from the surface to the aluminium core. Similar results were obtained for Pb(10)/Al. At the beginning, the tunnel pit cross sections presented a well-defined half-cubic shape, indicating that the tunnel walls are composed of {100} planes in agreement with previous works [111, 203]. However, the tunnel pits become more circular (or round) as the tunnels grow. In the literature [111], this behaviour has been related to a sharp tunnel pit front consisting of {111} planes rather than a square front. There are others factors which may affect the pit form, such as salt formation and temperature. The formation of a salt film with substantial thickness would result in smoothing and rounding of the crystallographic surfaces [106]. Furthermore, it has been reported that higher temperatures also tend to make

circular tunnels. Figure 8.4 also demonstrates that the number of pits decreases as the depth increases (*z* direction).

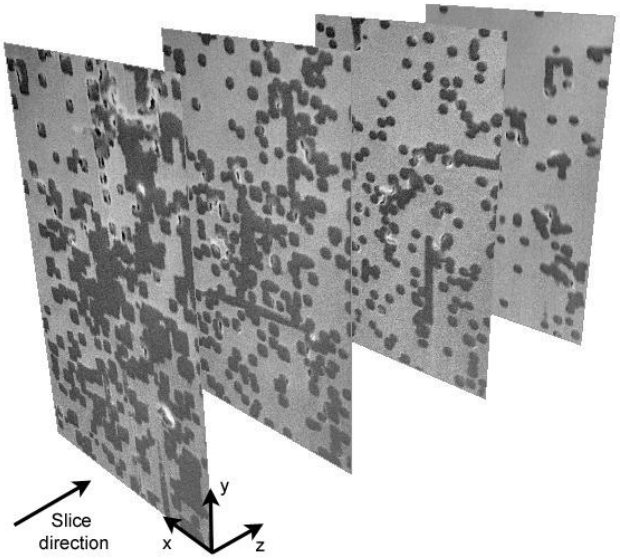

Figure 8.4. Slices of the *x-y* planes collected during the SEM serial sectioning of non-irradiated and electrochemically etched aluminium foil.

Besides the pit morphology changes, it is possible to observe that the tunnels not only grow perpendicular to the surface (*z* direction) but also in *x* and *y* directions (Fig. 8.4). In Fig. 8.5, the 3D rendering of aluminium and Pb(10)/Al electrochemically etched under similar conditions is provided. The *x-y* plane is a collected SEM image while the *x-z* and *y-z* planes are reconstructed by the software via triangulation.

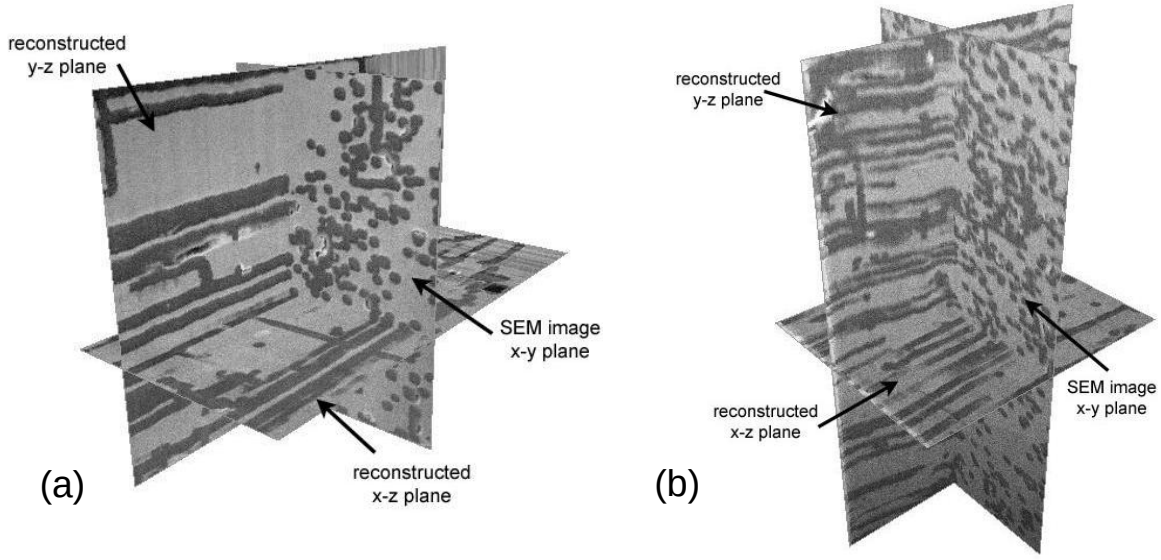

Figure 8.5. Orthogonal slices for 3D visualisation of electrochemically etched (a) annealed aluminium and (b) patterned Pb(10)/Al using 1890 mJ/cm^2 laser fluence. The *x-y* plane is a collected SEM image while the *x-z* and *y-z* planes are reconstructed by Amira software via triangulation.

The tunnel distribution (dark features) in the aluminium matrix (bright features) is more uniform and presents higher density of the etch pits for Pb(10)/Al (Fig. 8.5b) than for aluminium without lead (Fig. 8.5a). Moreover, the growth of the tunnels in different orientations seems to be more pronounced in the case of non-irradiated aluminium. This aspect will be analysed in Subsection 8.1.2.1.

A shape analysis of the real pit size with respect to the sample depth is depicted in Fig. 8.6. This study was carried out by analysis of the 2D sections (*x*-*y* planes) using A4i software. The mean Feret diameter (MeanFeret) was used as size parameter. It is best suited for this purpose because normally the pit cross sections present faceted forms which become round as the tunnels grow. The results show that the etched tunnels had square cross sections whose average size is about 2.0 µm for etched Al foil and 1.6 µm for Pb(10)/Al, as one can see from Fig. 8.6.

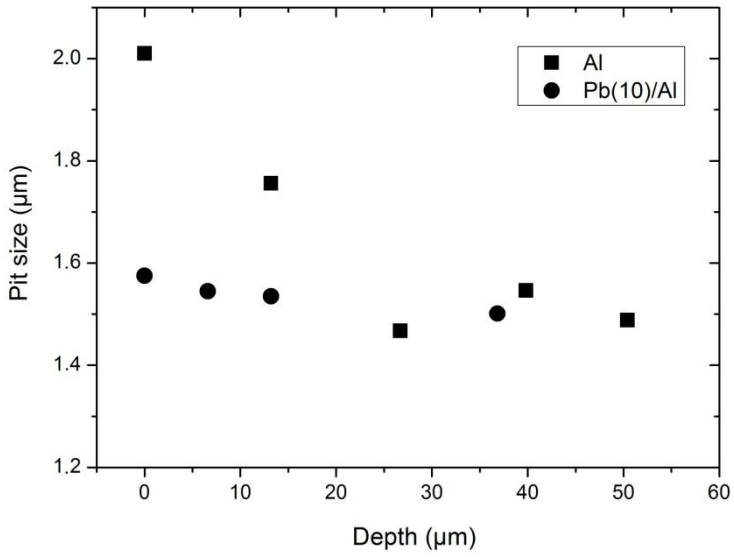

Figure 8.6. Pit size as a function of the sample depth for electrochemically etched Al and Pb(10)/Al.

This phenomenon indicates that the addition of lead content can refine the pit sites, which is helpful to enlarge the etched surface of aluminium foils for high voltage capacitors. However, some research reports that if the amount of lead addition is too large, many etched holes are produced, and the probability of combination (merging) increases, resulting in a reduction of the etched surface as well as a decrease of the capacitance [123]. The cross sectional size of the tunnel is almost constant or decreases very slowly with increasing depth (Fig. 8.6). Indeed, the variation of the pit size was more pronounced for aluminium than for Pb(10)/Al. One should point out that the bigger etched zones were not taken into account during the calculation of the pit size. The values provided in Fig. 8.6 represent the average of the pit sizes at different depths excepting the over-etched areas.

For further quantitative analysis, the tunnels were reconstructed by volume segmentation. The segmentation of the image stack was carried out with the purpose to separate the tunnel structures from the aluminium matrix. The volume segmentation is performed by selecting a suitable gray level threshold. Nevertheless, an eye-inspection and manual 3D segmentation are required in order to ensure an accurate selection of respective regions (Al matrix, and tunnel pits). A surface generation of the segmented regions is performed by the software via triangulation and the tunnels can be visualised in 3D (Fig. 8.7). In Fig. 8.7, it is possible to observe the real morphology and internal structures of the tunnels formed during the electrochemical etching of non-irradiated aluminium and Pb(10)/Al structured by using high laser fluence. In both cases, a high density of µm-wide fine tunnels mostly grew following the <100> direction (perpendicular to the surface).

Moreover, the distribution of the etch pits seems to be more uniform and with high density of them for Pb(10)/Al (Fig. 8.5b and Fig. 8.7b) than those presented in Fig. 8.5a and Fig. 8.7a for as-received aluminium. The results also demonstrate that the inner tunnel sidewalls had a rough corrugated morphology with regular ripples. In the literature this scatter has been related to the stepwise growth of the tunnel, indicating that dissolution of aluminium is pulsating at very low frequency (much lower than 18 s^{-1}) [187, 202]. These regular wall ripples are the result of interaction between the tip dissolution and wall passivation. More recently, Xiao *et al.* [202] proposed a tunnel growth model which reveals how hydrogen is transported out of tunnels, which may explain these ripple formations. The authors consider that the hydrogen bubble of nanometer dimensions is adsorbed on the tunnel wall surface during the pulse electrochemical etching process, and the saturated hydrogen at the end of the tunnel accumulates to form a large bubble before hydrogen is transported out of the tunnel. The large bubble will emanate from the end of the tunnel when the pressure in the bubbles is equal to that outside. The wall surface passivation phenomenon is explained by this model, reporting that the naturally corrugated texture with ripples of about 0.1 µm in the tunnel wall surface is considered to be produced by the periodical potential changes, which are caused by the large hydrogen bubble at the end of the tunnels [202]. So, the formation and transport of the large hydrogen bubbles at the tip of the tunnels may cause the naturally corrugated texture (periodical ripples). In this study, the resolution of the 3D reconstruction is in the same order of magnitude that the width of the wall ripples reported in the literature [109, 123, 204] (see Table 8.1). Therefore, an accurate measure of the ripple intervals could not be taken because it could lead to erroneous results.

As mentioned previously, there are two proposed ways to explain the tunnel growth [109]; one is parallel reactions of tip dissolution and wall passivation, and the other one is sequential dissolution and passivation. Many authors seem to support the first mechanism, in which the growth of the tunnels along <100> directions occurs with passive walls and reactive bottoms, and the tunnel growth rate increase rapidly with temperature increasing in an Arrhenius relationship [111, 203].

The etch pit area was extracted from the binarised voxel data and surface area from the triangulated data. In Fig. 8.8 the etch pit area per slices is depicted for electrochemically etched: (a) non-structured aluminium, (b) structured Pb(10)/Al using low laser fluence, and (c) structured Pb(10)/Al using high laser fluence. In order to facilitate the reading, low laser fluence and high laser fluence will be hereafter written as *LF* and *HF*, respectively. The morphology of the dot-like patterned LF-Pb(10)/Al sample (by using 845 $mJ.cm^{-2}$) consisted of an ablated Pb layer at the interference maxima and unmodified Pb layer at the interference minima. The 3D analysis results show that for LF-Pb(10)/Al the pit nucleation as well as the tunnel growth were inhibited. The total etch pits formed at the LF-Pb(10)/Al surface represented only 20% of the total area under study, corresponding to 80% of unetched aluminium (Fig. 8.8). As one can see from this figure, the total pit area per slices slowly decreases with increasing depth. As a matter of fact, the presence of lead on aluminium surface at the interference minima obstructs the surface dissolution in this positions, decreasing the number of etch pits and consequently the etched area. However, in HF-Pb(10)/Al, a completely different etch pit area was revealed, as shown in Fig. 8.8. At the beginning (sample surface), the pit area corresponded to 47% while the unetched aluminium matrix represented 53% approximately. This area proportion remains almost constant as the depth increases, but at about 3 µm depth the pit percentage decreases abruptly to approximately 40%.

Afterwards, a slight increase of the pit area is recognised and then the pit area percentage decreases progressively with the distance (aluminium depth). In all the sample conditions studied, the pit percentage decrease as the aluminium depth increases. These results are consistent with others reported in the literature [123, 205]. The activation of aluminium by lead is a self-destructive surface process because the activation is limited to a fraction of micrometers [205]. In this study, the abrupt decrease of etch pits at approximately 3 µm depth, can be related with the loss of the activating layer (wetting Pb particles) without generating new activating sites during the corrosion process. After that, the previously formed tunnel pits continue to grow forming the tunnel structures.

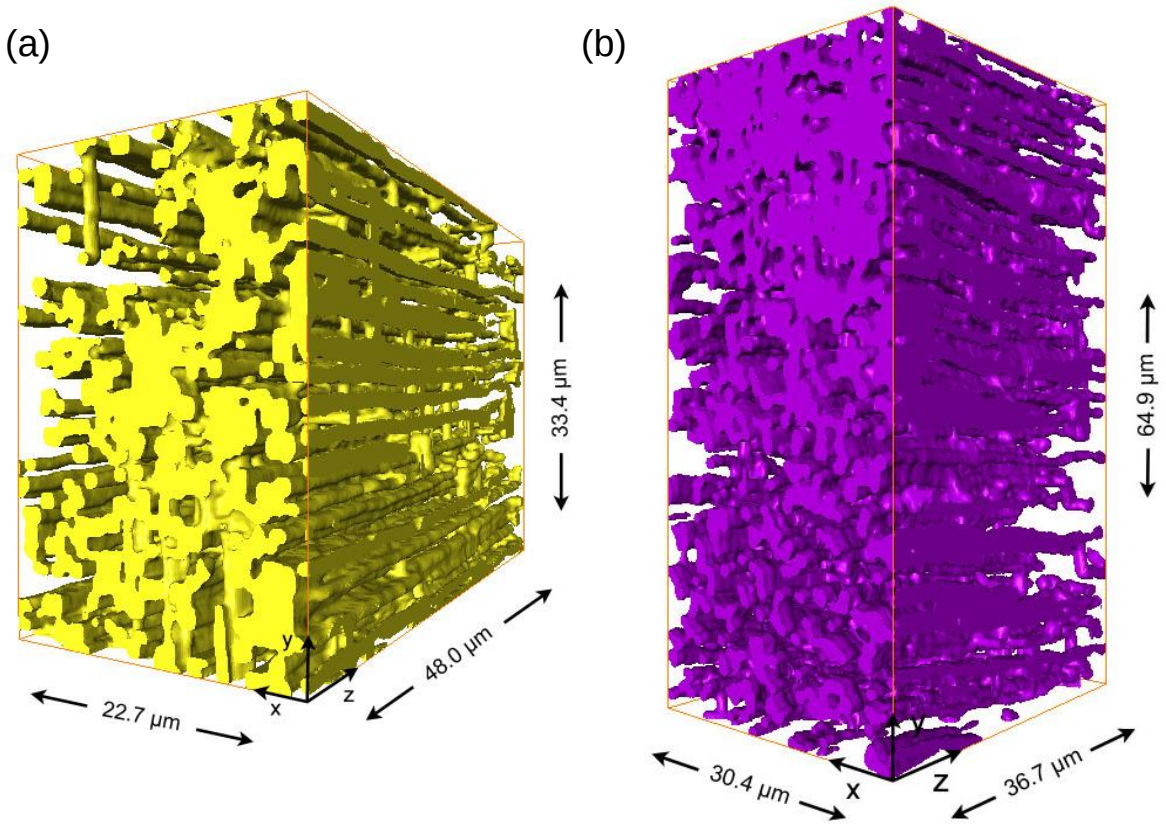

Figure 8.7. 3D reconstructed tunnels for (a) annealed aluminium and (b) structured Pb(10)/Al using high laser fluence (1890 mJ/cm^2).

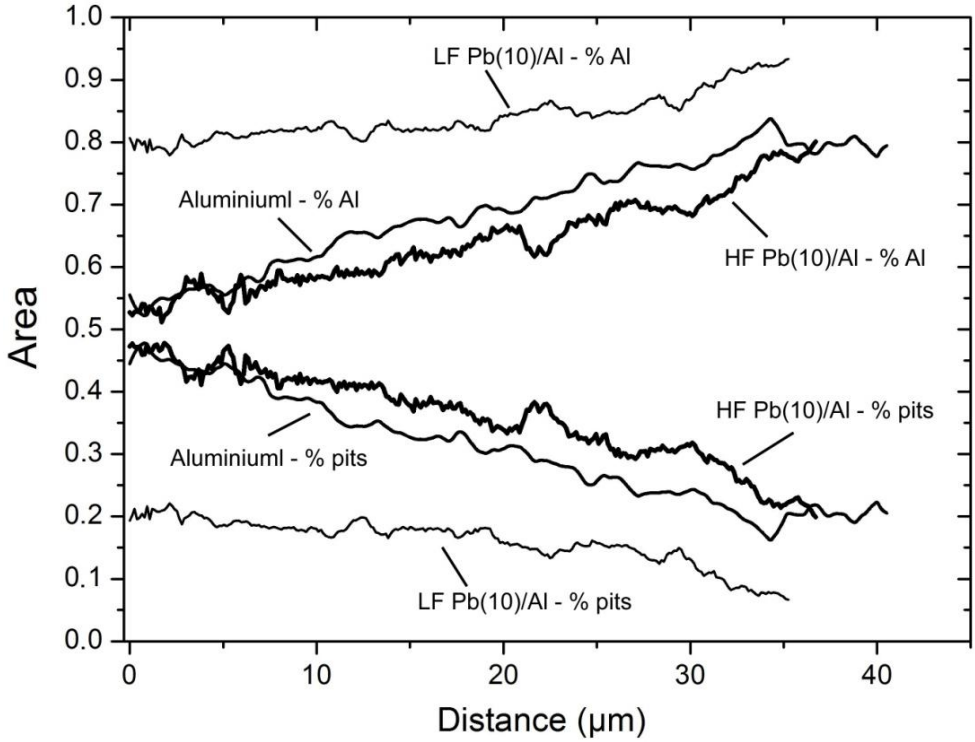

Figure 8.8. Area per slice of Al matrix and tunnel pits for electrochemically etched: as-received aluminium, and structured Pb(10)/Al using low fluence (*LF*) and high fluence (*HF*).

On the other hand, as-received aluminium foil was also analysed in order to compare the samples. Aluminium foil presented 44% pit area and 56% unetched zones at the beginning of the etching process. Although the percentages of etch pit area did not differ significantly for aluminium and HF-Pb(10)/Al (44% and 47% pit area, respectively), the pit percentage was higher at every instant for HF-Pb(10)/Al in comparison with unmodified aluminium, as is depicted in Fig. 8.8. The difference between the two curves reveals that lead addition promotes the formation of a high density of evenly distributed tunnel pits, which markedly influenced the final tunnel sites distribution. The high pit area percentage at the surface for Al foil could be related to the formation of large etched areas due to the agglomeration or combination of several etch pits, which is not favourable for obtaining a high capacitance. Nevertheless, since only a small region of the samples was used for the three-dimensional analysis of the tunnel structures, one should beware of using these results as representative of the samples as a whole.

FIB nano-tomography is a useful and powerful technique, which reveals quantitative information of smaller structural features, which cannot be acquired easily by other methods [142]. However, it is a very local technique, reason why the extrapolation of the outcome should be carefully made. In this work, the selection of the investigated zones was realised meticulously in order to study an etched zone that would be the most representative of the whole etched surface.

Furthermore, the total surface area S for the interface between the tunnels and aluminium matrix was determined. The total surface areas were 84503.03 μm^2 and 29205.33 μm^2 for HF-Pb(10)/Al and Al foil, respectively. Because the total sizes of the analysed areas were 1973.6 μm^2 and 757.4 μm^2 (corresponding to $x*y$ in Fig. 8.7) the area increase factor was 42.8 for HF-Pb(10)/Al and 38.5 for aluminium samples. Indeed, it was expected that the total surface area of HF-Pb(10)/Al increase in comparison with annealed foil due to the above results presented in Fig. 8.8. The highest specific surface area was obtained for HF-Pb(10)/Al due to the activation of aluminium by lead.

As it was previously mentioned (Section 7.1.2), lead does not seem to have a direct influence on the tunnel growth but is expected to play an important role in the initiation of tunnel pits. Lead can refine the size of the tunnel pits and activates the aluminium surface. This activation comes from the passivity destabilisation of the aluminium oxide, resulting in the depression of the pitting potential and ensuing high anodic current densities.

The lead incorporation and its distribution are controlled by laser patterning. Therefore, we can assure that the combined action of lead and laser structuring determined the tunnel pit distribution of the structured Pb/Al samples.

8.1.2.1 Anisotropy

For further quantitative analysis MAVI (Modular Algorithms for Volume Images) software was employed. This software permits the processing and analysis of 3D volume images as produced by micro computer tomography. MAVI is focused on the characterisation of the complex geometry of the structures as volume, surface, integral of curvatures, among others, for the whole structure or isolated objects. Anisotropies and preferred directions as well as their strength can also be measured. MAVI uses the cuboidal lattice for 3D images. For the cuboidal lattice there are 13 spatial directions, ω_i: 3 coordinate directions, 6 face diagonals and 4 space diagonals [189, 206].

With the purpose of studying the anisotropy of the tunnel structures formed in aluminium and HF-Pb(10)/Al samples, the following field features were measured:

A_i = area of the orthogonal projection in *i*-direction (ω_i),

L_i = length of the total projection corresponding to the direction of projection ω_i, and,

l_i = mean chord length corresponding to the chord direction ω_i. i= 1, 2, ..., 13.

A_i, L_i, and li quantities describe the anisotropy of a constituent [206].

A chord length is defined by the distance of two points of the contour, measured exactly across the centre of gravity of the projection area. It is not a diameter in its actual sense but the common basis of a group of diameters.

In order to visualise the anisotropy in three dimensions, it is normally supposed that the surface of the structures is made up of a large number of small patches of equal area. The direction associated with a patch is described by the local surface normal. If these vectors are distributed uniformly over the sphere that describes all possible orientations in three-dimensional space, then the feature set is said to be isotropic. If the distribution of vectors is not uniform on the sphere, but tends to cluster about certain directions, the feature set exhibits anisotropy [207].

Figure 8.9 shows the distribution of the tunnel area projections perpendicular to each direction. The preferred direction in space (anisotropy) seems to be different depending on the sample analysed. For non-irradiated and electrochemically etched aluminium foil (Fig. 8.9a),

the outer normal vector area A_i projected in [0y0] and [x00] directions, are bigger than in the other directions. This means that there are preferred orientations in theses directions.

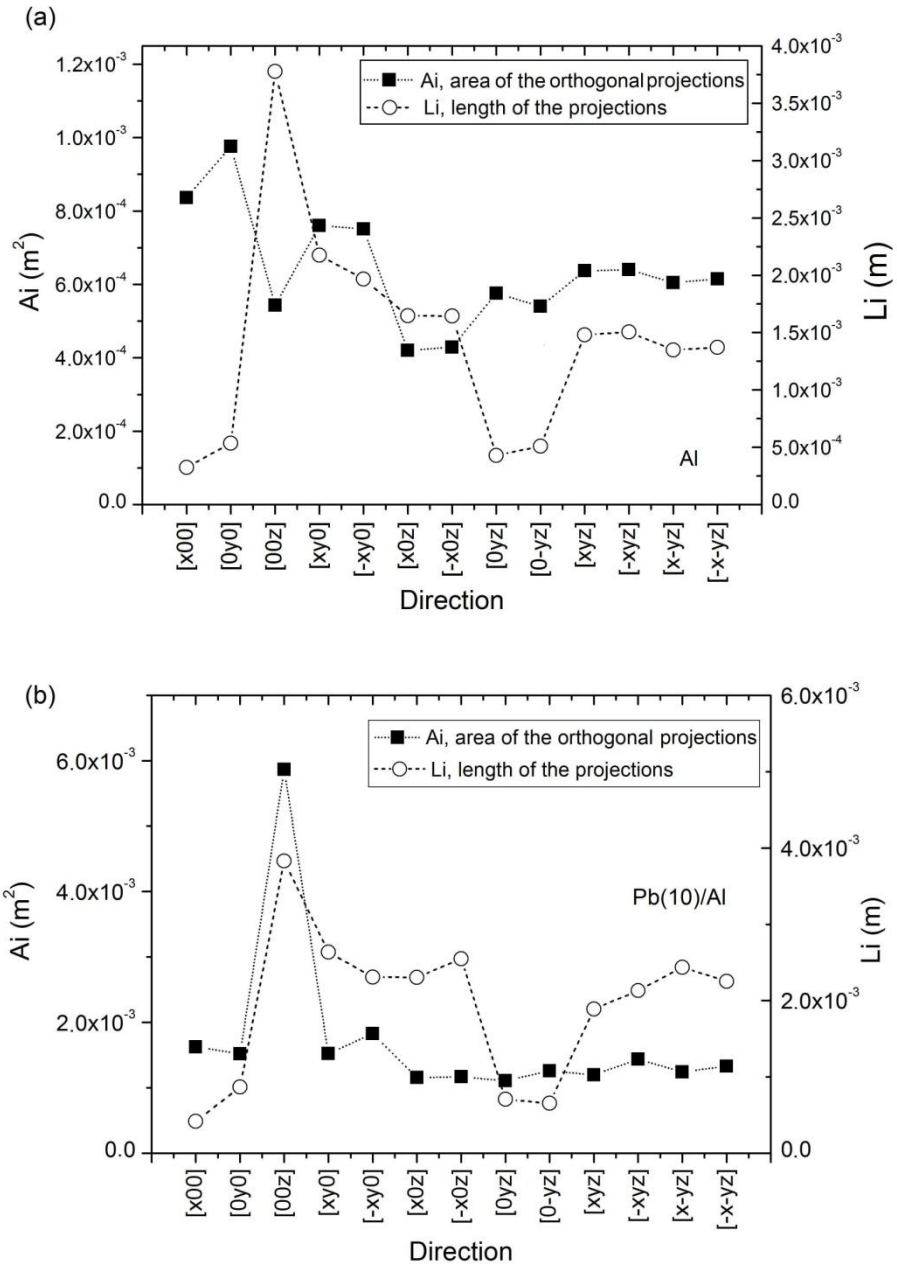

Figure 8.9. Area of the orthogonal projections, A_i, and the length of projections L_i i=1, …, 13, of the 3D tunnel structures for electrocheically etched: (a) aluminium foil and (b) HF-Pb(10)/Al.

Furthermore, a significant decrease of the tunnel area projection in the *z*-direction ([00z]) is also found, as is depicted in Fig. 8.9a. Otherwise, the results show that the length of the total projections Li corresponding to [0y0] and [x00] are smaller than the ones associated with [00z] direction. Therefore, the growth of the tunnels in these directions does not lead to large tunnel structures but rather to small ones. As a matter of fact, it was expected that the

higher length projection correspond to the *z*-direction due to the preferential tunnel growth in this crystallographic orientation.

The mean chord lengths l_i given in Fig. 8.10 are consistent with the above results. The image analyses show that the *z*-direction, ω_i= [00z], is the preferred direction for both samples (see Fig. 8.10a, b). However, the texture is stronger in the case of Pb(10)/Al (Fig. 8.10b), (where l_i reached values of ~ 8.2×10^{-6} m) than for the aluminium sample (Fig. 8.10a) whose maximum l_i is approximately 5×10^{-6} m as demonstrated in Fig. 8.10.

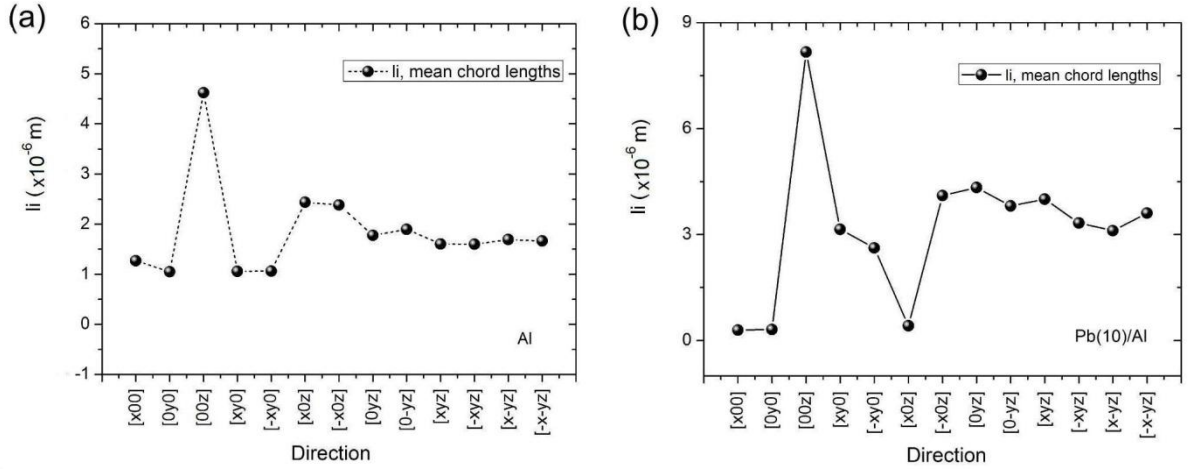

Figure 8.10. The mean chord lengths, l_i, corresponding to the spacial direction ω_i (i=1, 2, ..., 13), of the tunnel structures shown in Fig. 8.7.

Knowing the anisotropy results, one can conclude that for annealed aluminium foil (without Pb addition and pre-treatment laser patterning) there is a considerable tunnel density in the *x*-*z* planes and *y*-*z* planes which are perpendicular to *y*-direction and *x*-direction, respectively. This anisotropic behaviour can be related to the growth of the tunnels parallel to the sample surface. Some research [126] associates the superficial etching with rolling line effect, *i.e.*, the effect which results in concentrate etching along rolling lines. The rolling lines are strain areas where high concentrations of impurities and dislocations can be located which favoured pit initiation. Therefore, most of the pit sites tend to be concentrated along these zones. However, this phenomenon is prejudicial since it can lead to vast etched areas caused by the combination of several tunnel pits. This effect can not only modify the pit initiation sites but also facilitate the lateral tunnel growth. These results are consistent with the results obtained in Section 6.3 and are in accordance with others reported in the literature [110, 122].

On the other hand, the anisotropy results found for structured and electrochemically etched Pb(10)/Al demonstrated that the tunnel structures presented a strong outer texture in *z*-direction (Fig. 8.9b and Fig. 8.10b). In this case the area of the orthogonal direction and the

length of the projections show a significantly high value in ω_i= [00z], while in the other orientations, a homogenous distribution with minor deviations was observed. For Pb(10)/Al the area of the projections is almost six times higher than the bigger projected area identified for as-received aluminium (in ω_i= [0y0]), but the length of the projections seems to be similar. Based on these results, it is possible to conclude that the formation of homogenous tunnel structures perpendicular to the surface was improved by the combined action of lead and laser patterning.

CHAPTER 9

Conclusions

The capacity to produce desired functional micro-structures on metallic surfaces via laser interference structuring has been demonstrated in this work. By inducing suitable microstructural, physical or chemical changes it is possible to optimise the quality and to attain the adequate combination of surface properties.

The interaction of laser light with metallic surfaces for the formation of advanced periodic structures was investigated. Chapter 5, aimed at the structuring of metallic samples, presents a detailed analysis of the mechanisms involved in the formation of the micro-structures.

- The results show that the formation of micro-patterns is dominated by the flow of the molten material, which is a response to the forces acting within the molten pool. The main mechanism to imprint deformation during the nanosecond laser pulse is the effect of the surface-tension gradient induced by the lateral variation of temperature, known as Marangoni convection. Moreover, the fluence ranges in which the different forces prevail depend on the material used.
- The morphology of the periodic surfaces depends strongly on the laser fluence. By increasing the laser fluence, the temperature difference between the maxima and minima positions increases and larger molten depths are reached. Hence, larger structure depths can be obtained. Moreover, at high laser fluences the presence of droplets was observed, which was associated to Rayleigh instabilities and also in some cases, to the recoil pressure effect.
- Furthermore, a correlation was also observed between the period of the structure and the structure depth. Deeper structure depths are achieved for larger periods. As the period decreases, the temperature difference between maxima and minima decreases due to the thermal diffusivity of metals, leading to a more homogeneous heating of the surface. At large periods, the heat is highly localised at the interference maxima positions, giving rise to larger molten depths and deeper structures.
- The maximal structure depth attained for the micro-structures is related with the thermal conductivity of the metals and consequently with their thermal diffusivity (D) and diffusion lengths (L). The thermal diffusion length (or thermal penetration depth)

confines the maximal structure depths that can be reached during the structuring of metallic surfaces. For material with low thermal diffusivity (such as Ti) the heat cannot be easily evacuated to the rest of the volume and high convection is expected, producing structures with low aspect ratio and small structure depths.

- It was demonstrated that the dimensionless numbers is a useful tool to know the flow characteristic and the forces overcoming during the structuring process. Metals with low Prandtl numbers, Pr, demonstrate that the thermal conductivity play an important role in heat transport, leading to deep structures with hemispherical (concave) pool shapes. While high Pr numbers indicate a strong convectional flow producing molten pools with low aspect ratio and flat or also convex pool shapes. The Reynolds number showed that the flow regime during laser structuring is mainly laminar. In a similar way, the Peclet, capillary, Grahof, and Bond numbers were also analysed.

Furthermore, special attention was taken to tailoring the chemical and physical changes promoted by laser patterning. Anode aluminium foils for high-voltage (HV) capacitors were one of the widely investigated materials in this thesis. In the industry, the effective surface area of an anode foil is greatly enlarged by electrochemical etching in order to achieve the maximum capacitance available. However, the ideal enlargement of the surface area by electrochemical etching is difficult to achieve due to a disorderly pit distribution and the growth of merged pits by lateral dissolution. One of the main approaches of this work is to find a way to improve the pit initiation sites on aluminium foil. For this purpose, laser interference metallurgy is proposed as a useful tool for the controlling of the pit distribution. Chapter 6 focused on the chemical behaviour of aluminium modified by laser interference.

- The original preferred orientation (cubic texture) of aluminium was not modified by laser interference. Even using high laser fluences the cubic texture of aluminium remained unchanged.
- It was shown that laser interference metallurgy permits controlling the growth of a periodic and local oxide layer on aluminium. The nature of the oxide was identified as α-Al_2O_3 phase.
- The oxide layer thickness is determined by the laser fluence used and varies between the maximal and minimal interference positions. Thermal simulation showed that the oxide layer thickness grows almost linearly with the surface temperature.
- The periodically modulated film thickness controls the formation of tunnel pit sites during the etching process of aluminium. The etching process follows the ordered

array imprinted on the surface. The difference in oxide layer thickness between the maximal and minimal interference positions leads to a preferential and local etching of the samples.

- The etching occurs preferentially at the interference minima zones, where the oxide films are thinner. However, the structured aluminium surface becomes passive when the oxide layer thickness reaches or exceeds 10 nm.
- Laser structuring not only influences the initial etch pit distribution during the first stage of the etching process, but also the final morphology of the electrochemically etched aluminium.

Until now, the distribution of the pit initiation sites on aluminium has been improved by changing the chemical composition of the surface. This modification is generally induced by segregation of some impurities (*e.g.*, Fe, Cu, Sn, Mn, Pb, In, etc.) at the surface promoted by heat treatments. Chapter 7 is addressed to the study of the influence of lead and copper on the site-controlled pitting during the chemical etching of anode foil.

- The addition of small quantities of lead on Al substrate by PVD and its subsequent laser structuring has led to a selective and local etching of the surface. Lead incorporation into aluminium was promoted by Marangoni convection during the structuring of Pb/Al systems. The preferential etching takes place at the maximal interference areas, *i.e.*, where Pb/Al samples where irradiated, while the non-irradiated zones remain un-etched. This behaviour is completely opposite to that found during the structuring of aluminium without the presence of lead. Furthermore, lead addition strongly produced finer tunnel pits in comparison to structured aluminium etched under the same conditions.
- The structuring of Pb/Al using low laser fluences did not achieve the selective etching of the samples. Moreover, cell-like structures were found at the irradiated zones due to a strong segregation of Pb during sample solidification. This cellular morphology did not improve the etching process.
- At moderate and high laser fluences, the formation of a nano-film of metallic Pb nanoparticles is formed. The selective etching takes place only when the Pb particles are in contact with aluminium metal. The nonwetting Pb did not contribute to the selective etching of aluminium.
- The enrichment of Pb at the aluminium surface causes a significant electrochemical activation of the surface characterised by a significant negative shift of the pitting potential relative of the pitting potential of pure aluminium. Therefore, the selective

etching of structured Pb/Al is produced by anodic activation of the surface as a result of the enrichment with lead nanoparticles in the oxide–metal interface, causing passivity breakdown of the sample.

- On the other hand, copper addition also promotes the selective etching of aluminium. The preferential etching occurs at the minima interference areas, *i.e.*, the non-irradiated zones where the discontinuous Cu remains, while the maximal interference positions stay unetched. Nevertheless, it was possible to achieve the selective etching only at low laser fluences. The structuring of Cu/Al at high laser fluence (where the compact structures were formed) did not produce a control of the etching process. In fact, the samples were not etched at all.
- Therefore, it was concluded that the selective etching of Cu/Al is due to localised galvanic corrosion. As the corrosion potential of aluminium and copper are very different, local micro-cells can be formed during the etching of structured Cu/Al. Copper acts as a cathode and aluminium as an anode. The galvanic cells are not formed between the interference maxima and minima positions but rather between the discontinuous copper and exposed aluminium at the minimal interference zones.
- Even using low laser fluences, a thin oxide layer of Al is formed at the interference maxima zones and the introduction of some Cu inclusion, which can enhance the chemical stability of these areas (interference maxima positions).
- The etching behaviour denotes that Cu is not an anodic activator of aluminium but rather induced the development of the tunnel pits on Al foil due to galvanic corrosion and can influence the growth of the tunnels.
- For Cu/Al the etching times were considerably shorter than those used during the etching of structured Al foil, Pb/Al, and even as-received aluminium foil, to obtain similar results.

In chapter 8, the 3D characterisation of the tunnel morphology obtained by electrochemical etching of as-received aluminium and structured Pb(10)/Al was performed. The purpose of this study is to gain reliable information about the complex etching structures and to analyse the influence of lead on the tunnel formation.

- A method based on FIB tomography was developed in order to determine the real tunnel morphology in the depth direction and to obtain statistic analyses of the etched structures.

- The addition of lead together with laser structuring has led to avoid the excessive dissolution of aluminium and pit coalescence in comparison with non-irradiated aluminium foil. It was found that Pb/Al structured by using high laser fluence showed a refinement of the initial etching sites and an enhancement of their distribution. For Pb/Al irradiated with low laser fluence, the etching process was not improved. Indeed, a decrease of tunnel pits was obtained.
- The pit morphology changes as the aluminium depth increases. At the surface, the pit cross sections present a well-defined half cubic shape and become more round as the tunnel grows. However, the cross sectional size of the tunnel is almost constant or decreases very slowly with increasing depth.
- At any moment, the pit area fraction was higher for structured Pb/Al using high laser fluence (HF-Pb/Al) in comparison with unmodified aluminium. Moreover, the fraction of the pit area per slice slowly decreases with increasing sample depth. Furthermore, the highest specific surface area was obtained for HF-Pb/Al due to the activation of aluminium by lead.
- By etching, the effective surface area was enlarged around 38 times for as-received Al foil and 43 times for structured HF-Pb(10)/Al, as compared to their respective apparent areas.
- The anisotropies and preferred directions as well as their strength were also investigated. The results demonstrated that *z*-direction, ω_i= [00z], is the preferred direction for both samples. However, the texture is stronger in the case of Pb(10)/Al than for Al foil. It was found that as-received aluminium foil also showed preferential tunnel growth parallel to the sample surface.
- The lead addition itself does not help to improve the tunnel growth but rather the distribution of the pits. Therefore, the combination of lead and laser structuring improve the homogeneity of the etching process, avoiding the excessive pit formation along the rolling lines as well as their merging. This effect improves the pitting process homogeneity and finally the tunnel orientation, which may ultimate lead to an increase in capacitance for high-voltage aluminium capacitors.

References

[1] M. von Allmen, A.Blatter., Laser Beam Interactions with Materials, Springer, Berlin, 1995.

[2] M. F. Modest, Lia Handbook of Laser Material Processing New York, Laser Institute of America 2001.

[3] R. E. Hummel, Lia Handbook of Laser Materials Processing. New York, Laser Institute of America 2001.

[4] P. K. L. Drude, The Theory of Optics. New York, 1959.

[5] P. Grosse, Freie Elektronen in Festkörpern. Heidelberg, Springer, 1979.

[6] F. Wooten, Optical Properties of Solids. New York, Academic, 1972.

[7] E. Hagen, H. Rubens, Annals of Physics, 4 (1903) 873.

[8] W. M. Steen, Laser Material Processing. Berlin, Springer London Limited, 2003.

[9] M. F. Modest, Radiactive Heat Transfer. New York, McGraw-Hill, 1993.

[10] P. B. M. von Allmen, K. Affolter, and E. Stürmer, IEEE Journal of Quantum Electronics, 14 (1978) 85.

[11] K. Ujihara, Journal of Applied Physics, 43 (1972) 2376.

[12] A. M. Bonch-Bruevich, Y. A. Imas, G. S. Romanov, M. N. Liebenson, L. N. Maltsev, Soviet Physics - Technical Physics 13 (1968) 640.

[13] T. E. Zavecz, M. A. Saifi, M. Notis, Applied Physics Letters, 26 (1975) 165.

[14] J. F. Ready, IEEE Journal of Quantum Electronics, 12 (1976) 137.

[15] J. Boneberg, J. Bischof, P. Leiderer, Optics Communications, 174 (2000) 145.

[16] W. M. Brandenberg, NASA, SP-31 (1963) 75.

[17] L. K. Ang, Y. Y. Lau, R. M. Gilgenbach, H. L. Spindler, Applied Physics Letters, 70 (1997) 696.

[18] D. Bäuerle, Laser Processing and Chemistry, Springer, 1996.

[19] D. Von Der Linde, K. Sokolowski-Tinten, J. Bialkowski, Applied Surface Science, 109-110 (1997) 1.

[20] J. Zhu, G. Yin, M. Zhao, D. Chen, L. Zhao, Applied Surface Science, 245 (2005) 102.

[21] J. Powell, Co_2 Laser Cutting. New York, Springer London Ltd, 1998.

[22] Y. L. Yao, H. Chen, W. Zhang, International Journal of Advanced Manufacturing Technology, 26 (2005) 598.

[23] M. D. Shirk, P. A. Molian, Journal of Laser Applications, 10 (1998) 18.

[24] B. N. Chichkov, C. Momma, S. Nolte, F. Von Alvensleben, A. TuÌˆnnermann, Applied Physics A: Materials Science and Processing, 63 (1997) 109.

[25] A. Semerok, C. ChaleÌ • ard, V. Detalle, J. L. Lacour, P. Mauchien, P. Meynadier, C. Nouvellon, B. SalleÌ • , P. Palianov, M. Perdrix, G. Petite, Applied Surface Science, 138-139 (1999) 311.

[26] D. Von Der Linde, K. Sokolowski-Tinten, Applied Surface Science, 154 (2000) 1.

[27] B. Sallé, O. Gobert, P. Meynadier, M. Perdrix, G. Petite, A. Semerok, Applied Physics A: Materials Science and Processing, 69 (1999) S381.

[28] R. Kelly, A. Miotello, Nuclear instruments & methods in physics research. Section B, Beam interactions with materials and atoms, 91 (1994) 682.

[29] S. R. Franklin, R. K. Thareja, Applied Surface Science, 222 (2004) 293.

[30] X. Chen, Lia Handbook of Laser Material Processing New York, Laser Institute of America 2001.

[31] M. D. Perry, B. C. Stuart, P. S. Banks, M. D. Feit, J. A. Sefcik, Lia Handbook of Laser Material Processing. New York, Laser Institute of America, 2001.

[32] M. Wautelet, P. Quenon, C. Antoniadis, L. D. Laude, Semiconductor Science and Technology, 2 (1987) 453.

[33] D. R. Lide, Handbook of Chemistry and Physics, CRC, 2003.

[34] V. Y. Balandin, R. Niedrig, O. Bostanjoglo, Journal of Applied Physics, 77 (1995) 135.

[35] K. C. Mills, B. J. Keene, International Materials Reviews, 32 (1987) 1.

[36] B. J. Keene, International Materials Reviews, 33 (1988) 1.

[37] K. Mills, Recommended Values of Thermophysical Properties for Commercial Alloys. Abington, Woodhead, 2002.

[38] B. J. Keene, International Materials Reviews, 38 (1993) 157.

[39] J. M. Drezet, S. Pellerin, C. Bezençon, S. Mokadem, J. Phys. IV France, 120 (2004) 299.

[40] T. R. Anthony, H. E. Cline, Journal of Applied Physics, 48 (1977) 3888.

[41] Y. Lu, S. Theppakuttai, S. C. Chen, Applied Physics Letters, 82 (2003) 4143.

[42] C. Limmaneevichitr, S. Kou, Welding research supplement, (2000) 126.

[43] G. Tsotridis, H. Rother, E. D. Hondros, Naturwissenschaften, 76 (1989) 216.

[44] A. Blatter, C. Ortiz, Journal of Applied Physics, 73 (1993) 8552.

[45] M. Maillard, L. Motte, A. T. Ngo, M. P. Pileni, Journal of Physical Chemistry B, 104 (2000) 11871.

[46] P. V. Santos, A. R. Zanatta, U. Jahn, A. Trampert, F. Dondeo, I. Chambouleyron, Journal of Applied Physics, 91 (2002) 2916.

[47] T. D. Bennett, D. J. Krajnovich, C. P. Grigoropoulos, P. Baumgart, A. C. Tam, Journal of Heat Transfer, 119 (1997) 589.

[48] P. Kivitis, R. de Bont, B. Jacobs, P. Zalm, Thin Solid Films, 87 (1982) 215.

[49] G. M. Blom, Journal of Applied Physics, 54 (1983) 6175.

[50] C. Ortiz, A. Blatter, Thin Solid Films, 218 (1992) 209.

[51] J. Solis, K. A. Rubin, C. Ortiz, Journal of Materials Research, 5 (1990) 190.

[52] J. Solis, C. Ortiz, C. N. Alfonso, F. Catalina, Applied Physics A Solids and Surfaces, 54 (1992) 2181.

[53] V. Semak, A. Matsunawa, Journal of Physics D: Applied Physics, 30 (1997) 2541.

[54] S. I. Anisimov, Soviet Physics - JETP, 27 (1968) 182.

[55] F. Keilmann, Physical Review Letters, 51 (1983) 2097.

[56] Q. Wu, Y. Ma, R. Fang, Y. Liao, Q. Yu, X. Chen, K. Wang, Applied Physics Letters, 82 (2003) 1703.

[57] P. M. Fauchet, A. E. Siegman, Applied Physics Letters, 40 (1982) 824.

[58] J. E. Sipe, J. F. Young, J. S. Preston, H. M. Van Driel, Physical Review B, 27 (1983) 1141.

[59] Z. Guosheng, P. M. Fauchet, A. E. Siegman, Physical Review B, B26 (1982) 5366.

[60] G. Grorodetsky, J. Kanicki, T. Kazyaka, R. L. Melcher, Applied Physics Letters, 46 (1985) 547.

[61] S. I. Kudryashov, S. D. Allen, Journal of Applied Physics, 92 (2002) 5627.

[62] K. Regelskis, G. Račiukaitis, M. Gedvilas, Applied Surface Science, 253 (2007) 6584.

[63] T. Tomita, K. Kinoshita, S. Matsuo, S. Hashimoto, Applied Physics Letters, 90 (2007).

[64] S. Chandrasekhar, Hydrodynamic and Hydromagnetic Stability. Oxford, Clarendon, 1961.

[65] C. Wagner, Z. Phys. Chem., 2 (1933) 25.

[66] N. Cabrera, N. F. Mott, Reports on Progress in Physics, 12 (1948) 163.

[67] L. Nánai, R. Vajtai, T. F. George, Thin Solid Films, 298 (1997) 160.

[68] S. Beauvais-Réveillon, A. M. Huntz, G. Moulin, J. J. Bléchet, Oxidation of Metals, 43 (1995) 279.

[69] M. Wautelet, Applied Physics A Solids and Surfaces, 50 (1990) 131.

[70] S. M. Metev, V. P. Veiko, Laser-Assisted Micro-Technology. Berlin, 1998.

[71] M. Wautelet, L. D. Laude, F. Hanus, K. H. Heinig, Applied Physics A Solids and Surfaces, 47 (1988) 313.

[72] L. Baufay, F. A. Houle, R. J. Wilson, Journal of Applied Physics, 61 (1987) 4640.

[73] M. Wautelet, R. Andrew, Philosophical magazine B, 55 (1987) 261.

[74] P. B. Jhonson, R. W. Christy, Physical Review B, 9 (1974) 5056.

[75] I. Boyd, Transactions of the Materials Research Society of Japan, 17 (1993) 319.

[76] P. Mogyorósi, L. Nánai, K. Antal, Infrared Physics, 25 (1985) 625.

[77] L. Nánai, R. Vajtai, I. Hevesi, D. A. Jelski, T. F. George, Thin Solid Films, 227 (1993) 13.

[78] T. Dimogerontakis, R. Oltra, O. Heintz, Applied Physics A: Materials Science and Processing, 81 (2005) 1173.

[79] E. György, A. P. Del Pino, P. Serra, J. L. Morenza, Applied Physics A: Materials Science and Processing, 78 (2004) 765.

[80] A. Milosavljevic, M. Srec?kovic, S. Bojanic, M. Dinulovic, B. Ljubisavijevic, Vacuum, 47 (1996) 1413.

[81] Li JunChang, C. Langlade, A. B. Vannes, Surface and Coatings Technology, 115 (1999) 87.

[82] J. L. Jiménez Pérez, P. H. Sakanaka, M. A. Algatti, J. G. Mendoza-Alvarez, A. Cruz Orea, Applied Surface Science, 175-176 (2001) 703.

[83] D. M. Lipkin, H. Schaffer, F. Adar, D. R. Clarke, Applied Physics Letters, 70 (1997) 2550.

[84] V. K. Tolpygo, D. R. Clarke, Acta Materialia, 46 (1998) 5153.

[85] V. K. Tolpygo, D. R. Clarke, Acta Materialia, 46 (1998) 5167.

[86] G. C. Wood, F. H. Stott, The Development and Growth of Protective Alfa-Al2o3 Sacles on Alloys. Houston 1983.

[87] E. Bergsmark, C. J. Simensen, P. Kofstad, Materials Science and Engineering A, A120-1 (1989) 91.

[88] F. Stucki, M. Erbudak, G. Kostorz, Applied Surface Science, 27 (1987) 393.

[89] M. Geissler, Y. Xia, Advanced Materials, 16 (2004) 1249.

[90] Y. Chen, A. Pépin, Electrophoresis, 22 (2001) 187.

[91] M. A. McCord, M. J. Rooks, Handbook of Microlithography, Micrrofabrication and Microsystem. Washington, SPEI Press, 1997.

[92] D. A. Muller, Y. Tzou, R. Raj, J. Silcox, Nature, 366 (1993) 725.

[93] J. Fujita, H. Watanabe, Y. Ochiai, S. Manako, J. S. Tsai, S. Matsui, Applied Physics Letters, 66 (1995) 3065.

[94] M. J. Bowden, Introduction to Microlithography. Washington DC, Americal Chemical Society, 1994.

[95] J. H. Jang, C. K. Ullal, M. Maldovan, T. Gorishnyy, S. Kooi, C. Y. Koh, E. L. Thomas, Advanced Functional Materials, 17 (2007) 3027.

[96] D. Kim, S. K. Tripathy, L. Li, J. Kumar, Applied Physics Letters, 66 (1995) 1166.

[97] F. Yu, P. Li, H. Shen, S. Mathur, C. M. Lehr, U. Bakowsky, F. Mücklich, Biomaterials, 26 (2005) 2307.

[98] B. Rezek, C. E. Nebel, M. Stutzmann, Journal of Applied Physics, 91 (2002) 4220.

[99] A. Lasagni, C. Holzapfel, F. Mucklich, Applied Surface Science, 253 (2006) 1555.

[100] Z. Liu, X.K. Meng, T. Recktenwald, F. Mücklich, Materials Science and Engineering A, 342 (2003) 101.

[101] J. A. Stratton, Electromagnetic Theory. New York, McGraw-Hill, 1941.

[102] F. Mücklich, A. Lasagni, C. Daniel, International Journal of Materials Research, 97 (2006) 1337.

[103] A. F. Lasagni. Advanced Design of Periodical Structures by Laser Interference Metallurgy in the Micro/Nano Scale on Macroscopic Areas. Functional materials, vol. PhD. Saarbrücken: Saarland university, 2006. p.169.

[104] A. EPCOS, Aluminium Electrolytic Capacitors. Munich, 2003.

[105] T. Ebel, G. P. Chiavarotti, ATB Métallurgie, 43 (2003) 147.

[106] S. Ono, T. Makino, R. S. Alwitt, Journal of the Electrochemical Society, 152 (2005) B39.

[107] NICHICON. Technical Notes Cat. 8101c. 2001.

[108] E. McCafferty, Corrosion Science, 45 (2003) 1421.

[109] R. S. Alwitt, H. Uchi, T. R. Beck, R. C. Alkire, Journal of the Electrochemical Society, 131 (1984) 13.

[110] T. Martin, K. R. Hebert, Journal of the Electrochemical Society, 148 (2001) B101.

[111] J. H. Jeong, C. H. Choi, D. N. Lee, Journal of Materials Science, 31 (1996) 5811.

[112] H. Tsubakino, A. Nogami, Y. Yamamoto, A. Yamamoto, M. Terasawa, T. Mitamura, A. Kinomura, Y. Horino, Applied Surface Science, 238 (2004) 464.

[113] N. Osawa, K. Fukuoka, Corrosion Science, 42 (2000) 585.

[114] Z. Ashitaka, G. E. Thompson, P. Skeldon, G. C. Wood, H. Habazaki, K. Shimizu, Journal of the Electrochemical Society, 147 (2000) 132.

[115] H. Tsubakino, A. Nogami, T. Yamanoi, Applied Surface Science, 185 (2002) 298.

[116] J. Scherer, O. m. Magnussen, T. Ebel, R. J. Behm, Corrosion Science, 41 (1999) 35.

[117] R. A. Mirzoev, L.A. Pavlov, L.A. Kostelova, V. F. Pimenov, Journal of Applied Chemistry of the USSR, 63 (1990) 938.

[118] H. C. Chen, B. L. Ou, Journal of Materials Science: Materials in Electronics, 15 (2004) 297.

[119] K. Arai, T. Suzuki, T. Atsumi, Journal of the Electrochemical Society, 132 (1985) 1667.

[120] Y. W. Keuong, J. H. Nordlien, S. Ono, K. Nisancioglu, Journal of the Electrochemical Society, 150 (2003) B547.

[121] J. Song, W. Mao, H. Yang, H. Feng, Journal of Materials Science and Technology, 24 (2008) 718.

[122] W. Lin, G. Tu, C. F. Lin, Y. M. Peng, Corrosion Science, 39 (1997) 1531.

[123] H. C. Chen, B. L. Ou, Journal of Materials Science: Materials in Electronics, 15 (2004) 819.

[124] Z. Ashitaka, G. E. Thompson, P. Skeldon, G. C. Wood, K. Shimizu, Journal of the Electrochemical Society, 146 (1999) 1380.

[125] Y. Yu, Ø. Sævik, J. H. Nordlien, K. Nisancioglu, Journal of the Electrochemical Society, 152 (2005) B327.

[126] W. Lin, G. C. Tu, C. F. Lin, Y. M. Peng, Corrosion Science, 38 (1996) 889.

[127] Y. Minamino, T. Yasuda, H. Araki, T. Yasuda, Defect and Diffusion Forum, 66-69 (1989) 1251.

[128] A. Johansen, E. Johnson, L. Sarholt-Kristensen, S. Steenstrup, L. Yu, K. K. Bourdelle, Surface and Coatings Technology, 51 (1992) 461.

[129] P. Preuss. Brownian Motion in Metal. California: Berkeley lab, 2002.

[130] S. B. Saidman, S. G. Garcia, J. B. Bessone, Journal of Applied Electrochemistry, 25 (1995) 252.

[131] L. v. Alphen, P. Nauwen, J. Slakhort, Zeitschrift für Metallkunde, 70 (1979) 158.

[132] Z. Ashitaka. vol. Ph. D Thesis: University of Manchester Institute of Science and Technology (UMIST), 2004.

[133] Y. Tanno, E. Suganuma, Journal of The Surface Finishing Society of Japan, 58 (2007) 5.

[134] H. Asoh, K. Nakamura, S. Ono, Electrochimica Acta, 53 (2007) 83.

[135] H. Masuda, M.Tajima, K. Nishio, Chemistry Letter, 31 (2002) 1150.

[136] K. Nishio, K. Kanezawa, H. Masuda, Chemistry Letters, 35 (2006) 1096.

[137] S. Ono, K. Uchibori, H. Asoh, Surface and Interface Analysis, 42 (2010) 264.

[138] P. de Groot, R&D Technical Bulletin, Zygo Corporation, 9 (1993).

[139] Zygo, NewView 200 Operating Manual, OMP-0407C (1997).

[140] L. A. Giannuzzi, F. A. Stevie, Introduction to Focused Ion Beams: Instrumentation, Theory, Techniques and Practice. New York, Springer, 2004.

[141] A. J. Kubis, G. J. Shiflet, R. Hull, D. N. Dunn, Metallurgical and Materials Transactions A: Physical Metallurgy and Materials Science, 35 (2004) 1935.

[142] L. Holzer, F. Indutnyi, Ph. Gasser, B. Munch, M. Wegmann, J. Microsc. , 216 (2004) 84.

[143] S. Zaefferer, S. I. Wright, D. Raabe, Metallurgical and Materials Transactions A: Physical Metallurgy and Materials Science, 39 (2008) 374.

[144] P. G. Kotula, M. R. Keenan, J. R. Michael, Microscopy and Microanalysis, 12 (2006) 36.

[145] Zygo Corporation Omp-0362g Advanced Texture Metropro Application. 2004.

[146] G. Bäckström, Simple Fields by Finite Element Analysis. Malmö, Sweden, GB Publishing, 2005.

[147] F. Soldera, A. lasagni, F. Mücklich, T. Kaiser, K. Hrastnik, Computational Materials Science, 32 (2005) 123.

[148] W. T. Walter. Change in Reflectivity of Metals under Intense Laser Radiation. USA: Microwave Research Institute, 1981.

[149] A. Lasagni, M. D'Alessandria, R. Giovanelli, F. Mücklich, Applied Surface Science, 254 (2007) 930.

[150] M. D. Perry, B. C. Stuart, P. S. Banks, M. D. Feit, J. A. Sefcik, Ultrashort-Pulse Laser Machining. In: Ready JF, editor. Lia Handbook of Laser Material Processing. New York: Laser Institute of Amaerica, 2001. p.504.

[151] Q. Lu, S. S. Mao, X. Mao, R. E. Russo, Applied Physics Letters, 80 (2002) 3072.

[152] F. R. Sushmita, R. K. Thareja, Applied Surface Science, 222 (2004) 293.

[153] X. Chen, H.-X. wang, Journal of applied Physics D, 34 (2001) 2637.

[154] L. L. Kuznetsov, Quantum Electron., 23 (1999) 1035.

[155] M. von Allmen, W. Lüthy, K. Affolter, Applied Physics Letters, 33 (1978) 824.

[156] F. Nota, R. Savino, S. Fico, Acta Astronautica, 59 (2006) 20.

[157] D. K. Dijken, W. Hoving, J. T. M. De Hosson, Journal of Laser Applications, 15 (2003) 11.

[158] J. P. Longtin, K. Hijikata, K. Ogawa, International Journal of Heat and Mass Transfer, 42 (1999) 85.

[159] Y. P. Lei, H. Murakawa, Y. W. Shi, Y. Y. Li, Computational Materials Science, 21 (2001) 276.

[160] K. C. Mills, Y. C. Su, International Materials Reviews, 51 (2006) 329.

[161] A. Robert, T. Debroy, Metallurgical and Materials Transactions B, 32B (2001) 941.

[162] C. Limmaneevichitr, S. Kou, Welding Journal, 79 (2000) 231s.

[163] X. F. Peng, X. P. Lin, D. J. Lee, Y. Yan, B. X. Wang, International Journal of Heat and Mass Transfer, 44 (2001) 457.

[164] P. S. Mohanty, J. Mazumder, Lia Handbook of Laser Materials Processing. New York, Laser Institute of America 2001.

[165] L. D. Landau, E. M. Lifshitz, Statistical Physics, Part I. Oxford, Pergamon, 1980.

[166] R. Niedrig, O. Bostanjoglo, Journal of Applied Physics, 81 (1997) 480.

[167] D. Schwabe, A. Scharmann, F. Preisser, R. Oeder., Journal of Crystal Growth, 43 (1978) 305.

[168] W. Pitscheneder, T. DebRoy, K. Mundra, R. Ebner, Welding Journal, 75 (1996) 71.

[169] T. DebRoy, S. David, Rev. Mod. Phys., 67 (1995) 85.

[170] A. Matsunawa, Y. Shinichiro. Fluid Flow and Its Effect on Penetration Shape in Stationary Arc Welds. Recent Trends in Welding Science and Technology, eds. S. A. Ohio: ASM internationl, materials Park, 1990. p.31.

[171] J. A. Maroto, V. Pe?rez-Mu?uzuri, M. S. Romero-Cano, European Journal of Physics, 28 (2007) 311.

[172] M. Tanaka, H. Terasaki, M. Ushio, J. J. Lowke, Plasma Chemistry and Plasma Processing, 23 (2003) 585.

[173] D. R. Atthey, Journal of Fluid Mechanics Digital Archive, 98 (2006) 787.

[174] Y. Joshi, P. Dutta, D. espinosa, P. Schupp, Transactions ASME Jourmal of heat transfer, 119 (1997) 164.

[175] N. Chakraborty, Numerical Heat Transfer, 53 (2008) 273.

[176] W. Mao, J. Hirsch, K. Lücke. Influence of the Cube Starting Texture on Rolling and Recrystallization Texture Development. In: J. S. Kallend, Gottstein G, editors. The Metallurgical Society Inc. Pennsylvania, 1988. p.613.

[177] J. Xu, W. Mao, W. Feng, The Chinese Journal of Nonferrous Metals, 11 (2001) 42.

[178] N. Mateescu, M. Ferry, W. Xua, J. M. Cairney, Materials Chemistry and Physics, 106 (2007) 142.

[179] EDAX, TSL Data Collection Manual, EDAX Inc., (2006).

[180] W. Mao, L. Cheng, P. Ying, H. Huiping, Chinese Science Bulletin, 49 (2004) 2112.

[181] A. Atkinson, Reviews of Modern Physics, 57 (1985) 437.

[182] L. P. H. Jeurgens, W. G. Sloof, F. D. Tichelaar, E. J. Mittemeijer, Thin Solid Films, 418 (2002) 89.

[183] S. M. Metev, S. K. Savtchenko, K. V. Stamenov, V. P. Veiko, G. A. Kotov, G. D. Shandibina, IEEE Journal of Quantum Electronics, QE-17 (1981) 2004.

[184] W. C. Sleepy, Journal of the Electrochemical Society, 108 (1961) 1097.

[185] S. A. Impey, D. J. Simensen, P. Kofstad, Materials Science and Engineering A, 4 (1988) 1126.

[186] I. Ursu, L. Nanu, I. N. Mihailescu, Applied Physics Letters, 49 (1986) 109.

[187] H. Kaesche, Corrosion of Metals - Physicochemical Principels and Current Problems. Heidelberg, Springer, 2003.

[188] J. H. Ryu, J. H. Seo, J. H. Jeong, S. K. Kim, D. N. Lee, Journal of Applied Electrochemistry, 34 (2004) 879.

[189] J. Osher, F. Mücklich, Statistical Analysis of Microstructures in Materials Science. New York, Wiley, 2000.

[190] M. Hansen, N. Anderko, Constitution of Binary Alloys. New-york, McGraw-Hill, 1958.

[191] S. N. Tewari, Y.-H. Weng, G. L. Ding, R. Trivedi, Metallurgical and Materials Transactions A: Physical Metallurgy and Materials Science, 33A (2002) 1229.

[192] S. N. Tewari, Journal of Materials Science Letters, 8 (1989) 1098.

[193] K. I. Moore, D. L. Zhang, B. cantor, Acta Metallurgica Et Materialia, 38 (1990) 1327.

[194] E. Johnson, A. Johansen, S. Hinderberger, S. Q. Xiao, U. Dahmen, Interface Science, 3 (1996) 279.

[195] Y. Yu, Ø. Sævik, J. H. Nordlien, K. Nisancioglu. Characterization of Electrochemically Activated Surface on Rolled Commercial Aa8006 Alumnium. Materials Research Society Symposium Proceedings, vol. 843, 2005. p.347.

[196] Ø. Sævik, Y. Yu, J. H. Nordlien, K. Nisancioglu, Journal of the Electrochemical Society, 152 (2005) B334.

[197] J. R. Davis, Asm Speciality Handbook: Copper and Copper Alloys
Portland, Book News, Inc., 2001.

[198] I. Bakos, S. Szabo, Corrosion Science, 50 (2008) 200.

[199] R. Baboian. Localized Corrosion - Cause of Metals Failure. In: Henthorne M, editor. Annual Meeting of the American Society for Testing and Materials, vol. 2. Atlantic City, NJ: Carpenter Technology Corp., 1972. p.329.

[200] J. R. Wiersma, K. R. Hebert, Journal of the electrochemical society 138 (1991) 48.

[201] D. G. W. Goad, H. Uchi, Journal of Applied Electrochemistry, 30 (2000) 285.

[202] R. g. Xiao, K. p. Yan, J. x. Yan, J. z. Wang, Corrosion Science, 50 (2008) 1576.

[203] K. R. Hebert, R. C. Alkire, Journal of the Electrochemical Society, 135 (1988) 2447.

[204] Y. Zhou, R. Hebert, Journal of the Electrochemical Society, 145 (1998) 3100.

[205] J. T. B. Gundersen, A. Aytac, J. H. Nordlien, K. Nisancioglu, Corrosion Science, 46 (2004) 697.

[206] J. Armbrecht, T. Sych, K. Robb, Mavi - Modular Algorithms for Volume Images V1.2.2, Fraunhofer Institut für Techno- und Wirtschaftsmathematik (ITWM), 2006.

[207] J. C. Russ, R. T. Dehoff, Practical Stereology. New York, Plenum Press, 1999.

Appendix A

Periodic structures created on metal surfaces at different fluences and laser configurations:

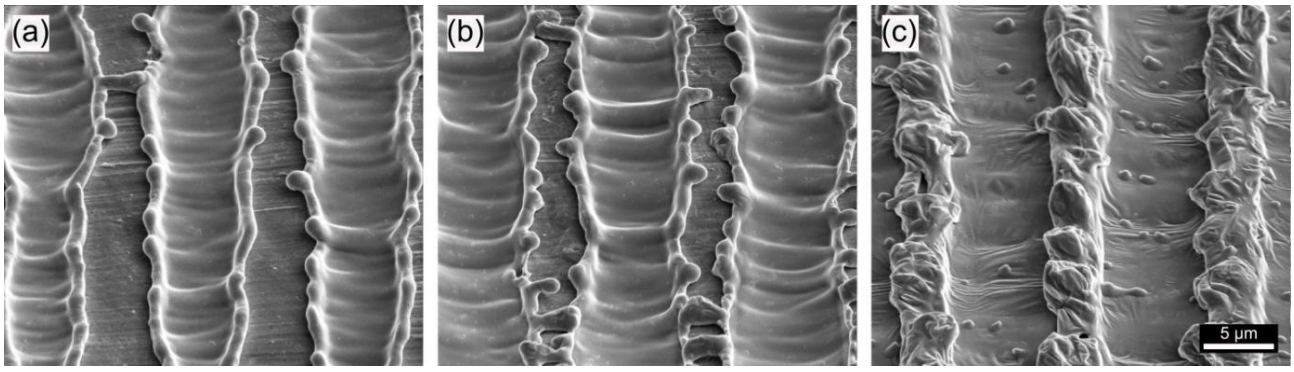

Appendix A.1 Periodic line-like structure on aluminium samples obtained by using two laser beams and symmetrical configuration. The selected laser fluences were: (a) 1287 mJ/cm^2, (b) 2070 mJ/cm^2 and (c) 2300 mJ/cm^2. Period: 10 µm. Tilt angle: 52°.

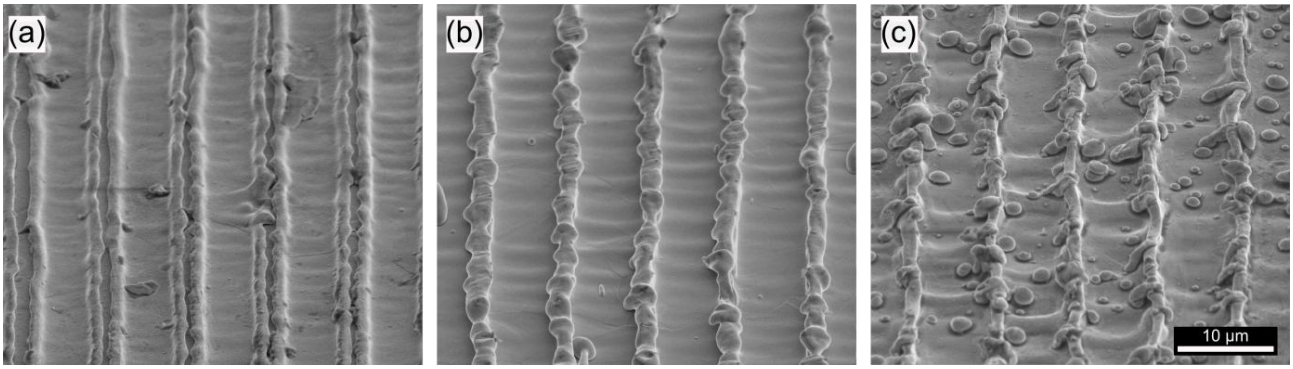

Appendix A.2 Periodic line-like structure on copper samples obtained by using two laser beams and symmetrical configuration. The selected laser fluences were: (a) 1507 mJ/cm^2, (b) 1900 mJ/cm^2 and (c) 2443 mJ/cm^2. Period: 7.5 µm. Tilt angle: 52°.

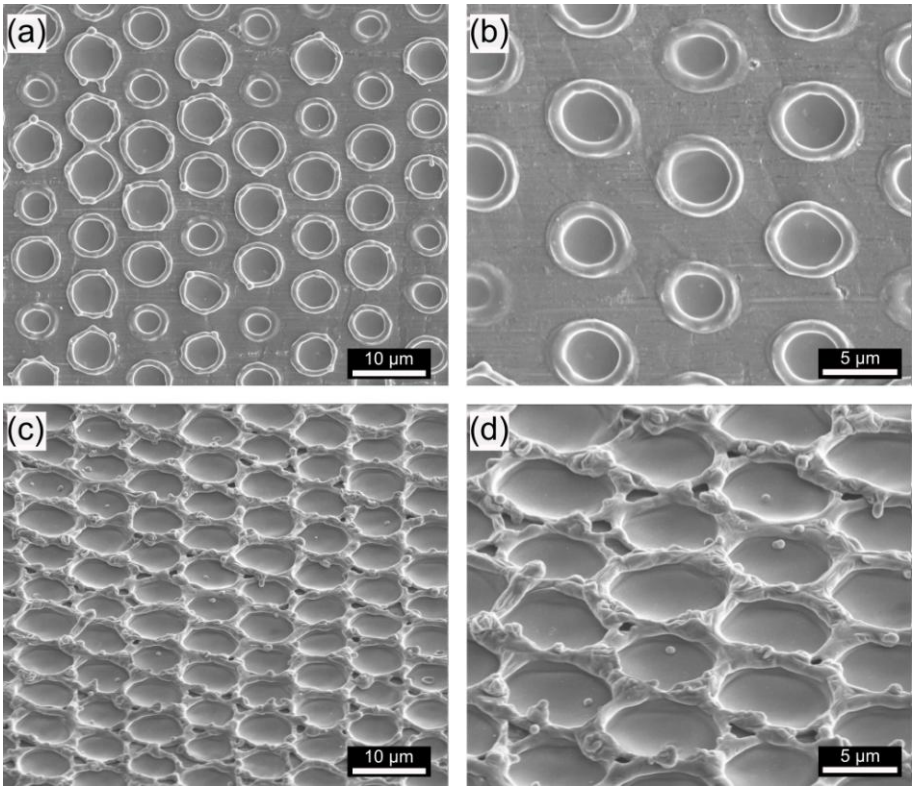

Appendix A.3 Periodic dot-like structure on aluminium samples obtained by using three laser beams and symmetrical configuration. The selected laser fluences were: (a,b) 1200 mJ/cm^2 and (c,d) 1770 mJ/cm^2. Tilt angles: (a, b) 0° and (c, d) 52°.

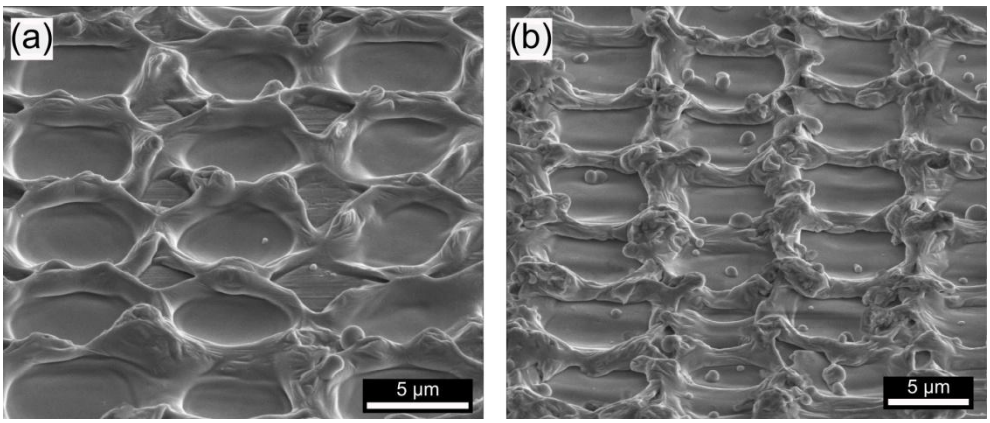

Appendix A.4 SEM images of periodic dot-like structure on aluminium samples obtained by using four laser beams and asymmetrical configuration. The selected laser fluences were: (a) 1445 mJ/cm^2, and (b) 1910 mJ/cm^2. Tilt angle: 52.

APPENDIX B

Properties of metals

Aluminium (Al)

Property		Symbol	Value
Melting temperature		T_m (K)	933
Boiling temperature		T_b (K)	2792
Latent heat of melting		L_m (J/g)	397
Latent heat of vaporisation		L_b (J/g)	10860
Density	(solid)	ρ (g/m^3)	$2.7 \cdot 10^6$
	(liquid)		$[2.365-(3.2 \cdot 10^{-4}) \times (T-T_m)]\ 10^6$
Thermal conductivity	(solid)	κ (W/m·K)	$[186.02+0.3271 \times T-6 \cdot 10^{-4} \times T^2+3 \cdot 10^{-7} \times T^3]$
	(liquid)		237 (at T_m)
Specific heat capacity	(solid)	c_p (J/g·K)	$0.1552 \cdot (4.94+2.96 \cdot 10^{-3} \times T)$
	(liquid)		0.897 (at T_m)
Reflectivity		R	0.93 (at λ= 355 nm)
Absorption coefficient		α (m^{-1})	$1.52 \cdot 10^8$
Dynamic viscosity		η (Kg/m·s)	$1.1 \cdot 10^{-3}$
Surface tension		γ (mN/m)	1070
Surface tension gradient		$\left\lvert d\gamma/dT \right\rvert$ (N/m·K)	$3.5 \cdot 10^{-4}$
Volume expansion coefficient		β_T (K^{-1})	$6.93 \cdot 10^{-5}$

Copper (Cu)

Property		Symbol	Value
Melting temperature		T_m (K)	1357
Boiling temperature		T_b (K)	2835
Latent heat of melting		L_m (J/g)	204.89
Latent heat of vaporisation		L_b (J/g)	4796
Density	(solid)	ρ (g/m^3)	$8.92 \cdot 10^6$
	(liquid)		$[8.0-8.01 \cdot 10^{-4} \times (T-T_m)] \cdot 10^6$
Thermal conductivity	(solid)	κ (W/m·K)	$4 \cdot 10^{-6} \times T^2-0.0737 \times T+422$
	(liquid)		400 (at T_m)
Specific heat capacity	(solid)	c_p (J/g·K)	$0{,}06589 \times (5.41+0.0014 \times T)$
	(liquid)		0.49 (at T_m)
Reflectivity		R	0.434 (at λ= 355 nm)
Absorption coefficient		α (m^{-1})	$6.7 \cdot 10^7$
Vapour pressure		P_s (N/m^2)	$101300 \times \mathrm{Exp}\ [3 \cdot 10^5 \times (T-T_b)/\ (8.31451 \cdot T \times T_b)]$
Dynamic viscosity		η (Kg/m·s)	$4.0 \cdot 10^{-3}$
Surface tension		γ (mN/m)	1320
Surface tension gradient		$\left\lvert d\gamma/dT \right\rvert$ (N/m·K)	$2.8 \cdot 10^{-4}$
Volume expansion coefficient		β_T (K^{-1})	$4.95 \cdot 10^{-5}$

Titanium (Ti)

Property		Symbol	Value
Melting temperature		T_m (K)	1941
Boiling temperature		T_b (K)	3560
Latent heat of melting		L_m (J/g)	295.6
Latent heat of vaporisation		L_b (J/g)	8895
Density	(solid)	ρ (g/m^3)	$4.51 \cdot 10^6$
	(liquid)		$[4.11-7.02 \cdot 10^{-4} \times (T- T_m)] \cdot 10^6$
Thermal conductivity	(solid)	κ (W/m·K)	22
	(liquid)		30
Reflectivity		R	0.443
Absorption coefficient		α (m^{-1})	$7.13 \cdot 10^{13}$
Dynamic viscosity		η (Kg/m·s)	0.0052
Surface tension		γ (mN/m)	1670
Surface tension gradient		$\left\lvert d\gamma/dT \right\rvert$ (N/m·K)	$1.6 \cdot 10^{-4}$

APPENDIX C

Oxide layer formed during laser structuring of aluminium

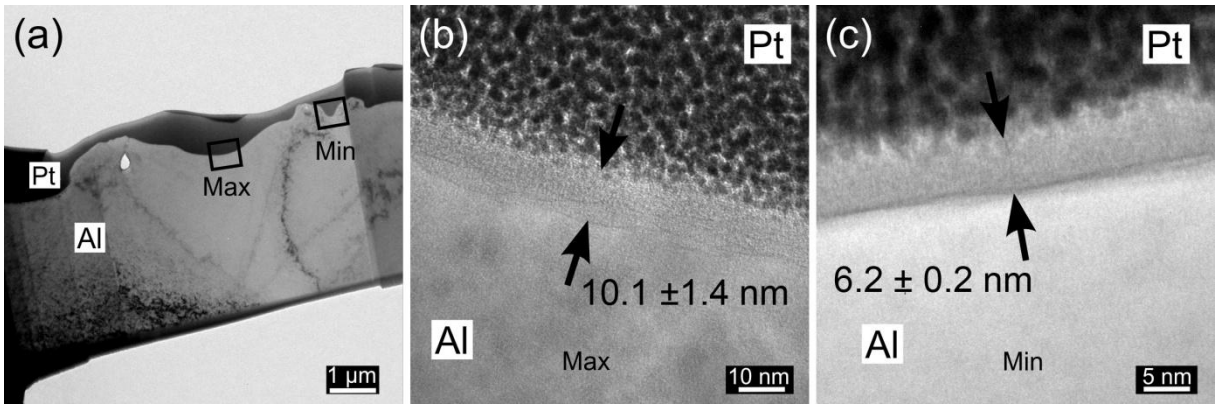

Appendix C.1 TEM investigation of the oxide layer formed during laser structuring of Al foil. The laser fluence used was 970 mJ/cm^{-2}.(a) TEM lamella showing the maximal and minimal interference positions; (b-c) high magnifications of oxide layer thickness at the maximal and minimal interference zones, respectively.

APPENDIX D

Additional information about Pb/Al system:

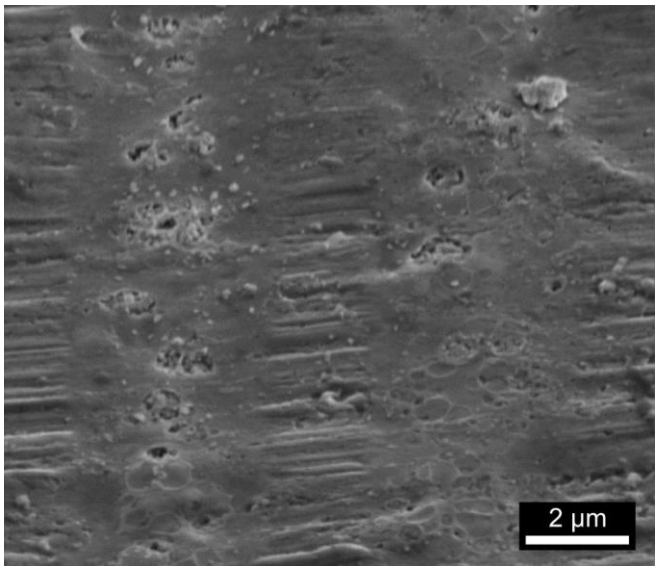

Appendix D.1 SEM image of the Pb(10)/Al sample presented in Fig. 7.2 a, b showing the un-etched areas. Etchant conditions: 1N HCl at 85°C for 30 s. Laser parameters: line-like pattern, F= 1000 mJ/cm^2, d= 5.7 µm.
Tilt angle: 52°.

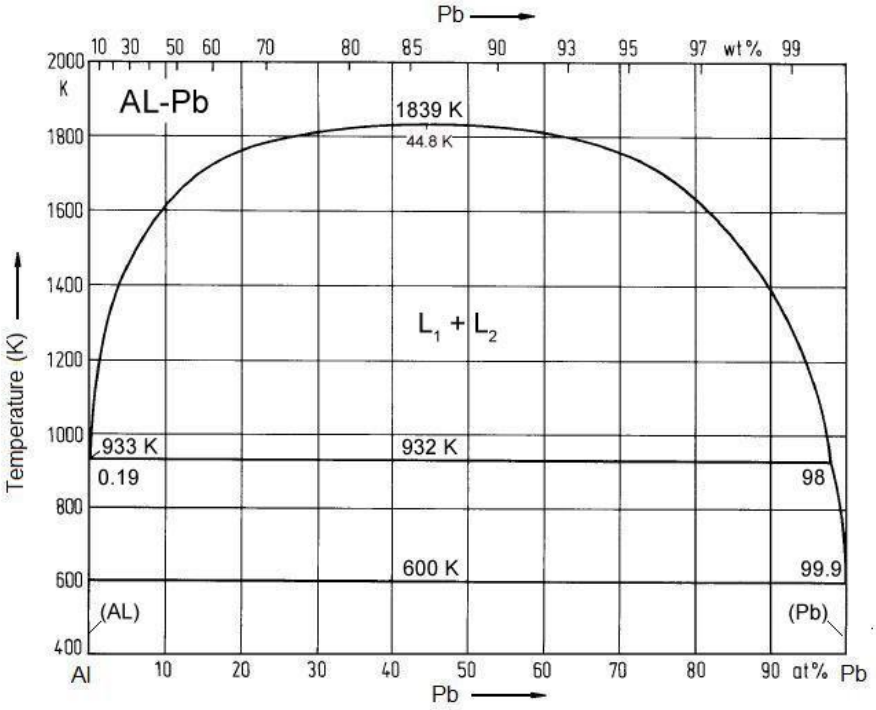

Appendix D.2 Aluminium–lead phase diagram.

Morphology of patterned Cu/Al after etching

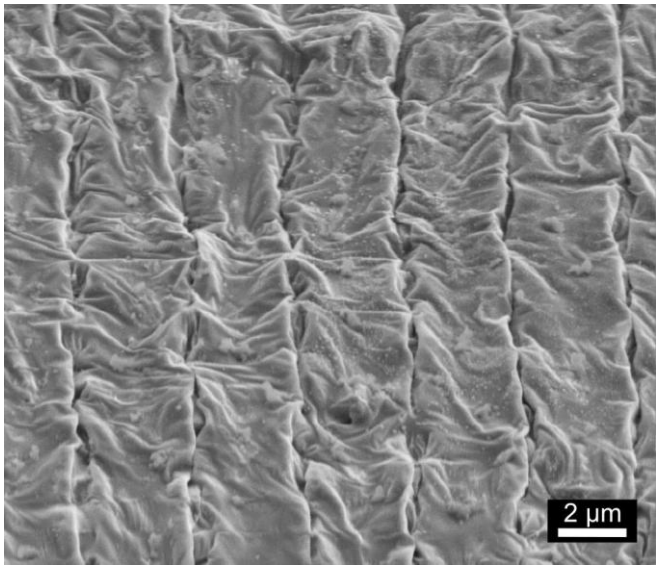

Appendix D.3 SEM image after etching of the Cu(10)/Al structured at high laser fluence, confirming the unetched surface. Etchant conditions: 1N HCl at 85°C for 30 s. Laser parameters: line-like pattern, F= 1603 mJ/cm^2, d= 3.3 µm. Tilt angle: 52°.

APPENDIX E

Additional information on aluminium foil and Pb/Al for 3D characterisation

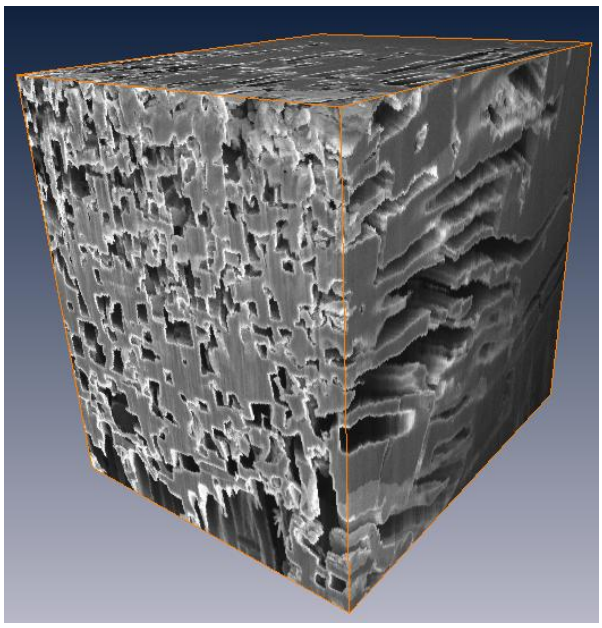

Appendix E.1 Reconstructed tunnel morphology of electrochemically etched aluminium foil. The tunnel deformation produced during the section cut is easily visible.

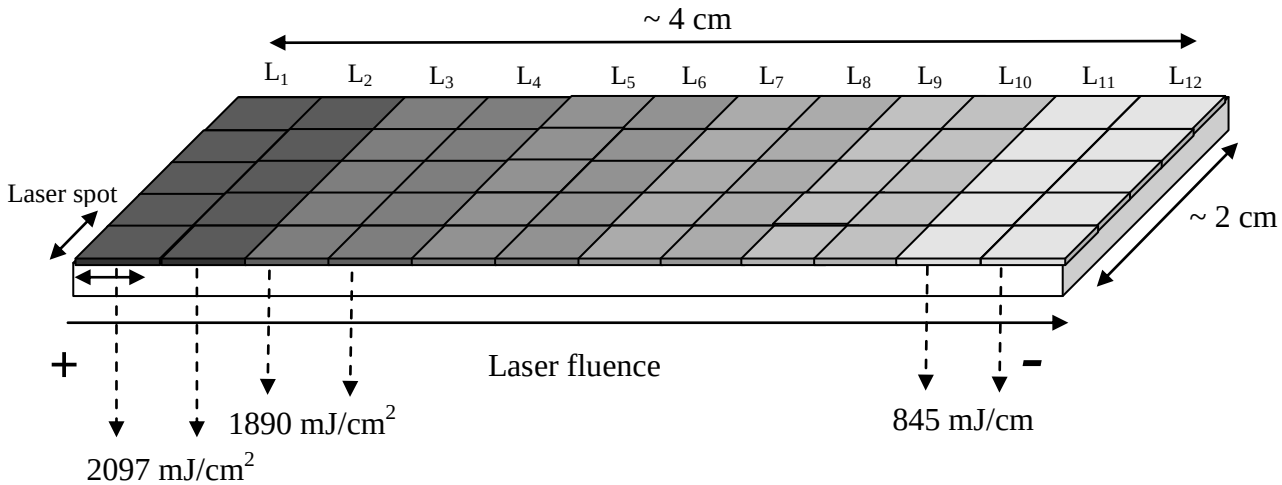

Appendix E.2 Schematic illustration of Pb(10)/Al sample structured with three laser beams by using a combinatory arrangement of laser fluences ranging from 845 to 2097 mJ/cm^2.

Table E.1 Description of the fluence values used during the structuring of Pb(10)/Al presented in Appendix E.2.

Structured lines	L_1–L_2	L_3–L_4	L_5–L_6	L_7–L_8	L_9–L_{10}	L_{11}–L_{12}
Fluences (mJ/cm^2)	2097	1890	1648	1421	1185	845

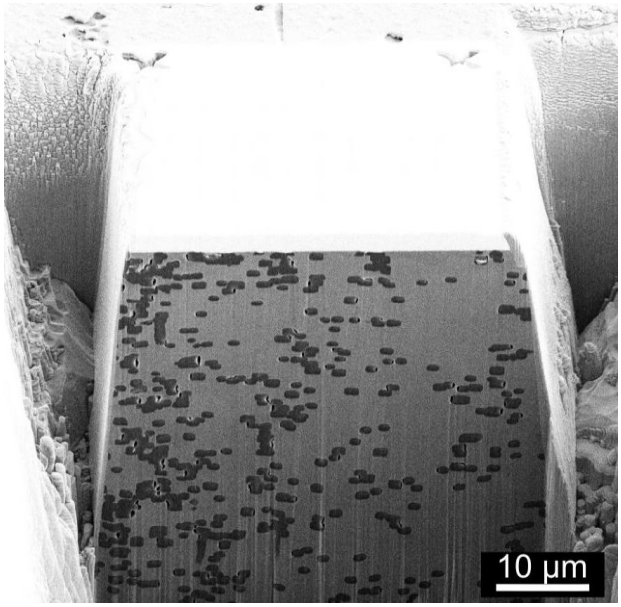

Appendix E.3 SEM image of structured Pb(10)/Al showing the initial tunnel-pit morphology. Structuring conditions: dot-like pattern and 845 mJ/cm^2 laser fluence. Tilt angle: 52°.